NONLINEAR TRANSFORMATIONS AND FILTERING THEORY FOR SPACE OPERATIONS

A Dissertation

by

RYAN MICHAEL WEISMAN

Submitted to the Office of Graduate Studies of
Texas A&M University
in partial fulfillment of the requirements for the degree of

DOCTOR OF PHILOSOPHY

Approved by:

Co-Chairs of Committee,	Kyle T. Alfriend
	John Valasek
Committee Members,	James D. Turner
	Alexander G. Parlos
Department Head,	Rodney D. W. Bowersox

December 2012

Major Subject: Aerospace Engineering

ABSTRACT

Decisions for asset allocation and protection are predicated upon accurate knowledge of the current operating environment as well as correctly characterizing the evolution of the environment over time. The desired kinematic and kinetic states of objects in question cannot be measured directly in most cases and instead are inferred or estimated from available measurements using a filtering process. Often, nonlinear transformations between the measurement domain and desired state domain distort the state domain probability density function yielding a form which does not necessarily resemble the form assumed in the filtering algorithm. The distortion effect must be understood in greater detail and appropriately accounted for so that even if sensors, state estimation algorithms, and state propagation algorithms operate in different domains, they can all be effectively utilized without any information loss due to domain transformations.

This research presents an analytical investigation into understanding how nonlinear transformations of stochastic, but characterizable, processes affect state and uncertainty estimation with direct application to space object surveillance and spacecraft attitude determination. Analysis is performed with attention to construction of the state domain probability density function since state uncertainty and correlation are derived from the statistical moments of the probability density function. Analytical characterization of the effect nonlinear transformations impart on the structure of state probability density functions has direct application to conventional nonlinear filtering and propagation algorithms in three areas: (1) understanding how smoothing algorithms used to estimate indirectly observed states impact state uncertainty, (2) justification or refutation of assumed state uncertainty distributions

for more realistic uncertainty quantification, and (3) analytic automation of initial state estimate and covariance in lieu of user tuning.

A nonlinear filtering algorithm based upon Bayes' Theorem is presented to account for the impact nonlinear domain transformations impart on probability density functions during the measurement update and propagation phases. The algorithm is able to accommodate different combinations of sensors for state estimation which can also be used to hypothesize system parameters or unknown states from available measurements because information is able to appropriately accounted for.

DEDICATION

For all those who have gone before,

Thank you for the impact on my life.

Harry Weisman II

Jerome Beach

Steven Beach

Darrell Beach

Caroline Weisman

Christopher Boyle

Marg Davidson

Dorothy Schisler

Serenity Prayer:

"God grant me the Serenity to accept the things I cannot change,

the Courage to change the things I can,

and the Wisdom to know the difference."

ACKNOWLEDGEMENTS

First and foremost, I would like to thank my co-chairs, Dr. Kyle T. Alfriend and Dr. John Valasek, who have been sources of great insight throughout my time at Texas A&M. Without Dr. Valasek, I never would have attended Texas A&M nor been given the opportunity to work with and conduct analysis on actual flying experimental unmanned aerial vehicles. Dr. Alfriend was kind enough to agree to advise me upon my receipt of a scholarship for researching astrodynamics, and has provided a much needed perspective on what is available and what is lacking in the community. I would also like to thank my other committee members, Dr. James D. Turner and Dr. Alexander G. Parlos, who graciously agreed to be on my committee and have given great feedback both for research and academic studies.

I would like to thank Dr. Manoranjan Majji, who served as the spark to this research path and whose advice along the way has been invaluable and much appreciated. I am grateful to Dr. Drew Woodbury for lending his advice and experience to my many different endeavors. I would also like to thank colleagues I have been able to work with during my past summer internships. Dr. Morgan Baldwin and Dr. Shawn Allgeier gracefully allowed me to use them as sounding boards for my research approach while Dr. Moriba Jah and Dr. Kyle DeMars gave much needed insight into research areas and current approaches. While in College Station, both Dr. Anshu Narang-Siddarth and Matthew Harris provided valuable discussions and much appreciated outside perspectives on my research approach and results.

I am very much indebted to Dr. Agamemnon Crassidis, without whom I would not be where I am today. It is because of his advisement and continuous encouragement during my undergraduate and master of science work that I considered going

farther than I ever thought I could go. Even though I had to attend a different institution to pursue my Ph.D., Dr. Crassidis was always there to provide advice when I needed it, both inside and outside the academic arena.

Last but not least, I would like to thank all of my friends and family who have helped and supported me along my long and winding journey through undergraduate and graduate studies. Neither I or they had any clue about where my academic pursuits would take me, but they were always there time and time again to offer their love, support, and understanding, even though they were not sure what I was talking about.

TABLE OF CONTENTS

LIST OF FIGURES

FIGURE Page

LIST OF TABLES

TABLE Page

1. INTRODUCTION

Whenever measurements of an object's parameters are recorded, e.g. size, shape, distance and/or angle from observer, they are subject to measurement error typically characterized by a metric known as the standard deviation [1]. The standard deviation is a statistical measure representing the amount by which the measured parameter can vary, thereby producing a region about the measurement which the truth is deemed to lie inside. The shape of the region is dictated by the probability density function [2] which is an analytical expression of the shape of the uncertainty region centered upon the measurement. Sometimes, the probability density function requires more than the standard deviation to describe the uncertainty region, but these parameters are always available when the analytical expression of the uncertainty region is reported. Many a time, one wishes to compute the uncertainty associated with an indirect parameter which can be computed from the measured parameters, e.g. Cartesian position with respect to the observer when only range and angle measurements are available. The transformation of uncertainty from one set of basis functions, i.e. measurement space, to a new set of basis functions, such as Cartesian position, requires careful attention to insure that all uncertainty information will be conserved when the transform is applied. This is especially true when the object is undergoing motion subject to nonlinear differential equations utilizing state parameters that are nonlinearly related to measurement of the motion.

Examination of the effect nonlinear transformations impart on state estimation and uncertainty characterization is conducted by assessing how a known analytic form of a probability density function is altered when the given set of basis functions are exchanged for a new set of basis functions to allow for more convenient problem

analysis. An example of such an alteration is the exchange of Cartesian coordinates for description of rectilinear motion while the object is observed using line-of-sight range and angle measurements. Junkins et al. [3] demonstrated that different state coordinate choices produced different results with respect to the accuracy of state uncertainty computed by the use of linear error theory for propagation. Since the physics underlying object motion are apathetic to the coordinate system chosen to mathematically describe the motion, it is clear that the effect of nonlinearity on state uncertainty is not appropriately characterized if different state coordinate descriptions produce different estimates. To minimize the effect of the nonlinearity between the two domains, one would typically choose a state coordinate system which is most conducive to the observed motion [3, 4] such as spherical coordinates for curvilinear motion or Cartesian coordinates for rectilinear motion since these choices produce the most linear forms of the equations of motion.

For problems such as orbital motion, a myriad of coordinate descriptions exist to allow for relatively easy analysis of motion [5], e.g. surveillance, rendezvous, perturbation analysis, uncertainty analysis, etc. For orbital motion, it has been repeatedly shown that using either Keplerian or equinoctial elements for state propagation preserves the initial probability density function character of the state uncertainty longer than other state representations [3, 6, 7]. The length of time that certain state representations will maintain their initial uncertainty character vary drastically depending upon orbit type. Junkins et al. [3] demonstrated that propagation of the Cartesian representation of uncertainty for an orbit possessing an eccentricity of 0.2, a perigee altitude of 300 kilometers, and subjected to drag will remain Gaussian for approximately half of the orbit period. Sabol et al. [7] demonstrated that, for a relatively circular low Earth orbit subjected to only the J_2 perturbation, propagation of the Cartesian representation of uncertainty remained Gaussian for up to approximately

three days while the equinoctial element representation remained Gaussian for up to ten days. Both Junkins et al. [3] and Sabol et al. [7] noted that the first and second moment of the true distribution were matched fairly well by the Cartesian representation, this demonstrated that merely matching the first and second moment of a probability density does not imply that the higher moment character or correlation is appropriately characterized.

Scheeres et al. [8] proposed fundamental limits on spacecraft orbit uncertainty propagation for Keplerian motion in the Cartesian domain, however the uncertainty distribution was required to be Gausssian at the orbit epoch. For increased accuracy in propagation of state estimates and the associated covariance, higher-order state transition tensors have been explored to provide corrections to the propagated mean and covariance once the state domain is established, such as Cartesian elements shown by Park and Scheeres [9] or orbital Poincaré elements shown by Fujimoto et al. [10]. Higher-order state transition tensors and universal elements was proposed by Majji [11] for solution to the Two-Body problem and could be used in lieu of the approach of Fujimoto [10]. The data structure and procedure for higher-order tensor calculations outlined by Turner [12] generated a perturbation model determined by the nonlinear system's solution. This approach allowed for solutions to open and closed loop control and was used by Majji et al. [13, 14] for estimation of dynamic system estimation in the form of the J^{th} Moment Extended Kalman Filter (JMEKF) and its perturbed variant (PJMEKF).

Even with the use of the state coordinate system which best preserves the initial uncertainty character during propagation, significant nonlinearities are introduced when observing object motion. The degree of nonlinearity introduced to the system by the observations requires appropriate quantification to make sure assumptions of the applied state estimation routine are not violated. Violation of the estimation

algorithm assumptions with respect to uncertainty character typically stem from an invalid linearization range within the state domain or an assumed state posterior density form. The nonlinear mapping between coordinate descriptions of the same space can significantly impact the amount of uncertainty associated with the state estimate, especially if the nonlinearity is significant at orders higher than one or the measurement probability density function is not symmetric.

Alteration of the probability density function due to the exchange of domains must be careful examined and understood since state estimate and uncertainty computations are derived from an approximated posterior probability density function. The posterior probability density is calculated by Bayes' Theorem which optimally combines present statistical observation information with previous statistical knowledge [2]. Approximation of the posterior probability density function to compensate for the change of domains is performed by either sampling the probability density function [15] or by assuming the probability density function can be characterized by only the first and second moments [16]. Approximation of the probability density function in the form of the first and second moments, mean and covariance, can produce different state estimates and confidence levels depending upon the degree of nonlinearity possessed by the transform, either between the measurement and state domains or the present and future state domains.

Vallado and Seago [17] sought to find statistical tests of hypotheses to aid in assessment of whether or not the propagated position covariance could be considered realistic. However, their definition of a "realistic" covariance needed the true error distribution be multivariate normal and zero mean, which required high accuracy observation data and orbit determination solutions. Additionally, even with the normality hypothesis accepted, the covariance computed by the batch orbit determination process was found to be biased or incorrectly scaled. The bias and incorrect

scaling of the covariance result is common to the differential corrections process since the bias tends to zero and the uncertainty decreases as the number of observations increases. The concept of covariance realism is utilized in this research and used interchangeably with covariance accuracy. A covariance is considered realistic if it agrees well in comparison with the true covariance computed numerically via Monte Carlo analysis of the modeled process. Computation of a realistic covariance and appropriate characterization of higher-order statistical moments of a multivariate state distribution requires the probability density function of the state domain be appropriately constructed. The derived probability density function must correctly account for the mapping of statistical information available from either the measurement domain at present time or the state domain at a previous time. Commonly, the distortion of range and angle measurements are debiased [18, 19] to form a better Cartesian position and position uncertainty estimate. However, these proposed corrections are developed only for statistical distributions that are symmetrical in nature and more importantly Gaussian. If the sensor probability density function is not Gaussian or cannot be completely characterized by the first two statistical moments, the debiased solution could lead to a biased estimate.

The transformation of variables technique [2] allows for exact mapping of the probability density function given in a specified domain into a different domain. The technique allows for the exact expression of the probability density function in a desired domain when (1) the analytic form of probability density function is known in a different domain and (2) the mapping between initial and desired domains is known, is at least once differentiable, and is bijective. The exact mapping produces precise knowledge of the system likelihood distribution, statistical characterization of present measurement knowledge, to allow for a better idea of the combination of system states which generated the measurement. Since the likelihood distribution

is exactly mapped between domains, Bayesian estimation can be easily carried out given the prior distribution is appropriately characterized, previous knowledge in statistical form. The posterior probability produced from Bayes' Theorem allows for availability of all statistical moments and not just the mean and covariance as with conventional filtering techniques. Availability of the state probability density function given a single measurement set can allow for automation of the covariance initialization needed for conventional filtering, thereby decreasing the amount of tuning needed to ensure proper filter operation. For systems requiring multiple observation times to be rendered observable, the transformation of variables approach can be applied to assess the amount of uncertainty associated with the smoothing process used to compute all observed states at a particular time instant.

The application of Bayes' Theorem for object surveillance applications has been explored previously, but in different capacities. Stone et al. [20] showed an application of Bayesian filtering to submarine and surface ship position and velocity estimation as well as object association/correlation via multiple hypothesis testing. However, domain transformations between sensing and state were not considered. Studies on correlating and tracking space debris [21] as well as asteriod orbit determination, sensor tasking, and collision probability [22–24] have been carried out, but utilized statistical sampling techniques, i.e. Markov Chain Monte Carlo, to numerically compute the posterior distribution of the desired state domain utilizing angular measurements with proposed range and range-rate domains. However, these methods were shown to be computationally burdensome and required proposing an initial prior distribution of the desired states as well as an acceptance criteria for proposed points. The proposed prior densities were computed multiple ways including trial and error, multiple Markov Chain Monte Carlo runs [21], multiplication of batch least-squares analysis with different scaling constants and application of a

chi-squared acceptance criteria [22,23], or normalizing the prior distribution to make it invariant to domain transformation [24]. The statistical sampling algorithms were found to be extremely sensitive to the proposed prior distribution which could stem from the algorithms' dependence upon log-likelihood of the measurements' multivariate Gaussian distribution. The studies did not account for the domain transform affect on the scalar multiplying the exponential term which is typically not constant, e.g. the polar to Cartesian transform [25].

The transformation of variables technique has been previously used in the astrodynamics community to examine the probability density function of eccentric anomaly given the probability density of mean anomaly over a range of eccentricity values [26]. The generalization of the transformation of variables technique via use of the Dirac Delta function [27], with further examples given by [28–30], has been utilized by Izzo [31–33] to intuit the spatial density of orbital debris or asssess the effect of orbital element distributions on the distributions of spherical observations or the square of velocity. Meshcheryakov [34, 35] used the Dirac generalization to compute the singly-averaged spatial density of orbital debris and a uniform field of particles for application to collision and impact analysis. For these applications however, the distribution of the orbital elements was treated as a known instead of an unknown, which is opposite of the problem of state estimation using spherical measurements with characterized uncertainty.

In a recent contribution, Weisman et al. [25] applied the transformation of variables technique for nonlinear sequential state estimation of linear and nonlinear systems where Cartesian state estimates and uncertainties were computed and compared to Monte Carlo results for position and velocity and position only polar measurements. The likelihood density function computed from the transformation of variable technique was found to closely track the Monte Carlo uncertainty results for

the cases considered and allowed for automated initialization of conventional nonlinear sequential state estimation routines and even improved convergence properties of the extended Kalman filter [25, 36]. The studies also showed that with available previous data, the transformation of variables procedure could be applied to compute the prior density function, thereby allowing for a Bayesian filter or smoother to be implemented. Additionally, Weisman et al. [36] were able to apply the technique for estimation of state uncertainty and state correlation stemming from an analytic initial orbit determination routine where position measurements are linked via Two-Body dynamics to estimate the object's velocity at a given time.

The approach of applying transformation of variables in a Bayesian filter framework for astrodynamic state estimation and uncertainty is in contrast to the method of Fujimoto and Scheeres [37–39], for initial orbit determination because the uncertainty is computed directly from the analytical form of the measurement probability density function instead of numerically computed from Monte Carlo analysis over a pre-defined region. The method is also different from statistical sampling techniques [21–24] since the posterior is computed analytically from the transformed likelihood and prior density functions, centered only upon the recorded measurements, instead using heuristically proposed prior densities, scaled likelihood densities, or a linear transformation of covariance.

With regard to propagation of probability density functions, Majji et al. [40] were able to demonstrate that if an initial probability density function was analytically available then the propagation of uncertainty for Two-Body motion in Keplerian variables without any perturbations was able to be effectively carried out through use of the technique. It was shown that the solution flow of the Keplerian variables inherently satisfied Liouville's Equation, the Fokker-Planck-Kolmogorov Equation without diffusion, due to the linear time update for mean anomaly.

In addition to space surveillance, the idea of using probability density functions for spacecraft attitude filtering was addressed by Shuster [41] who found that the Wahba problem was equivalent to that of maximum likelihood estimation of sensor measurement probability density functions. Additionally, measurements could be examined to judge whether or not they were defective and measurements from various sources could be integrated together for processing [42], such a practice is commonly called Data Fusion. However, maximum likelihood estimation does not provide an easily understandable form of uncertainty associated with the state estimate since most conventional state estimation routines utilize the minimum variance error criterion for their derivation.

The transformation of variables technique has been applied in other disciplines for solution of what is known as the "inverse problem" where "data from indirect measurements are used to estimate unknown parameters of physical systems" [43]. Mosegaard and Tarantola [43] presented the technique for computation of spatial domain probabilities for application of Bayes' Theorem in seismology and considered the example of estimating the probability density function of an object's position as it fell in a constant gravity field but, the corrupted position and velocity measurements were in the same domain as the dynamic model state variables. Kadry [44] paired the transformation of variables technique with conventional finite element analysis for improvement of the solution of stochastic differential equations for structural analysis, but noted that the technique was hard to generalize due to the nonhomogenity of stiffness matrix.

The need for the transformation to be bijective can lead to problems in mapping probability density between domains all in one step since there are times when the desired domain has a smaller number of basis functions than the initial domain. In this case, auxiliary variables [2] can be utilized to make the transform one-to-one

with a nonsingular determinant of the differential volumes, the auxiliary variables are then integrated over to produce the desired probability density function. For bijective cases involving circular functions, i.e. trigonometric functions, the domain must be split up into regions of bijectivity then summed together for the complete solution. An alternative to using auxiliary variables is the use of the Dirac Delta function [27] where the roots to the transformation still need to be available and a partial derivative computed, but the need for a computing a large matrix determinant is alleviated.

The rest of this dissertation is outlined as follows: Section 2 presents background theory on propagation of dynamical system states via use of the state transition and parameter sensitivity matrices as well as canonical transformations which allow for alleviation of nonlinear equations of motion, Section 3 presents theory underlying conventional state estimation routines as well the proposed Bayesian filter using transformation of variables for direct state estimation and state estimation via differential correction, Section 4 presents the results of Bayesian filter using transformation of variables compared to conventional estimation routines for different surveillance examples of increasing complexity as well as an example of three dimensional attitude estimation, and Section 5 presents conclusions as well as future work directions resulting from this research.

2. DYNAMICAL SYSTEMS THEORY

The conventional mathematical representation of continuous state dynamics and measurement models for linear and nonlinear relationships is shown in Equation (2.1). The differential equation governing the evolution of the system states, $\mathbf{x}$, is a function of the present system states and control inputs, $\mathbf{u}$. If the state dynamic model is not exactly known or higher-order forcing terms are neglected, a stochastic correction term known as process noise, $\mathbf{w}(t)$, is introduced to compensate. Likewise, the measurement model is typically only a function of the present states but instances of input transmission can be considered and, like the process model, can be corrupted by measurement noise, $\mathbf{v}(t)$, of known stochastic character. For a system to be considered nonlinear, either the dynamic model or measurement model or both are mathematically modeled as nonlinear equations.

Dynamic Model:

$$\dot{\mathbf{x}}(t) = \begin{cases} A(t)\,\mathbf{x}(t) + B(t)\,\mathbf{u}(t) + G(t)\,\mathbf{w}(t) & \text{Linear} \\ \mathbf{f}(\mathbf{x}(t), \mathbf{u}(t), \mathbf{w}(t)) & \text{Nonlinear} \end{cases}$$

$$\mathbf{x}(t_0) \text{ known}, \quad \mathbf{w}(t) \text{ distribution known}$$

Measurement Model:

$$\tilde{\mathbf{y}}(t) = \begin{cases} H(t)\,\mathbf{x}(t) + D(t)\,\mathbf{u}(t) + \mathbf{v}(t) & \text{Linear} \\ \mathbf{h}(\mathbf{x}(t), \mathbf{v}(t)) & \text{Nonlinear} \end{cases}$$

$$\mathbf{v}(t) \text{ distribution known} \tag{2.1}$$

In the modeling of dynamic systems, process and measurement noise are typically assumed to be additive and assumed to have a simple stochastic character, e.g.

Gaussian with known mean and variance. However if a process is subject to a normalization constraint, such as attitude quaternion dynamics [16], or if an object is tracked via bearings-only measurements, a multiplicative error model allows for preservation of the unitary norm. Extreme care and sometimes restraint should be exercised with the incorporation of process noise. Since process noise is often used as a substitute of neglected higher-order effects, it should only exist at the highest order of the state differential equation since integration to lower orders is exact.

For the discrete time state-space formulation, the measurement equation is the same as the continuous time formulation except, the measurement noise is a discrete random variable. For the discrete process model different approximations are applied to transform from continuous to discrete, but the most common transform is to apply a zero-order hold whereby the value is assumed to be constant until a specified amount of time, Δt, has elapsed. The transformed equations for a deterministic, continuous, linear, and time-invariant system are given by Equation (2.2) without derivation, see [16], since the state transition matrix and its application to nonlinear systems is presented in following sections.

Dynamic Model:

$$\dot{\mathbf{x}}(t) = A\mathbf{x}(t) + B\mathbf{u}(t) \quad \Rightarrow \begin{cases} \mathbf{x}_K &= \mathbf{\Phi}\mathbf{x}_{K-1} + \mathbf{\Gamma}\mathbf{u}_{K-1} \\ \mathbf{\Phi} &= \exp[A\Delta t] \\ \mathbf{\Gamma} &= \left[\int_0^{\Delta t} \exp[At]\, dt\right] B = \mathbf{\Phi}^{-1}\left(\left(\mathbf{\Phi} - \mathbf{1}_{n\times n}\right) B\right) \end{cases}$$

Measurement Model:

$$\mathbf{y}(t) = H\mathbf{x}(t) + D\mathbf{u}(t) \quad \Rightarrow \mathbf{y}_K = H\mathbf{x}_K + D\mathbf{u}_K \tag{2.2}$$

2.1 Deterministic State Mapping for Linear Systems

The *State Transition Matrix* [16] allows for computing the time history of the states as stand alone functions of the initial conditions and time and does not require the integration of the state differential equation. The generic state transition matrix definition for a deterministic, process noise free, is given in Equation (2.3) with properties of the state transition matrix listed in Equation (2.4).

$$\begin{gathered}\mathbf{x}(t) = \mathbf{\Phi}(t, t_0)\,\mathbf{x}(t_0) \\ \begin{bmatrix} x_1(t) \\ \vdots \\ x_n(t) \end{bmatrix} = \begin{bmatrix} \Phi_{11}(t, t_0) & \dots & \Phi_{1n}(t, t_0) \\ \vdots & \ddots & \vdots \\ \Phi_{n1}(t, t_0) & \dots & \Phi_{nn}(t, t_0) \end{bmatrix} \begin{bmatrix} x_1(t_0) \\ \vdots \\ x_n(t_0) \end{bmatrix}\end{gathered} \tag{2.3}$$

$$\begin{array}{lcll} \text{Initial Condition} & : & \mathbf{\Phi}(t_0, t_0) & = \mathbf{1}_{n\times n} \\ \text{Inversion} & : & \mathbf{\Phi}(t_i, t_0) & = \mathbf{\Phi}^{-1}(t_0, t_i) \\ \text{Recursion} & : & \mathbf{\Phi}(t_j, t_0) & = \mathbf{\Phi}(t_j, t_i)\,\mathbf{\Phi}(t_i, t_0) \end{array} \tag{2.4}$$

The differential equation governing the evolution of the state transition matrix can be derived by substituting the time derivative of Equation (2.3) for the left hand side of the generalized form of Equation (2.1), then substituting the mapping between final and initial conditions into the right hand side of the generalized form of Equation (2.1). The resulting differential equation for nontrivial solutions of all the substitutions is then given by Equation (2.5) with the integral solution given by Equation (2.6), otherwise known as the "Matrix Volterra Integral Equation" [16].

$$\dot{\mathbf{\Phi}} = A(t)\,\mathbf{\Phi}(t, t_0) \quad , \quad \mathbf{\Phi}(t_0, t_0) = \mathbf{1}_{n\times n} \tag{2.5}$$

$$\mathbf{\Phi}(t, t_0) = \mathbf{1}_{n\times n} + \int_{t_0}^{t} A(\tau)\,\mathbf{\Phi}(\tau, t_0)\,d\tau \tag{2.6}$$

If the state mapping matrix, $A(t)$, is constant then the solution of Equation (2.6) is the matrix exponential solution, $\mathbf{\Phi}(t, t_0) = \exp[A(t - t_0)]\,\mathbf{x}(t_0)$. If the state mapping matrix is not constant in time, numerical integration of Equation (2.5) is required, if series expansions are too slow to converge, [16].

2.2 Deterministic State Mapping for Nonlinear Systems

Section 2.1 considered only linear mappings between the state initial conditions and final conditions but, many a time nonlinear systems are of the most interest. The concept of the state transition matrix can be applied to nonlinear systems when a reference of state motion is already known and it is relatively close to the actual state history [16], e.g. reference model of motion. When a reference motion or trajectory is already known, the state transition matrix can be applied to map departures, or error, from state initial conditions to a time of interest. As with the presentation of Section 2.1, the nonlinear system is assumed to be completely deterministic.

Assuming a deterministic nonlinear system reference model is available, a reference time history of the states and observations can be generated by simple integration of the nonlinear dynamic model equation. Using the reference model states, controls, and observations plus small deviations to produce the true state and applied control inputs at the time interest, shown by Equation (2.7), the evolution of the states, controls, and observations can be computed in a linearized neighborhood of the nonlinear reference model.

$$\begin{aligned} \mathbf{x}(t) &= \mathbf{x}_{Ref}(t) + \delta\mathbf{x}(t) \\ \mathbf{u}(t) &= \mathbf{u}_{Ref}(t) + \delta\mathbf{u}(t) \\ \mathbf{y}(t) &= \mathbf{y}_{Ref}(t) + \delta\mathbf{y}(t) \end{aligned} \tag{2.7}$$

Given the decomposition of the true state, input, and observation into reference

model and deviation values, Equation (2.8) can be applied to compute the state deviations using a first-order Taylor Series expansion of the dynamic model.

$$\begin{aligned}
\delta\dot{\mathbf{x}}(t) &= \dot{\mathbf{x}}(t) - \dot{\mathbf{x}}_{Ref}(t) \\
&= \underbrace{\mathbf{f}\left(\mathbf{x}_{Ref}(t) + \delta\mathbf{x}(t), \mathbf{u}_{Ref}(t)\right)}_{\text{First-Order Taylor Expansion}} - \mathbf{f}\left(\mathbf{x}_{Ref}(t), \mathbf{u}_{Ref}(t)\right) \\
&= \mathbf{f}\left(\mathbf{x}_{Ref}(t), \mathbf{u}_{Ref}(t)\right) + \left.\frac{\partial \mathbf{f}}{\partial \mathbf{x}}\right|_{\mathbf{x}_{Ref},\mathbf{u}_{Ref}} \delta\mathbf{x} \\
&\quad + \left.\frac{\partial \mathbf{f}}{\partial \mathbf{u}}\right|_{\mathbf{x}_{Ref},\mathbf{u}_{Ref}} \delta\mathbf{u} - \mathbf{f}\left(\mathbf{x}_{Ref}(t), \mathbf{u}_{Ref}(t)\right) \\
&= \left.\frac{\partial \mathbf{f}}{\partial \mathbf{x}}\right|_{\mathbf{x}_{Ref},\mathbf{u}_{Ref}} \delta\mathbf{x} + \left.\frac{\partial \mathbf{f}}{\partial \mathbf{u}}\right|_{\mathbf{x}_{Ref},\mathbf{u}_{Ref}} \delta\mathbf{u}
\end{aligned} \tag{2.8}$$

In a likewise fashion, the first-order mapping from state and control perturbations to perturbations in observations can be computed and is shown in a short-hand form given by Equation (2.9) with the partial derivative matrices given by Equation (2.10).

$$\begin{aligned}
\delta\dot{\mathbf{x}} &= F(t)\,\delta\mathbf{x}(t) + B(t)\,\delta\mathbf{u}(t) \\
\delta\dot{\mathbf{y}} &= H(t)\,\delta\mathbf{x}(t) + D(t)\,\delta\mathbf{u}(t)
\end{aligned} \tag{2.9}$$

$$\begin{aligned}
F(t) &= \left.\frac{\partial \mathbf{f}}{\partial \mathbf{x}}\right|_{\mathbf{x}_{Ref},\mathbf{u}_{Ref}} \quad , \quad B(t) = \left.\frac{\partial \mathbf{f}}{\partial \mathbf{u}}\right|_{\mathbf{x}_{Ref},\mathbf{u}_{Ref}} \\
H(t) &= \left.\frac{\partial \mathbf{h}}{\partial \mathbf{x}}\right|_{\mathbf{x}_{Ref},\mathbf{u}_{Ref}} \quad , \quad D(t) = \left.\frac{\partial \mathbf{h}}{\partial \mathbf{u}}\right|_{\mathbf{x}_{Ref},\mathbf{u}_{Ref}}
\end{aligned} \tag{2.10}$$

2.3 Deterministic State and Parameter Mapping for Nonlinear Systems

Sections 2.1 and 2.2 considered only mappings between the initial state condition and final state condition or the initial condition state error and final state error. However systems are often functions of parameters, model constants denoted by $\mathbf{p}$, whose influence over state dynamics is shown by Equation (2.11). The system

parameters are considered to be at a steady-state condition, but may be poorly known so observation of state dynamics allows for refinement of parameter estimates. Integration of Equation (2.11) then partial differentiation with respect to initial state conditions and system parameters, Equation (2.12), allows for the derivation of the state transition matrix, $\mathbf{\Phi}$, and the parameter sensitivity matrix, $\mathbf{\Psi}$. The time derivatives of Equation (2.12) compute the differential equations of the state transition matrix and the parameter sensitivity matrix with initial conditions taken from Equation (2.12), summarized in Equation (2.13).

$$\begin{aligned} \dot{\mathbf{x}}(t) &= \mathbf{f}(\mathbf{x}(t), \mathbf{u}(t), \mathbf{p}) \\ \dot{\mathbf{p}}(t) &= \mathbf{0} \end{aligned} \tag{2.11}$$

$$\begin{aligned} \mathbf{x}(t) &= \mathbf{x}(t_0) + \int_{t_0}^{t} \mathbf{f}(\mathbf{x}(\tau), \mathbf{u}(\tau), \mathbf{p})\, d\tau \\ \mathbf{\Phi}(t, t_0) = \frac{\partial \mathbf{x}(t)}{\partial \mathbf{x}(t_0)} &= \mathbf{1}_{n\times n} + \int_{t_0}^{t} \frac{\partial \mathbf{f}(\mathbf{x}(\tau), \mathbf{u}(\tau), \mathbf{p})}{\partial \mathbf{x}(\tau)} \frac{\partial \mathbf{x}(\tau)}{\partial \mathbf{x}(t_0)} d\tau \\ \mathbf{\Psi}(t, t_0) = \frac{\partial \mathbf{x}(t)}{\partial \mathbf{p}} &= \int_{t_0}^{t} \left(\frac{\partial \mathbf{f}(\mathbf{x}(\tau), \mathbf{u}(\tau), \mathbf{p})}{\partial \mathbf{p}} + \frac{\partial \mathbf{f}(\mathbf{x}(\tau), \mathbf{u}(\tau), \mathbf{p})}{\partial \mathbf{x}(\tau)} \frac{\partial \mathbf{x}(\tau)}{\partial \mathbf{p}} \right) d\tau \end{aligned} \tag{2.12}$$

$$\begin{aligned} \dot{\mathbf{\Phi}}(t, t_0) &= F(t)\, \Phi(t, t_0) \quad , \quad \mathbf{\Phi}(t_0, t_0) = \mathbf{1}_{n\times n} \\ \dot{\mathbf{\Psi}}(t, t_0) &= F(t)\, \Psi(t, t_0) + \frac{\partial \mathbf{f}(\mathbf{x}(t), \mathbf{u}(t), \mathbf{p})}{\partial \mathbf{p}} \quad , \quad \mathbf{\Psi}(t_0, t_0) = \mathbf{0}_{n\times n} \\ F(t) &= \frac{\partial \mathbf{f}(\mathbf{x}(\tau), \mathbf{u}(\tau), \mathbf{p})}{\partial \mathbf{x}(t)} \end{aligned} \tag{2.13}$$

Comparing Equation (2.13) with Equation (2.9) and utilizing the results of Sections 2.1 and 2.2, the derivative matrices, $\mathbf{\Phi}(t, t_0)$ and $\mathbf{\Psi}(t, t_0)$, can be used to linearly map perturbations of the initial conditions and parameters to a future or

past time given a reference model, shown in Equation (2.14).

$$\mathbf{x}(t) = \mathbf{x}_{Ref} + \underbrace{\mathbf{\Phi}(t, t_0)\,\delta\mathbf{x}(t_0) + \mathbf{\Psi}(t, t_0)\,\delta\mathbf{p}}_{\delta\mathbf{x}(t)} \tag{2.14}$$

2.4 Hamiltonian Mechanics

As an alternative to system modeling at the acceleration level, thereby generating n second-order differential equations, i.e. Newton's second law and Lagrange's Equations, the Hamiltonian formulation relies upon generating $2n$ first-order differential equations, thus relegating system modeling to only the velocity level [45]. Hamilton's Equations of motion are derived using the concept of system energy as in the Lagrange formulation, but generalized momenta are exchanged for generalized velocity, which are derived from the Lagrangian of the system's generalized coordinates and generalized velocities.

The topic of Hamiltonian mechanics is of interest to this research since it provides much of the background for statistical mechanics in addition to forming the basis of many perturbation approaches [45]. The Hamiltonian approach does not typically tame problem complexity, what it does do is allow for different abstractions of the underlying physics. Thus, initially defined quantities of generalized coordinates and momenta can be transformed into different parameterizations, through use of a generating function, to allow for increased insight into specific system behavior while still preserving the canonical form of the equations of motion.

2.4.1 Hamilton's Canonical Equations

Assuming a system is already posed in a set of generalized coordinates, $\mathbf{q}$, with respective velocities, $\dot{\mathbf{q}}$, the conjugate momenta, $\mathbf{p}$, are computed from the Lagrangian, the difference of kinetic (T) and potential (V) energies, of the given system as shown

by Equation (2.15) [45].

$$\begin{aligned}\mathbf{p} &= \nabla_{\dot{\mathbf{q}}}\mathscr{L}\left(\mathbf{q},\dot{\mathbf{q}},t\right)\\ &= \frac{\partial\mathscr{L}\left(\mathbf{q},\dot{\mathbf{q}},t\right)}{\partial\dot{\mathbf{q}}} = \frac{\partial\left(T\left(\dot{\mathbf{q}}\right)-V\left(\mathbf{q}\right)\right)}{\partial\dot{\mathbf{q}}}\\ &= \frac{\partial T\left(\dot{\mathbf{q}}\right)}{\partial\dot{\mathbf{q}}}\end{aligned} \tag{2.15}$$

The Hamiltonian function is derived from the Lagrangian via the Legendre transformation given by Equation (2.16). The Hamiltonian will be equal to the total energy of the system, $\xi = T + V$, when the transformation of generalized coordinates between reference frames are not explicit functions of time and all forces external to the system are derivable from a potential, $\mathbf{f}_{Ext} = -\nabla_{\mathbf{q}}V\left(\mathbf{q}\right)$.

$$\mathscr{H}\left(\mathbf{q},\mathbf{p},t\right) = \mathbf{p}^T\dot{\mathbf{q}} - \mathscr{L}\left(\mathbf{q},\dot{\mathbf{q}},t\right) \tag{2.16}$$

Hamilton's equations of motion for the generalized coordinates and momenta, otherwise known as the canonical equations of Hamilton, are derived by equating the coefficients in the material derivative of the Legendre transformation and the desired form of the Hamiltonian. The material derivative of the Hamiltonian is shown in Equation (2.17) with the equations of motion given by Equation (2.18).

$$\begin{aligned}d\mathscr{H}\left(\mathbf{q},\mathbf{p},t\right) &= \frac{\partial\mathscr{H}}{\partial\mathbf{q}}^T d\mathbf{q} + \frac{\partial\mathscr{H}}{\partial\mathbf{p}}^T d\mathbf{p} + \frac{\partial\mathscr{H}}{\partial t}dt\\ &= \mathbf{p}^T d\dot{\mathbf{q}} + \dot{\mathbf{q}}^T d\mathbf{p} - \left(\frac{\partial\mathscr{L}}{\partial\mathbf{q}}^T d\mathbf{q} + \frac{\partial\mathscr{L}}{\partial\dot{\mathbf{q}}}^T d\dot{\mathbf{q}} + \frac{\partial\mathscr{L}}{\partial t}dt\right)\\ &= \mathbf{p}^T d\dot{\mathbf{q}} + \dot{\mathbf{q}}^T d\mathbf{p} - \left(\frac{\partial\mathscr{L}}{\partial\mathbf{q}}^T d\mathbf{q} + \frac{\partial\mathscr{L}}{\partial\dot{\mathbf{q}}}^T d\dot{\mathbf{q}} + \frac{\partial\mathscr{L}}{\partial t}dt\right)\\ &= \cancelto{0 \text{ by } (2.15)}{\left(\mathbf{p} - \frac{\partial\mathscr{L}}{\partial\dot{\mathbf{q}}}\right)^T} d\dot{\mathbf{q}} + \dot{\mathbf{q}}^T d\mathbf{p} - \left(\frac{\partial\mathscr{L}}{\partial\mathbf{q}}^T d\mathbf{q} + \frac{\partial\mathscr{L}}{\partial t}dt\right)\end{aligned} \tag{2.17}$$

$$\begin{aligned} \dot{\mathbf{q}} &= \frac{\partial \mathscr{H}(\mathbf{q}, \mathbf{p}, t)}{\partial \mathbf{p}} \\ \dot{\mathbf{p}} &= -\frac{\partial \mathscr{H}(\mathbf{q}, \mathbf{p}, t)}{\partial \mathbf{q}} \\ \frac{\partial \mathscr{H}(\mathbf{q}, \mathbf{p}, t)}{\partial t} &= -\frac{\partial \mathscr{L}(\mathbf{q}, \dot{\mathbf{q}}, t)}{\partial t} \end{aligned} \tag{2.18}$$

Inserting the differential equation relationships of Equation 2.18 into the first line of Equation (2.17) demonstrates that the total differential of the Hamiltonian with respect to time is equivalent of the partial of the Hamiltonian with respect time. Additionally, if the Hamiltonian is not a function of generalized coordinates then the system momenta are constant and their respective generalized coordinates are referred as either cyclic or ignorable [45]. The last line of Equation (2.18) shows that if the Lagrangian is not an explicit function of time, the Hamiltonian will be a constant of motion.

2.4.2 Canonical Transformations

A canonical transformation is one in which Hamilton's equations of motion remain satisfied after an initial set of generalized coordinates and momenta, $(\mathbf{q}, \mathbf{p})$, is exchanged for a different set of coordinates and momenta, $(\mathbf{Q}, \mathbf{P})$. The reason for the transformation could be to produce a desired result with respect to the mathematical interpretation of system behavior or for a different understanding, via abstraction, of the underlying physics. For example, if a satellite's motion is described using geocentric distance, geocentric latitude, and right ascension and one were to transform into a space with generalized coordinates of geocentric distance, geocentric latitude, and geocentric longitude they would find the Hamiltonian, which was time varying in the initial domain, is now constant in the transformed domain [46].

For the transformed phase space variables to remain canonical, a specific relation of the initial and transformed Hamiltonians is required and produced via Hamilton's

principle and the concept of the action integral. Hamilton's principle states that the motion of a system from one instant in time to another is such that the action integral has a stationary value for the true path of motion [45]. The action integral is the integral of the sum of the Lagrangian and any work done by nonconservative forces over the time span in question. If the external forces are all derivable from potentials, the action integral is simply over the Lagrangian with respect to the time interval in question. The stationary solution of the action integral is the particular solution which has Lagrange's equations holding for all times within the time interval of interest and is computed by setting the variation of the action integral to zero yielding Hamilton's Principle [45], shown by Equation (2.19).

$$\begin{aligned} \text{Action Integral: } I &= \int_{t_1}^{t_2} \left(\mathscr{L}\left(\mathbf{q}, \dot{\mathbf{q}}, t\right) + W_{NonCon} \right) dt \\ \text{Hamilton's Principle: } 0 &= \delta \int_{t_1}^{t_2} \left(\mathscr{L}\left(\mathbf{q}, \dot{\mathbf{q}}, t\right) + W_{NonCon} \right) dt \end{aligned} \tag{2.19}$$

For the generalized coordinates and momenta to be canonical with respect to their given Hamiltonian, Hamilton's principle must be satisfied when the Lagrangian is replaced with the result of solving the Legendre transformation for the Lagrangian. This condition is deemed necessary and sufficient to achieve canonical behavior [46]. Hamilton's principle must be satisfied by both the initial phase space variables and transformed phase space variables at every time instance within the time interval. Satisfaction of Hamilton's principle over the same time span by the initial and transformed phase space domains allows for their integrands equated via Equation (2.20).

$$\begin{aligned} &\delta \int_{t_1}^{t_2} \left(\mathbf{p}^T \dot{\mathbf{q}} - \mathscr{H}\left(\mathbf{q}, \mathbf{p}, t\right) \right) dt = 0 \\ &\delta \int_{t_1}^{t_2} \left(\mathbf{P}^T \dot{\mathbf{Q}} - K\left(\mathbf{Q}, \mathbf{P}, t\right) \right) dt = 0 \\ \Rightarrow &\lambda \left(\mathbf{p}^T \dot{\mathbf{q}} - \mathscr{H}\left(\mathbf{q}, \mathbf{p}, t\right) \right) = \mathbf{P}^T \dot{\mathbf{Q}} - K\left(\mathbf{Q}, \mathbf{P}, t\right) + \frac{dS}{dt} \end{aligned} \tag{2.20}$$

The function S is the generating function allowing for the transformed phase space domain Hamiltonian, K, to be computed from the initial phase space domain Hamiltonian. The generating function is typically only a function of one initial phase space domain variable and one transformed phase space domain variable. The generating function can have its form selected a priori or it can be computed based upon the initial phase space variables and selected transformed phase space variables. The λ is a constant scale factor arising from the change of bases from initial to transformed phases spaces, $\lambda = 1$ is associated with canonical transformations, and is equivalent to the determinant of the mapping Jacobian between the two sets of bases. Goldstein [45] and Vinti [46] give the four basic canonical generating functions, the latter derives all of them, which are restated in Table 2.1 without derivation. Once given the transformation between the initial and final phase space variables, the generating function can be derived thus allowing for the transformed phase space Hamiltonian to be computed from Equation (2.20). If the relationship is one of the four shown in Table 2.1 then the transformed Hamiltonian is given by Equation (2.21).

$$K\left(\mathbf{Q},\mathbf{P},t\right) = \mathscr{H}\left(\mathbf{q},\mathbf{p},t\right) + \frac{\partial S}{\partial t} \tag{2.21}$$

A point transformation is defined as a transformation which renders the generalized coordinates to be only functions of the initial generalized coordinates while the transformed generalized momenta are computed from Equation (2.15). If one were to select a generating function of the form $S = \mathbf{q}^T\mathbf{Q}$, the resulting transform would simply exchange the coordinates and momenta. The exchange would lead to an abstraction of the idea of coordinates and momenta to the level where they are simply codependent variables designated by some $(\boldsymbol{\alpha},\boldsymbol{\beta})$ and related by Hamilton's equations. An important generating function to the world of orbital mechanics is a

special instance of Case 2 in Table 2.1 where $S = \mathbf{q}^T\mathbf{P}$ is used to separate and study short-period, long-period, and secular behavior of Keplerian orbital elements [47]. The result of such a transformation renders the momenta to be constants of motion thereby allowing for the coordinates to be simply propagated in time in lieu of integration, which is of great utility in the Two-Body problem subject to gravitational perturbations. This special instance of Case 2 is called an identity transformation because the resulting Hamiltonian, representing the total energy of the conservatively forced system, is unchanged in scalar value even though it is expressed as a function of different variables.

Table 2.1: Canonical Transformation Properties

Case	Generating Function	Generating Function Initial Relation	Generating Function Transformed Relation
1	$S = S(\mathbf{q}, \mathbf{Q}, t)$	$\mathbf{p} = \frac{\partial S}{\partial \mathbf{q}}$	$\mathbf{P} = -\frac{\partial S}{\partial \mathbf{Q}}$
2	$S = S(\mathbf{q}, \mathbf{P}, t) - \mathbf{Q}^T\mathbf{P}$	$\mathbf{p} = \frac{\partial S}{\partial \mathbf{q}}$	$\mathbf{Q} = \frac{\partial S}{\partial \mathbf{P}}$
3	$S = S(\mathbf{p}, \mathbf{Q}, t) + \mathbf{q}^T\mathbf{p}$	$\mathbf{q} = -\frac{\partial S}{\partial \mathbf{p}}$	$\mathbf{P} = -\frac{\partial S}{\partial \mathbf{Q}}$
4	$S = S(\mathbf{p}, \mathbf{P}, t) + \mathbf{q}^T\mathbf{p} - \mathbf{Q}^T\mathbf{P}$	$\mathbf{q} = -\frac{\partial S}{\partial \mathbf{p}}$	$\mathbf{Q} = \frac{\partial S}{\partial \mathbf{P}}$

2.4.3 Canonical System Order Reduction

Often, canonical transformations are employed to reduce the order of a dynamical system to gain insight into system behavior from a perturbation point of view. As alluded to in the previous section, particular canonical transformations can be applied to produce a new set of variables where the momenta are constant, thereby allowing system order reduction. This reduction of system order allows one to better understand the effects imparted on a system reference model by perturbations. However,

computation of the generating function for the new desired coordinate and momenta variable set can be carried out using different approaches whose solutions can yield different results, but are all correct based upon the assumptions made before carrying out the particular method [48, 49]. For example, Brouwer [47] utilized von Zeipel's method of computing a generating function that was composed of old and new variables in order to eliminate slowly varying coordinates, while Kozai [50] used the method of averaging to directly to eliminate the slowly varying angular coordinates with both methods producing approximately the same solution. Additionally, Hori's method of defining the generating function to be solely a function of new coordinates and momenta was shown to produce the same solution as von Zeipel's method up through third order of the perturbing parameter, i.e. zonal geopotential of Earth, but when applied to motion about the moon, the theories produced different Hamiltonians [51, 52].

To illustrate how canonical transformations can be utilized to reduce the system order and study the effect of perturbing parameters, consider a nominal system model expressed via the Hamiltonian approach whose Hamiltonian and equations of motion are given by Equations (2.16) and (2.18). If the nominal model is analogous to a mass-spring system but, the spring constant changes depending upon the deformed length of the spring, one could still study the long-term or secular trajectory effects of such a perturbation. This can be done by finding a generating function which isolates such effects over the period of oscillation, or even longer time scales, without the need for integration of the instantaneous equations of motion.

For project SPACETRACK [53, 54], Brouwer utilized von Zeipel's method of successive canonical transformations to eliminate coordinates in the Hamiltonian for computation of secular motion due to geopotential perturbations starting with the Two-Body geopotential perturbed Hamiltonian expressed in Delaunay variables.

The two canonical transformations produced a Hamiltonian devoid of coordinates thus, the conjugate momenta were constant and the corresponding coordinates varied linearly in time. Lyddane [55] later modified Brouwer's theory by exchanging the Delaunay variables for Poincaré variables in order to avoid problems with small eccentricity and inclination. Analytic characterization of perturbed object motion was of necessity at that time due to computational requirements onboard naval ships and onshore tracking stations [53]. However due to the large amount of space objects and debris which cannot be continuously tracked, analytic characterization of orbital motion is still required for data processing. Today, Brouwer's theory with Lyddane's modification still stands and is used in conjunction with some terms derived by Kozai [50], relating mean motion to semi-major axis, for the Navy's satellite prediction model(PPT3) and Air Force's prediction models(SGP, SGP4, SDP) which differ with respect to resonance and atmospheric model characterization [53].

The von Zeipel method [48] provides a procedure with which to calculate the partial differential equations for the generating function at given orders of the perturbing parameter, $\boldsymbol{\epsilon}$, assuming the form of the generating function is composed of old coordinates and new momenta. Let the form of the original Hamiltonian, $\mathscr{H}(\mathbf{q}, \mathbf{p}, \boldsymbol{\epsilon})$, be given by Equation (2.22), which shows it can be decomposed into the summation of terms in ascending powers of the perturbing parameter up to order N and let the new Hamiltonian, $\mathscr{H}^*(\mathbf{Q}, \mathbf{P}, \boldsymbol{\epsilon})$, take the same form but with new variables in lieu of the old variables. The subscript i denotes the order of the perturbing parameter. Let the generating function which goes from the old variables to the new variables be decomposable, like the Hamiltonians, and let the generating function at zeroth-order be the dot product of the old coordinates with the new momenta as shown by

Equation (2.23).

$$\mathscr{H}\left(\mathbf{q},\mathbf{p},\boldsymbol{\epsilon}\right)=\sum_{i=0}^{N}\mathscr{H}_i\left(\mathbf{q},\mathbf{p},\boldsymbol{\epsilon}^i\right)+\mathcal{O}\left(\boldsymbol{\epsilon}^{N+1}\right) \tag{2.22}$$

$$\begin{aligned} S\left(\mathbf{q},\mathbf{P}\right)&=\sum_{i=0}^{N}S\left(\mathbf{q},\mathbf{P},\boldsymbol{\epsilon}^i\right)+\mathcal{O}\left(\boldsymbol{\epsilon}^{N+1}\right)\\ S_0\left(\mathbf{q},\mathbf{P}\right)&=\mathbf{q}^T\mathbf{P} \end{aligned} \tag{2.23}$$

For the von Zeipel method, the old and new Hamiltonians are equated and expanded in a Taylor Series about the perturbing parameter while being expressed as functions of the generating function and the old and new variables. The coordinates to be eliminated are chosen by finding those coordinates not in the nominal solution and proposing a canonical transform, particularly the point transform, where their conjugate momenta are constant, thereby allowing for a system order reduction.

$$\begin{aligned} \mathscr{H}_0\left(\mathbf{q},\mathbf{p}=\frac{\partial S}{\partial\mathbf{p}}\right)+\mathscr{H}_1\left(\mathbf{q},\mathbf{p}=\frac{\partial S}{\partial\mathbf{p}},\boldsymbol{\epsilon}\right)+\mathscr{H}_2\left(\mathbf{q},\mathbf{p}=\frac{\partial S}{\partial\mathbf{p}},\boldsymbol{\epsilon}^2\right)+\cdots=\\ \mathscr{H}_0^*\left(\mathbf{Q}=\frac{\partial S}{\partial\mathbf{P}},\mathbf{P}\right)+\mathscr{H}_1^*\left(\mathbf{Q}=\frac{\partial S}{\partial\mathbf{P}},\mathbf{P}\right)+\mathscr{H}_2^*\left(\mathbf{Q}=\frac{\partial S}{\partial\mathbf{P}},\mathbf{P}\right)+\ldots \end{aligned} \tag{2.24}$$

Before system order reduction, the von Zeipel method assumes that the old and new coordinates and momenta will differ by at least the order of perturbing parameter. If the zeroth-order generating function is assumed to be the identity transformation, this assumption will make the zeroth-order Hamiltonian equal to the nominal Hamiltonian and yield a partial differential equation solution for the first-order part of the generating function [48]. The consequence of this approach for computing the generating function is that solutions at orders higher than first will be functions of terms involving the perturbing parameter of higher orders, e.g. the first-order

solution of the generating function will contain second-order terms. This can lead to extremely long and complicated solutions [47,56] when one is trying to study periodic effects of the artificial satellite problem and not simply just secular.

In an attempt to reduce complexity, Izsak [57] proposed and derived the short-period equations of motion using the Hill canonical variable set within Brouwer's theory, simply exchanging the mean anomaly and argument of perigee coordinates for the radius and argument of latitude. Aksnes [58] later completed the theory by deriving the long-period equations and compared the results of the Hill variable formulation with the Delaunay [47], Kepler [50], and Poincaré [55] variable sets. Aksnes showed that the produced equations were singularity free at zero eccentricity and appeared to produce a more compact algorithm. It should be noted that the chosen variable set is typically dictated directly by the type of operations being conducted. For example, in surveillance one is typically interested in an object's perigee location, whereas for proximity or rendezvous operations one is more concerned about where the object is located in the shared orbit plane with regard to the node vector.

3. STOCHASTIC STATE ESTIMATION

Stochastic or statistical estimation of system states and/or specific parameters, slowly time varying or time invariant, utilizes a decision making algorithm to compute the "best" estimate of system states or parameters. The "best" estimate typically seeks to minimize a given error criterion with the error defined via comparison of empirical measurement data corrupted by some type of random process with output generated from mathematical system model that may neglect higher order effects. System constants or an initial state vector can typically be estimated via batch estimation techniques while system state variables are more situation dependent. System state variables characterize an object's instantaneous dynamic behavior and are used for control, tracking, or decision making purposes because they can be used to predict object motion given an appropriate motion model. Statistical estimation algorithms seek to accurately calculate the values of system states and parameters while appropriately capturing state and parameter uncertainty due to measurement corruption.

For nonlinear systems, governed by either a nonlinear state, measurement model, or both, typical assumptions of linear system estimation routines are commonly applied for nonlinear system estimation without thought as to whether the assumptions are valid or not. As such, the user must first take care to understand the assumptions of the applied estimation routine so that they are not violated, else the result is misuse of the technique. For nonlinear stochastic estimation, one of the most important assumptions is that of the form or shape of the uncertainty of the system states and parameters as well as their respective correlations during system operation.

3.1 Bayesian Inferencing

Bayesian inference combines the Likelihood Principle with knowledge of prior information about parameter(s) of interest. The Likelihood Principal states that a specific function, known as the likelihood function, when evaluated at the observed system events is a complete summary of the information in the observations and the likelihood of unobserved events is irrelevant [20]. The likelihood function, analytic or numerically obtained through repeated experiments or Monte Carlo trials, expresses the probability of observed events as a function of unknown system states and is the link between observed events and the unknown system states. The Likelihood Principal is combined with prior information because there is always some type of *a priori* information that can help eliminate improbable events due to physical system constraints, e.g. speed, or other statistical knowledge. The likelihood and prior probability information are combined using Bayes' Theorem [2,16,59] to produce the posterior probability, which can then be used for decision making purposes such as control or tasking actions. Bayes' Theorem can be applied for batch estimation via maximum likelihood estimation but is also able to be recursively implemented. As long as the observational errors are independent, the posterior at the previous observation time can be mapped to the present time and used as the prior for calculation of the posterior at the present observation time.

Bayes' Theorem [2], Equation (3.1), quantifies the amount in belief for possible state values, $\mathbf{x}_K$, given the present observation, $\mathbf{z}_K$, and prior information, $p\left(\mathbf{x}_K^-\right)$, at a specific instant in time, K. The likelihood function, $p\left(\mathbf{z}_K|\mathbf{x}_K\right)$, expresses the likelihood that $\mathbf{z}_K$ would be the outcome given specific instances of the state vector $\mathbf{x}_K$. The prior density function, $p\left(\mathbf{x}_K^-\right)$, represents all information available immediately before the present measurement. The denominator is a normalizing factor so

that the produced posterior distribution satisfies the definition of a probability density function, i.e. $p\left(\mathbf{x}_K|\mathbf{z}_K\right) \geq 0$ and the sum, or integral if continuous distribution, of the conditional posterior over all random variables is 1. The likelihood, prior, and posterior can all be expressed as probability density functions(PDFs), which are interpreted as functions expressing the frequency of a particular outcome over the state-space, and are characterized either analytically or numerically. Traditionally, when the probability function is continuous it is called a probability density function with its discrete counterpart called a probability mass function, computed as the integral of the continuous function of a defined region expressed at the midpoint of the region [2].

$$p\left(\mathbf{x}_K|\mathbf{z}_K\right) = \begin{cases} \dfrac{p\left(\mathbf{z}_K|\mathbf{x}_K\right) p\left(\mathbf{x}_K^-\right)}{\sum\limits_{\mathbf{x}_K} p\left(\mathbf{z}_K|\mathbf{x}_K\right) p\left(\mathbf{x}_K^-\right)}, & \text{Discrete} \\ \dfrac{p\left(\mathbf{z}_K|\mathbf{x}_K\right) p\left(\mathbf{x}_K^-\right)}{\int_{-\infty}^{\infty} p\left(\mathbf{z}_K|\mathbf{x}_K\right) p\left(\mathbf{x}_K^-\right) d\mathbf{x}_K}, & \text{Continuous} \end{cases} \tag{3.1}$$

Knowledge of the posterior distribution enables computation of the optimal state estimate with respect to any criterion, e.g. maximum likelihood, minimum error, or minimum variance [15]. However, the state estimate utilizing the posterior result from Bayes' Theorem can be calculated differently depending upon the error criterion one wishes to minimize [16]. This work utilizes the minimum variance estimate conditioned upon available data, which is the expectation of the conditional posterior distribution produced by Bayes' Theorem for a given random variable vector, $\mathbf{x}$. The Expectation operator [2], $E\left\{\bullet\right\}$, for discrete and continuous conditional random variable distributions is given by Equation (3.2). Expectation of functions of a random variable are computed by replacing the leading term in the integrand by the

function in question.

$$E\left\{\alpha|\beta\right\} = \begin{cases} \sum_{i=1}^{N} \alpha_i p\left(\alpha_i|\beta\right), & \text{Discrete Random Variables} \\ \int_{-\infty}^{\infty} p\left(\alpha|\beta\right) d\alpha, & \text{Continuous Random Variables} \end{cases} \tag{3.2}$$

Equation (3.3) shows the computation of the first moment for discrete random variables from a multidimensional conditional distribution. For nomenclature, X_i represents a column vector of possible values which a specific random variable x_i can take with $i \in [1, n]$ where n is the total number of states. Additionally, X_i^j represents a specific scalar element of X_i vector with $j \in [1, N]$ and N is the total number of different elements in X_i.

$$\hat{\mathbf{x}} = \begin{bmatrix} \hat{x}_1 \\ \vdots \\ \hat{x}_n \end{bmatrix} = E\left\{\mathbf{x}|\mathbf{z}\right\} = \begin{bmatrix} \sum_{j=1}^{N} X_1^j p\left(X_1^j|\mathbf{z}\right) \\ \vdots \\ \sum_{j=1}^{N} X_n^j p\left(X_n^j|\mathbf{z}\right) \end{bmatrix} \tag{3.3}$$

Equation (3.3) requires use of a random variable's conditional marginal density which is computed from the joint posterior density by either integrating(continuous random variables) or summing(discrete random variables) over all random variable vectors which are not of interest. For discrete densities this operation is shown in Equation (3.4).

$$p\left(X_i|\mathbf{z}\right) = \sum_{\substack{X_k \\ k \neq i}} p\left(X_1, X_2, \ldots, X_n|\mathbf{z}\right) \tag{3.4}$$

With the minimum variance estimate and the joint posterior density, the covariance matrix, summarizing second-order statistical moment of variance and the state

correlation, can be calculated using Equation (3.5).

$$\operatorname{cov}\{\hat{x}_i, \hat{x}_k\} = E\left\{ (X_i - \hat{x}_i)(X_k - \hat{x}_k)^T \middle| \mathbf{z} \right\} \quad ; \quad i,k \in [1,n] \tag{3.5}$$

In general, Bayes' Theorem is not always analytically determinate, but restrictive cases do exist where the posterior density is completely and exactly computed. The lack of general determinacy for typical nonlinear systems is due to hard *a priori* constraints, which introduce nonlinearites that can truncate the proposed probability density function character. However, incorporation of any relatively accurate knowledge should improve estimation accuracy. For instance, sensor noise characteristics are typically reported with respect to on-average behavior via the Central Limit Theorem [2], there can be cases where the reported measurement will lie outside the typically applied three standard deviation bound. This will not impact estimation applications for data rich environments, but can be problematic when measurements are sparse. Additionally, the computation of the prior distribution requires storage of all previous measurements, which is not always possible so one must consider using only a subset of previous measurements, known as limited-memory filtering [59].

Approximation of Bayes' Theorem can produce computationally efficient and relatively accurate but, sub-optimal estimates. They can be broadly grouped into four rather large families of nonlinear sequential filtering [15]: (a) analytic(linear) approximation, (b) numerical approximation, (c) Gaussian Sum or Multiple Model, and (d) Posterior Distribution Sampling. The conventional filters examined in this work are from the first and fourth families and the proposed Bayes' filter utilizing transformation of variables falls into the second category because it constructs the likelihood and prior probabilities to produce the posterior distribution even though it requires a grid generation structure similar to posterior sampling solutions.

3.2 Linear System Approximation

The Kalman filter is the optimal sequential estimator for linear systems [16], so it becomes rather natural to want to take advantage of its simplicity by linearizing the system model about a given operating point. The most common analytic approximation made is to linearize the system model and apply the optimal sequential linear estimation framework of the Kalman filter, resulting in the extended Kalman filter(EKF). Traditionally, the Kalman filter structure is used to directly compute state estimates based upon current measurements and previous system knowledge, however the framework can also be adapted to estimate a differential correction to a pre-existing state estimate. The latter form is especially useful in computing vehicle attitude since the pre-existing attitude would be updated via a multiplication of a the current attitude estimate and the computed differential correction update, this leads to the multiplicative extended Kalman filter(MEKF). [16]

3.2.1 Direct State Estimation

Depending on the degree of nonlinearity of the state process and measurement model, the EKF has been shown to work well for many applications in aircraft, spacecraft, and passive sensing [5, 15, 16]. The EKF utilizes the Kalman filter framework by linearizing the system model, Equation (2.1), about the present state estimate, $\hat{\mathbf{x}}_K^-$, shown in Equation (3.6).

$$\begin{gathered}
\mathbf{x}_{K+1} = \mathbf{\Phi}_K \mathbf{x}_K + \mathbf{\Gamma}_K \mathbf{u}_K + \mathbf{\Upsilon}_K \mathbf{w}_K \\
\mathbf{z}_K = \mathbf{H}_K \mathbf{x}_K + \mathbf{v}_K \\
\mathbf{H}_K = \left.\frac{\partial \mathbf{h}_K}{\partial \mathbf{x}}\right|_{\hat{\mathbf{x}}_K^-}, \ \mathbf{\Phi}_K = \left.\frac{\partial \mathbf{f}_K}{\partial \mathbf{x}}\right|_{\hat{\mathbf{x}}_K^-}, \ \mathbf{\Gamma}_K = \frac{\partial \mathbf{f}_K}{\partial \mathbf{u}_K}, \ \mathbf{\Upsilon}_K = \frac{\partial \mathbf{f}_K}{\partial \mathbf{w}_K}
\end{gathered} \tag{3.6}$$

Using the linearization of Equation (3.6) and given an initial state estimate and

covariance, $\hat{\mathbf{x}}_0^- = \hat{\mathbf{x}}_0$ and $P_0 = E\left\{\hat{\mathbf{x}}_0\hat{\mathbf{x}}_0^T\right\}$, the filter proceeds with the update and propagation equations shown by Equation (3.7).

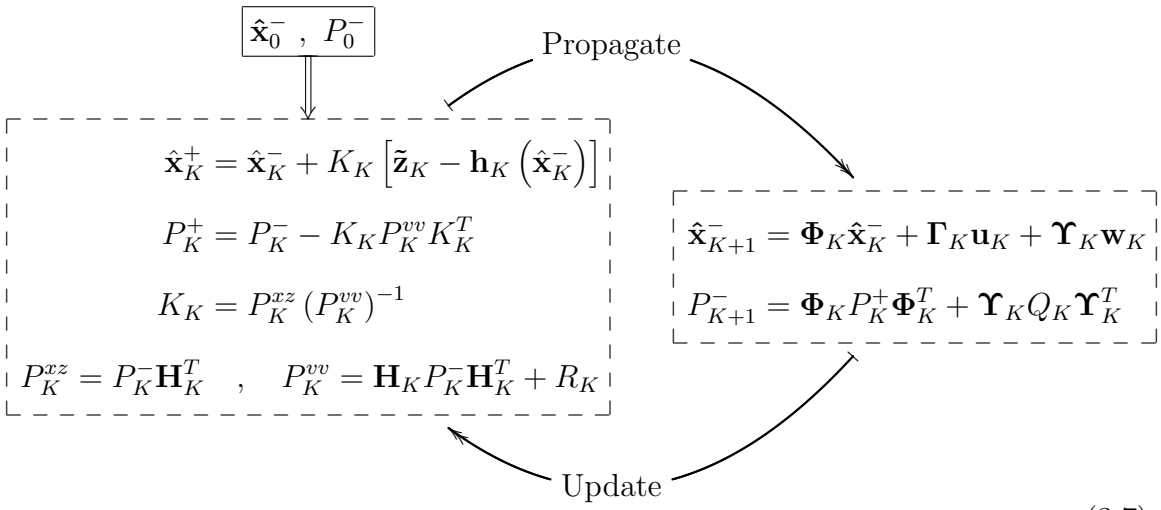

(3.7)

Due to the linearization used by the EKF to enable use of the optimal linear system solution, problems may arise during operation due to significant neglect of nonlinearity. The EKF assumes the posterior state probability density function is always Gaussian, which is not generally true for nonlinear systems. A judicious choice of state coordinates can allow for the posterior PDF to remain Gaussian for a longer period of time, e.g. orbital elements to keep the dynamics relatively linear or curvilinear coordinates to match measurement output [3]. Linearization of the state and measurement processes can create problems with filter initialization as well as consistency and accuracy. Filter initialization errors can result from the initial state estimate being outside the applicable range of linearization or initializing the state covariance incorrectly, either too small or incorrectly assessing the correlation structure. Incorrect covariance initialization causes the filter to ignore new measurement information due to bias towards the process model.

Proper characterization of uncertainty and state correlation in problems can be-

come an issue during filter operation since a first-order tensor mapping is used between the state and measurement domain for the filter gain equation, as well as between the present and future observation times for the covariance propagation. For systems with measurement nonlinearities present at orders higher than one, the updated covariance will not respond in an appropriate or timely manner, especially after a significant number of measurements have been received. For systems with slow manifestation of measurement nonlinearity, the system can become overconfident and will begin to ignore additional measurements until the measurement Jacobian becomes significant enough to counteract the pole-shifting nature of the covariance update inherited from the traditional Kalman filter. To combat linearization errors, many tweaks for the EKF have been developed such as the addition of Gaussian noise to the state process, increasing the initial state covariance, and iterating on the present estimate [16].

3.2.2 State Differential Correction Estimation

In lieu of the typical approach to Kalman filtering where object states are directly updated via the measurement residual and the Kalman gain, the state update equation can be modified to estimate a differential correction to a pre-existing estimate of the current state much like Gaussian least-squares with differential corrections (GLSDC) [16]. This is especially applicable in attitude filtering where one is seeking to estimate the orientation of a spacecraft with respect to a given fixed frame. However, since orientation is described by rotation, the computed differential update would be a corrective rotation applied to the pre-existing attitude estimate. However, one must note that the covariance matrix computed using the differential correction approach is associated with the differential corrections and not directly with the state. If the update to the state is linear then the covariance matrix is

associated with the state error but if the update is not linear than the covariance must be transformed also.

For state differential correction estimation utilizing the Kalman framework, Equations (3.6) and (3.7) are recast in terms of the state error, $\boldsymbol{\Delta}\mathbf{x} = \mathbf{x}_{True} - \hat{\mathbf{x}}_{Est}$, and the first-order linearization of the state dynamics and covariance is taken around the updated state estimate, $\mathbf{x}_K^+$. The propagation equations for the differential correction and its associated covariance are given by Equations (3.8) and (3.9).

$$\begin{aligned}
\boldsymbol{\Delta}\mathbf{x}_{K+1}^- &= \mathbf{x}_{True,K+1} - \hat{\mathbf{x}}_{K+1}^- \\
&= \mathbf{f}_K\left(\mathbf{x}_{True,K}, \mathbf{w}_K\right) - \mathbf{f}_K\left(\hat{\mathbf{x}}_K, \mathbf{w}_K\right) \\
&= \mathbf{f}_K\left(\hat{\mathbf{x}}_K^+\right) + \left.\frac{\partial \mathbf{f}_K}{\partial \mathbf{x}}\right|_{\hat{\mathbf{x}}_K^+} \left(\mathbf{x}_{True,K} - \hat{\mathbf{x}}_K^+\right) + \left.\frac{\partial \mathbf{f}_K}{\partial \mathbf{w}}\right|_{\mathbf{w}_K} \mathbf{x}_{True,K} - \mathbf{f}_K\left(\hat{\mathbf{x}}_K^+\right) \\
&= \boldsymbol{\Phi}_K \boldsymbol{\Delta}\mathbf{x}_K^+ + \boldsymbol{\Upsilon}_K \mathbf{w}_K
\end{aligned} \tag{3.8}$$

$$\begin{aligned}
P_{K+1}^- &= E\left\{\boldsymbol{\Delta}\mathbf{x}_{K+1}^- \left(\boldsymbol{\Delta}\mathbf{x}_{K+1}^-\right)^T\right\} \\
&= \boldsymbol{\Phi}_K P_K^+ \boldsymbol{\Phi}_K^T + \boldsymbol{\Upsilon}_K Q_K \boldsymbol{\Upsilon}_K^T
\end{aligned} \tag{3.9}$$

The update equation for the covariance associated with the differential correction to the propagated previous state update is the same as given in Equation (3.7). The state estimate can then be updated after the differential correction is updated by the measurement innovation. Equation (3.10) shows the update to the differential correction assuming a linear update rule to the actual state estimate. Even if a nonlinear update to the state estimate is applied, e.g. $\hat{\mathbf{q}}_K^+ = \delta\mathbf{q}_K \otimes \hat{\mathbf{q}}_K^-$, the update rule for the differential correction still holds.

$$\begin{aligned}
\boldsymbol{\Delta}\mathbf{x}_{K+1}^+ &= K_{K+1}\left[\tilde{\mathbf{z}}_{K+1} - \mathbf{h}_{K+1}\left(\hat{\mathbf{x}}_{K+1}^-\right)\right] \\
\hat{\mathbf{x}}_{K+1}^+ &= \hat{\mathbf{x}}_{K+1}^- + \boldsymbol{\Delta}\mathbf{x}_{K+1}^+
\end{aligned} \tag{3.10}$$

For spacecraft attitude filtering, the commonly used state parameterization is the quaternion since it is free of orientation singularities and its dynamics can be written in a linear fashion. However the quaternion is a four dimensional representation of three-dimensional orientation, so the unity constraint of the quaternion must be handled in some form. A reduction from four parameters to three is accomplished through assuming that only small corrections of the quaternion are required, thus the model is able to be reduced to estimating differential corrections for the vector part of the quaternion since the scalar part is assumed constant. This is a very good approximation since the sampling frequency for attitude determination is typically high. The MEKF starts off by proposing a differential correction to a pre-existing estimate of the attitude in quaternion form where the updated quaternion estimate is computed, not linearly as previously shown but, via the quaternion composition shown by Equation (3.11), the composition mathematics are given by Equation (3.12). The initial attitude estimate for the MEKF can come from any one of the many pre-existing attitude determination algorithms, e.g. q-Method [60, 61] or TRIAD [62].

$$\hat{\mathbf{q}}_K^+ = \delta\mathbf{q}_K \otimes \hat{\mathbf{q}}_K^- \tag{3.11}$$

$$\begin{aligned}
\hat{\mathbf{q}}_2 \otimes \hat{\mathbf{q}}_1 &= \left[\Psi\left(\hat{\mathbf{q}}_2\right) \;\; \hat{\mathbf{q}}_2\right]\hat{\mathbf{q}}_1 \\
\hat{\mathbf{q}}_2 \otimes \hat{\mathbf{q}}_1 &= \left[\Xi\left(\hat{\mathbf{q}}_1\right) \;\; \hat{\mathbf{q}}_1\right]\hat{\mathbf{q}}_2 \\
\Xi\left(\hat{\mathbf{q}}\right) &= \begin{bmatrix} q_S\mathbf{I}_{3\times 3} + [q_V\times] \\ -q_V^T \end{bmatrix} \\
\Psi\left(\hat{\mathbf{q}}\right) &= \begin{bmatrix} q_S\mathbf{I}_{3\times 3} - [q_V\times] \\ -q_V^T \end{bmatrix} \\
\hat{\mathbf{q}} &= \begin{bmatrix} q_V^T & q_S \end{bmatrix}^T \quad ; \quad |\hat{\mathbf{q}}| = 1
\end{aligned} \tag{3.12}$$

Quaternion dynamics are given by Equation (3.13) assuming an estimated angular velocity and gyro bias from a noise and bias corrupted measurement where the bias is subject to random walk.

$$\begin{aligned}
\dot{\hat{\mathbf{q}}} &= \frac{1}{2}\Xi\left(\hat{\mathbf{q}}\right)\hat{\boldsymbol{\omega}} = \frac{1}{2}\Omega\left(\hat{\boldsymbol{\omega}}\right)\hat{\mathbf{q}} \\
\hat{\boldsymbol{\omega}} &= \underbrace{\boldsymbol{\omega}_{True} + \boldsymbol{\beta} + \boldsymbol{\eta}_{Gyro}}_{Gyro\ \ Measurement} - \hat{\boldsymbol{\beta}} = \tilde{\boldsymbol{\omega}} - \hat{\boldsymbol{\beta}} \\
\dot{\boldsymbol{\beta}} &= \boldsymbol{\eta}_{Bias}
\end{aligned} \tag{3.13}$$

From the quaternion composition, when a quaternion is composed with the inverse of itself results in the unit quaternion, $\delta\mathbf{q} \otimes \hat{\mathbf{q}}^{-1} = [0\ 0\ 0\ 1]^T$. This is a key part of the development of the MEKF because if the updated quaternion is assumed to be close to the propagated updated quaternion from the previous time, then the scalar part should remain constant and one only has to deal with computing differential corrections to the vector part of the quaternion. The direction cosine matrix, which rotates inertial vectors, $\mathbf{r}$, into body frame vectors, $\mathbf{b}$, can be computed from a given quaternion using Equation (3.14). Noting that successive rotations can be accomplished through quaternion composition yields the results of Equation (3.15). The equation shows how the differential quaternion correction can be used to update a previous quaternion estimate given a new body frame measurement, $\mathbf{b}_K$.

$$\begin{aligned}
C\left(\hat{\mathbf{q}}\right) &= \mathbf{I}_{3\times 3} - 2q_S\left[q_V\times\right] + 2\left[q_V\times\right]\left[q_V\times\right] \\
&= \Xi\left(\hat{\mathbf{q}}\right)^T \Psi\left(\hat{\mathbf{q}}\right)
\end{aligned} \tag{3.14}$$

$$\begin{aligned}
\mathbf{b}_K &= C\left(\hat{\mathbf{q}}_K^+\right)\mathbf{r}_K \\
&= C\left(\delta\mathbf{q}_K \otimes \hat{\mathbf{q}}_K^-\right)\mathbf{r}_K
\end{aligned} \tag{3.15}$$

Referring to Equation (3.14) and assuming that the scalar quaternion part re-

mains constant and neglecting second order terms, the direction cosine matrix can be approximated as simply a linear function of the vector part of the quaternion. Assuming that the star measurements and rate gyro measurements are corrupted by a given level of noise and the gyro bias is subject to random walk, the differential correction states estimated by the MEKF are $\Delta\mathbf{x} = [\delta\boldsymbol{\alpha}\ \Delta\boldsymbol{\beta}]^T$. Where $\delta\boldsymbol{\beta}$ is the correction to the pre-existing estimate of the gyro bias and $\delta\boldsymbol{\alpha}$ is twice the differential correction for simplification of equations.

3.2.2.1 State and Covariance Propagation

The MEKF discrete error model for state propagation is given by Equation (3.16) where the updated angular velocity and bias estimate are assumed to remain constant over the propagation interval. The quaternion state transition matrix is given by Equation (3.17), [16]. The typical EKF nomenclature of The "+" meaning updated and "-" meaning propagated is adopted.

$$\begin{aligned} \hat{\mathbf{q}}_{K+1}^{-} &= \bar{\boldsymbol{\Omega}}\left(\hat{\boldsymbol{\omega}}_K^{+}\right)\hat{\mathbf{q}}_K^{+} \\ \hat{\boldsymbol{\omega}}_K^{+} &= \tilde{\boldsymbol{\omega}}_K - \hat{\boldsymbol{\beta}}_K^{+} \\ \hat{\boldsymbol{\beta}}_{K+1}^{-} &= \hat{\boldsymbol{\beta}}_K^{+} \end{aligned} \tag{3.16}$$

$$\begin{aligned} \bar{\boldsymbol{\Omega}}\left(\hat{\boldsymbol{\omega}}_K^{+}\right) &= \begin{bmatrix} \cos\left(\frac{1}{2}|\hat{\boldsymbol{\omega}}_K^{+}|\Delta t\right) I_{3\times 3} - \left[\psi_K^{+}\times\right] & \psi_K^{+} \\ \left(-\psi_K^{+}\right)^T & \cos\left(\frac{1}{2}|\hat{\boldsymbol{\omega}}_K^{+}|\Delta t\right) \end{bmatrix} \\ \psi_K^{+} &= \frac{\sin\left(\frac{1}{2}|\hat{\boldsymbol{\omega}}_K^{+}|\Delta t\right)\hat{\boldsymbol{\omega}}_K^{+}}{|\hat{\boldsymbol{\omega}}_K^{+}|} \end{aligned} \tag{3.17}$$

The discrete time propagation of the covariance associated with the differential corrections is computed using the typical EKF covariance propagation equation. Equation (3.18) gives the explicit matrix formulations for a gyro with measurement

noise with a bias subject to random walk [16].

$$
\begin{aligned}
P_{K+1}^{-} &= \mathbf{\Phi}_K P_K^{+} \mathbf{\Phi}_K^T + \mathbf{\Upsilon}_K Q_K \mathbf{\Upsilon}_K^T \\
\mathbf{\Upsilon}_K &= \begin{bmatrix} -I_{3\times3} & 0_{3\times3} \\ 0_{3\times3} & I_{3\times3} \end{bmatrix} \\
Q_K &= \begin{bmatrix} \left(\sigma_{Gyro}^2 \Delta t + \frac{1}{3}\sigma_{Bias}^2 \Delta t^3\right) I_{3\times3} & -\left(\frac{1}{2}\sigma_{Bias}^2 \Delta t^2\right) I_{3\times3} \\ -\left(\frac{1}{2}\sigma_{Bias}^2 \Delta t^2\right) I_{3\times3} & \left(\sigma_{Bias}^2 \Delta t\right) I_{3\times3} \end{bmatrix} \\
\Phi_K &= \begin{bmatrix} \Phi_{11} & \Phi_{12} \\ 0_{3\times3} & I_{3\times3} \end{bmatrix} \\
\Phi_{11} &= I_{3\times3} - [\hat{\boldsymbol{\omega}}\times] \frac{\sin\left(|\hat{\boldsymbol{\omega}}|\Delta t\right)}{|\hat{\boldsymbol{\omega}}|} + [\hat{\boldsymbol{\omega}}\times]^2 \frac{1-\cos\left(|\hat{\boldsymbol{\omega}}|\Delta t\right)}{|\hat{\boldsymbol{\omega}}|^2} \\
\Phi_{12} &= [\hat{\boldsymbol{\omega}}\times] \frac{1-\cos\left(|\hat{\boldsymbol{\omega}}|\Delta t\right)}{|\hat{\boldsymbol{\omega}}|^2} - I_{3\times3}\Delta t - [\hat{\boldsymbol{\omega}}\times]^2 \frac{|\hat{\boldsymbol{\omega}}|\Delta t - \sin\left(|\hat{\boldsymbol{\omega}}|\Delta t\right)}{|\hat{\boldsymbol{\omega}}|^3}
\end{aligned}
\tag{3.18}
$$

3.2.2.2 State and Covariance Update

With the propagated or initial quaternion and gyro bias estimate along with the covariance associated with the differential corrections, once a measurement of a star becomes available the propagated solution can be updated. This research utilizes Murrell's version of the update so that measurements are processed one at a time to avoid inversion of a $3n \times 3n$ matrix, n corresponds to the number of star measurements available at a given time. The "ith" measurement at time K is assumed to be corrupted by additive Gaussian noise and is given by Equation (3.19).

$$
\begin{aligned}
\tilde{\mathbf{b}}_K, i &= C\left(\hat{\mathbf{q}}_{K,True}\right) \hat{\mathbf{r}}_i + \mathbf{v}_{K,i} = \mathbf{h}_K\left(\hat{\mathbf{q}}_{K,True}\right) + \mathbf{v}_{K,i} \\
\mathbf{v}_{K,i} &\sim \mathcal{N}\left(\mathbf{0}_{3\times1}, \sigma_{Meas}^2 I_{3\times3}\right)
\end{aligned}
\tag{3.19}
$$

The pseudo-measurement used for computing the measurement residual, or inno-

vation, from the propagated previous updated quaternion, $\hat{\mathbf{q}}_K^-$, can be calculated by applying Equation (3.19) without the measurement noise and using the estimated quaternion in place of the true quaternion. For computation of the measurement sensitivity matrix, H_K, the partial derivative of the measurement residual is taken with respect to the differential state corrections and shown by Equation (3.20).

$$\begin{aligned} H_K\left(\hat{\mathbf{x}}_K^-\right) &= \frac{\partial\left(C\left(\hat{\mathbf{q}}_{K,True}\right)\mathbf{r}_{K,i} - C\left(\hat{\mathbf{q}}_K^-\right)\mathbf{r}_{K,i}\right)}{\partial\Delta\mathbf{x}} \\ &= \left[\left[\left(C\left(\hat{\mathbf{q}}_K^-\right)\mathbf{r}_{K,i}\right)\times\right]0_{3\times3}\right] \end{aligned} \tag{3.20}$$

Using the measurement sensitivity matrix and the propagated covariance of the differential corrections, the differential corrections can be updated by cycling through each measurement at the given measurement time. The updated differential correction covariance and differential correction states are given by Equation (3.21). Using Murrell's version, at the start of each measurement time, the updated differential corrections are set to zero, $\Delta\hat{\mathbf{x}}_K^- = 0_{6\times1}$, while the covariance is initialized from the propagated previously updated covariance then all measurements are cycled through for updating of the differential corrections and their covariance.

$$\begin{aligned} P_K^+ &= \left[I_{6\times6} - K_K H_K\right]P_K^- \\ \Delta\hat{\mathbf{x}}_K^+ &= \Delta\hat{\mathbf{x}}_K^- + K_K\left[\tilde{\mathbf{b}}_{K,i} - C\left(\mathbf{q}_K^-\right)\mathbf{r}_{K,i} - H_K\Delta\hat{\mathbf{x}}_K^-\right] \\ K_K &= P_K^- H_K^T\left(H_K P_K^- H_K^T + R_K\right)^{-1} \\ R_K &= \sigma_{Meas}^2 I_{3\times3} \end{aligned} \tag{3.21}$$

After all measurements have been processed, the quaternion and bias states are updated via Equation (3.22), then an angular velocity measurement is taken and corrected with the updated bias states. The quaternion and differential covariance

are then propagated according to Equation (3.16) and Equation (3.18). Before the quaternion can be propagated, it must be renormalized after the differential correction update to maintain unit value.

$$\begin{aligned}
\hat{\mathbf{q}}_K^+ &= \begin{bmatrix} \frac{1}{2}\delta\hat{\boldsymbol{\alpha}}^+ \\ 1 \end{bmatrix} \otimes \hat{\mathbf{q}}_K^- \\
&= \hat{\mathbf{q}}_K^- + \frac{1}{2}\Xi\left(\hat{\mathbf{q}}_K^-\right)\delta\hat{\boldsymbol{\alpha}}^+ \\
\hat{\boldsymbol{\beta}}_K^+ &= \hat{\boldsymbol{\beta}}_K^- + \delta\hat{\boldsymbol{\beta}}^+ \\
\Delta\hat{\mathbf{x}}_K^+ &= \begin{bmatrix} \delta\hat{\boldsymbol{\alpha}}^+ \\ \delta\hat{\boldsymbol{\beta}}^+ \end{bmatrix}
\end{aligned} \tag{3.22}$$

3.3 Posterior Density Sampling Approximation

Sampling filters use statistical linearization to approximate the posterior state PDF then propagate the PDF using the nonlinear state equations. Approximations made for sampling the posterior PDF produce their own shortcomings, such as only propagating the first two statistical moments instead of the entire PDF or the need to reinitialize the weighting structure when the user-defined PDF is not the exact posterior. The two most common sampling filters are the unscented Kalman filter(UKF) and particle filter(PF), which utilize the nonlinear equations of motion and measurement with linear updates for the state estimate and covariance. However, use different techniques for weighting possible state estimates, i.e. generating the posterior PDF, are utilized. The UKF approximates the posterior PDF using a small set of deterministically chosen samples while the PF uses a rather large set of random samples [15]. The filters are summarized with respect to their approaches to allow for comparison with the Bayes' filter, a formal writeup and comparison can

be found by van der Merwe et al. [63].

3.3.1 Unscented Kalman Filter

The unscented Kalman filter utilizes the same update structure as the extended Kalman filter, but uses the nonlinear process equations to propagate the state estimate and "sigma points" to propagate the posterior PDF up through the second moment, third moment if the distribution is symmetric. The sigma points are deterministically selected depending upon the distribution shape and system nonlinearity via the scheme shown in Equation (3.23) given a previous state estimate vector, $\hat{\mathbf{x}}_{K-1}$, and state covariance, P^{+}_{K-1}. The state estimate is then propagated to the next time using the nonlinear process equations while the covariance is propagated utilizing sigma points selected to capture the posterior PDF character. Selection of the sigma points depends upon (a) the number of process states, (b) if the user wishes to estimate the process and/or measurement noise vectors, and (c) user-defined parameters dictating the scaling of the sigma points. Equation (3.24) defines how the sigma points are weighted depending on the dimensionality and nonlinearity of the system. The weights form a pseudo-probability density function except the sum of the weights does not necessarily equal one.

$$\mathcal{X}_{K-1} = \left[\hat{\mathbf{x}}^{+}_{K-1} \quad \hat{\mathbf{x}}^{+}_{K-1} \pm \sqrt{(L+\lambda)\, P^{+}_{K-1}}\right] \tag{3.23}$$

$$\left.\begin{aligned} W_1^{mean} &= \frac{\lambda}{L+\lambda} \\ W_1^{cova} &= W_1^{mean} + \left(1 - \alpha^2 + \beta\right) \\ W_i^{mean} &= W_i^{cova} = \frac{1}{2\,(L+\lambda)} \\ i &\in [2, 2L+1] \end{aligned}\right| \begin{aligned} &L = \dim\left(\hat{\mathbf{x}}^{+}_{K-1}\right) \\ &\lambda = \alpha^2\,(L+\kappa) - L \\ &\alpha \in [\,0, 1\,] \quad , \quad \kappa \geq 0 \end{aligned} \tag{3.24}$$

The first scaling parameter, α, determines the spread of the sigma points and is

usually small to combat nonlinearity effects [63]. The second user-defined parameter, κ, allows for exploitation of prior knowledge about higher moments of the distribution. If κ is set to $3-L$, the mean square error may be minimized up to fourth-order, but if the parameter is negative, the predicted covariance may become nonpositive semidefinate [16]. The β parameter affects the weight of the initial sigma point, i.e. the propagated estimate from the previous time. If knowledge of the distribution of state variables is known, this parameter can be used to minimize higher-order errors [63]. With the given sigma point and weight calculation equations, propagation of the covariance requires $2L+1$ sigma points, each of dimension L, with weight vectors of length $2L+1$ for the mean and covariance, but only the first element of the weight vectors is different. The propagation stage of the UKF is shown in Equations (3.25) and (3.26) [63]. The UKF uses the same measurement update for the state and covariance as the EKF update, Equation (3.7), but the innovation covariance, P_K^{vv}, and cross covariance, P_K^{xz}, are calculated based upon propagation of sigma points from the previous measurement update.

$$\begin{aligned} \mathcal{X}_K^- &= \mathbf{f}_{K-1}\left(\mathcal{X}_{K-1}, \mathbf{u}_{K-1}, t, \mathbf{w}_{K-1}\right) \\ \hat{\mathbf{x}}_K^- &= \sum_{i=1}^{2L+1} W_i^{mean} \mathcal{X}_K^- \end{aligned} \qquad \left| \quad P_K^- = \sum_{i=1}^{2L+1} W_i^{cova} \left(\mathcal{X}_K^- - \hat{\mathbf{x}}_K^-\right)\left(\mathcal{X}_K^- - \hat{\mathbf{x}}_K^-\right)^T \right. \tag{3.25}$$

$$\begin{aligned} \mathcal{Z}_K^- &= \mathbf{h}_K\left(\mathcal{X}_K^-, \mathbf{v}_K\right) \\ \hat{\mathbf{z}}_K^- &= \sum_{i=1}^{2L+1} W_i^{mean} \mathcal{Z}_K^- \end{aligned} \qquad \left| \begin{aligned} P_K^{zz} &= \sum_{i=1}^{2L+1} W_i^{cova} \left(\mathcal{Z}_K^- - \hat{\mathbf{z}}_K^-\right)\left(\mathcal{Z}_K^- - \hat{\mathbf{z}}_K^-\right)^T \\ P_K^{vv} &= P_K^{zz} + R_K \\ P_K^{xz} &= \sum_{i=1}^{2L+1} W_i^{cova} \left(\mathcal{X}_K^- - \hat{\mathbf{x}}_K^-\right)\left(\mathcal{Z}_K^- - \hat{\mathbf{z}}_K^-\right)^T \end{aligned} \right. \tag{3.26}$$

After calculation of the present state estimate and covariance, the cycle then starts back at Equation (3.23) to generate an updated set of sigma points, Equa-

tion (3.25) is used to propagate the sigma points to the next measurement time, and so on. The UKF possesses increased computational burden compared with the EKF, but the use of sigma points relieves the need to compute Jacobians. Additionally, sigma point scaling contingent on system nonlinearity allows for higher-order validity so the expected error is lower than the EKF.

3.3.2 Particle Filter

Particle filters utilize Monte Carlo sampling to approximate the posterior PDF via random samples with appropriately chosen weights. Monte Carlo simulation is applied in conjunction with importance sampling to allow for state estimation using weights computed from a sampled posterior density. Importance sampling computes the weights of generated samples and requires the user to define the analytic character of the posterior state PDF, known as the importance or proposed density [15]. If the posterior PDF is not known exactly, as is common in most problems, a posterior approximation must be used, which renders the PF suboptimal. If the posterior PDF is relatively well known, the number of samples must be rather large so that the importance density approaches the true posterior PDF.

A generic PF is presented utilizing Sequential Importance Sampling(SIS) with Bayesian weight inference and resampling. The SIS step forms the backbone for most PFs and is shown by Equation (3.27) [15]. Besides appropriate proposition of the importance density, $q\left(\mathbf{x}_K|\mathbf{x}_{K-1}, \tilde{\mathbf{z}}_K\right)$, the number of particles, N, must be chosen to produce an accurate and consistent estimate without producing a large computational burden as the state vector dimension, n, grows. For nomenclature, at time K, let $\mathcal{X}_K$ represent the set of particles and be of dimension n x N and let W_K represent the $1 \times N$ vector of weights. Then let $\mathcal{X}_K^i$ represent the i^{th} sample of the state domain and W_K^i representing its respective scalar weight. Given an initial

set of particles with respective weights at time $K-1$ and a measurement at time K the generic PF is carried out sequentially.

$$\begin{aligned}
\mathcal{X}_K^i &\sim q\left(\mathcal{X}_K|\mathcal{X}_{K-1}^i, \tilde{\mathbf{z}}_K\right) \\
W_K^i &= \frac{\tilde{W}_K^i}{\sum_{i=1}^{N} \tilde{W}_K^i} \\
\tilde{W}_K^i &= W_{K-1}^i \frac{p\left(\tilde{\mathbf{z}}_K|\mathcal{X}_K^i\right) p\left(\mathcal{X}_K^i|\mathcal{X}_{K-1}^i\right)}{q\left(\mathcal{X}_K^i|\mathcal{X}_{K-1}^i, \tilde{\mathbf{z}}_K\right)}
\end{aligned} \tag{3.27}$$

The importance density in Equation (3.27), $q\left(\mathbf{x}_K|\mathbf{x}_{K-1}, \tilde{\mathbf{z}}_K\right)$, is typically selected to fit the assumption that state variable uncertainties are of Gaussian character with mean and covariance given by $\mathbf{f}_{K-1}\left(\mathbf{x}_{K-1}, \mathbf{u}_{K-1}, t\right)$ and Q_{K-1} respectively. The Gaussian assumption for the importance density produces a suboptimal filter for nonlinear problems. Even if the Gaussian assumption is valid for a certain state variable, it may not be valid for others. Using the Gaussian distribution assumption, the importance density becomes equivalent to the prior, $p\left(\mathbf{x}_K|\mathbf{x}_{K-1}\right)$. Since the importance density is selected to be equivalent to the prior the Bayes' update for the weights, Equation (3.27) simply reduces to the product of the prior weights and present likelihood distribution.

If the chosen importance density is not exactly the posterior distribution, the variance of the importance weights has been shown to increase as the number of recursive steps increases leading to only one particle possessing a nonzero weight. This is known as degeneracy and resampling is carried out to combat this problem [15]. The resampling step eliminates samples with low importance and increases the number of samples with high importance to avoid excessive computational resources for near zero weights. However, resampling requires a measure of degeneracy,such as the

inverse of the sum of the square weights, and a user-defined threshold for triggering the resampling procedure.

The typically utilized resampling procedure maps the current samples and respective weights to a new domain where the weights are uniform and uses the Cumulative Sum of Weights(CSW) as the measure for eliminating or spawning particles [15]. The resampling step is not shown here, but can be found in Ristic et al. [15] or van der Merwe et al. [63]. Whether the resampling is triggered or not, the result is a set of particles at the present time, $\mathcal{X}_K$, with respective weights, W_K. The state estimate and covariance at the present time is calculated similarly to how a random variable's mean and variance are calculated if one possessed the PDF of the random variable, Equation (3.28). After the state estimate and covariance are updated, the PF propagates the particles forward to the next measurement time and SIS carried out utilizing the previous time step's particle weights. With the SIS procedure completed, degeneracy is checked and resampling is carried out if needed with the new state estimate and covariance produced from the newly calculated particles and weights. With the initial tuning parameters of the number of particles and the importance density selected, other refinements exist to improve importance density evolution and sample diversity [15].

$$\begin{aligned} \hat{\mathbf{x}}_K^+ &= \sum_{i=1}^{N} W_K^i \mathcal{X}_K^i \\ P_K^+ &= \sum_{i=1}^{N} W_K^i \left(\mathcal{X}_K^i - \hat{\mathbf{x}}_K^+\right)\left(\mathcal{X}_K^i - \hat{\mathbf{x}}_K^+\right)^T \end{aligned} \tag{3.28}$$

The added computation burden of the PF compared with the UKF is readily apparent, typically the number of particles is much larger than the number of sigma points utilized by the UKF, $N \gg 2L+1$. Thus, tuning the number particles is needed to appropriately balance the trade-off between accuracy and computational burden.

However, utilization of the importance density can allow for increased filter accuracy and performance. Accordingly, appropriate selection of the importance density is crucial to PF operation since incorrect selection can result in divergence or excessive degeneracy. Refinement methods have been introduced to increase the accuracy of the importance density in various ways: (a) using intermediate densities between time steps to reweight the particles which are resampled, (b) using the measurement at time K to refine the particles at time $K-1$ before propagation, or (c) applying an EKF or UKF to generate a Gaussian approximation for the importance density [15].

Sample diversity is an important concern since degeneracy is inherent to SIS particle filters and resampling can cause diversity loss among particles. Thus, other methods such as regularization or the Markov Chain Monte Carlo(MCMC) move step have been implemented to maintain diversity, which can be hard to accomplish especially for systems with little or no process noise. The regularized PF combats loss of diversity by jittering the particles selected from the importance density by a proposed kernel density. Since particle jittering can cause divergence from the true posterior, addition of a MCMC move step, utilizing the Metropolis-Hastings acceptance probability dictating jittering acceptance, can improve operation.

3.4 Transformation of Variables Technique

The transformation of variables(TOV), or change of variables [2], technique allows for exact mapping of a probability density function given in a specified domain into a different domain. The technique allows for the exact expression of the probability density function in a desired domain when (1) the analytic form of the initial probability density function is known and (2) the mapping between initial and desired domains is known, at least once differentiable, and is bijective. Equation (3.29)

summarizes the requirements for TOV.

$$
\begin{aligned}
&p(\mathbf{y}) \Longrightarrow p(\mathbf{x}) \text{ if :} \\
&1.\ p(\mathbf{y}) \text{ given with known analytic form} \\
&2.\ \mathbf{y} = \boldsymbol{\psi}(\mathbf{x})\ ;\ \boldsymbol{\psi}(\bullet) : \Re^n \Longrightarrow \Re^n \text{ and is at least } C^1
\end{aligned}
\tag{3.29}
$$

The TOV technique is based on the integral invariant property of the total probability of an event. Namely, the total probability of a particular event, $P(E)$, occurring within a defined space is invariant of the coordinate system description as long as the basis functions completely span the space. Figure 3.1 displays the integral invariant property of total probability.

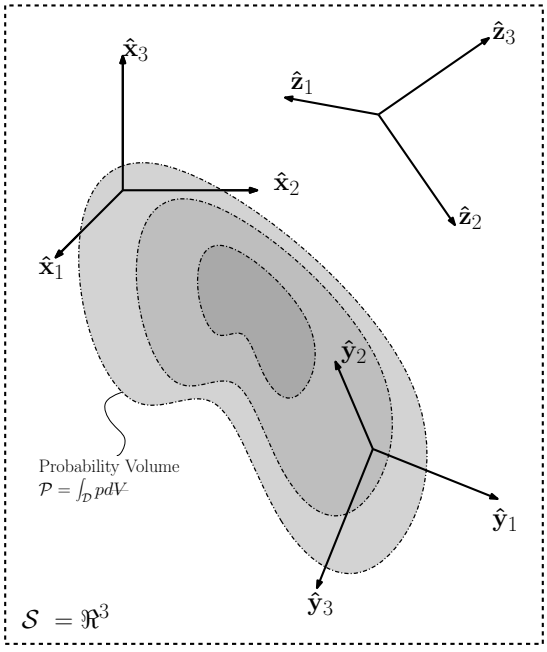

Figure 3.1: Integral Invariant Property of Probability

Figure 3.1 shows that even with three different sets of basis functions spanning the same space, the total probability as dictated by the integration of the probability volume will not change. Equation (3.30) displays the relationship demonstrated

by Figure 3.1 utilizing continuous PDFs of two different coordinate systems which fully span the same n-dimensional space. It is from this relationship that the transformation of variables technique is directly derived. The minimum realization of the basis directions is typically utilized to produce orthogonal basis functions, but non-orthogonal basis functions can be used, however they result in a more complex solution.

$$\begin{aligned} P(E) &= P(\mathbf{y}) = P(\mathbf{x}) \\ &= \int_{\mathcal{D}^{\mathbf{y}}} p(\mathbf{y})\, d\not{V}(\hat{\mathbf{e}}_y) = \int_{\mathcal{D}^{\mathbf{x}}} p(\mathbf{x})\, d\not{V}(\hat{\mathbf{e}}_x) \end{aligned} \tag{3.30}$$

The differential volumes in Equation (3.30) are computed using the wedge product,Equation (3.31). The wedge product is the n-dimensional form used to compute the volume occupied by an n-dimensional parallelpiped spanned by a given set of basis vectors, $\hat{\mathbf{e}} = [\hat{e}_1, \ldots, \hat{e}_n]$. The wedge product uses vector arguments to compute a signed scalar value measuring the size of the space encompassed by a given set of basis functions. Since the wedge product calculates a signed scalar, the Levi-Civita permutation symbol, $\epsilon_{ijk\ldots n}$ is used to compute whether the scalar exists and if it is positive or negative.

$$\begin{aligned} d\not{V}(\hat{\mathbf{e}}) &= d\hat{e}_1 \wedge d\hat{e}_2 \wedge \cdots \wedge d\hat{e}_n \\ &= \eta(\hat{\mathbf{e}})\, \epsilon_{ijk\ldots n} d\hat{e}_1 \wedge d\hat{e}_2 \wedge \cdots \wedge d\hat{e}_n \end{aligned} \tag{3.31}$$

The volume density, $\eta(\hat{\mathbf{e}})$, used in Equation (3.31) is a scalar measure of the amount of distance spanned by the basis functions and is irrespective of order in which basis directions are utilized. Equation (3.32) shows how the volume density is calculated based upon using a distance metric of L_2 type. Common L_2 distance measure scalars are $ds^2 = dx^2 + dy^2 + dz^2$ for Cartesian and $ds^2 = dr^2 + r^2 d\theta^2 +$

$r^2 \sin(\theta)^2 d\phi^2$ for spherical.

$$\begin{aligned} \eta(\hat{\mathbf{e}}) &= \sqrt{\det(G(\hat{\mathbf{e}}))} \\ G(\hat{\mathbf{e}}) &= \frac{\partial^2(ds^2)}{\partial \hat{e}_i \, \partial \hat{e}_j} \quad , \quad i,j \in [1,n] \end{aligned} \tag{3.32}$$

3.4.1 Transformation of Variables Procedure

Let the initial domain of n-independent basis functions completely spanning the space of interest be denoted by $\mathbf{y}$, $\mathbf{y} = [y_1, y_2, \ldots, y_n]$, with $p(\mathbf{y})$ designating the known analytic form of the probability density function which is desired to be transformed. Let $\mathbf{x}$ designate the desired domain spanned by a different set of n-independent basis functions and be related to the initial basis functions by a one-to-one transform which is at least once differentiable over the range to be mapped, Equation (3.29).

The TOV technique given by Equation (3.33) allows for a known PDF in the initial domain, $p(\mathbf{y})$, to be mapped exactly to a desired domain, $p(\mathbf{x})$. For instances where the inverse of the mapping between domains yields multiple solutions, e.g. $y = x^2$, the mapped PDF solution is the sum of all piecewise solutions for the inverse of the mapping function.

$$\begin{aligned} p(\mathbf{x}) &= \begin{cases} \left[p(\mathbf{y}) \, |J|^{-1} \right]_{\mathbf{y}=\boldsymbol{\psi}(\mathbf{x})} , & \text{Single Solution} \\ \sum\limits_{\mathbf{y}_i=\boldsymbol{\psi}_i(\mathbf{x})} \left[p(\mathbf{y}) \, |J|^{-1} \right]_{\mathbf{y}_i=\boldsymbol{\psi}_i(\mathbf{x})} , & \text{Multiple Solutions} \end{cases} \\ J_{\alpha\beta} &= \frac{\partial \boldsymbol{\psi}^{-1}(y_\alpha)}{\partial y_\beta} \quad ; \quad \alpha,\beta \in [1, n = \dim(\mathbf{y})] \end{aligned} \tag{3.33}$$

Equation (3.33) is utilized when it is more convenient to compute partial derivatives of the desired domain functions written in terms of the initial domain functions.

When it is more convenient to compute the derivatives of the initial domain functions written in terms of the desired domain functions, Equation (3.34) can be utilized.

$$\begin{aligned} p(\mathbf{x}) &= p(\mathbf{y})_{\mathbf{y}=\boldsymbol{\psi}(\mathbf{x})} |K| \\ K_{\alpha\beta} &= \frac{\partial \psi(x_\alpha)}{\partial x_\beta} \end{aligned} \tag{3.34}$$

The determinant of the partial derivative matrix between bases in Equations (3.33) and (3.34) arises from the ratio of differential volume elements of the respective domains, rearranging Equation (3.30) for the domain of interest, not a Taylor series expansion of the mapping between domains [43]. Since the determinant of the Jacobian serves as a scale factor between the differential domains, its absolute value is needed instead of its signed value. The sign of the determinant simply dictates whether or not the new domain reflects the initial domain's PDF.

Once the transform between domains is complete, the statistical moment characteristics of the PDF in the new domain can be computed based upon information provided in the initial domain. Assuming that the initial domain bases are constructed from measurements while the desired domain bases are dynamic states, the uncertainty characteristics of the transformed PDF can be used to justify or refute assumptions made about the indirectly observed state distributions or utilized as the likelihood distribution for Bayesian inferencing. The TOV technique can also be applied to stochastic difference equations for solutions of prior densities for Bayesian inferencing [59].

3.4.1.1 Transformation of Variables for $\Re^n \rightarrow \Re^m$, $m = n$

To illustrate the application of TOV, consider the two-dimensional mapping of Cartesian coordinates, $\mathbf{x} \doteq (x, y)$, from a range and angle pair set, $\mathbf{z} \doteq (\rho, \alpha)$, with their relationship given by Equation (3.35). Let the spherical domain be the initial

domain with a given continuous joint PDF, $p(\mathbf{z})$, the Cartesian domain PDF, $p(\mathbf{x})$, is computed by applying Equation (3.33) and the result shown in Equation (3.36). Note that the Jacobian is much easier to evaluate in terms of the measurement domain then transfer to the Cartesian domain and the singularity remains at the origin.

$$\begin{array}{rcl|rcl} \rho & = & \sqrt{x^2+y^2} & x & = & \rho\cos(\alpha) \\ \alpha & = & \arctan\left[\dfrac{x}{y}\right] & y & = & \rho\sin(\alpha) \end{array} \tag{3.35}$$

$$p(\mathbf{x}) = p\Big(\mathbf{z} = \boldsymbol{\psi}(\mathbf{x})\Big)\Big|\rho\Big|^{-1}_{\mathbf{z}=\boldsymbol{\psi}(\mathbf{x})} \tag{3.36}$$

3.4.1.2 Transformation of Variables for $\Re^n \rightarrow \Re^m$, $m < n$ (Auxiliary Variable Method)

There exist cases where one is only concerned with a subset of variables that are related to the initial domain, but do not span the entire space with respect to their basis directions. As an example, consider the same domain mapping given in the above example except that the state of interest is only x. In this case, the method of auxiliary variables [2] can be applied with the auxiliary variable defined as the angle, α, resulting in the Jacobian shown by Equation (3.37) and the joint and marginal PDFs shown in Equation (3.38). Alternatively, had the auxiliary variable been defined as ρ, Equation (3.38) would instead take the form of Equation (3.39). The solutions of Equations (3.38) and (3.39) are derived differently based upon elimination

of auxiliary variables but are equivalent due to the invariance of total probability.

$$\frac{\partial\left(x,\alpha\right)}{\partial\left(\rho,\ \alpha\right)}=\underbrace{\begin{bmatrix}\cos(\alpha) & -\rho\sin(\alpha)\\ 0 & 1\end{bmatrix}}_{J}\begin{bmatrix}\rho\\ \alpha\end{bmatrix} \tag{3.37}$$

$$\begin{aligned} p\left(x,\ \alpha\right)&=p\left(\rho=\frac{x}{\cos(\alpha)},\ \alpha=\alpha\right)\left|\cos(\alpha)\right|^{-1}\\ p\left(x\right)&=\int_{\alpha_0}^{\alpha_f}p\left(x,\ \alpha\right)d\alpha \end{aligned} \tag{3.38}$$

$$\begin{aligned} p\left(x,\ \rho\right)&=p\left(\rho=\rho,\ \alpha=\arccos(x/\rho)\right)\left|\ \rho\sin(\alpha)\right|^{-1}_{\alpha=\arccos(x/\rho)}\\ p\left(x\right)&=\int_{\rho_0}^{\rho_f}p\left(x,\ \rho\right)d\rho \end{aligned} \tag{3.39}$$

3.4.1.3 Transformation of Variables for $\Re^n \rightarrow \Re^m$, $m < n$ (Dirac Delta Method)

From the above example, the complete Jacobian needed to be calculated even when only the PDF of a particular subset of variables was desired. The reduced state variable PDF representation can be computed in an alternative way which avoids the need for a one-to-one transformation between all variables [27]. The method applies the Dirac generalized function in order to transform only the needed variables to the state(s) of interest, for discrete random variables the application is given by Theorem 1.

Theorem 1. *Suppose that z_i, $i = [1, n]$, are discrete random variables with joint probability distribution $p\left(z_1,\ z_2, \ldots,\ z_n\right)$. Let $\mathcal{D}$ be the n-dimensional set of every possible outcome of the z_i's. Then the discrete random variable*

$$x=\boldsymbol{\psi}^{-1}\left(z_1,\ z_2, \ldots,\ z_n\right)$$

has the probability distribution given by use of the Kronecker delta $\delta_{a,b}$ in the form

$$p(x) = \sum_{z_i \in \mathcal{D}} p(z_1,\ z_2, \ldots,\ z_n)\, \delta\left[\boldsymbol{\psi}^{-1}(z_1,\ z_2, \ldots,\ z_n) - x\right]. \tag{3.40}$$

Where

$$\delta_{a,b} = \delta[a-b] = \begin{cases} 1, & a = b \\ 0, & a \neq b \end{cases}.$$

The Kronecker delta can also be applied for computation of continuous random variable PDFs given relationships to other known continuous random variable distributions. The conversion process is outlined by Theorem 2.

Theorem 2. *Suppose that z_i, $i = [1, n]$, are continuous random variables with joint probability distribution $p(z_1,\ z_2, \ldots,\ z_n)$. Let $\mathcal{D}$ be the n-dimensional set of every possible outcome of the z_i's. Then the continuous random variable*

$$x = \boldsymbol{\psi}^{-1}(z_1,\ z_2, \ldots,\ z_n)$$

has the probability distribution given by use of the Kronecker delta $\delta_{a,b}$ in the form

$$p(x) = \int_{\mathcal{D}^{\mathbf{z}}} p(z_1,\ z_2, \ldots,\ z_n)\, \delta\left[\boldsymbol{\psi}^{-1}(z_1,\ z_2, \ldots,\ z_n) - x\right] dz_1 dz_2 \ldots dz_n. \tag{3.41}$$

In order to compute the result of Theorems 1 and 2, properties of the Kronecker delta are required and given by Equation (3.42). The composition property in Equation (3.42) is computed using the roots, y_n, of the function f, hence $f(y_n) = 0$. For the translation property the limits of integration can be over any domain surrounding

the critical points where the Kronecker delta is not zero.

$$
\begin{aligned}
&\textit{Scaling} \\
&\qquad \delta(ay) \quad = \left|\frac{\partial(ay)}{\partial a}\right|^{-1} \delta(y) = \frac{1}{|a|}\delta(y) \\
&\textit{Translation}(\textit{sifting}) \\
&\qquad f(a) \quad = \int_{-\infty}^{\infty} f(y)\delta(y-a)dy \\
&\textit{Composition} \\
&\qquad \delta\Big(f(y)\Big) \quad = \sum_n \delta(y-y_n)\left|\frac{\partial f(y)}{\partial y}\right|_{y_n}^{-1} \\
&\qquad \text{Where:} \qquad f(y_n) = 0 \text{ and } \frac{\partial f(y)}{\partial y} \neq 0
\end{aligned}
\tag{3.42}
$$

Application of Theorem 2 allows for Equation (3.38) to be computed without the need for evaluating the 2×2 Jacobian, shown in Equation (3.43). The roots of $x - \rho\cos(\alpha) = 0$ are $\rho = x/\cos(\alpha)$ and $\alpha = \arccos(x/\rho)$, using the first root to replace the range random variable results in the scaling factor to be $\frac{\partial}{\partial x}\left(x/\cos(\alpha)\right) = \sec(\alpha)$. Once the distribution is properly scaled, it can then be sifted to alleviate dependence on the range random variable, leaving only the angle random variable to be integrated over to produce the desired marginal PDF.

$$
\begin{aligned}
p(x) &= \int_{\mathcal{D}^\rho}\int_{\mathcal{D}^\alpha} p(\rho,\alpha)\,\delta\left[\rho\cos(\alpha) - x\right] d\rho d\alpha \\
&= \int_{\mathcal{D}^\rho}\int_{\mathcal{D}^\alpha} \frac{p(\rho,\alpha)}{\cos(\alpha)}\delta\left[\rho - \frac{x}{\cos(\alpha)}\right] d\rho d\alpha \quad \Big) \textit{Scale} \\
&= \int_{\alpha_0}^{\alpha_f} \frac{1}{\cos(\alpha)} p\left(\rho = \frac{x}{\cos(\alpha)}, \alpha\right) d\alpha \quad \Big) \textit{Sift}
\end{aligned}
\tag{3.43}
$$

Equation (3.39) can be reproduced in a similar manner by utilizing the angle root, $\alpha = \arccos(x/\rho)$, and using its derivative with respect to the state of interest,

x, for the scaling factor as shown by Equation (3.44).

$$\begin{aligned} p(x) &= \int_{\mathcal{D}^\rho}\int_{\mathcal{D}^\alpha} p(\rho,\alpha)\,\delta\left[\rho\cos(\alpha)-x\right]d\rho d\alpha \\ &= \int_{\mathcal{D}^\rho}\int_{\mathcal{D}^\alpha} \frac{p(\rho,\alpha)}{\rho\sin(\alpha)}\delta\left[\alpha-\arccos\left(\frac{x}{\rho}\right)\right]d\rho d\alpha \\ &= \int_{\rho_0}^{\rho_f}\left|\frac{1}{\rho\sin(\alpha)}\right|_{\alpha=\arccos\left(\frac{x}{\rho}\right)} p\left(\rho=\rho,\alpha=\arccos\left(\frac{x}{\rho}\right)\right)d\rho \end{aligned} \tag{3.44}$$

3.4.2 Comparison of Transformation of Variables to the Similarity Transform Method

The similiarity transform [64] has been used in previous communities along with astrodynamics [49, 65] to compute the covariance matrix of a desired domain from a pre-existing covariance matrix of a different domain. The transformation of the covariance from one domain to another can be derived in the exact same manner as the propagation phase of the Kalman filter, Equation (3.7). In the computation, one assumes a linear mapping, evaluated at the current estimate, holds between the domains over the entire region encompassed by the initial domain's covariance hypervolume. The similiarity transform is given by Equation (3.45) and maps a covariance matrix from the initial domain via the Jacobian between the domains evaluated at the present state estimate to the new domain.

$$\begin{aligned} P(\hat{\mathbf{x}}',\hat{\mathbf{x}}') &= \left[\frac{\partial \mathbf{x}'}{\partial \mathbf{x}}\right]_{\hat{\mathbf{x}}'=f(\hat{\mathbf{x}})} P(\hat{\mathbf{x}},\hat{\mathbf{x}}) \left[\frac{\partial \mathbf{x}'}{\partial \mathbf{x}}\right]^T_{\hat{\mathbf{x}}'=f(\hat{\mathbf{x}})} \\ P(\hat{\mathbf{x}},\hat{\mathbf{x}}) &= E\left\{(\mathbf{x}-\hat{\mathbf{x}})(\mathbf{x}-\hat{\mathbf{x}})^T\right\} \end{aligned} \tag{3.45}$$

The resulting mapping is not unlike the inertia tensor mapping used when rotating basis directions [66]. However, in inertia tensor computations, when bases are exchanged and not just merely rotated, one must compute the inertia in the new do-

main by applying the integral definition of inertia to preserve all information across the mapping and not simply applying a linear mapping [67].

In a trivial, but valuable, example taken from Stark and Woods [68], consider two two-dimensional domains linked via a simple rotation, θ, about the out-of-plane axis of the initial domain resulting in the relationship given by Equation (3.46).

$$\begin{aligned} x' &= x\cos(\theta) + y\sin(\theta) \\ y' &= -x\sin(\theta) + y\cos(\theta) \end{aligned} \tag{3.46}$$

The determinant of the Jacobian of the simple rotation with respect to the unprimed variables is +1. Assuming the unprimed variables are Gaussian, the multivariate probability density function given by Equation (3.47), with mean $\boldsymbol{\mu}$ and covariance $\boldsymbol{\Sigma}$, the transformed PDF would be the same as the original except that $\mathbf{v}'$ replaces $\mathbf{v}$ where $\mathbf{v}$ = [x',y']^T. The transformation of variables result is that the computed covariance for the primed domain is the same as the covariance for the unprimed domain. The mean of the primed domain is the mean of the unprimed domain mapped into the prime domain.

$$\mathcal{N}(\mathbf{v};\boldsymbol{\mu},\boldsymbol{\Sigma}) = \frac{1}{\left(\det\left(2\pi\boldsymbol{\Sigma}\right)\right)^{1/2}} \exp\left[-\frac{1}{2}\left(\mathbf{v}-\boldsymbol{\mu}\right)^T \boldsymbol{\Sigma}^{-1}\left(\mathbf{v}-\boldsymbol{\mu}\right)\right] \tag{3.47}$$

Generalizing and expanding the given example, if there existed a double primed domain differing from the primed domain by a matrix of constant values, $\mathbf{v}'' = \boldsymbol{\alpha}\mathbf{v}'$, the resulting PDF is computed by applying transformation of variables and is shown by Equation (3.48). Since the double primed and single primed domains are linearly related then the mean of the double prime domain is easily computed from the expectation operator, $E\{\mathbf{v}''\}$=$\boldsymbol{\mu}_{\mathbf{v}''} = \boldsymbol{\alpha}\boldsymbol{\mu}$, allowing for the mean of the single primed domain to be expressed as a function of the double primed domain mean as is done

in Equation (3.48).

$$p\left(\mathbf{v}''\right) = \frac{\left|\det\left(\boldsymbol{\alpha}\right)\right|^{-1}}{\left(\det\left(2\pi\boldsymbol{\Sigma}\right)\right)^{1/2}} \exp\left[-\frac{1}{2}\left(\boldsymbol{\alpha}^{-1}\mathbf{v}'' - \boldsymbol{\alpha}^{-1}\boldsymbol{\mu}_{\mathbf{v}''}\right)^{T}\boldsymbol{\Sigma}^{-1}\left(\boldsymbol{\alpha}^{-1}\mathbf{v}'' - \boldsymbol{\alpha}^{-1}\boldsymbol{\mu}_{\mathbf{v}''}\right)\right] \tag{3.48}$$

Comparing Equation (3.48) to Equation (3.47), it is easy to see that the double primed domain PDF can be expressed in terms of a Gaussian PDF, $\mathcal{N}\left(\mathbf{v}''; \boldsymbol{\mu}_{\mathbf{v}''}, \boldsymbol{\Sigma}_{\mathbf{v}''}\right)$, with the covariance matrix of the double primed domain is expressed as $\boldsymbol{\Sigma}_{\mathbf{v}''} = \boldsymbol{\alpha}\boldsymbol{\Sigma}_{\mathbf{v}}\boldsymbol{\alpha}^{T}$. This example shows how the similarity transform is easily derived from TOV when the initial distribution is Gaussian. In the example, the linear transformation could also have taken the form of $\mathbf{v}'' = \boldsymbol{\alpha}\mathbf{v}' + \boldsymbol{\beta}$ where $\boldsymbol{\beta}$ is a constant. The presence of the additional constant only serves to alter the mean value of the double primed domain by translating it in addition to rotating it about a fixed point.

In Equations (3.47) and (3.48), if the matrix argument of the exponential is set equal to the square of an integer, $\left(\mathbf{v} - \boldsymbol{\mu}\right)^{T}\boldsymbol{\Sigma}^{-1}\left(\mathbf{v} - \boldsymbol{\mu}\right) = d^{2}$, the equation of the probability ellipsoid [16,69] is formed. Due to the nature of the Gaussian distribution, principal direction and scale decomposition of the probability ellipsoid allows for a complete assessment of state uncertainty and correlation within the hypervolume. The similiarity transform is a shortcut method, which can be employed when one is simply rotating bases about a point, but the initial distribution must possess the same linear type of behavior as the Gaussian distribution, and only be characterized by the first two statistical moments. The similarity transform preserves the characteristic values of the original matrix, thus the lengths of the probability ellipsoid are constant but simply rotated due a change in the eigenvectors since the covariance matrix has been transformed.

Even if the initial distribution was Gaussian, a nonlinear transformation will not allow for the exponential argument to be reduced down to a Gaussian exponential

argument form. Many a time, the nonlinear transformation between domains is state dependent which yields a nonconstant scale factor resulting from the determinant of the Jacobian. An example of a nonconstant Jacobian determinant is given by Equation (3.49), where one seeks to transform from the two-dimensional polar domain to the two-dimensional Cartesian domain.

$$\text{Given} : \mathbf{z} = \begin{bmatrix} \rho \\ \theta \\ \dot{\rho} \\ \dot{\theta} \end{bmatrix} = \begin{bmatrix} \sqrt{x^2+y^2} \\ \arctan\left[\frac{y}{x}\right] \\ \rho^{-1}\left(x\dot{x}+y\dot{y}\right) \\ \rho^{-2}\left(x\dot{y}-\dot{x}y\right) \end{bmatrix} \Longrightarrow |J|_{\mathbf{z}=\mathbf{h}(\mathbf{x})} = \rho^2_{\mathbf{z}=\mathbf{h}(\mathbf{x})} = x^2+y^2 \quad (3.49)$$

The determinant for the three-dimensional transformation from spherical position to Cartesian position is $\rho^2 \sin(\phi)$, where ϕ is measured from the Cartesian vertical axis [67]. Due to the existence of a nonconstant scaling betweeen the domains, a simple point transformation about the present state estimate can produce a covariance matrix that may not be appropriate, in size or shape, in the new state domain especially as the number of states increases and/or the Jacobian determinate becomes increasingly nonlinear. When the similiarity transform is used for analysis of space surveillance systems, the transformed covariance must, many a time, be multiplied by a scalar constant in order to make the transformed covariance more realistic [49].

Another reason why one should start with transforming the PDF then proceed with state estimation is to make sure that the new domain variables do possess finite statistical moments. Consider a second example from Stark and Woods [68], where the double primed domain is nonlinearly related to the single primed domain, given by Equation (3.50), and the transformation possesses multiple solutions. Assuming the single primed domain is Gaussian with no correlation and the same

variance for each variable, transformation of variables is carried out for each of the unique solutions over the appropriate regions and results in the PDF given by Equation (3.51) [68].

$$\begin{array}{l|l} x'' = \left(x'^2 + y'^2\right)^{1/2} & x'_{1,2} = \pm x'' \left(1 + y''^2\right)^{-1/2} \\ y'' = \dfrac{y'}{x'} & y'_{1,2} = y'' x'_{1,2} \end{array} \qquad (3.50)$$
$$\Rightarrow |J| = \frac{1 + y''^2}{x''}$$

$$\begin{aligned} p\left(x', y'\right) &= \frac{1}{2\pi\sigma} \exp\left[-\frac{1}{2\sigma^2}\left(x'^2 + y'^2\right)\right] \\ p\left(x'', y''\right) &= \frac{x''}{\sigma^2} \exp\left[-\frac{x''^2}{2\sigma^2}\right] \frac{1}{\pi\left(1 + y''^2\right)}\ ,\ x'' \geq 0,\ y'' \in (-\infty, \infty) \end{aligned} \qquad (3.51)$$

The PDF solution given by Equation (3.51) of the double primed domain shows both variables remain independent and that the x'' variable is Rayleigh distributed while the y'' variable is Cauchy distributed. If one were to apply the similarity transform to compute the covariance of the new domain they would be doing so improperly because the Cauchy distribution does not have any statistical moments defined, only its median. This example shows that one must start with transforming the PDF from one domain to another then proceed with computing the higher order moments if possible, otherwise information may be lost or misrepresented.

3.4.3 Comparison of Transformation of Variables to the Method of Characteristics

The TOV technique is often thought of in terms of transforming between domains at a given instant in time, but the technique can also be used to propagate uncertainty in systems with state evolutions subject to differential equations through use of the state transition matrix. Weisman et al. [25,36] used the TOV technique and exploited the availability of exact state transition matrix formulations for state propagation to

construct the prior PDF for surveillance applications. In Majji et al. [40], the same group showed that the TOV approach provided the solution to Liouville's equation, which is a partial differential equation dictating the evolution of the probability density function of a Hamiltonian system, the Fokker-Planck-Kolomogorov equation without process noise.

The method of characteristics is a solution method for linear or quasi-linear partial differential equations in which partial differential equations are reduced to ordinary differential equations so that a solution flow for the PDF can be generated from known initial conditions. To show that the TOV technique gives the same solution as the method of characteristics, the example used by Majji et al. [40] to compare to the method of characteristics solution by Halder and Bhattacharya [70] is again utilized.

Considering a one-dimensional system subject to the differential equation of $\dot{x} = -x^2$ with the initial state and PDF conditions given by x_0 and $p(x_0, t_0)$. The solution of the differential equation is $x = x_0 \left(1 + (t - t_0)\, x_0\right)^{-1}$, which allows for TOV to be used in computing the time varying solution of the initial PDF, given by Equation (3.52). The solution is equivalent to the method of characteristics solution and does not require any additional integration of the dynamics since the state transition is already defined and is exact.

$$\begin{aligned} p\left(x\right) &= \left|\frac{\partial x_0}{\partial x}\right| p\left(x_0 = \frac{x}{1 - x(t - t_0)}\right) \\ &= \left|\frac{1}{1 - x(t - t_0)} + \frac{xt}{(1 - x(t - t_0))^2}\right| p\left(x_0 = \frac{x}{1 - x(t - t_0)}\right) \\ &= \frac{1}{(1 - x(t - t_0))^2} p\left(x_0 = \frac{x}{1 - x(t - t_0)}\right) \end{aligned} \tag{3.52}$$

3.5 Use of Transformation of Variables for Bayesian Inferencing

Exact mapping of the probability density function between domains enabled by TOV produces exact knowledge of the system likelihood distribution which allows for a better idea of the combination of system states that generated the measurement. Since the likelihood distribution is exactly mapped between domains, Bayesian estimation can be easily carried out given the prior distribution is appropriately characterized. The posterior probability produced from Bayes' Theorem allows for all statistical moments to be assessed, not just the mean and covariance as with conventional filtering techniques. Availability of the state probability density function can allow for automation of covariance initialization needed for conventional filtering, thereby decreasing the amount of tuning needed to ensure proper filter operation. For systems requiring more than one measurement time to be rendered observable, due to sensing limitations, the transformation of variables approach can be applied to assess the amount of uncertainty associated with the process.

The TOV technique is applied to the measurement and process equations to generate the likelihood and prior distributions respectively for implementation of Bayes' Theorem. It is assumed that an analytic form of the measurement noise PDF exists so the likelihood function can be constructed and TOV applied to map the measurement PDF to the state domain. The prior PDF is generated by applying TOV to map the present state domain backward to allow use of previous measurements. Once the analytic form of the likelihood and prior are constructed, they must be evaluated over a domain of possible state values which generated the measurement(s).

This research uses a simple perturb-then-grid technique, shown in Figure 3.2, similar to sigma point generation, except the measurement is perturbed in the measurement domain using the known standard deviations with the results then mapped

into the state domain. The figure shows examples of how to proceed when the states are fully observable at the given time instant or when additional measurements and a smoothing operation are required to fully observe the system states, e.g. using two consecutive position measurements to estimate velocity at the previous measurement time. After the points are mapped into the state domain, they are redicritized to equally span the space between the extremal points computed from the mapping of the measurement domain points. The technique is not meant to be optimal since the focus of the work is on applying TOV for sequential state estimation instead of optimal sigma point, particle, or grid point generation. The nomenclature is similar to that of the Unscented Kalman Filter [63], $\mathcal{X}_K$ represents the set of all possible state combinations at time K computed from its measurement domain counterpart $\mathcal{Z}_K$, which represents the collection of all measurement domain points resulting from perturbing the observations by a specified amount. The dimension of $\mathcal{X}_K$ is N^n, e.g. for three states the dimension is N x N x N.

As shown in Figure 3.2, generation of a complete probable state domain requires assembling the minimal number of measurements required to render the dynamic states observable. For scenarios where the number of independent basis function measurements are equal to the number of dynamic states, $m = n$, the measurement domain grid can be generated at each time instant. For scenarios where the number of independent measurements are less than the number of dynamic states, $m < n$, one must wait until the dynamic process is rendered observable, then apply a smoothing routine to estimate the higher derivative states, e.g. use successive position measurements to estimate initial velocity. Once the dynamic process is rendered observable, assuming all measurements are statistically independent, the joint likelihood is the product of the individual likelihood PDFs shown by Equation (3.53). The measurement function in Equation (2.1) is utilized to map the state variables

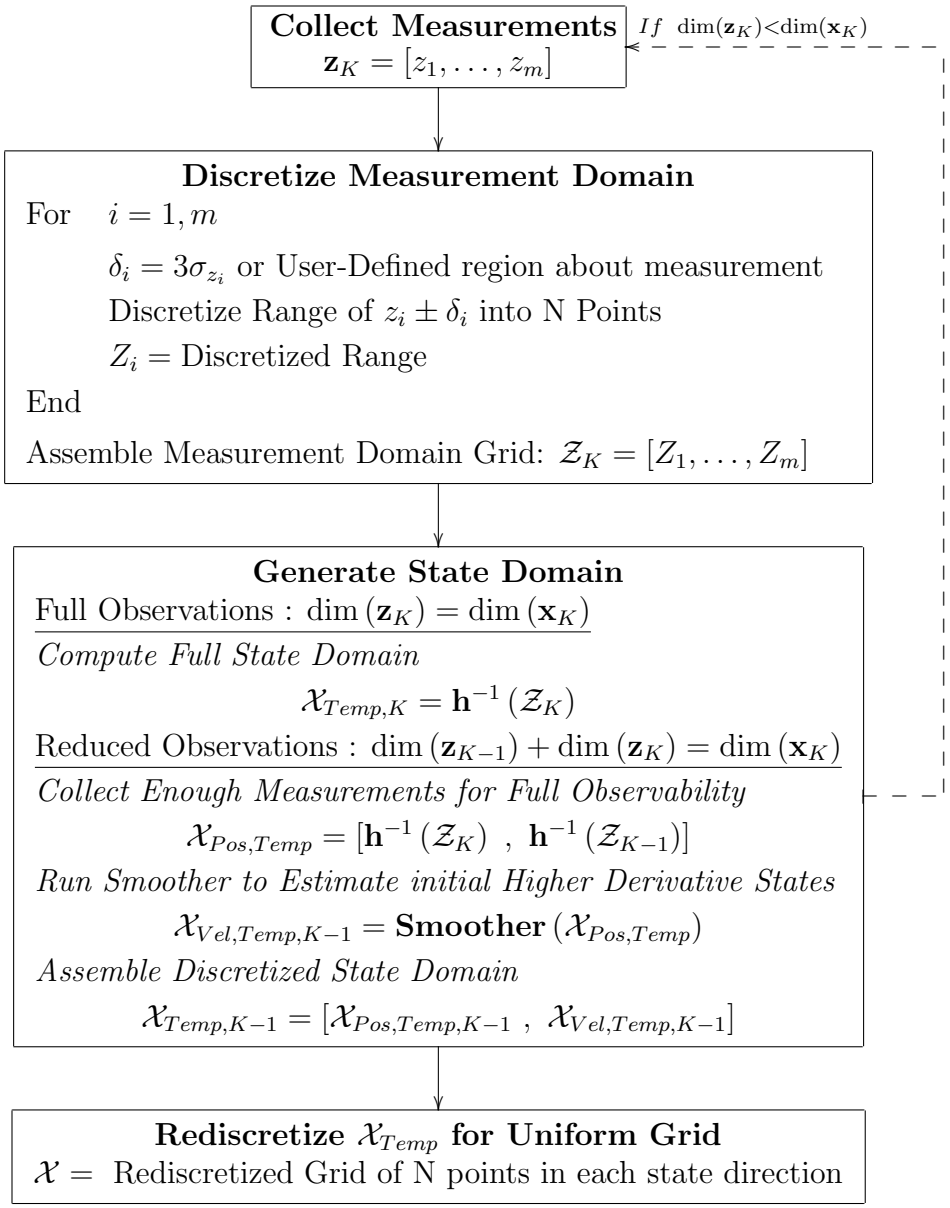

Figure 3.2: Perturb-then-Grid State Domain Generation from Measurement Information

into the observation variables corrupted by a stationary noise process whose analytic form exists. The joint likelihood, as a function of state variables and the present measurement vector, is calculated by applying Equation (3.33) to Equation (3.53)

resulting in Equation (3.54).

$$p\left(\tilde{\mathbf{z}}_K|\mathcal{Z}_K\right) = \prod_{i=1}^{m} p\left(\tilde{z}_i|Z_i\right)_K \tag{3.53}$$

$$p\left(\tilde{\mathbf{z}}_K|\mathcal{X}_K\right) = \left[p\left(\tilde{\mathbf{z}}_K|\mathcal{Z}_K\right)|J|^{-1}\right]_{\mathcal{Z}_K=\mathbf{h}_K(\mathcal{X}_K)} \tag{3.54}$$

3.5.1 Direct State Estimation

3.5.1.1 Full Observation State Estimation

The likelihood PDF, $p\left(\tilde{\mathbf{z}}_K|\mathcal{X}_K\right)$, gives a probability measure, in the form of frequency, expressing the amount of belief that a given combination of state variables generated the present measurement. An example likelihood for a Gaussian corrupted measurement process transformed into the state domain is given by Equation (3.55). Equation (3.55) resembles the typical assumption of the likelihood distribution being Gaussian except for the Jacobian scale factor, which may not be invariant over the domain demonstrating the assumption can be invalid. As an example, the polar to Cartesian mapping yields different scale factors over the entire polar domain that are functions of the random state position variables, Equation (3.49), which results in a non-Gaussian state likelihood.

$$p\left(\tilde{\mathbf{z}}_K|\mathcal{X}_K\right) = \frac{|J|^{-1}_{\tilde{\mathbf{z}}=\mathbf{h}_K(\mathcal{X}_K)}}{\det\left(2\pi R_K\right)^{1/2}} \exp\left\{-\frac{1}{2}\left(\mathbf{h}_K\left(\mathcal{X}_K\right)-\tilde{\mathbf{z}}_K\right)R_K^{-1}\left(\mathbf{h}_K\left(\mathcal{X}_K\right)-\tilde{\mathbf{z}}_K\right)^T\right\} \tag{3.55}$$

With the likelihood function posed in state variable form, all that is left is to compute the state prior PDF so that Bayes' Theorem can be evaluated to compute the state posterior PDF. Construction of the prior PDF takes advantage of the nature of the process model Equation (2.1), which is considered to be a Markov process because the process noise is statistically stationary causing the predicted state to

be dependent only upon the present state [59]. The form of the prior for a Markov process is given by Equation (3.56) and reflects the likelihood of the current state being arrived at via the equations of motion and knowledge about the distribution of the previous state. The summation is used to resolve the joint conditional PDF from the present and previous state domains to the present state domain. The prior density is typically initialized assuming a uniform distribution within the generated state domain since all other available information has been exhausted, $p\left(\mathbf{x}_0^-\right) \sim \mathcal{U}(0,1)$.

$$p\left(\mathbf{x}_K^-\right) = \sum_{\mathbf{x}_{K-1}} p\left(\mathbf{x}_K|\mathbf{x}_{K-1}\right) p\left(\mathbf{x}_{K-1}^-\right) \tag{3.56}$$

At the first measurement time, $K = 1$, Bayes' Theorem is carried out using Equations (3.54) and (3.56), with the assumption of a uniform prior distribution and normalizing the result. The structure of the resulting posterior distribution can then be utilized for computing the prior PDF at the next measurement time. Construction of the next prior uses TOV and the process equations to map between the time domains, shown by Equation (3.57). Transformation of variables is used to construct the prior by using the process equations as the mapping between the present and previous time domains as shown by Equation (3.57). The first measurement is assumed to occur at $K = 1$, so a uniform prior is assumed, $p\left(\mathbf{x}_1^-\right) = p\left(\mathbf{x}_0^-\right) \sim \mathcal{U}(0,1)$.

$$\begin{aligned} p\left(\mathbf{x}_K|\mathbf{x}_{K-1}\right) &= \left[p\left(\mathbf{x}_{K-1}|\tilde{\mathbf{z}}_{K-1}\right)|J|^{-1}\right]_{\mathbf{x}_{K-1}=\mathbf{f}_K^{-1}(\mathbf{x}_K,\mathbf{u}_{K-1},t)} \\ &= p\Big(\mathbf{f}_K^{-1}\left(\mathbf{x}_K,\mathbf{u}_{K-1},t\right)\Big|\tilde{\mathbf{z}}_{K-1}\Big)\Big|\mathbf{\Phi}\left(t_K,t_{K-1}\right)\Big|^{-1} \\ \text{Where: } \mathbf{\Phi}\left(t_K,t_{K-1}\right) &= \frac{\partial \mathbf{x}_K}{\partial \mathbf{x}_{K-1}} \text{ and } \mathbf{x}_K = \mathbf{f}_K\left(\mathbf{x}_{K-1},\mathbf{u}_{K-1},t\right) \end{aligned} \tag{3.57}$$

Note that the Jacobian of the mapping between the previous and present state

domains is the conventional forward state transition matrix. For a linear process model, the determinant of the Jacobian should be one since the basis functions of the solution of the differential equations reside in the same domain and are orthogonal. For nonlinear dynamics, the inverse of the state transition matrix must be computed at each time step, but if the time step is small or the dynamics are relatively linear the determinant will be close to one. The prior PDF using TOV is then found by substituting Equation (3.57) into Equation (3.56) recursively. However, the recursion structure of the prior PDF requires previous measurements to be stored since $p\left(\mathbf{x}_{K-1}^{-}\right)$ is a function of the all previous measurements. To illustrate how the prior is dependent on previous measurements, the first three prior calculations are shown in Equation (3.58).

$$
\begin{aligned}
&\text{Assume}: \; p\left(\mathbf{x}_1^{-}\right) \sim \mathcal{U}(0,1) \\
&p\left(\mathbf{x}_2^{-}\right) = \begin{cases} p\left(\mathbf{x}_2|\mathbf{x}_1\right) &= p\Big(\mathbf{f}_2^{-1}\left(\mathbf{x}_2, \mathbf{u}_1, t\right) \Big| \tilde{\mathbf{z}}_1\Big) \Big| \mathbf{\Phi}\left(t_1, t_2\right) \Big|^{-1} \\ p\left(\mathbf{x}_1^{-}\right) &= \mathcal{U}(0,1) \end{cases} \\
&p\left(\mathbf{x}_3^{-}\right) = \begin{cases} p\left(\mathbf{x}_3|\mathbf{x}_2\right) &= p\Big(\mathbf{f}_3^{-1}\left(\mathbf{x}_3, \mathbf{u}_2, t\right) \Big| \tilde{\mathbf{z}}_2\Big) \Big| \mathbf{\Phi}\left(t_2, t_3\right) \Big|^{-1} \\ p\left(\mathbf{x}_2^{-}\right) &= p\Big(\mathbf{f}_2^{-1}\left(\mathbf{f}_3^{-1}\left(\mathbf{x}_3, \mathbf{u}_2, t\right), \mathbf{u}_1, t\right) \Big| \tilde{\mathbf{z}}_1\Big) \Big| \mathbf{\Phi}\left(t_1, t_2\right) \Big|^{-1} \mathcal{U}(0,1) \end{cases}
\end{aligned}
\tag{3.58}
$$

If the utilized process model is incorrect, Equation (3.56) will be biased toward the incorrect model resulting in the posterior beginning to ignore new measurement information, i.e. the low agreement between the likelihood and prior distributions will produce a more uniform posterior within the generated domain. Filter divergence can result when present measurements have little effect on the posterior calculation due dominance of the process model. This behavior has been previously observed with regard to linearization considerations in the Kalman filter. A way to combat

possible bias resulting from an incorrect process model is use of limited-memory filtering [59], which considers only data from the recent past.

The amount of previous data considered can be evaluated by examining the amount of information gained through incorporation of additional previous measurements. This can be done via use of PDF agreement metrics, e.g. Kullback distance content [43], but care should be exercised so as not to introduce unnecessary user-defined tuning parameters. From the computed likelihood and prior joint PDFs, Bayes' Theorem calculates the joint posterior PDF, dimension N^n, for the generated state domain conditioned upon the present measurement and the previous measurements utilized in the calculation of the prior. For individual state estimates, the joint posterior is resolved into marginal PDFs for each state by summing over all the indicies not associated with the state in question. The state estimate and covariance can then be calculated using Equations (3.3) and (3.5).

3.5.1.2 Reduced Observation State Estimation

The TOV technique can be used to quantify the amount of uncertainty associated with calculating the smoothed estimates of indirectly observed states at time $K-j$ given directly observed states at time $K-j$ through K, and the state process model which satisfies the system observability criterion [16] at a given point in time. This is accomplished by recording enough measurements to yield the system observable, then using the state process model to establish the prior PDF using transformation of variables. The result is then used in conjunction with the transformed likelihood PDF at the time of interest to compute the smoothed estimate of the states at the desired time.

Consider the dimension of the measurement vector, m, to be half the dimension of the state vector, n, this corresponds to position only observations of a process

dictated by position and velocity level variables. Velocity smoothing is required while filtering position measurements to form a complete estimate of the system states. Let $\tilde{\mathbf{z}}_K$ represent a vector of independent position observations at time K while $\mathbf{x}_K$ and $\dot{\mathbf{x}}_K$ represent the state position and velocity states at time K respectively.

The position likelihood PDF, at each measurement time, can be generated from the measurement vector using Equation (3.54). Position state filtering can be carried out as described in the full sensing case, but only assuming a uniform prior distribution since the prior distribution requires velocity information at the present time for backward propagation. Once enough position measurements are received to fully observe the velocity state variables at the time of interest, $K-j$, the velocity domain can be generated and TOV applied to estimate the uncertainty associated with the smoothing process. Equation (3.59) is a general expression for calculating the domain of the velocity variable at the time of interest subject to the modeled dynamics and measurements from the time of interest up to the present time K. The j index represents the number of measurements prior to the present time K needed to render all states observable given the process equations of motion and reduced observation measurements. For a two-dimensional problem possessing linear dynamics, a minimum of two measurement times, $K-1$ and K, are needed for full observability of the velocity variables at time $K-1$.

$$\dot{\mathcal{X}}_{K-j|K-j,\ldots,K} = \mathcal{F}\left(\mathcal{X}_{K-j}, \ldots, \mathcal{X}_K, \mathbf{u}_{K-j}, \ldots, \mathbf{u}_{K-1}, t\right) \tag{3.59}$$

After the velocity states are observable at time $K-j$, the joint likelihood of the position measurements is computed then mapped via TOV to be a function of only the position and velocity domains at the time of interest. Equation (3.60) forms the joint likelihood of the position likelihood PDFs at the required measurement times

then applies the TOV technique to produce a PDF that is solely a function of state variables at the time of interest, $K-j$. Since the velocity domain is computed from differencing multiple position domains the Jacobian, J_{K-i}, will not be square so the determinant cannot be evaluated. However, use of the method of auxiliary variables [2] and judiciously choosing the position variables at the time of interest to be the auxiliary variables, the Jacobian will be square. The dimension of the joint PDF will be increased because both the position and velocity variables at the current time are now treated as random variables in the PDF, but the velocity likelihood can be resolved from the joint by summing over the position variables.

$$
\begin{aligned}
p\left(\tilde{\mathbf{z}}_{K-j},\ldots,\tilde{\mathbf{z}}_{K}|\mathcal{X}_{K-j},\ldots,\mathcal{X}_{K}\right) &= \prod_{i=j}^{0} p\left(\tilde{\mathbf{z}}_{K-i}|\mathcal{X}_{K-i}\right) \\
p\left(\tilde{\mathbf{z}}_{K-j},\ldots,\tilde{\mathbf{z}}_{K}|\mathcal{X}_{K-j},\dot{\mathcal{X}}_{K-j}\right) &= \prod_{i=j}^{0}\Big[p\left(\tilde{\mathbf{z}}_{K-i}|\mathcal{X}_{K-i}\right)\left|J_{K-i}\right|^{-1}\Big]_{\mathcal{X}_{K-i}=\mathbf{f}\left(\mathcal{X}_{K-j},\dot{\mathcal{X}}_{K-j},\mathbf{u}_{K-j},t\right)}
\end{aligned}
\tag{3.60}
$$

An example of Equation (3.60) is shown in Equation (3.61) for a two dimensional problem with constant acceleration, $\tau = t_K - t_{K-1}$. With the domain and likelihood generated for the velocity states at time $K-j$, all that is left is the computation of the prior, $p\left(\mathbf{x}_{K-j}^{-},\dot{\mathbf{x}}_{K-j}^{-}\right)$. Following the same procedure outlined in the full sensing case, the prior for the $K-j$ velocity estimate is calculated by propagating the $K-j$ domains backward in time and centering their results about the previous measurements. The resulting prior possesses a similar flow to that shown by Equation (3.58) and is shown by Equation (3.62). Bayes' Theorem can be evaluated to compute the posterior distribution for the generated position and velocity domains at the $K-j$ measurement. The reduction from joint PDF to marginal PDF can be carried out to produce the marginal distributions from the joint posterior so that smoothed velocity

and position estimates can be calculated using Equations (3.3) and (3.5). Figure 3.3 presents a flowchart for the initialization of the reduced sensing TOV Bayesian filter for position and smoother for velocity.

$$\left[\begin{array}{c}\mathbf{x}\\ \hline \dot{\mathbf{x}}\end{array}\right]_{K-1} = \left[\begin{array}{c}x\\ y\\ \hline \dot{x}\\ \dot{y}\end{array}\right]_{K-1} = \underbrace{\left[\begin{array}{cccc} 1 & 0 & 0 & 0\\ 0 & 1 & 0 & 0\\ -\frac{1}{\tau} & 0 & \frac{1}{\tau} & 0\\ 0 & -\frac{1}{\tau} & 0 & \frac{1}{\tau}\end{array}\right]}_{\det(J_{K-1})=\tau^{-2}} \left[\begin{array}{c} x_{K-1}\\ y_{K-1}\\ x_K - 0.5a_x\tau^2\\ y_K - 0.5a_y\tau^2\end{array}\right]$$

$$p\left(\tilde{\mathbf{z}}_K, \tilde{\mathbf{z}}_{K-1}|\mathcal{X}_{K-1}, \dot{\mathcal{X}}_{K-1}\right) = p\left(\tilde{\mathbf{z}}_{K-1}|\mathcal{X}_{K-1}\right) p\left(\tilde{\mathbf{z}}_K|\mathbf{f}_{K-1}\left(\mathcal{X}_{K-1}, \dot{\mathcal{X}}_{K-1}\right)\right)|J_{K-1}|^{-1} \tag{3.61}$$

$$\text{Assume}: p\left(\mathbf{x}_1^-, \dot{\mathbf{x}}_1^-\right) \sim \mathcal{U}(0,1)$$

$$p\left(\mathbf{x}_2^-, \dot{\mathbf{x}}_2^-\right) = \begin{cases} p\left(\mathbf{x}_2, \dot{\mathbf{x}}_2|\mathbf{x}_1, \dot{\mathbf{x}}_1\right) &= p\left(\mathbf{f}_2^{-1}\left(\mathbf{x}_2, \dot{\mathbf{x}}_2, \mathbf{u}_1, t\right)\left|\tilde{\mathbf{z}}_1\right.\right)\left|J_1\right|^{-1}\\ p\left(\mathbf{x}_1^-, \dot{\mathbf{x}}_1^-\right) &= \mathcal{U}(0,1)\end{cases}$$

$$p\left(\mathbf{x}_3^-, \dot{\mathbf{x}}_3^-\right) = \begin{cases} p\left(\mathbf{x}_3, \dot{\mathbf{x}}_3|\mathbf{x}_2, \dot{\mathbf{x}}_2\right) &= p\left(\mathbf{f}_3^{-1}\left(\mathbf{x}_3, \dot{\mathbf{x}}_3, \mathbf{u}_2, t\right)\left|\tilde{\mathbf{z}}_2\right.\right)\left|J_2\right|^{-1}\\ p\left(\mathbf{x}_1^-, \dot{\mathbf{x}}_1^-\right) &= p\left(\mathbf{f}_2^{-1}\left(\mathbf{f}_3^{-1}\left(\mathbf{x}_3, \dot{\mathbf{x}}_3, \mathbf{u}_2, t\right), \mathbf{u}_1, t\right)\left|\tilde{\mathbf{z}}_1\right.\right)\left|J_1\right|^{-1}\mathcal{U}(0,1)\end{cases} \tag{3.62}$$

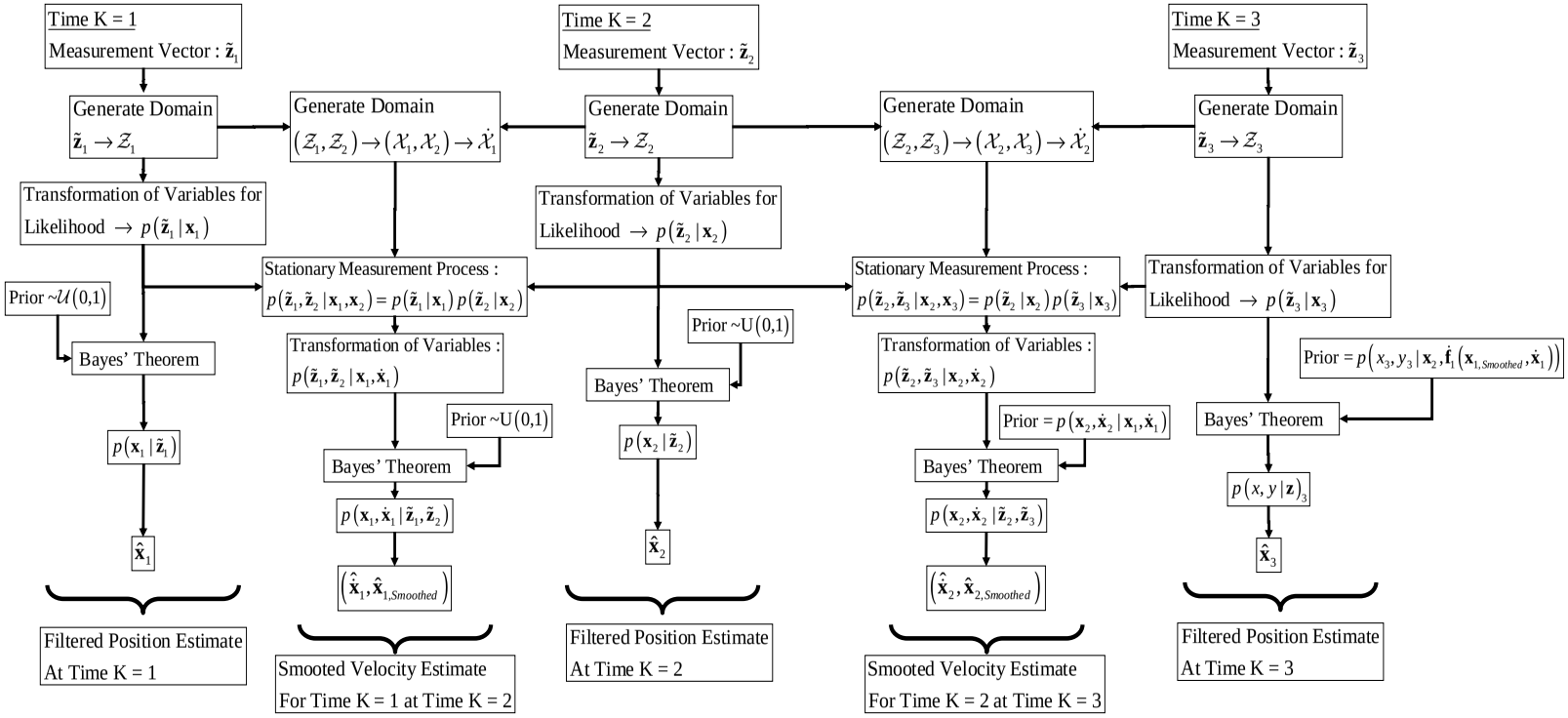

Figure 3.3: Flowchart of Reduced Sensing Estimation for First 3 Measurements

3.5.1.3 Full State Observation with State and Parameter Estimation

For systems with all states fully observable at every instant in time, parameter estimation can be carried out in a manner similar to that of the reduced measurement case. State PDFs at consecutive, or more largely spaced, times can be joined to form a joint PDF where time evolution of the states is governed by a mathematical model with some parameter uncertainty. Assuming the mathematical model used to compute the state transition matrix was not exact with respect to the value used for the parameters, $\mathbf{p}$, TOV can be applied to sequentially estimate the parameters when the model estimates do not agree with what is presently measured. With the appropriate conditions met to trigger the parameter estimation, e.g. propagated states do not agree with present measurements or the propagation time interval is significant, TOV can be applied to map the joint PDF of present states and previous states to the joint PDF of parameters in question, with present or previous states used as auxiliary variables if necessary.

Equation (3.63) applies TOV to compute the resulting joint likelihood PDF of a set of unknown parameters given previous and present full state measurements. Assuming no other information about the parameters uncertainties is available, $p(\mathbf{p}^-) \sim \mathcal{U}(0,1)$, Bayes' Theorem can be applied to compute the posterior PDF. The nomenclature of $[\mathbf{aux}]$ is taken to be the use of any auxiliary variables in order to provide a square Jacobian while $\mathbf{x}(t_K, \ldots, t_{K-i})$ and $\mathbf{z}(t_K, \ldots, t_{K-i})$ represent the i number of state and measurement vectors needed to properly estimate the given parameter vector.

$$p\left(\mathbf{z}(t_K, \ldots, t_{K-i}) \middle| \mathbf{p}, [\mathbf{aux}]\right) = \left[p\left(\mathbf{x}(t_K \ldots t_{K-i})\right) |K|\right]_{\mathbf{x}(t_K \ldots t_{K-i}) = \boldsymbol{\psi}(\mathbf{p}, [\mathbf{aux}])} \quad (3.63)$$

Where:

$$K = \left[\begin{array}{ccc:c} \dfrac{\partial \psi_1}{\partial p_1} & \cdots & \dfrac{\partial \psi_1}{\partial p_{end}} & \dfrac{\partial \psi_1}{\partial \left[\mathbf{aux}\right]^T} \\ \vdots & \ddots & \vdots & \vdots \\ \dfrac{\partial \psi_{end}}{\partial p_1} & \cdots & \dfrac{\partial \psi_{end}}{\partial p_{end}} & \dfrac{\partial \psi_{end}}{\partial \left[\mathbf{aux}\right]^T} \end{array}\right]$$

For initialization of the parameter domain, one can simply take the range of values based upon insight into the behavior of the system. Utilizing the initial parameter estimate given by marginalizing the joint PDF given in Equation (3.63), one can proceed until conditions are such that the parameter must be updated again, e.g. the propagated states not lying within a specified region about the present state estimates defined by the present state uncertainties. Additionally, instead of using the initial parameter domain over, one could apply the same tactic used in the perturb-then-grid method and simply take the present parameter estimate and perturb by some multiple of its uncertainty to generate the new domain.

3.5.1.4 Reduced State Observation with State and Parameter Estimation

Consideration of parameter uncertainty in the reduced sensing case requires additional manipulation and care in execution since the smoothed smoothed state estimates are derived not only from the available measurement data, but from the assumed and erroneous model which is in error. This can lead to a sort of chicken and egg problem reminiscent of an iterated extended Kalman filter which incorporates model parameters in the estimated state vector.

3.5.2 State Differential Correction

This section presents a discussion of using the TOV Bayes' filter for state differential correction like the MEKF presented in Section 3.2.2. The discussion in this section is not as general as the direct state estimation section, instead the TOV

Bayes' filter analog to the MEKF is derived for spacecraft attitude estimation which maps body frame measurements and uncertainties into the differential quaternion frame.

3.5.2.1 Likelihood Density Computation

For the TOV Bayes' attitude filter, the TOV approach is applied to map the additive measurement uncertainty in the body frame into the differential quaternion domain via the same type of decomposition used by the MEKF, shown by Equation (3.64). The likelihood of the differential corrections computed by ToV for all the measurements at time K is shown by Equation (3.65) where n is the number of measurements at time K. Note that since one is able to express the measurement as a function of the desired variables, the latter matrix version of the TOV approach, Equation (3.34), can be used.

$$\begin{aligned}\tilde{\mathbf{b}}_{K,i} &= C\left(\hat{\mathbf{q}}_{True}\right)\hat{\mathbf{r}}_{K,i} + \mathbf{v}_{K,i} \\ &= C\left(\delta\mathbf{q}\right)C\left(\hat{\mathbf{q}}_K^-\right)\hat{\mathbf{r}}_{K,i} + \mathbf{v}_{K,i} \\ &\Rightarrow \mathbf{v}_{K,i} = \tilde{\mathbf{b}}_{K,i} - C\left(\delta\mathbf{q}\right)C\left(\hat{\mathbf{q}}_K^-\right)\hat{\mathbf{r}}_{K,i}\end{aligned} \tag{3.64}$$

$$p\left(\mathbf{v}_{K,i}|\delta\mathbf{q}\right) = \sum_{i=1}^{n} p\left(\mathbf{v}_{K,i} = \tilde{\mathbf{b}}_{K,i} - C\left(\delta\mathbf{q}\right)C\left(\hat{\mathbf{q}}_K^-\right)\hat{\mathbf{r}}_{K,i}\right)\left|\frac{\partial\mathbf{v}_{K,i}}{\partial\delta\mathbf{q}}\right| \tag{3.65}$$

The probability density function of the measurement noise is assumed to be Gaussian and uncorrelated in time, Cartesian position, and successive measurements, thus the joint probability density function for the measurement noise for each measurement is given by Equation (3.66). The PDF for a Gaussian distributed random vector with mean, $\boldsymbol{\mu}$, and covariance, $\boldsymbol{\Sigma}$, is given by Equation (3.47). For the case

of zero mean Gaussian noise, $\boldsymbol{\mu} = \mathbf{0}$, and $\boldsymbol{\Sigma} = \sigma^2_{Meas} I_{3\times 3}$.

$$\begin{aligned} p\left(\mathbf{v}_{K,i}\right) &= p\left(x_{K,i}, y_{K,i}, z_{K,i}\right) = p\left(z_{K,i}|x_{K,i}, y_{K,i}\right) p\left(y_{K,i}|x_{K,i}\right) p\left(x_{K,i}\right) \\ &= p\left(z_{K,i}\right) p\left(y_{K,i}\right) p\left(x_{K,i}\right) \\ &\sim \mathcal{N}\left(\mathbf{v}_{K,i}; \mathbf{0}, \mathbf{1}_{3\times 3}\sigma^2_{Meas}\right) \end{aligned} \tag{3.66}$$

If one were to consider the case of a single measurement, Equation (3.65) would take the form of Equation (3.67). Equation (3.67) uses the shorthand notation of $\mathbf{c} = C\left(\hat{\mathbf{q}}^-_K\right)\hat{\mathbf{r}}_K$ with individual elements denoted by $\mathbf{c}\left(1,\ 2,\ \text{or } 3\right)$ and C_{ij} denoting elements of $C\left(\delta\mathbf{q}\right)$ which are computed from Equation (3.14).

$$\begin{aligned} p\left(\mathbf{v}_{K,i}|\delta\mathbf{q}\right) &= \mathcal{N}\left(\mathbf{v}; \mathbf{0}, \boldsymbol{\Sigma}\right)|K| \\ \mathbf{v} &= \begin{bmatrix} \mathbf{v}\left(x\right) \\ \mathbf{v}\left(y\right) \\ \mathbf{v}\left(z\right) \end{bmatrix} = \begin{bmatrix} \tilde{\mathbf{b}}\left(x\right) - \left(C_{11}\mathbf{c}\left(1\right) + C_{12}\mathbf{c}\left(2\right) + C_{13}\mathbf{c}\left(3\right)\right) \\ \tilde{\mathbf{b}}\left(y\right) - \left(C_{21}\mathbf{c}\left(1\right) + C_{22}\mathbf{c}\left(2\right) + C_{23}\mathbf{c}\left(3\right)\right) \\ \tilde{\mathbf{b}}\left(z\right) - \left(C_{31}\mathbf{c}\left(1\right) + C_{32}\mathbf{c}\left(2\right) + C_{33}\mathbf{c}\left(3\right)\right) \end{bmatrix} \\ K &= \begin{bmatrix} \dfrac{\partial\mathbf{v}\left(x\right)}{\partial\ \delta q_1} & \dfrac{\partial\mathbf{v}\left(x\right)}{\partial\ \delta q_2} & \dfrac{\partial\mathbf{v}\left(x\right)}{\partial\ \delta q_3} \\ \vdots & \ddots & \vdots \\ \dfrac{\partial\mathbf{v}\left(z\right)}{\partial\ \delta q_1} & \cdots & \dfrac{\partial\mathbf{v}\left(z\right)}{\partial\ \delta q_3} \end{bmatrix} \end{aligned} \tag{3.67}$$

For computation of the Jacobian matrix elements, the process is straightforward with an example of computing the partial derivatives of the first element given by Equation (3.68). Since the absolute value of the determinate is taken, all partial derivatives are taken using $-\mathbf{v}_{K,i}$ instead of $\mathbf{v}_{K,i}$ to avoid the negative sign everywhere. Note that $\delta q_4 = 1$ because the scalar part of the quaternion is assumed constant. For reference, the first row of the multiplied out direction cosine matrix as

a function of elements is given by Equation (3.69)

$$\begin{aligned}\frac{\partial \mathbf{v}\left(x\right)}{\partial\ \delta q_1} &= \frac{\partial C_{11}}{\partial\ \delta q_1}\mathbf{c}\left(1\right) + \frac{\partial C_{12}}{\partial\ \delta q_1}\mathbf{c}\left(2\right) + \frac{\partial C_{13}}{\partial\ \delta q_1}\mathbf{c}\left(3\right) \\ &= 2\delta q_1 \mathbf{c}\left(1\right) + 2\delta q_2 \mathbf{c}\left(2\right) + 2\delta q_3 \mathbf{c}\left(3\right)\end{aligned} \tag{3.68}$$

$$\begin{aligned}C\left(\delta\mathbf{q}\right)_{Row\ 1} &= \left[\begin{array}{ccc} C_{11} & C_{12} & C_{13} \end{array}\right] \\ &= \left[\begin{array}{c} \delta q_4^2 + \delta q_1^2 - \delta q_2^2 - \delta q_3^2 \\ 2\left(\delta q_1 \delta q_3 + \delta q_4 \delta q_2\right) \\ 2\left(\delta q_1 \delta q_3 - \delta q_4 \delta q_3\right) \end{array}\right]^T\end{aligned} \tag{3.69}$$

3.5.2.2 Prior Density Computation

A similar procedure for the generation of the prior PDF exists for the Bayes' filter. The structure of the prior results from the Markov nature of Equation (2.1), where future states predicated only on the present states. Equation (3.56) gives the form of the prior, $\delta\mathbf{q}$ substituted for $\mathbf{x}$, which reflects the likelihood of the current state being arrived at via the equations of motion and knowledge about the PDF of the previous state [59]. The summation in the equation resolves the joint conditional PDF of the present and previous state domains to the marginal PDF of the current state domain.

The form of the conditional PDF in Equation (3.56) is inherited from the previous measurement time posterior PDF. Let $\tilde{\mathbf{z}}_{K-1}$ stand for the array of all concatenated measurements at the previous time, $\tilde{\mathbf{z}}_{K-1} = [\hat{\mathbf{r}}_{K-1,1} \cdots \hat{\mathbf{r}}_{K-1,n}]$. The previous measurement time prior is computed by applying Equation (3.56) for $K-1$ instead of K. Equation (3.57) applies TOV to represent the conditional PDF as only a function of the present state domain using the equations of motion as the mapping between the present and previous state domains. Equation (3.57), with $\delta\mathbf{q}$ substituted for $\mathbf{x}$,

shows that the computation of the prior requires the filter to store previous measurements. This dependency on previous measurements renders the TOV Bayes' filter a limited memory filter since the user dictates how many previous measurements are considered in the computation of the prior PDF. The Bayes' filter is typically initialized assuming a uniform prior distribution since all present measurement information has been completely used in the generation of the likelihood distribution.

To compute the prior distribution of the prior domain of quaternion differential corrections based upon collections of star measurements at previous times, consider the discrete propagation of quaternion updated states from Equations (3.16) and (3.17) decomposed into a previous estimate and a differential correction shown by Equation (3.70). Solving Equation (3.70) for only the domain of the quaternion differential corrections at the previous time in Equation (3.70) yields the solution given by Equation (3.71).

$$\begin{aligned}
\hat{\mathbf{q}}_K^+ &= \bar{\mathbf{\Omega}}\left(\hat{\boldsymbol{\omega}}_K\right)^{-1}\hat{\mathbf{q}}_{K+1}^- \\
\begin{bmatrix} \delta\mathbf{q}_K \\ 1 \end{bmatrix} \otimes \hat{\mathbf{q}}_K^- &= \bar{\mathbf{\Omega}}\left(\hat{\boldsymbol{\omega}}_K\right)^{-1}\left(\begin{bmatrix} \delta\mathbf{q}_{K+1} \\ 1 \end{bmatrix} \otimes \hat{\mathbf{q}}_{K+1}^-\right) \\
\begin{bmatrix} \delta\mathbf{q}_K \\ 1 \end{bmatrix} \otimes \hat{\mathbf{q}}_K^- &= \bar{\mathbf{\Omega}}\left(\hat{\boldsymbol{\omega}}_K\right)^{-1}\begin{bmatrix}\Xi\left(\hat{\mathbf{q}}_{K+1}^-\right) & \hat{\mathbf{q}}_{K+1}^-\end{bmatrix}\begin{bmatrix} \delta\mathbf{q}_{K+1} \\ 1 \end{bmatrix}
\end{aligned} \tag{3.70}$$

$$\begin{aligned}
\begin{bmatrix} \delta\mathbf{q}_K \\ 1 \end{bmatrix} &= \bar{\mathbf{\Omega}}\left(\hat{\boldsymbol{\omega}}_K\right)^{-1}\begin{bmatrix}\Xi\left(\hat{\mathbf{q}}_{K+1}^-\right) & \hat{\mathbf{q}}_{K+1}^-\end{bmatrix}\begin{bmatrix} \delta\mathbf{q}_{K+1} \\ 1 \end{bmatrix} \otimes \left(\hat{\mathbf{q}}_K^-\right)^{-1} \\
&= \begin{bmatrix}\Xi\left(\left(\hat{\mathbf{q}}_K^-\right)^{-1}\right) & \left(\hat{\mathbf{q}}_K^-\right)^{-1}\end{bmatrix}\bar{\mathbf{\Omega}}\left(\hat{\boldsymbol{\omega}}_K\right)^{-1}\begin{bmatrix}\Xi\left(\hat{\mathbf{q}}_{K+1}^-\right) & \hat{\mathbf{q}}_{K+1}^-\end{bmatrix}\begin{bmatrix} \delta\mathbf{q}_{K+1} \\ 1 \end{bmatrix}
\end{aligned} \tag{3.71}$$

From Equation (3.71), the domain mapping for the differential corrections relies

upon the propagated previous updated quaternion solutions at time $K-1$ and K. For long propagation times or consideration of many measurement times, this could prove troublesome due to small errors stacking up at time increases or the number of previous measurement times increases. For the solution of the determinant of the state transition matrix between the differential domains at different times, the result is one or nearly one depending upon the propagation time considered. The determinant serves as a way to check if the propagation time is too long because the bases are not changed, i.e. stay in differential quaternion space, so if the determinant starts to decline from one then the state transition matrix solution over that propagation time begins to lose accuracy.

3.5.2.3 Computation of Differential Quaternion Domain from Measurements

Equations (3.65) and (3.71) compute the probability density functions for the differential quaternion element values, however the domain of the differential quaternion corrections needs to be specified without being too general or too narrow in range. One does not want to use the entire possible range of values which the quaternion elements since $\hat{\mathbf{q}}$ and $-\hat{\mathbf{q}}$ describe the same orientation. This problem can be alleviated by choosing the scalar part of the quaternion to be positive, corresponding to the shortest rotation [66]. Alternatively, one does not want to narrow the range of values which the differential corrections take so that possible orientations are not ignored.

The possible domain of differential quaternion correction values can be computed based upon perturbing available measurement, then mapping these perturbations into differential quaternion space. After all measurements have been perturbed and mapped, the domain is generated by discretizing between the extremum values in the differential quaternion correction domain. With the measurement equation de-

composed into the differential quaternion rotation and the propagated quaternion rotation, an expression of the rotation resulting from the differential quaternion can be computed for each measurement using the Moore-Penrose pseudo-inverse as shown by Equation (3.72). Equation (3.72) can then be decomposed into the differential quaternion parts and, noting that δq_4 is always the largest, Equation (3.73) can be applied to compute the differential quaternion correction domain.

$$C\left(\delta\mathbf{q}\right) = \tilde{\mathbf{b}}_{K,i}\left[\left(C\left(\hat{\mathbf{q}}_K^-\right)\hat{\mathbf{r}}_{K,i}\right)^T\left(C\left(\hat{\mathbf{q}}_K^-\right)\hat{\mathbf{r}}_{K,i}\right)\right]^{-1}\left(C\left(\hat{\mathbf{q}}_K^-\right)\hat{\mathbf{r}}_{K,i}\right)^T \tag{3.72}$$

$$\begin{aligned}
\delta q_{4,Temp} &= \frac{1}{2}\left(1 + \text{trace}\left(C\left(\delta\mathbf{q}\right)\right)\right)^{1/2} \\
\delta\mathbf{q}_{Temp} &= \frac{1}{4\delta q_{4,Temp}}\begin{bmatrix} C_{23} - C_{32} \\ C_{31} - C_{13} \\ C_{12} - C_{21} \end{bmatrix} \\
\begin{bmatrix}\delta\mathbf{q}^T & \delta q_4\end{bmatrix}^T &= \text{Normalized } \begin{bmatrix}\delta\mathbf{q}_{Temp}^T & \delta q_{4,Temp}\end{bmatrix}^T
\end{aligned} \tag{3.73}$$

Equations (3.72) and (3.73) map the given corrupted measurement into the differential quaternion space. To generate a possible domain of differential quaternion values, the character of the corrupting noise is utilized to perturb the measurement so that the entire space does not need to be analyzed. Computation of the perturbed possible domain can be performed different ways but this research utilizes the perturb-then-grid method utilized by Weisman et al. [25,36]. Since the measurement is assumed to be corrupted by a zero-mean Gaussian noise with known variance, the corrupt measurement, $\tilde{\mathbf{b}}_{K,i}$, in Equation (3.72) is exchanged for $\tilde{\mathbf{b}}_{K,i} \pm k\sigma_{Meas}$, $k = 3$ or 4, then Equation (3.73) maps the extremal points into the differential quaternion space so that proper ranges can be generated for the particular corrections to the vector part of the quaternion.

When evaluating the joint likelihood or prior using many measurements, a more accurate domain is generated by mapping each perturbed measurement then using the ensemble extremals instead of applying Equation (3.72) in a batch sense, i.e. setting $\tilde{\mathbf{b}}_K = \left[\tilde{\mathbf{b}}_{K,1} \cdots \tilde{\mathbf{b}}_{K,n}\right] + k\sigma_{Meas}$ and $\hat{\mathbf{r}}_K = [\hat{\mathbf{r}}_{K,1} \cdots \hat{\mathbf{r}}_{K,n}]$ then carrying out Equation (3.72). Equation (3.72) depends upon a propagated or current best estimate of vehicle attitude before the current measurements are used to update the estimate. This can pose problems when the propagation interval is long and/or the angular velocity estimate possesses inaccuracies. When utilizing prior measurement times, care must be taken to ensure that when the generated domain is propagated backward, it contains the perturbations of the previous measurements mapped into differential correction space.

4. APPLICATION EXAMPLES*

This section illustrates the application of the TOV technique in a Bayes' Theorem framework for various filtering applications. The first two examples possess linear dynamics in the state domain with observations that are nonlinear functions of the states. The examples are used to illustrate certain behaviors of the TOV Bayes' filter versus conventional nonlinear filtering techniques. The last two examples are particular applications of the TOV Bayes' filter to space surveillance and spacecraft attitude determination.

The first example of a simple arcing mass in a constant gravity field is used to demonstrate fundamentals of the TOV Bayes' filter approach as well as illustrate how the geometry of the observation can affect state estimation. The example also demonstrates how the TOV Bayes' filter approach can be used to assess the effect of applying a smoother for state estimation as well as the effect of incorporating previous data on correctly estimating state uncertainty and correlation.

The linear oscillator example is used as an analog to the periodic nature of orbiting spacecraft as well as conducting state estimation over data drop-outs. The example shows how the TOV Bayes' filter can be used to estimate system parameters by hypothesizing, and then refining the hypotheses after more data has been collected.

The third example, initial orbit determination and object tracking, shows the merit of using TOV to estimate the uncertainty associated with a nonlinear smoothing method which over-constrains the desired states. The form of the probability density functions associated with state domains typically used for space surveillance

*Part of this section is reprinted with permission from "Analytic Assessment of Sensor Uncertainty for Application to Space Object Tracking and Correlation" by Ryan M. Weisman, Manoranjan M. Majji, and Kyle T. Alfriend, 2011. 62nd International Astronautical Congress, Cape Town, South Africa. Copyright 2011 by Ryan M. Weisman, Manoranjan M. Majji, and Kyle T. Alfriend.

analysis are computed and examined. Finally, the technique is shown as a way to automate the initialization of conventional nonlinear filters' initial state estimates and state covariances, which can improve their tracking performance and convergence.

The last example, attitude filtering, demonstrates how the TOV Bayes' filter can be used for spacecraft attitude filtering, as an alternative to the MEKF, especially when measurements are few and far between. The attitude determination example is a departure from previous examples because it shows how the TOV Bayes' filter can be used in a state differential correction framework instead of a direct state estimation framework.

4.1 Planar Arcing Mass in Constant Gravity Field

4.1.1 Geometry

Preliminary evaluation of the TOV Bayes' filter with full and reduced sensing is conducted using a simulation possessing linear state domain dynamics and nonlinearly related measurements. The discrete time system model of two dimensional planar motion for a point mass falling in a gravity field free of drag, $a_x = 0$ and $a_y = -9.81 m/s^2$ is given by rearranging Equation (3.61). The relation of the Cartesian states and polar measurements is shown in Figure 4.1.

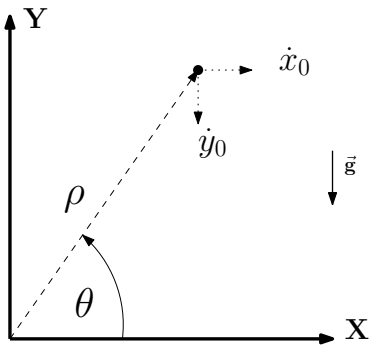

Figure 4.1: Geometry of Falling Mass in Constant Gravity Field with Polar Measurements of Cartesian States

The tracking station is located at the Cartesian origin with measurements taken every two seconds. The object's initial conditions were set to (15, 60) kilometers for position and (1, −1) kilometers per second for velocity. The measurement noise is modeled as mean Gaussian with measurement standard deviations of 0.1km for range, 0.001rad for elevation angle, 0.01km/s for range-rate, and 0.0001rad/s for elevation-rate. For the reduced sensing case, only range and elevation angle are measured. Figure 4.2 illustrates the simple perturb-then-grid method utilized for generating the state domain from the measurement domain.

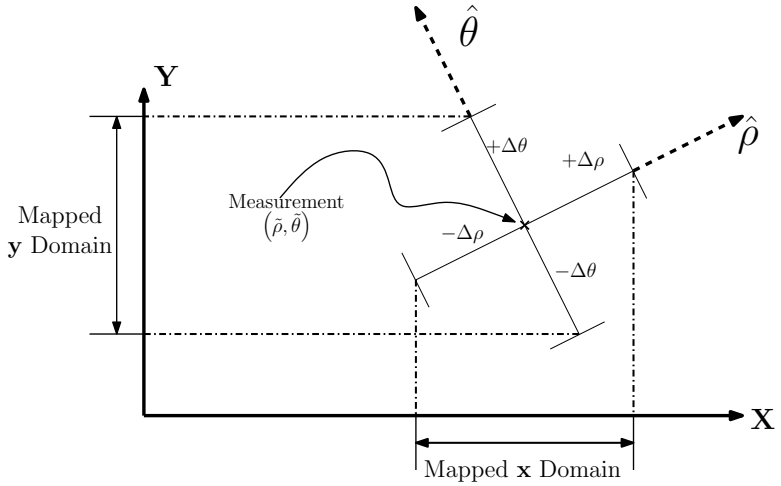

Figure 4.2: Illustration of Perturb-then-Grid Technique Utilized for State Domain Generation

4.1.2 Full Sensing Results

For the scenario of observing as many independent quantities as there are states, the TOV Bayes' filter performance is compared against an extended Kalman filter and an unscented Kalman filter. For tuning of the Kalman filters, only the initial covariance was tuned while the sigma point scaling parameters for the UKF were selected based upon typical approaches [16, 63]. Both the EKF and UKF used the same initial state estimate, computed by mapping the polar measurements to the

Cartesian space, with the initial covariance selected as a diagonal matrix of 1×10^5. Due to the linearity of the process dynamics, the UKF results are extremely close to the results of the EKF, so the results of the UKF operation are omitted for comparison clarity to the TOV Bayes' filter.

The tuning for the TOV Bayes' filter consisted of (a) selecting the number of grid points along each state direction, (b) the amount the measurement was perturbed in each observation basis direction to generate the measurement domain, and (c) how many previous measurements should be used in the computation of the prior distribution. The number of grid points along each direction was selected to be 15 over a domain defined by the measurement being perturbed 3σ in each observation basis direction. To demonstrate the effect of incorporating different amounts of previous measurement data into the prior calculation, the number of considered previous measurements was varied between zero and ten.

A Monte Carlo analysis was performed using 10,000 corrupted measurements at each observation point on the true trajectory. The corrupted measurements were then mapped to the Cartesian domain and used to calculate a numerical mean, $\bar{\mathbf{x}}_K$, and covariance, P_K, for the state domain at each time, K. Equation (4.1) displays the numerical computation for the first two statistical moments with $\mathbf{h}\left(\tilde{\mathbf{y}}\right)$ representing the nonlinear transformation of the measurements into the state domain.

$$\begin{aligned}\bar{\mathbf{x}}_K &= \frac{1}{N_{Trials}}\sum_{i=1}^{N_{Trials}}\mathbf{h}\left(\tilde{\mathbf{y}}_{i,K}\right)\\ P_K &= \frac{1}{N_{Trials}-1}\sum_{i=1}^{N_{Trials}}\left(\mathbf{h}\left(\tilde{\mathbf{y}}_{i,K}\right)-\bar{\mathbf{x}}_K\right)\left(\mathbf{h}\left(\tilde{\mathbf{y}}_{i,K}\right)-\bar{\mathbf{x}}_K\right)^T\end{aligned} \tag{4.1}$$

The numerical covariance served as the metric dictating the true dispersion of states which could have generated the measurement. The numerical covariance was compared with the covariance computed by the EKF and the TOV Bayes' filter

utilizing different amounts of previous data in order to assess uncertainty and correlation performance of the different filters. Figure 4.3 plots the standard deviation and correlation coefficient errors computed from covariance matrix elements generated by the EKF and TOV Bayes' filter using zero and three previous measurements for calculation of the prior PDF.

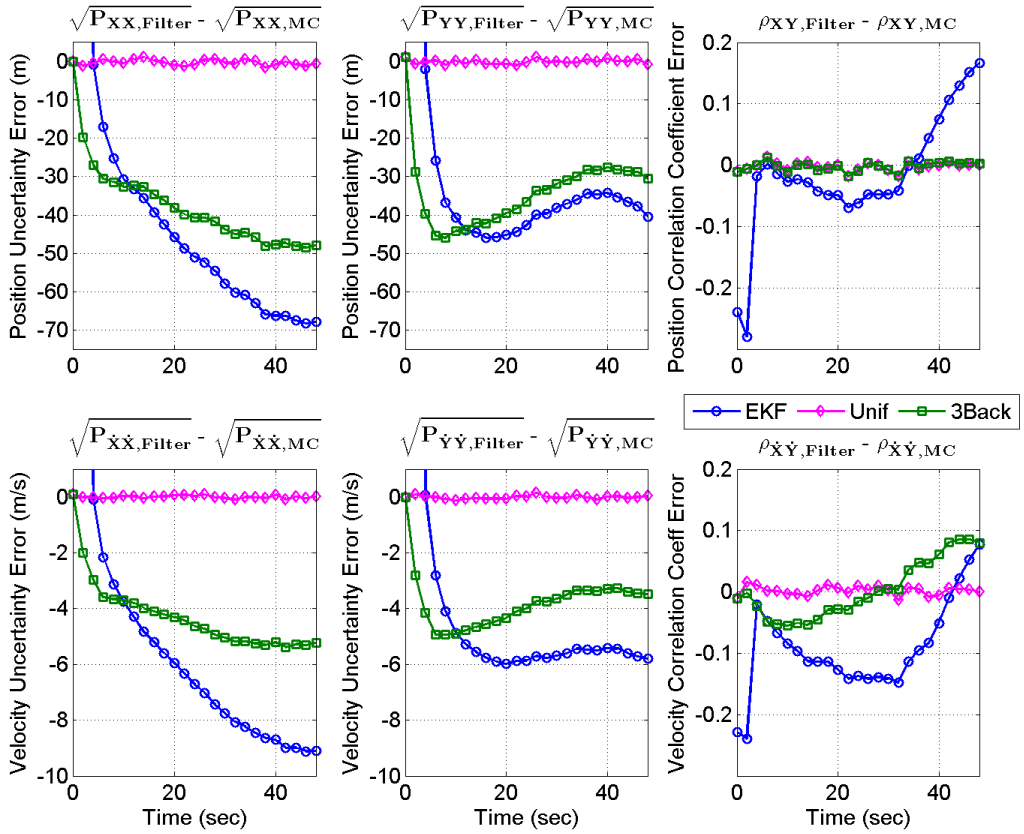

Figure 4.3: Arcing Mass Position and Velocity Measurement: Covariance Element Comparison of the EKF and TOV Bayes' Filter with Different Priors vs. the Numerical Covariance ($\sigma_\theta = 0.001$rad)

Figure 4.3 shows that the Bayes' filter assuming a uniform prior, i.e. the likelihood PDF solution, for the state distribution best replicates actual error distribution, both for the diagonal elements and the correlation terms, the other correlation terms showed the same results. This is to be expected since the TOV likelihood solution

represents the PDF solution which the Monte Carlo solution is sampling from while the solutions utilizing prior information are concentrating the PDF solution because more information is available for solution refinement. Figures 4.4 and 4.5 compare the state error and 3σ covariance bound behavior of the EKF and TOV Bayes' filter using zero, one, three, and ten previous measurements respectively. The estimator errors and error bounds are separated into different plots for easier discrimination but all errors were within their respective 3σ bounds.

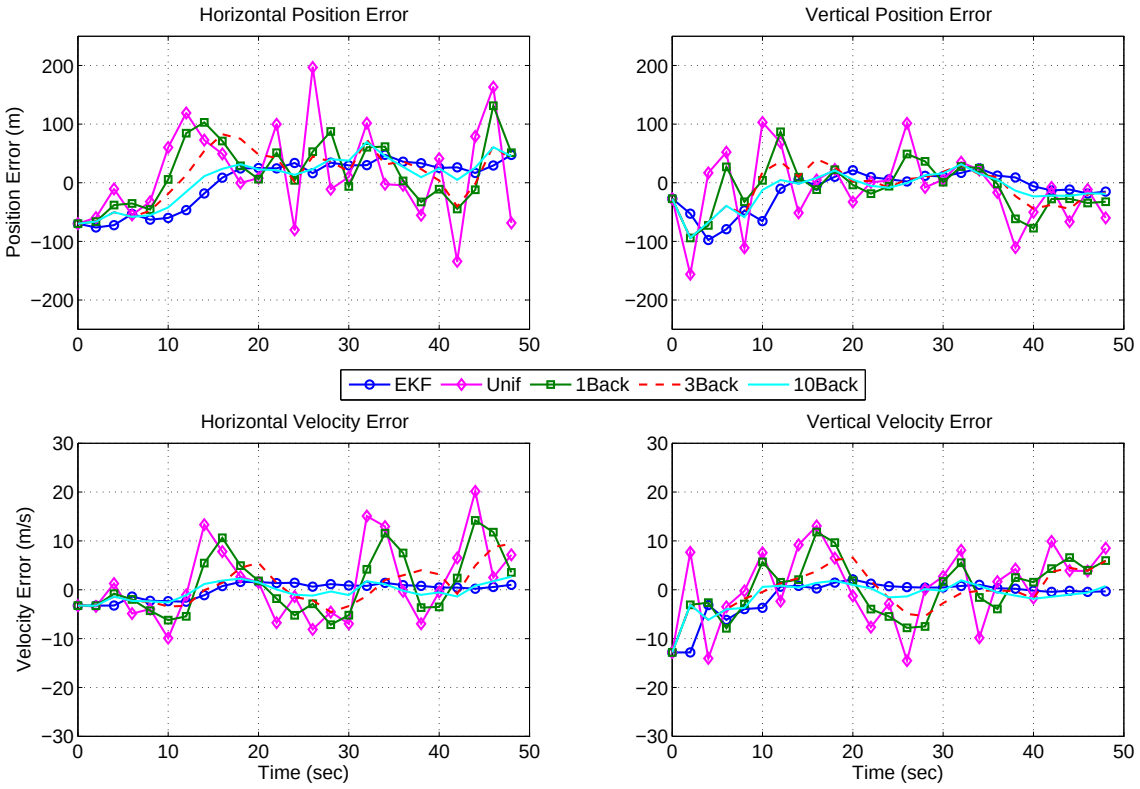

Figure 4.4: Arcing Mass Position and Velocity Measurement: Error for EKF and TOV Bayes' Filter with Different Priors ($\sigma_\theta = 0.001$rad)

Behavior of the state error and 3σ covariance bounds for the Bayes' filter in Figures 4.4 and 4.5 demonstrates that as the prior distribution incorporates more data, the dynamic model is trusted more and the filter is less susceptible to observation variance. Examining the true state time histories and uncertainty bounds generated

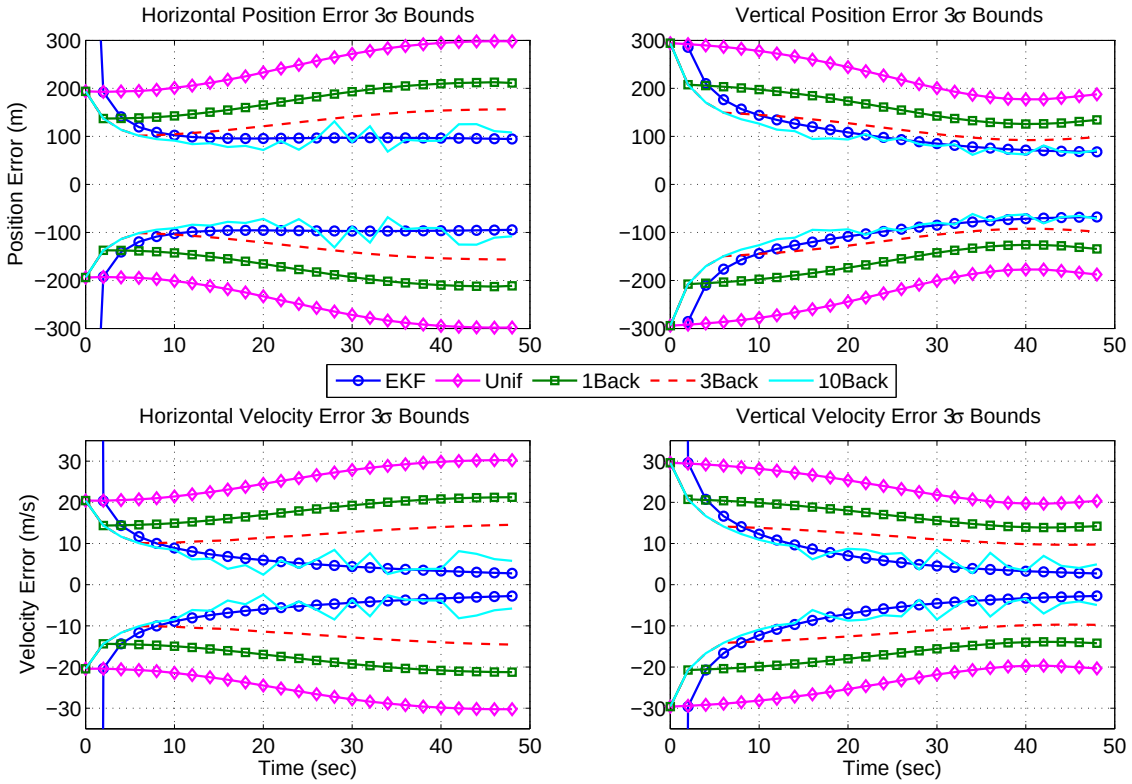

Figure 4.5: Arcing Mass Position and Velocity Measurement: Covariance Bounds for EKF and TOV Bayes' Filter with Different Priors ($\sigma_\theta = 0.001$rad)

by the Bayes' filter using zero to three previous measurements shows the inflection point of the covariance bounds occurs at the point of closest approach of the object, approximately 25 seconds. For the Bayes' filter using zero to three previous measurements, the state estimate is dominated by the likelihood PDF due to the increase in the uncertainty for the horizontal position and velocity estimates.

From Figure 4.5, the range observation noise is the dominating measurement noise because the uncertainty in the horizontal position is increasing as the elevation angle goes to zero. One would expect growing uncertainty in the vertical position as the elevation angle goes to zero since the sine function is more sensitive to changes in angle as the elevation angle decreases, unless the elevation angle noise was being overshadowed. Figure 4.5 also shows that as more previous measurements are

considered, the TOV Bayes' filter uncertainty bounds settle to those of the EKF, which should be expected since the dynamics are linear and the measurements are only slightly nonlinear. Figure 4.6 displays the state error and covariance results for the case where the prior considers the past three measurements and the elevation angle noise standard deviation is raised from 0.001rad to 0.005 rad. The uncertainty increase causes the elevation angle noise to dominate, resulting in increasing vertical position error as the object falls.

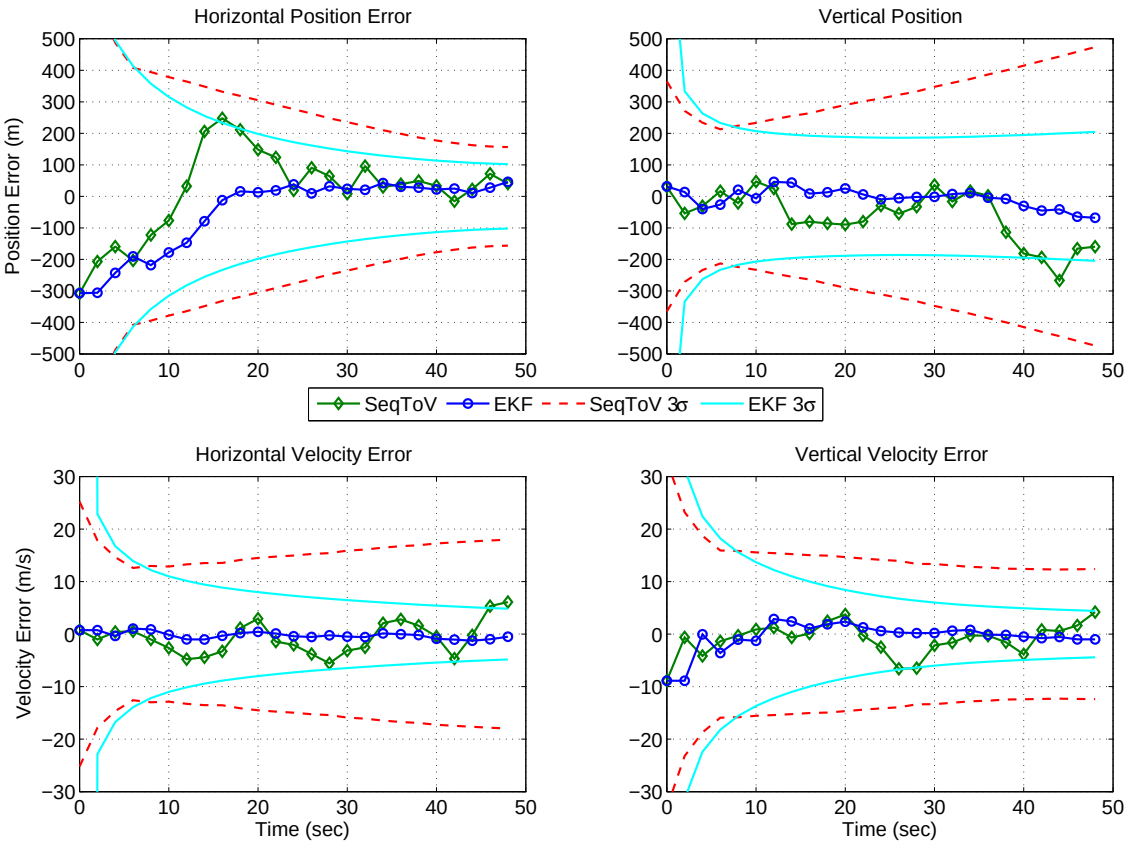

Figure 4.6: Arcing Mass Position and Velocity Measurement: Error and 3σ Bounds for EKF and TOV Bayes' Filter with Prior using 3 Previous Measurements (σ_θ = 0.005rad)

Since the TOV Bayes' filter can generate a state estimate and covariance given a single measurement vector, the output of the filter at the first measurement can

be used to autonomously initialize the state estimate and covariance of the EKF. Figure 4.7 displays the state error and covariance bound results of the EKF initialized by the Bayes' filter output versus the user-tuned covariance for the original measurement noise character set.

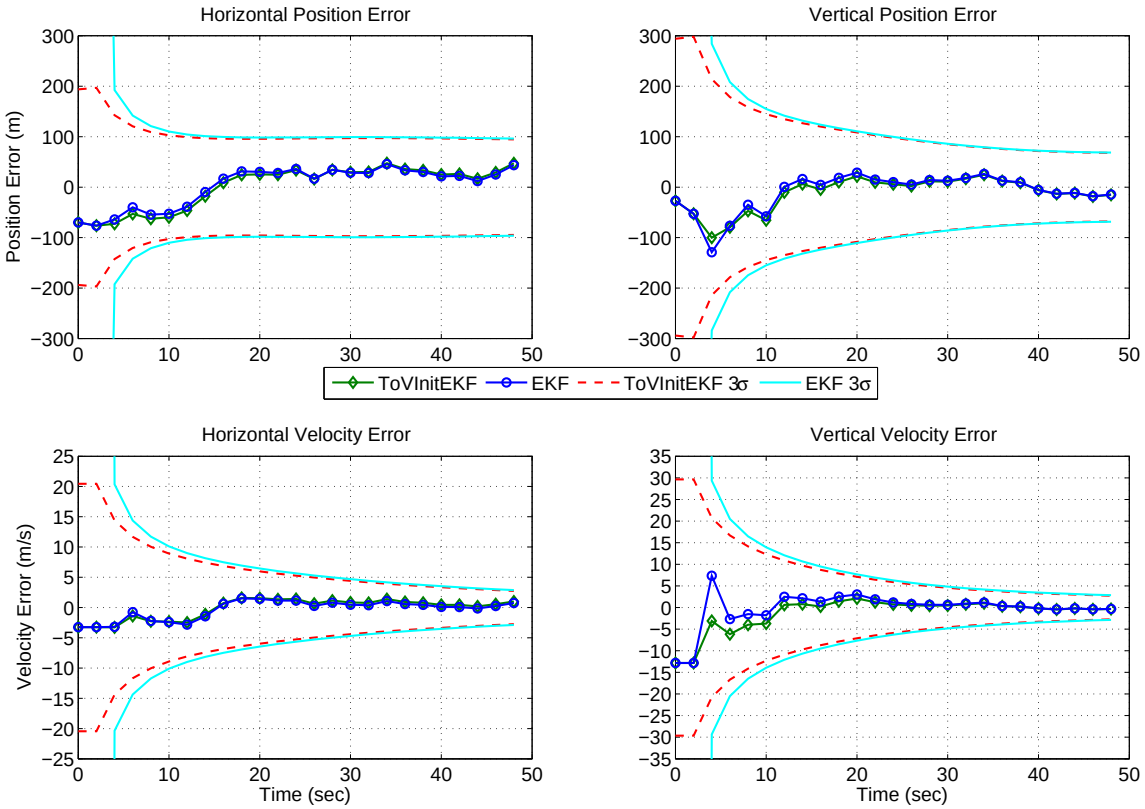

Figure 4.7: Arcing Mass Position and Velocity Measurement: Error and 3σ Bounds for EKF initialized with P_0 =diag$[1 \times 10^5]$ and by output of TOV Bayes' Filter at First Measurement ($\sigma_\theta = 0.001$rad)

Figure 4.7 shows that a TOV Bayes' filter can be useful in automating the tuning of initial estimate, especially the covariance of conventional nonlinear filters which are typically derived heuristically or by trial and error. Additional analysis showed that if the initial user-tuned covariance for the EKF were chosen inside the initial covariance bounds of the Bayes' filter, the EKF filter would converge to the same bounds as the Bayes' filter, once the simulation time increased past 10 seconds.

4.1.3 Reduced Sensing Results

When multiple observation times must be utilized to fully observe the system, the TOV Bayes' filter operation is compared against an EKF and a generic PF. The PF tuning consisted of the number of particles, the estimated variance of the velocity states, and the selection of the importance density. The number of particles was set to 10,000, the importance density was selected to be Gaussian, and the estimated velocity variances were set to 5 meters/sec and 0.0001 rad/sec respectively. The tuned velocity variances were found by trial and error with an acceptance criteria of keeping the state error within the 3σ bounds. The tuning parameters for the EKF covariance and position state estimates remained the same as those in the full sensing case, but the object was assumed to possess zero horizontal and vertical velocity. For the TOV Bayes' filter, the number of grid points remained the same, the prior for all position filtering was assumed uniform, and the prior for velocity smoothing was set to use only the most recent measurement previous to the time the velocity is being estimated. For example, measurements K and $K-1$ were utilized to estimate the velocity states at time $K-1$ and the measurement at time $K-2$ was utilized to construct the prior PDF.

Figure 4.8 displays the filters' state error results for the reduced sensing case. The error and uncertainty plots are separated for easier performance discrimination, but all errors were within their respective 3σ bounds. Figure 4.8 shows that the state errors produced by the Bayes' filter and the EKF were larger than the full sensing case, approximately double those shown in Figure 4.4. As with previous results, the TOV Bayes' filter results are not as smooth as the other conventional filters. By not considering all previous data, a larger state domain is produced which satisfies the generated prior PDF.

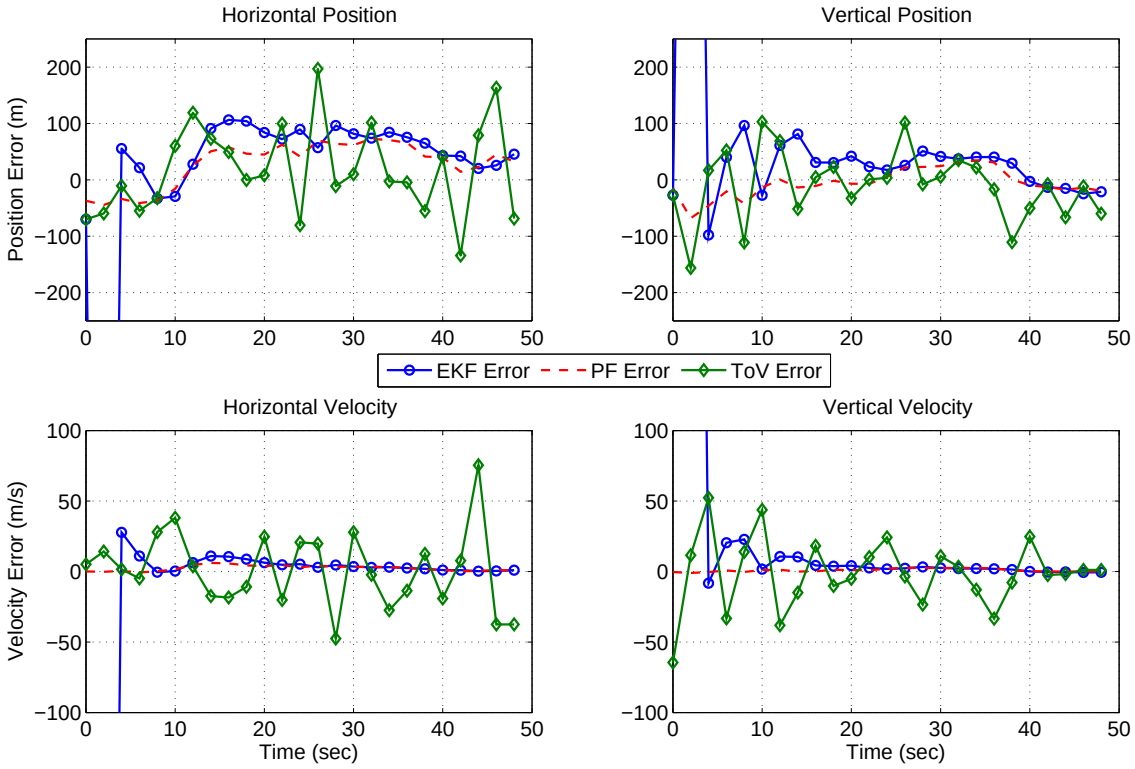

Figure 4.8: Arcing Mass Position Only Measurement: Error for EKF, Generic PF, and TOV Bayes Filter with Prior using 1 Previous Measurement ($\sigma_\theta = 0.001$rad)

The position covariance bounds shown in Figure 4.9 for the TOV Bayes' filter are equivalent to the uniform prior full sensing Bayes' filter bounds shown in Figure 4.5. The velocity covariance bounds for the TOV Bayes' filter are much larger for the reduced sensing scenario than the full sensing scenario, approximately five times by comparison when using one previous measurement. When comparing the reduced sensing smoothed covariance bounds with the full sensing covariance bounds, the smoothed covariance bounds lie between the prior considering one previous measurements and three previous measurements. This behavior should be expected since a total of three measurements are used to make a decision about the smoothed position states.

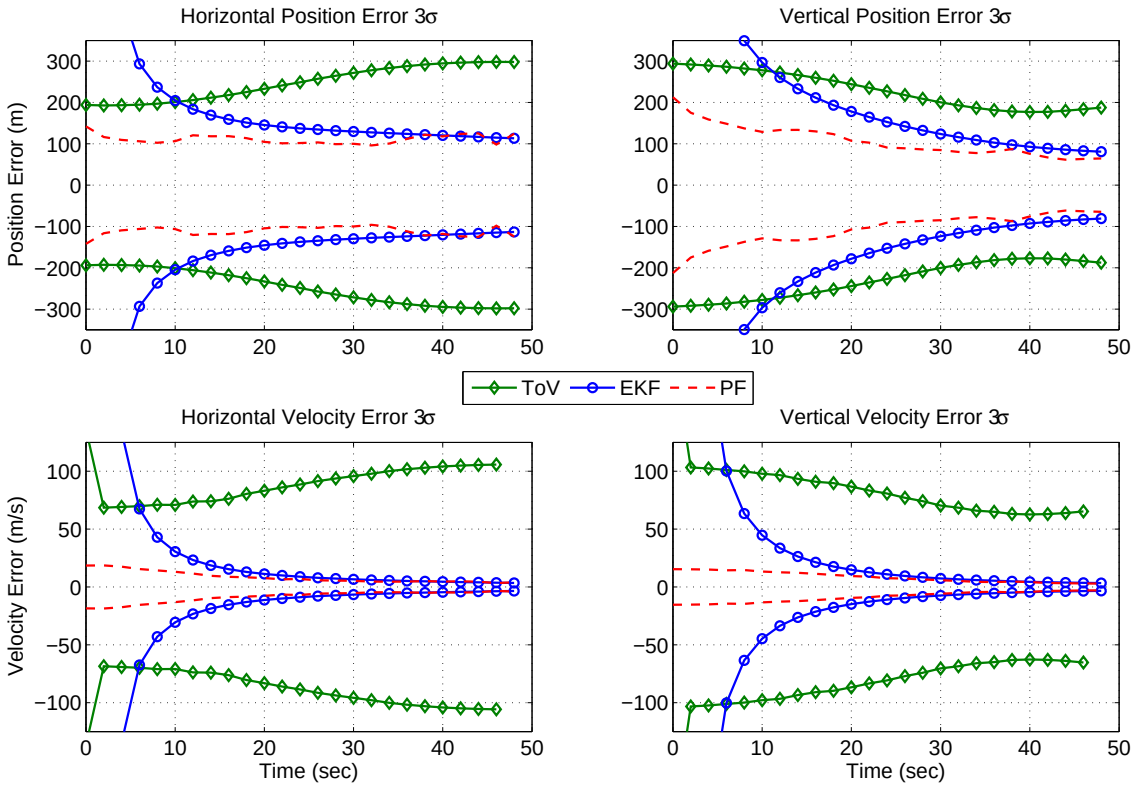

Figure 4.9: Arcing Mass Position Only Measurement: 3σ Bounds for EKF, Generic PF, and TOV Bayes Filter with Prior using 1 Previous Measurement ($\sigma_\theta = 0.001$rad)

4.2 Linear Harmonic Oscillator

4.2.1 Geometry and Equations of Motion

State and parameter estimation are now considered for a one-dimensional linear oscillator shown by Figure 4.10. The system parameters, m, c, k, h, are mass, damping ratio, spring constant, and height of observer, respectively, and are initially assumed known and constant. The desired state vector, $\mathbf{x}$, is composed of horizontal position and velocity, $(x, \dot{x})$, with measurements, $\tilde{\mathbf{y}}$, of the angle formed by the horizontal position and vertical height, $\left(\theta, \dot{\theta}\right)$. Both measurements are assumed to be corrupted by a zero mean Gaussian processes with known variances.

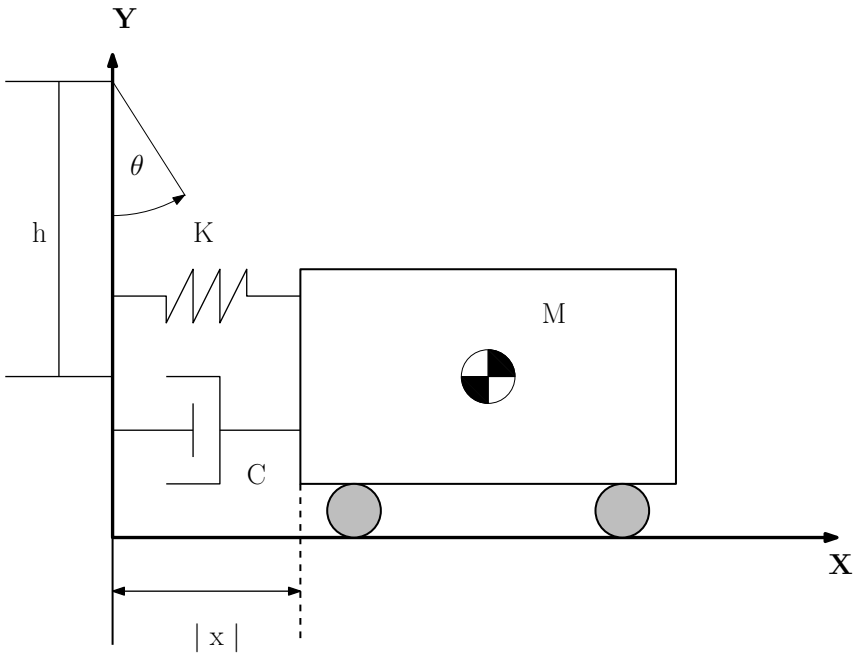

Figure 4.10: Geometry of Harmonic Oscillator Problem

For simplicity, the oscillator is assumed to be put into motion by initial condition perturbation, while being unforced for all time, $\mathbf{u} = \mathbf{0}\ \forall t$. The equations of motion are exactly known at the acceleration level, so the process noise is unnecessary to make up for modeling error, $\mathbf{w}(t) = \mathbf{0}$. The angular position and rate measurements are assumed to be statistically independent of each other and the measurement processes are assumed stationary, independent of the particular observation time. Using these assumptions, Equation (4.2) shows the state-space model for the system.

$$\begin{aligned}
\begin{bmatrix} \dot{x} \\ \ddot{x} \end{bmatrix} &= \begin{bmatrix} 0 & 1 \\ -\dfrac{k}{m} & -\dfrac{c}{m} \end{bmatrix} \begin{bmatrix} x \\ \dot{x} \end{bmatrix} \\
\begin{bmatrix} \tilde{y}_1 \\ \tilde{y}_2 \end{bmatrix} &= \begin{bmatrix} \tan^{-1}\left(\dfrac{x}{h}\right) \\ \dfrac{\dot{x}}{h}\left(1+\left(\dfrac{x}{h}\right)^2\right)^{-1} \end{bmatrix} + \mathbf{v} \quad , \quad \mathbf{v} \sim \mathcal{N}(\mathbf{0}, R) \quad , \quad E\{\tilde{y}_1 \tilde{y}_2\} = 0
\end{aligned} \tag{4.2}$$

The solution of the second-order linear differential equation represented by the state-space model is given by by Equation (4.3). Two different fitted exponential solutions are presented depending upon the system type, either critically damped, $c^2 = 4mk$, or under/over-damped, $c^2 \neq 4mk$. The roots of the characteristic equation for the second-order linear differential equation are found via use of the characteristic equation.

$$\begin{array}{c|c} c^2 \neq 4mk & c^2 = 4mk \\ x = A\exp(r_1\tau) + B\exp(r_2\tau) & x = (A + B\tau)\exp(r\tau) \\ r_{1,2} = \dfrac{-c \pm \sqrt{c^2 - 4mk}}{2m} & r = \dfrac{-c}{2m} \end{array} \qquad \tau = t - t_0 \tag{4.3}$$

Given initial conditions of the system, $\mathbf{x}(t_0) = [x(t_0), \dot{x}(t_0)]^T$, the constant coefficients, (A, B), in Equation (4.3) can be directly solved for, the results are given by Equation (4.4). The solutions of these constants in terms of the initial conditions and characteristic roots allows for the state transition matrix [16] to propagate the initial conditions to any point in time, hence TOV can be used for uncertainty propagation.

$$\begin{aligned} &\underline{c^2 \neq 4mk} \\ &\begin{bmatrix} A \\ B \end{bmatrix} = \frac{1}{r_2 - r_1} \begin{bmatrix} r_2 x(t_0) - \dot{x}(t_0) \\ -r_1 x(t_0) + \dot{x}(t_0) \end{bmatrix} \\ &\underline{c^2 = 4mk} \\ &\begin{bmatrix} A \\ B \end{bmatrix} = \begin{bmatrix} x(t_0) \\ -r_1 x(t_0) + \dot{x}(t_0) \end{bmatrix} \end{aligned} \tag{4.4}$$

Utilizing the concept of the state transition matrix, Equations (2.3) and (2.4), the solutions for the critically and not critically damped cases are given by Equa-

tion (4.5). For the under-damped case, $c^2 < 4mk$, the first state transition matrix in Equation (4.5) can be further simplified using trigonometric functions, shown by Equation (4.6).

$$
\begin{aligned}
&\underline{c^2 \neq 4mk} \\
&\mathbf{\Phi}_{U/O}\left(t, t_0\right) = \frac{1}{r_2 - r_1}\begin{bmatrix} r_2\exp(r_1\tau) - r_1\exp(r_2\tau) & -\exp(r_1\tau) + \exp(r_2\tau) \\ r_1 r_2\left(\exp(r_1\tau) - \exp(r_2\tau)\right) & -r_1\exp(r_1\tau) + r_2\exp(r_2\tau) \end{bmatrix} \\
&\underline{c^2 = 4mk} \\
&\mathbf{\Phi}_{C}\left(t, t_0\right) = \begin{bmatrix} (1 - r\tau)\exp(r\tau) & \tau\exp(r\tau) \\ -r^2\tau\exp(r\tau) & (1 + r\tau)\exp(r\tau) \end{bmatrix} \\
&\tau = t - t_0
\end{aligned}
\tag{4.5}
$$

$$
\begin{aligned}
\mathbf{\Phi}_{U}\left(t, t_0\right) &= \exp(-\zeta\omega_n\tau)\begin{bmatrix} \cos(\omega_d\tau) + \dfrac{\zeta\omega_n}{\omega_d}\sin(\omega_d\tau) & \dfrac{1}{\omega_d}\sin(\omega_d\tau) \\ -\omega_d\sin(\omega_d\tau) + \zeta\omega_n\cos(\omega_d\tau) & \cos(\omega_d\tau) \end{bmatrix} \\
r_{1,2} &= -\zeta\omega_n \pm j\omega_d = -\frac{c}{2m} \pm j\frac{\sqrt{4mk - c^2}}{2m} \\
\omega_d &= \omega_n\sqrt{1 - \zeta^2} \\
\tau &= t - t_0
\end{aligned}
\tag{4.6}
$$

4.2.2 State Estimation Procedure

4.2.2.1 State Estimation with Full Measurements and Parameter Certainty

Using the nonlinear relationship of system states and measurements in Equation (4.2) and assuming the multivariate measurement space PDF is Gaussian, the state domain PDF can be computed by carrying out TOV, shown by Equation (4.7). Equation (4.7) makes use of the statistical independence of the measurement vari-

ables, allowing for the joint PDF of the measurement domain to be computed by simply taking the product of the two independent distributions, shown by Equation (4.8).

$$
\begin{aligned}
p\left(\mathbf{x}\right) &= p\left(\mathbf{y} = \mathbf{h}(\mathbf{x})\right) \left| \frac{\partial \mathbf{h}(\mathbf{x})}{\partial \mathbf{x}} \right| \\
p\left(x, \dot{x}\right) &= \frac{\left(1 + (x/h)^2\right)^{-2}}{2\pi h^2 \sigma_{y_1} \sigma_{y_2}} \exp\left[-\frac{1}{2} \frac{\left(\tan^{-1}\left(\frac{x}{h}\right) - \tilde{y}_1 \right)^2}{\sigma_{y_1}^2} \right] \\
&\quad \times \exp\left[-\frac{1}{2} \frac{\left(\left(1 - (x/h)^2\right)^{-1} \frac{\dot{x}}{h} - \tilde{y}_2 \right)^2}{\sigma_{y_2}^2} \right]
\end{aligned}
\tag{4.7}
$$

$$
\begin{aligned}
p\left(\mathbf{y}\right) &= p\left(y_1\right) p\left(y_2\right) = p\left(y_1, y_2\right) \\
p\left(y_1\right) &= \frac{1}{\sqrt{2\pi}\sigma_{y_1}} \exp\left[-\frac{1}{2} \frac{\left(\tilde{y}_1 - \mu_{y_1}\right)^2}{\sigma_{y_1}^2} \right] \\
p\left(y_2\right) &= \frac{1}{\sqrt{2\pi}\sigma_{y_2}} \exp\left[-\frac{1}{2} \frac{\left(\tilde{y}_2 - \mu_{y_2}\right)^2}{\sigma_{y_2}^2} \right]
\end{aligned}
\tag{4.8}
$$

Equation (4.7) serves as the spatial map between the measurement domain joint PDF and the state domain joint PDF at a specific time. To compute the marginal PDF of a specific state, Equation (4.7) is simply integrated over with respect to the unneeded state variable. Mapping of the state domain joint PDF forward or backward in time can be carried out by applying TOV and using the state transition matrix as the mapping functional. Equation (4.9) shows the TOV solution for propagating the state PDF using the state transition matrix solution, given by either Equation (4.5) or (4.6), depending upon the system type. Computation of Equation (4.9) requires Equation (4.7) to be calculated first with the end result being the joint PDF of the measurements, $\tilde{\mathbf{y}}$, at time t_i or t_j conditioned upon the states, $\mathbf{x}$, at time t_j. The measurement is conditioned upon the states because the measure-

ment is generated from the system being at a given state. The strict notation of Equations (4.7) and (4.9) is given by Equation (4.10).

$$\begin{aligned} p\Big(\mathbf{x}(t_i)\Big) &= p\bigg(\mathbf{x}(t_j) = \mathbf{\Phi}\left(t_j, t_i\right)\mathbf{x}(t_i)\bigg)\left|\frac{\partial \mathbf{x}(t_j)}{\partial \mathbf{x}(t_i)}\right| \\ &= p\bigg(\mathbf{x}(t_j) = \mathbf{\Phi}\left(t_j, t_i\right)\mathbf{x}(t_i)\bigg)\left|\mathbf{\Phi}\left(t_j, t_i\right)\right| \end{aligned} \tag{4.9}$$

$$p\Big(\tilde{\mathbf{y}}\left(t_j\right)\Big|\mathbf{x}(t_i)\Big) = p\bigg(\tilde{\mathbf{y}}\left(t_j\right)\bigg|\mathbf{x}(t_j) = \mathbf{\Phi}\left(t_j, t_i\right)\mathbf{x}(t_i)\bigg)\left|\mathbf{\Phi}\left(t_j, t_i\right)\right| \tag{4.10}$$

4.2.2.2 State Estimation with Full Measurements and Parameter Uncertainty

Assuming the mathematical model used to compute the state transition matrix was not exact with respect to the value used for the damping force, c, TOV can be applied to sequentially estimate the damping force parameter and its associated PDF. When the appropriate conditions are satisfied to trigger parameter estimation, e.g. propagated position and velocity do not agree with present measurements or the propagation time interval is greater half the system cycle, TOV can be applied to map the joint PDF of present position, previous position, and previous velocity to the joint PDF of damping force parameter, previous position, and previous velocity.

The joint PDF of the present and previous positions and the previous velocity is chosen as the analysis starting point due to the relationship between the present position and previous states, shown in Equations (4.3) and (4.4). The damping parameter can then be exchanged for the present position by using TOV and the state transition matrix, shown by Equation (4.11).

$$p\left(c, x\left(t_{K-1}\right), \dot{x}\left(t_{K-1}\right)\right) = \left[p\left(x\left(t_K\right), x\left(t_{K-1}\right), \dot{x}\left(t_{K-1}\right)\right)|K|\right]_{x(t_K)=\psi(c,x(t_{K-1}),\dot{x}(t_{K-1}))} \tag{4.11}$$

Equation (4.11) shows the application of TOV to compute the resulting joint PDF of damping force, position, and velocity at the previous measurement time. Equation (4.12) shows the Jacobian solution resulting from the exchange of present position to previous measurement time damping coefficient. If one were to observe sequential decaying oscillations of the system, the ψ function in Equation (4.11) could be assumed to be that of the under-damped oscillator given in Equation (4.3). The absolute value of the determinant of the Jacobian can then be computed according to Equation (4.13).

$$K = \begin{bmatrix} \dfrac{\partial \psi}{\partial c} & \dfrac{\partial \psi}{\partial x\left(t_{K-1}\right)} & \dfrac{\partial \psi}{\partial \dot{x}\left(t_{K-1}\right)} \\ 0 & 1 & 0 \\ 0 & 0 & 1 \end{bmatrix} \rightarrow |K| = \left| \frac{\partial \psi}{\partial c} \right| \tag{4.12}$$

$$\begin{aligned} \left| \frac{\partial \psi}{\partial c} \right| &= \left| \left(\frac{\partial A}{\partial c} + A\tau \frac{\partial r_1}{\partial c} \right) \exp\left[r_1 \tau\right] + \left(\frac{\partial B}{\partial c} + B\tau \frac{\partial r_2}{\partial c} \right) \exp\left[r_2 \tau\right] \right| \\ r_{1,2} &= \frac{-c \pm \sqrt{c^2 - 4mk}}{2m} \\ \frac{\partial r_{1,2}}{\partial c} &= \frac{-1 \pm c\left(c^2 - 4mk\right)^{-1/2}}{2m} \\ \tau &= t_2 - t_1 \end{aligned} \tag{4.13}$$

For initialization of the damping force parameter domain, one can simply take the range of undamped to critically damped, $\left[0, 2\sqrt{mk}\right]$. Utilizing the parameter estimate given by marginalizing the joint PDF given in Equation (4.11), one can proceed until significant disagreement is observed between the current measurement and propagated solution. After parameter initialization, instead of using the initial parameter domain, one could apply the same tactic used in the perturb-then-grid method and simply take the present parameter estimate and perturb by some multiple of its uncertainty to generate the new domain of damping coefficient. In

this manner, the TOV approach allows for one to pose different hypotheses for the damping coefficient and reject hypotheses that do not allow agreement between the measurements and the mathematical model.

4.2.2.3 State Estimation with Reduced Measurements and Parameter Certainty

If only the position measurement from Equation (4.2) was available, but the velocity state was desired to be estimated, TOV can be carried out by using enough measurements to render the system states observable. The result is TOV operating as a smoother, future states used to estimate previous states, instead of a filter just as with the previous case of full measurements with parameter uncertainty. For the oscillator, either a present and future or a present and past position measurement set is required to estimate the velocity at the present time.

Considering the state transition matrix formulation for mapping between initial and final states, equation rearrangement can allow for mapping of initial and final positions from initial position and velocity. This rearrangement is shown by Equation (4.14), Equation (4.15) demonstrates how the properties of the state transition matrix can be exploited to compute the states at time t_j based upon states at the initial condition time, t_0, and states at a previous time, t_i. For generality, it is assumed that the initial position is not measured in the reduced measurement scenario.

$$\begin{array}{l}\underline{\text{Full Observation}} \\ \begin{bmatrix} x(t_j) \\ \dot{x}(t_j) \end{bmatrix} = \left[\begin{array}{c|c} \Phi_{11}(t_j,t_i) & \Phi_{12}(t_j,t_i) \\ \hline \Phi_{21}(t_j,t_i) & \Phi_{22}(t_j,t_i) \end{array}\right] \begin{bmatrix} x(t_i) \\ \dot{x}(t_i) \end{bmatrix} = \mathbf{\Phi}(t_j,t_i)\,\mathbf{x}(t_i) \\ \underline{\text{Position Only Observation}} \\ \begin{bmatrix} x(t_j) \\ x(t_i) \end{bmatrix} = \left[\begin{array}{c|c} \Phi_{11}(t_j,t_0) & \Phi_{12}(t_j,t_0) \\ \hline \Phi_{11}(t_i,t_0) & \Phi_{12}(t_i,t_0) \end{array}\right] \begin{bmatrix} x(t_0) \\ \dot{x}(t_0) \end{bmatrix} = \mathbf{\Xi}(t_j,t_i,t_0)\,\mathbf{x}(t_0) \end{array} \tag{4.14}$$

$$\begin{bmatrix} \Phi_{11}(t_j,t_0) \\ \\ \Phi_{12}(t_j,t_0) \end{bmatrix} = \begin{bmatrix} \Phi_{11}(t_j,t_i)\,\Phi_{11}(t_i,t_0) + \Phi_{12}(t_j,t_i)\,\Phi_{21}(t_i,t_0) \\ \\ \Phi_{11}(t_j,t_i)\,\Phi_{12}(t_i,t_0) + \Phi_{12}(t_j,t_i)\,\Phi_{22}(t_i,t_0) \end{bmatrix} \tag{4.15}$$

The key assumption in this analysis is that the PDFs generated for each position state are statistically independent of each other in time. This assumption is appropriate since the noise used to generate the position measurements is a stationary process. Due to the stationarity of the measurement function, the joint PDF of the position states at times t_i and t_j is computed by taking the product of the two PDFs, shown by Equation (4.16).

$$\begin{aligned} p\Big(y(t_j),y(t_i)\Big|x(t_j),x(t_i)\Big) &= p\Big(y(t_j)\Big|x(t_j)\Big)p\Big(y(t_i)\Big|x(t_i)\Big) \\ &= \frac{\left(1+(x(t_i)/h)\right)^{-1}}{2\pi h^2\sigma_{y_1}^2}\left(1+(x(t_j)/h)^2\right)^{-1} \\ &\quad\times\exp\left[-\frac{1}{2}\frac{\left(\tan^{-1}(x(t_j)/h)-\tilde{y}_1(t_j)\right)^2}{\sigma_{y_1}^2}\right] \\ &\quad\times\exp\left[-\frac{1}{2}\frac{\left(\tan^{-1}(x(t_i)/h)-\tilde{y}_1(t_i)\right)^2}{\sigma_{y_1}^2}\right] \end{aligned} \tag{4.16}$$

The spatial PDF given by Equation (4.16) can then be mapped to the position and velocity states in the t_0 domain by using the reduced state transition matrix mapping given by Equation (4.14). Equation (4.17) displays the joint PDF at time t_i conditioned upon the initial position and velocity of the system via the TOV solution using position measurements at times t_i and t_j and the state transition matrix. Equation (4.18) displays the intermediate variables used to condense Equation (4.17). If information about the initial position was available, Equation (4.17) would reduce to a form similar to Equation (4.16), shown by Equation (4.19) which results when t_0 is set equal to t_i. Equation (4.20) displays the intermediate variables used to

condense Equation (4.19) so that it is easier to read and implement computationally.

$$\begin{aligned} p\left(y(t_j), y(t_i)\middle| x(t_0), \dot{x}(t_0)\right) &= p\left(y(t_j), y(t_i)\middle| \left[x(t_j), x(t_i)\right] = \boldsymbol{\Xi}(t_j, t_i, t_0)\mathbf{x}(t_0)\right) \\ &\quad \times \left|\boldsymbol{\Xi}\left(t_j, t_i, t_0\right)\right| \\ &= \frac{\left|\boldsymbol{\Xi}\left(t_j, t_i, t_0\right)\right|}{2\pi h^2 \sigma_{y_1}^2} \left(1+\boldsymbol{\alpha}^2\right)^{-1} \left(1+\boldsymbol{\beta}^2\right)^{-1} \\ &\quad \times \exp\left[-\frac{1}{2}\frac{\left(\tan^{-1}\left(\boldsymbol{\alpha}\right) - \tilde{y}_1(t_j)\right)^2}{\sigma_{y_1}^2}\right] \\ &\quad \times \exp\left[-\frac{1}{2}\frac{\left(\tan^{-1}\left(\boldsymbol{\beta}\right) - \tilde{y}_1(t_i)\right)^2}{\sigma_{y_1}^2}\right] \end{aligned} \tag{4.17}$$

$$\begin{aligned} \boldsymbol{\alpha} &= \frac{\Phi_{11}\left(t_j, t_0\right) x(t_0) + \Phi_{12}\left(t_j, t_0\right) \dot{x}(t_0)}{h} \\ \boldsymbol{\beta} &= \frac{\Phi_{11}\left(t_i, t_0\right) x(t_0) + \Phi_{12}\left(t_i, t_0\right) \dot{x}(t_0)}{h} \end{aligned} \tag{4.18}$$

$$\begin{aligned} p\left(y(t_j), y(t_i)\middle| x(t_i), \dot{x}(t_i)\right) &= p\left(y(t_j), y(t_i)\middle| \left[x(t_j), x(t_i)\right] = \boldsymbol{\Xi}(t_j, t_i)\mathbf{x}(t_i)\right)\left|\boldsymbol{\Xi}\left(t_j, t_i\right)\right| \\ &= \frac{\left(1+\left(x(t_i)/h\right)^2\right)^{-1}}{2\pi h^2 \sigma_{y_1}^2} \left(1+\boldsymbol{\alpha}^2\right)^{-1} \\ &\quad \times \exp\left[-\frac{1}{2}\frac{\left(\tan^{-1}\left(\boldsymbol{\alpha}\right) - \tilde{y}_1(t_j)\right)^2}{\sigma_{y_1}^2}\right] \\ &\quad \times \exp\left[-\frac{1}{2}\frac{\left(\tan^{-1}\left(\frac{x_{t_i}}{h}\right) - \tilde{y}_1(t_i)\right)^2}{\sigma_{y_1}^2}\right]\left|\Phi_{12}\left(t_j, t_i\right)\right| \end{aligned} \tag{4.19}$$

$$\begin{aligned} \boldsymbol{\alpha} &= \frac{\Phi_{11}\left(t_j, t_i\right) x(t_i) + \Phi_{12}\left(t_j, t_i\right) \dot{x}(t_i)}{h} \\ \boldsymbol{\Xi}\left(t_j, t_i\right) &= \left[\begin{array}{c:c} \Phi_{11}\left(t_j, t_i\right) & \Phi_{12}\left(t_j, t_i\right) \\ \hdashline 1 & 0 \end{array}\right] \end{aligned} \tag{4.20}$$

4.2.2.4 State Estimation with Reduced Measurements and Parameter Uncertainty

Parameter uncertainty in the reduced sensing case requires additional manipulation and care in execution since the smoothed velocity estimate is derived not only from position measurement data, but also from the assumed model which possesses error. As in the full sensing case with parameter uncertainty, three measurement PDFs are used to compute the joint PDF to be transformed into the desired domain, however three position measurements are used instead of two position and one velocity.

Position and velocity state estimation with uncertainty in the damping force parameter for the under-damped linear oscillator becomes the problem of mapping the joint PDF of three position measurements, $p\left(x\left(t_i\right), x\left(t_{i-1}\right), x\left(t_{i-2}\right)\right)$, to the desired state domain, $p\left(c, x\left(t_{i-1}\right), \dot{x}\left(t_{i-1}\right)\right)$. The Jacobian resulting from mapping the three position measurements to the time of interest is given by Equation (4.21). The intermediate partials for Equation (4.21) are given by Equation (4.22). Note that the bookend measurements, t_{i-2} and t_i, must be nonsymmetric about the middle measurement time, t_{i-1}, so that the determinant of the Jacobian is nonzero.

$$K_{i-1} = \begin{bmatrix} A\left(t_i, t_{i-1}\right) & \Phi_{11}\left(t_i, t_{i-1}\right) & \Phi_{12}\left(t_i, t_{i-1}\right) \\ 0 & 1 & 0 \\ A\left(t_i, t_{i-2}\right) & \Phi_{11}\left(t_i, t_{i-2}\right) & \Phi_{12}\left(t_i, t_{i-2}\right) \end{bmatrix} \tag{4.21}$$

$$A\left(t_A, t_B\right) = \frac{\partial \Phi_{11}\left(t_A, t_B\right)}{\partial c} x\left(t_{i-1}\right) + \frac{\partial \Phi_{12}\left(t_A, t_B\right)}{\partial c} \dot{x}\left(t_{i-1}\right) \tag{4.22}$$

Assuming the form of the under-damped state transition matrix is given by Equation (4.5), the partial derivatives with respect to the damping force coefficient are given by Equations (4.23) and (4.24). The partial derivatives of the roots used

Equations (4.23) and (4.24) are given by Equation (4.13).

$$\begin{aligned}\frac{\partial \Phi_{11}}{\partial c} = & \frac{-1}{(r_2 - r_1)^2}\left(\frac{\partial r_2}{\partial c} - \frac{\partial r_1}{\partial c}\right)(r_2 \exp[r_1\tau] - r_1 \exp[r_2\tau]) \\ & + \frac{1}{r_2 - r_1}\left\{\frac{\partial r_2}{\partial c}(\exp[r_1\tau] - r_1\tau \exp[r_2\tau])\right. \\ & \left. + \frac{\partial r_1}{\partial c}(r_2\tau \exp[r_1\tau] - \exp[r_2\tau])\right\}\end{aligned} \tag{4.23}$$

$$\begin{aligned}\frac{\partial \Phi_{12}}{\partial c} = & \frac{-1}{(r_2 - r_1)^2}\left(\frac{\partial r_2}{\partial c} - \frac{\partial r_1}{\partial c}\right)(-\exp[r_1\tau] + \exp[r_2\tau]) \\ & + \frac{1}{r_2 - r_1}\left(-\frac{\partial r_1}{\partial c}\tau \exp[r_1\tau] + \frac{\partial r_2}{\partial c}\exp[r_2\tau]\right)\end{aligned} \tag{4.24}$$

The initialization of the damping domain can be carried out in the same way as done for the full measurement case. The domain for the velocity can be computed by inverting the state transition matrix relationships between the $i-1$ observation time and the i and $i-2$ observation times, shown in Equation (4.25). Note that nonsymmetric measurement intervals about the $i-1$ observation are required so that the determinant used in computing the velocity is nonzero. As an example, consider the sequential track case with data gaps, the last position measurement of the previous track and the first two position measurements of the new track should be used.

$$\begin{bmatrix} x(t_i) \\ x(t_{i-2}) \end{bmatrix} = \begin{bmatrix} \Phi_{11}(t_i, t_{i-1}) & \Phi_{12}(t_i, t_{i-1}) \\ \Phi_{11}(t_{i-2}, t_{i-1}) & \Phi_{12}(t_{i-2}, t_{i-1}) \end{bmatrix} \begin{bmatrix} x(t_{i-1}) \\ \dot{x}(t_{i-1}) \end{bmatrix}$$

$$\Rightarrow \begin{bmatrix} x(t_{i-1}) \\ \dot{x}(t_{i-1}) \end{bmatrix} = \frac{1}{\Delta}\begin{bmatrix} \Phi_{12}(t_{i-2}, t_{i-1}) & -\Phi_{12}(t_i, t_{i-1}) \\ -\Phi_{11}(t_{i-2}, t_{i-1}) & \Phi_{11}(t_i, t_{i-1}) \end{bmatrix} \begin{bmatrix} x(t_i) \\ x(t_{i-2}) \end{bmatrix}$$

$$\Delta = \Phi_{11}(t_i, t_{i-1})\,\Phi_{12}(t_{i-2}, t_{i-1}) - \Phi_{12}(t_i, t_{i-1})\,\Phi_{11}(t_{i-2}, t_{i-1}) \tag{4.25}$$

4.2.3 State Estimation Results

The TOV Bayes' filter, as outlined by the state and parameter estimation procedures, is applied to the linear oscillator system given by Equation (4.2). The system parameters, initial conditions, and Gaussian measurement noise characteristics are listed in Table 4.1. The table also reports the value for the critically damped system to give a reference for how lightly damped the utilized damping force coefficient of 0.5 Ns/m makes the system.

Table 4.1: True Model Parameters for Linear Harmonic Oscillator

Parameter	Value
Mass (kg)	10
Spring Force Coefficient (N/m)	1.0
Damping Force Coefficient (Ns/m) (Critically Damped=$2\sqrt{10} \approx 6.3246$)	0.5
Initial Position (m)	1.0
Initial Velocity (m/s)	0.1
Position Observation Noise (rad,rad^2)	$\sim \mathcal{N}(0, 2.5 \times 10^{-1})$
Velocity Observation Noise (rad/sec,rad^2/sec^2)	$\sim \mathcal{N}(0, 2.5 \times 10^{-3})$

Figure 4.11 shows the system response for the lightly damped, LD, and critically damped, CD, systems. For the lightly damped case, an additional constraint was added for state estimation where observations were only available when the system was experiencing a positive velocity. This scenario was used to illustrate how subsequent tracks can be used to estimate the damping force coefficient when the modeled parameter value was not equivalent to the simulated parameter. Figure 4.12 displays the tracking results for uncorrupted observations and noise corrupted observations that are only available when the horizontal velocity is positive.

Computation of a representative "true" mean and covariance from the corrupted measurements is computed using Monte Carlo analysis. To compute the mean and

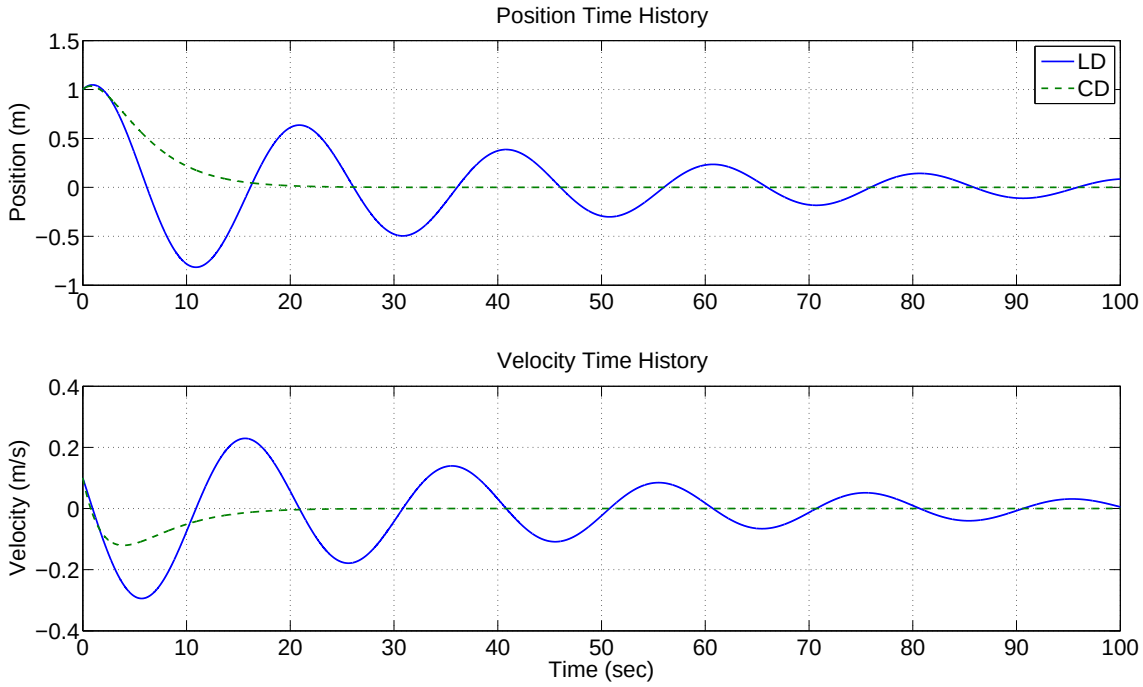

Figure 4.11: Linear Harmonic Oscillator System Response

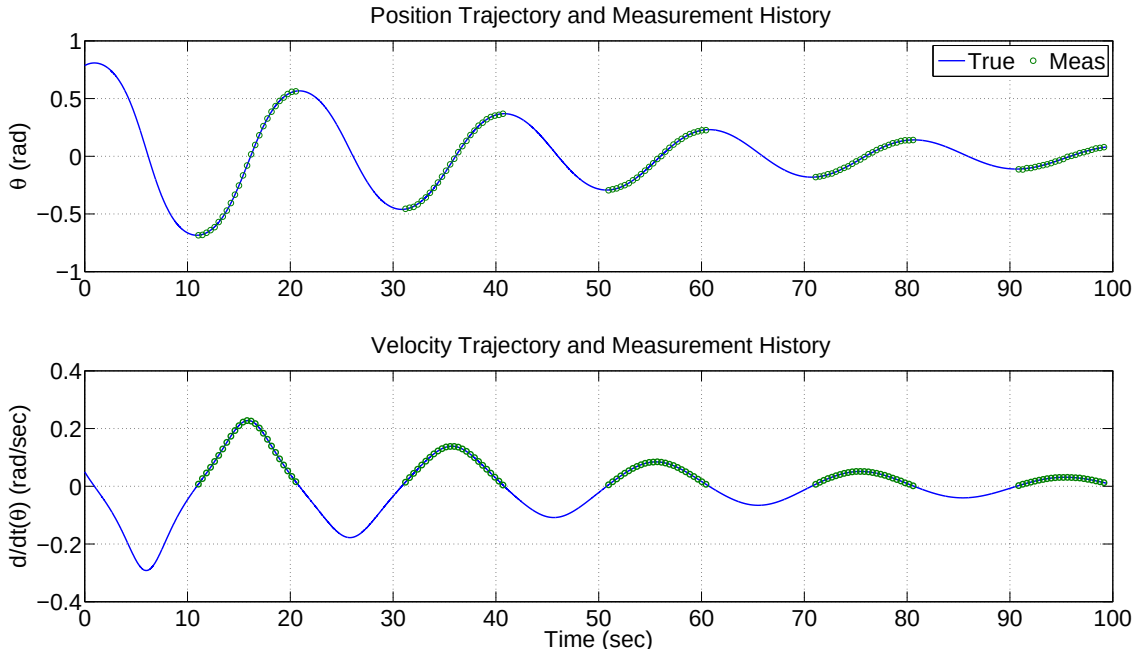

Figure 4.12: Observation Results for Noise Free and Noise Corrupted with Positive Velocity Only Observation

covariance of the state at each observation time, a large number of corrupted observation pairs about the true trajectory are simulated, mapped to the state domain, and their numerical mean, $\bar{\mathbf{x}}$, and covariance, P, are computed at each measurement time. Equation (4.1) displays the computation of the numerical mean and state covariance at each measurement time, designated by K. The number of trials for computation of the numerical mean and covariance was set to 10,000.

4.2.3.1 Full Observation State Estimation Results

Parameter Certainty: Figures 4.13 and 4.14 present the results of applying TOV for computing the likelihood solution of the full observation with parameter certainty case. The figures show the same results of the TOV solution tracking the Monte Carlo solution that were seen for the arcing mass system are seen for a damped linear oscillator. This shows that the TOV solution is appropriately constructing the state domain PDF which the Monte Carlo solution is sampling.

Figure 4.13 plots the state estimation error and the three standard deviation bounds solution from the TOV likelihood with the Monte Carlo three standard deviation bounds overlaid. Figure 4.14 plots the tracking error ratio of the covariance elements computed from the TOV likelihood compared with the numerical covariance computed from Monte Carlo analysis of the state errors, for the percent error one simply has to multiply the error ratio by 100. Figure 4.14 shows the position and velocity uncertainties were able to be tracked within three percent of the Monte Carlo uncertainty estimate. The oscillatory nature and decay of the system significantly impacts computation of the correlation coefficient error ratio but, the overlay of the TOV solution on top of the Monte Carlo correlation solution shows they are in good agreement.

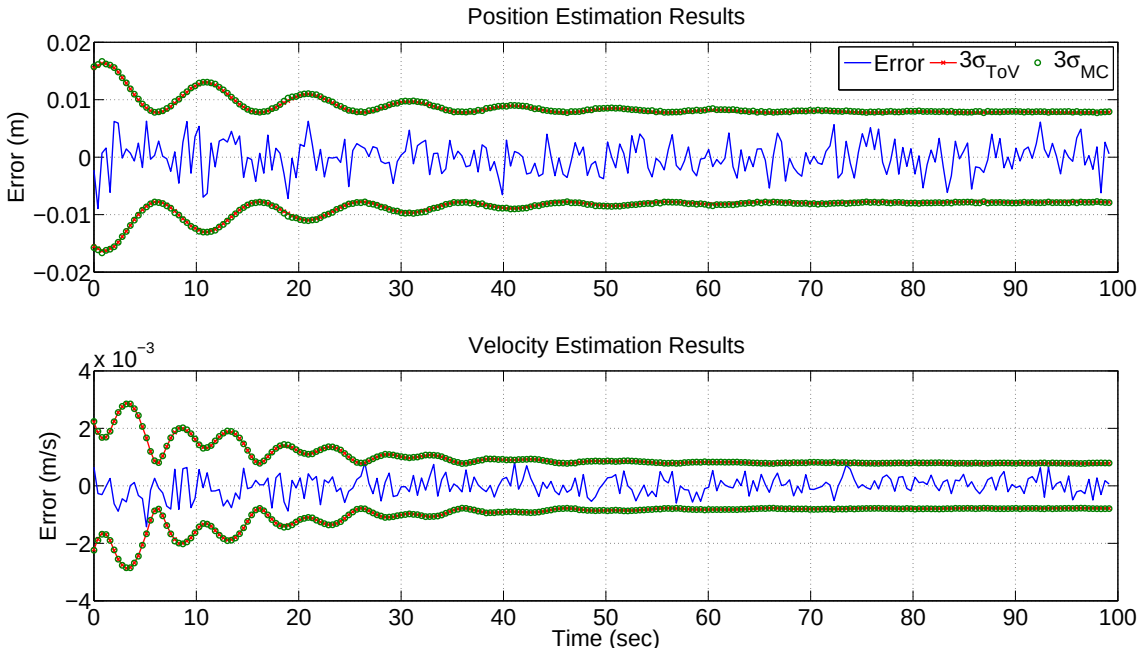

Figure 4.13: Linear Oscillator State Estimation Results: Full Observations with Parameter Certainty

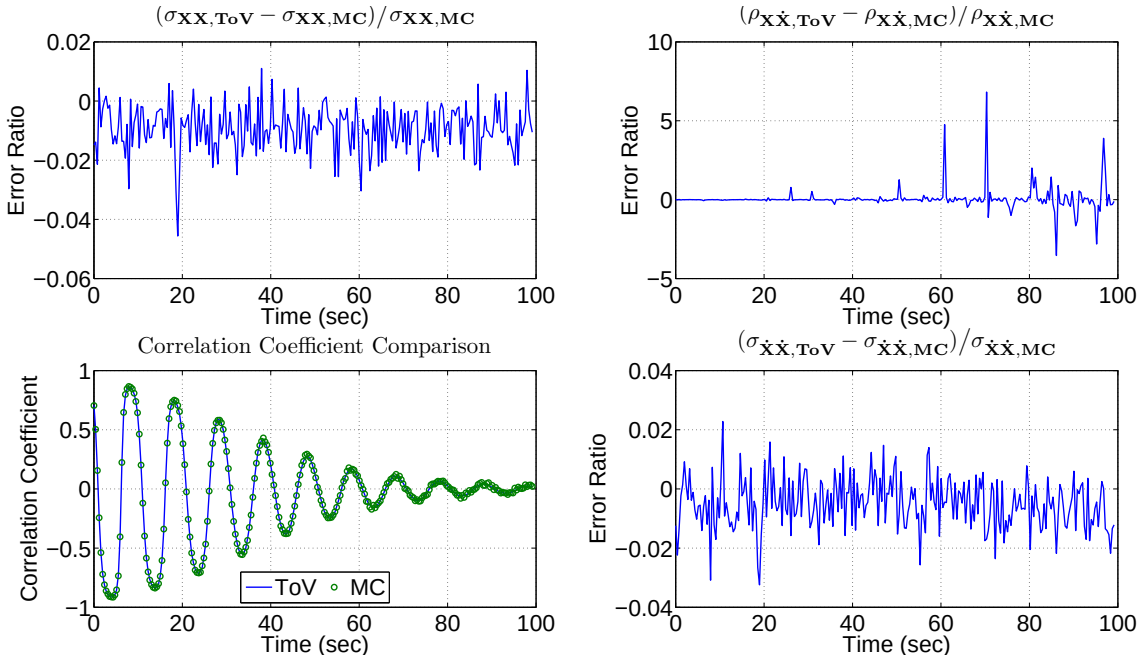

Figure 4.14: Linear Oscillator Covariance Tracking Results: Full Observations with Parameter Certainty

Parameter Uncertainty: For assessment of the performance of the state and parameter estimation procedure outlined for full state sensing, the damping force coefficient of the system model is initially assumed to be zero even though the true system is lightly damped, $c = 0.5$. The system was also observed only when the true system velocity was positive, thereby producing consecutive "tracks" of system motion. Figure 4.15 compares the true state time history versus the time history simulated by the incorrect assumed system model, $c = 0$, parameter during the trackable time periods.

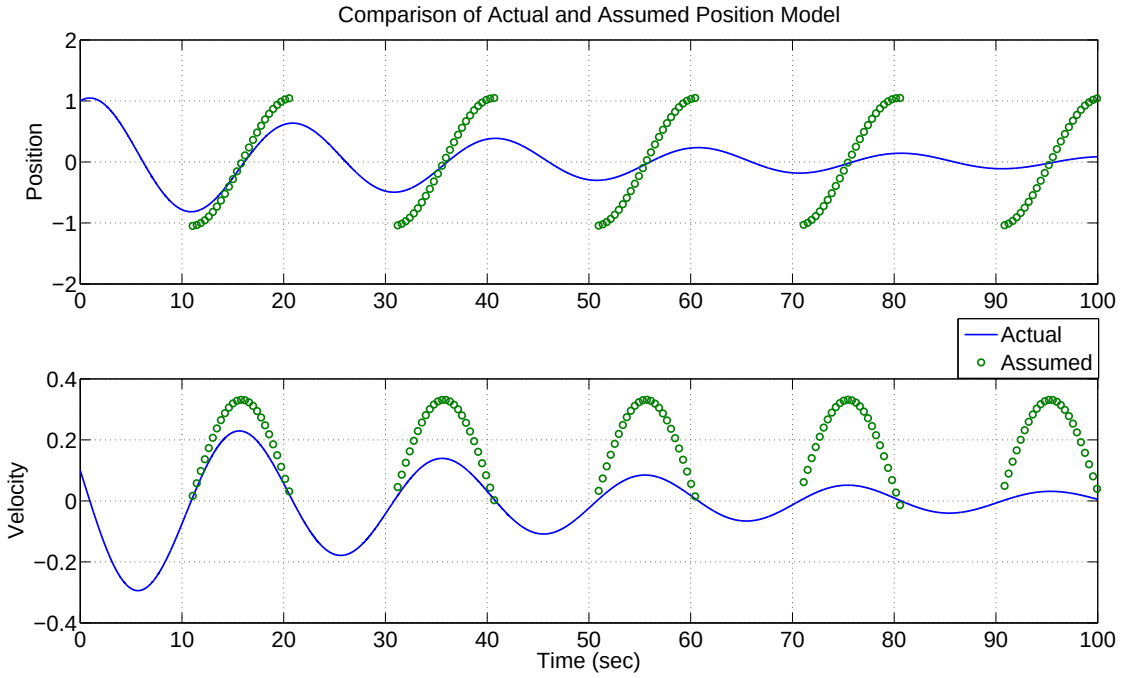

Figure 4.15: Linear Oscillator Results: Assumed vs. Actual Model

Table 4.2 presents the estimation results for the damping coefficient using different triggering conditions for parameter estimation. The first set of results were computed by estimating the damping coefficient only when a new track was started, while the second set of results utilized sequential tracks as well as whether or not the propagated states agreed with the results of the next measurement within each

individual track. The latter triggering condition allows for parameter estimation to be executed during the present track while the former will not update its parameter estimate until a new track has been started. The state disagreement triggering condition was met when the propagated solution did not lie within the state domain produced by the perturbed position measurements mapped to the time of interest.

Table 4.2: Damping Coefficient Estimation Results: Full Observations

Estimate Parameter when New Track Starts			
Time (sec)	Damping Coefficient (Ns/m)	Uncertainty (Ns/m)	Update Trigger
0	0	N/A	Initial Guess
31.600	0.5068	0.0100	New Track
51.350	0.4970	0.0072	New Track
71.495	0.4890	0.0064	New Track
91.245	0.4818	0.0064	New Track
Estimate Parameter when New Track Starts or Propagation does not agree with Measurements			
Time (sec)	Damping Coefficient (Ns/m)	Uncertainty (Ns/m)	Update Trigger
0	0	N/A	Initial Guess
16.195	0.5641	0.0217	Propagated $\dot{\mathbf{x}}$ Disagree
31.600	0.5441	0.0140	New Track
51.350	0.5247	0.0110	New Track
71.495	0.5098	0.0091	New Track
91.245	0.4982	0.0079	New Track

Figures 4.16 and 4.17 display the estimated state error with three standard deviation uncertainty bounds and the covariance element errors for the entire simulation time using the state and parameter estimation procedure used for full state sensing using the second set of parameter estimation trigger conditions. Comparing the parameter uncertainty and parameter certainty resultsshows that the TOV likelihood estimation procedure with parameter uncertainty produces state error and covariance results that are on par with the results obtained from parameter certainty.

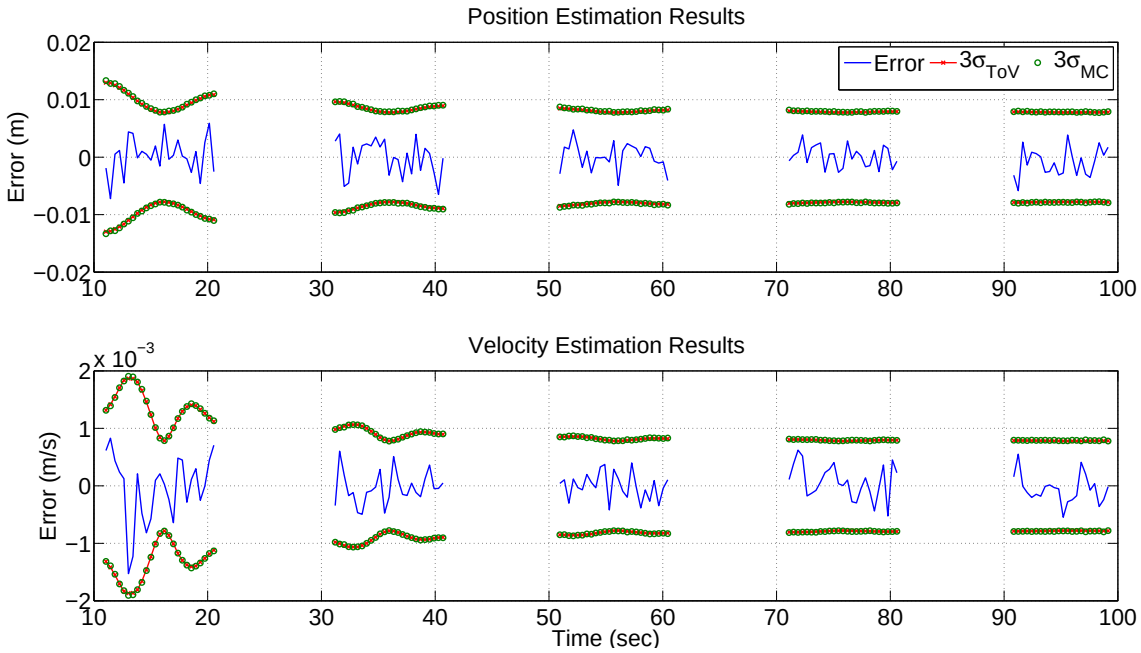

Figure 4.16: Linear Oscillator State Estimation Results: Full Observations with Parameter Uncertainty

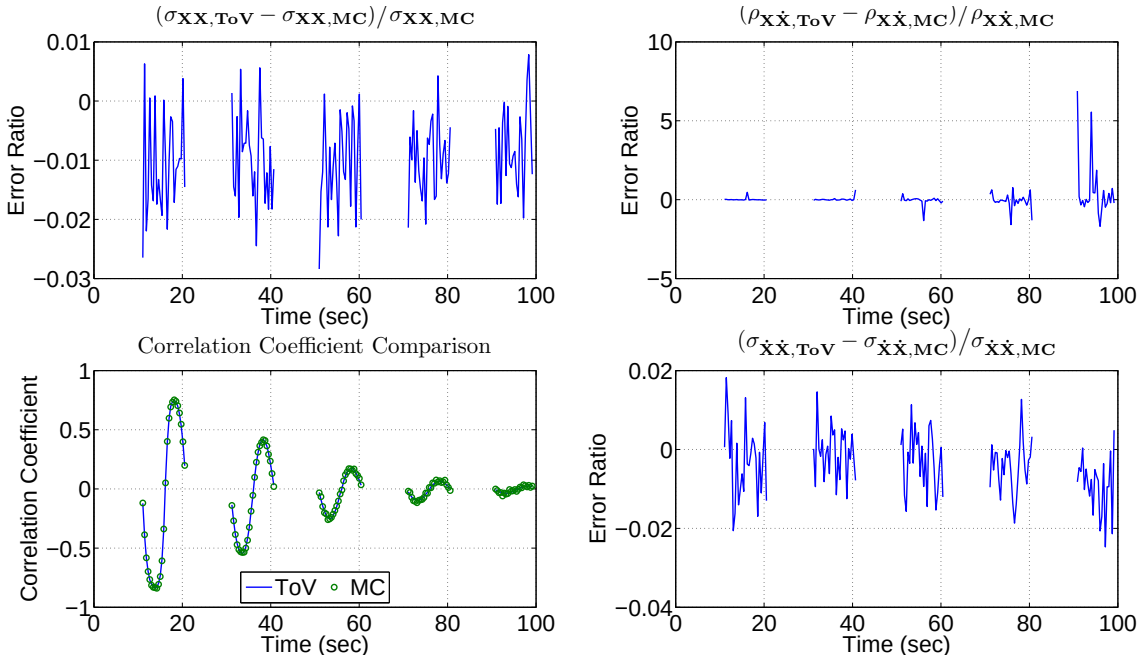

Figure 4.17: Linear Oscillator Covariance Tracking Results: Full Observations with Parameter Uncertainty

4.2.3.2 Reduced Observation State Estimation Results

Parameter Certainty: Figures 4.18 and 4.19 present the results of applying the TOV procedure for position only observations with parameter certainty. Figure 4.18 plots the state estimation error and the three standard deviation bounds computed from the TOV likelihood and overlays the Monte Carlo sampling solution. The figure demonstrates that the TOV likelihood solution for the reduced sensing case agrees well with the Monte Carlo solution. Figure 4.18 shows the position state and uncertainty errors are on par with the full observation case, but the velocity state and uncertainty errors are approximately an order of magnitude larger since two corrupted position measurements have to be used to compute a smoothed state estimate.

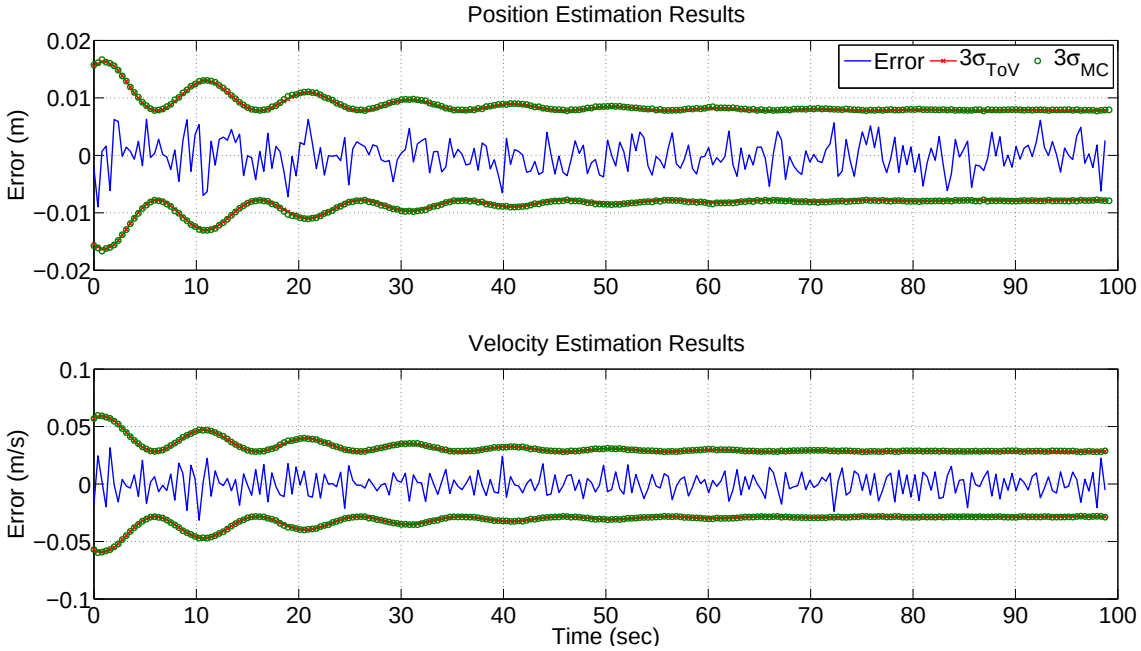

Figure 4.18: Linear Oscillator State Estimation Results: Position Only Observations with Parameter Certainty

Figure 4.19 plots the tracking error of the covariance elements computed from the likelihood state probability density compared with the numerical covariance com-

puted from Monte Carlo analysis of the state errors. Even with the increase in state estimation error, Figure 4.19 shows the covariance results of the TOV likelihood solution are comparable to the Monte Carlo solution of the reduced observation scenario.

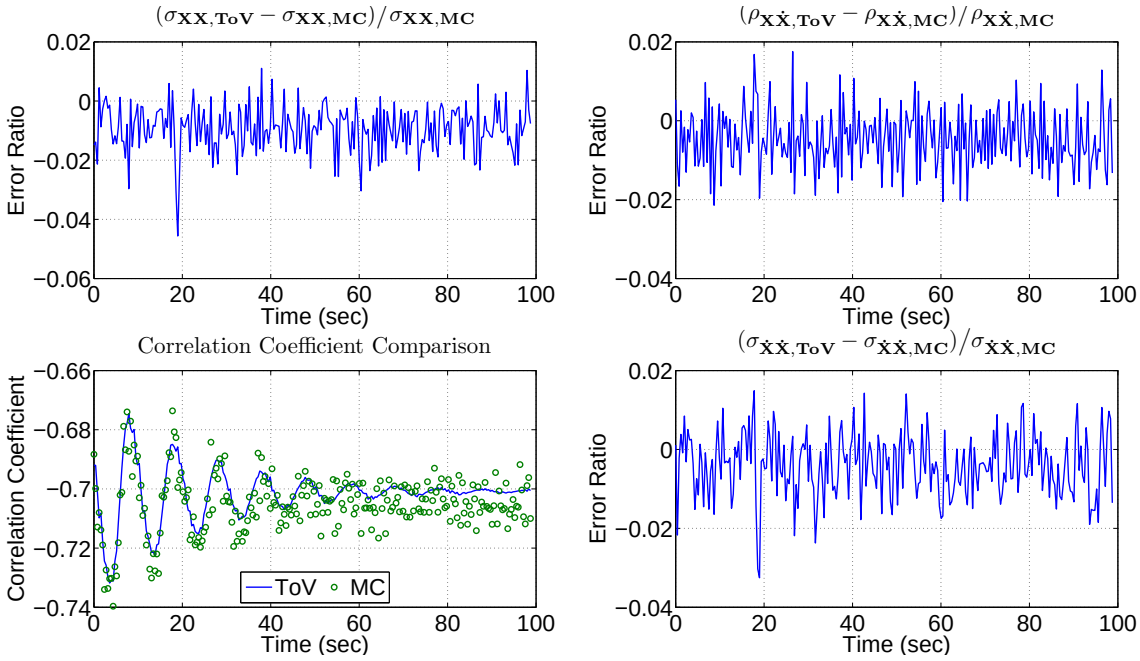

Figure 4.19: Linear Oscillator Covariance Tracking Results: Position Only Observations with Parameter Certainty

Parameter Uncertainty: For the reduced observation case possessing damping parameter uncertainty and observation drop-out, Table 4.3 presents the estimation results for the damping coefficient using the new track triggering condition for parameter estimation. Only the start of a new track was used to trigger parameter estimation since it serves as worse case scenario during the tracks. Compared with the full sensing results shown in Table 4.2, the reduced sensing TOV smoother performs rather well and is relatively accurate, the higher parameter uncertainty is to be expected since velocity is no longer measured.

Table 4.3: Damping Coefficient Estimation Results: Reduced Observations

Estimate Parameter when New Track Starts			
Time (sec)	Damping Coefficient (Ns/m)	Uncertainty (Ns/m)	Update Trigger
0	0	N/A	Initial Guess
31.600	0.4942	0.0442	New Track
51.350	0.4690	0.0325	New Track
71.495	0.4652	0.0469	New Track
91.245	0.4840	0.0630	New Track

Figures 4.20 and 4.21 display the estimated state error and uncertainty bounds and the covariance element errors for the TOV likelihood solution compared with the Monte Carlo solution. Comparison of the figures with the reduced sensing parameter certainty case shows that the algorithm is able to accommodate parameter uncertainty without a large penalty inflicted upon the state estimation or uncertainty characterization results.

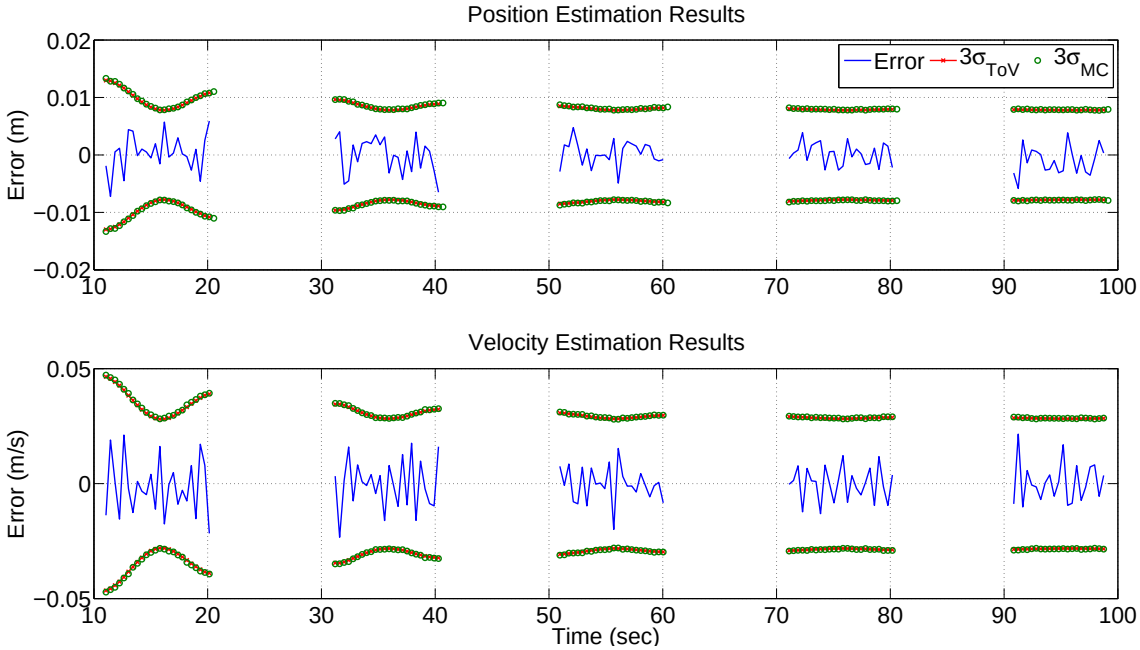

Figure 4.20: Linear Oscillator State Estimation Results : Position Only Observations with Parameter Uncertainty

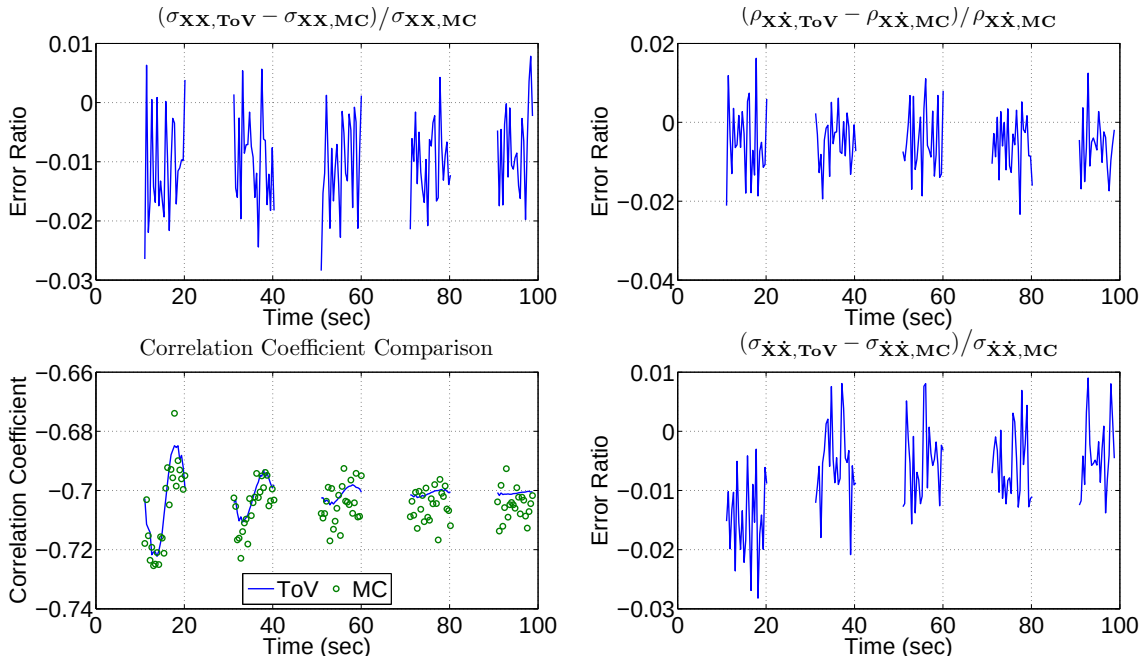

Figure 4.21: Linear Oscillator Covariance Tracking Results : Position Only Observations with Parameter Uncertainty

4.3 Space Object Surveillance

4.3.1 Introduction

The arcing mass and linear oscillator examples served as toy problems which isolated certain key features of the problems encountered during surveillance of resident space objects (RSOs). The arcing mass example demonstrated the effects of the linear smoothing process, consideration of previous data, as well as the behavior of the Cartesian state error and uncertainty bounds due to the decreasing elevation angle and the magnitude of range and angle uncertainties. The linear oscillator example demonstrated how measurements could be linked across data drop-outs to allow for effective state and parameter estimation for a periodic system. This section brings together the lessons learned from the previous examples and applies them for state and covariance initialization via a nonlinear smoothing algorithm, object tracking

using the TOV Bayes' filter, and trajectory prediction of RSOs residing in or transiting through low Earth orbit(LEO) in three different state domains commonly used for space object surveillance.

4.3.2 Initial Orbit Determination

Initial Orbit Determination(IOD) is often required since the states of most orbiting objects are not instantaneously fully observable, so multiple observations are required to render the object's states fully observable. There are many different routines, see Escobal [71], depending upon the data type and amount of information available, such as two position vectors and time, three position vectors, angles-only measurements, consecutive measurement time histories, etc.

The Herrick-Gibbs method for IOD is well documented and frequently used in space surveillance because of its applicability to closely spaced observations of an RSO [71,72]. The routine uses three Earth Centered Inertial(ECI) position measurements and their observation times to compute the velocity at the second observation time. The algorithm expresses the first and third position measurements as fourth-order Taylor Series expansions about the second measurement while assuming the RSO is influenced by Two-Body dynamics only. Equation (4.26) shows the equation governing Two-Body dynamics and the fourth-order Taylor Series expansion about the second ECI position vector, μ is the gravitational constant of Earth. The fourth-order expansion about the second position vector thereby introduces an uncertainty on the order of the fifth time derivative of the second position vector.

$$\begin{aligned} \ddot{\mathbf{r}} &= -\frac{\mu}{||\mathbf{r}||^3}\mathbf{r} \\ \mathbf{r}_i &= \mathbf{r}_2 + \tau_{i2}\dot{\mathbf{r}}_2 + \frac{\tau_{i2}^2}{2}\ddot{\mathbf{r}}_2 + \frac{\tau_{i2}^3}{6}\dddot{\mathbf{r}}_2 + \frac{\tau_{i2}^4}{24}\ddddot{\mathbf{r}}_2 + \mathcal{O}\left(\mathbf{r}_2^{\mathrm{v}}\right) \\ \tau_{ij} &= t_i - t_j \end{aligned} \tag{4.26}$$

The Herrick-Gibbs equation for computing the velocity at the second observation time is given by Equation (4.27) without derivation. See Vallado [5] or Battin [72] for the complete derivation.

$$\begin{aligned}\dot{\mathbf{r}}_2 = HG\left(\mathbf{r}_1, \mathbf{r}_2, \mathbf{r}_3\right) = t_{23}\left(\frac{1}{t_{21}t_{31}} + \frac{\mu}{12r_1^3}\right)\mathbf{r}_1 + t_{21}\left(\frac{1}{t_{31}t_{32}} + \frac{\mu}{12r_3^3}\right)\mathbf{r}_3 \\ + \left(t_{32} - t_{21}\right)\left(\frac{1}{t_{21}t_{32}} + \frac{\mu}{12r_2^3}\right)\mathbf{r}_2 \\ r_i = ||\mathbf{r}_i||\end{aligned} \tag{4.27}$$

The form of the Herrick-Gibbs IOD routine requires the inputs to be represented in the ECI frame whose primary axis points towards the Vernal Equinox. This research assumes that the tracking station observes a space object using range, azimuth, and elevation, which are relative to the local topocentric frame and the Earth Centered Earth Fixed(ECEF) frame. The ECEF frame is assumed to have its tertiary axis aligned with the tertiary axis of the ECI frame, but the primary axis remains fixed and extends outward through the Prime Meridian. For this analysis, the ECEF frame is assumed to differ only from the ECI frame by a rotation about the ECI tertiary axis through the Greenwich Mean Sidereal Time angle, θ_{GMST}. This assumption is often exercised since the precession of the Vernal Equinox causes more of discrepancy between the frames than the precession or nutation of the North Pole of the ECEF frame [5]. For a more in-depth discussion with respect to coordinate frames, transformations for the Two-Body problem, and for justification of the single rotation between ECI and ECEF see Appendix A.

The equations relating the local measurement frame triad(SEZ), composed of axes pointing locally Southernly, Easternly, and along the local vertical, to the ECI frame are given by Equation (4.28). The angle pairs of (el, β) and $(\phi, \lambda)_{TS}$ represent the local elevation and azimuth angles measured by the tracking station at a

given latitude and longitude respectively. The **Rot**[{1,2, or 3}, angle] nomenclature stands for the direction cosine matrix representing an angular displacement about the primary, secondary or tertiary axes. The local measurement vector and the tracking station position vector in the ECEF coordinate frame are resolved in their local frames according to Equation (4.29), using the justification given in Appendix A.1.2.

$$\mathbf{r}_{ECI} = \mathbf{Rot}\left[3, \theta_{GMST}\right]\left(\mathbf{R}_{TS-ECEF} + \mathbf{Rot}\left[3, \lambda_{TS}\right]^{T}\mathbf{Rot}\left[2, \pi/2 - \phi_{TS}\right]^{T}\boldsymbol{\rho}_{SEZ}\right) \tag{4.28}$$

$$\begin{aligned} \boldsymbol{\rho}_{SEZ} &= \rho\begin{bmatrix} -\cos(el)\cos(\beta) \\ \cos(el)\sin(\beta) \\ \sin(el) \end{bmatrix} \\ \mathbf{R}_{TS-ECEF} &= (R_{Earth} + Alt_{TS})\begin{bmatrix} \cos(\phi_{TS})\cos(\lambda_{TS}) \\ \cos(\phi_{TS})\sin(\lambda_{TS}) \\ \sin(\phi_{TS}) \end{bmatrix} \end{aligned} \tag{4.29}$$

Another local measurement frame can be constructed by assuming that spherical measurements are made with respect to a local coordinate system whose axes are parallel with that of the ECI coordinate system, $\hat{K}_t \parallel \hat{K}_{ECI}$ and $\hat{X}_t \parallel \hat{X}_{ECI}$. The topocentric spherical measurements are given by range, topocentric right ascension, and topocentric declination, $(\rho, \alpha_T, \delta_T)$, and are related to the position and velocity vectors in ECI frame by Equation (4.30) after the simplifying assumptions of alignment.

$$\begin{aligned} \mathbf{r}_{ECI} &= \boldsymbol{\rho}_{ECI} + \mathbf{R}_{T.S.-ECI} \\ &= \rho\begin{bmatrix} \cos(\alpha_T)\cos(\delta_T) \\ \sin(\alpha_T)\cos(\delta_T) \\ \sin(\delta_T) \end{bmatrix} + \mathbf{Rot}\left[3, -\theta_{GMST}\right]\mathbf{R}_{TS-ECEF} \end{aligned} \tag{4.30}$$

Figure 4.22 illustrates the SEZ frame along with the relationship between the ECEF and ECI frames while Figure 4.23 displays the geometry of using a measurement triad parallel to the ECI frame. Figure 4.22 shows that the typically measurement distance vector is ρ_{ECEF} but, according to Newton's Second Law, $\mathbf{r}_{ECI}$ must be used in Equation (4.26). Thus, Equation (4.28) is used to transform the measured topographical measured distance into the inertial frame. Likewise, Figure 4.23 shows that the distance vector ρ_{TOPO} must be transformed into the inertial frame, which is done by using Equation (4.30).

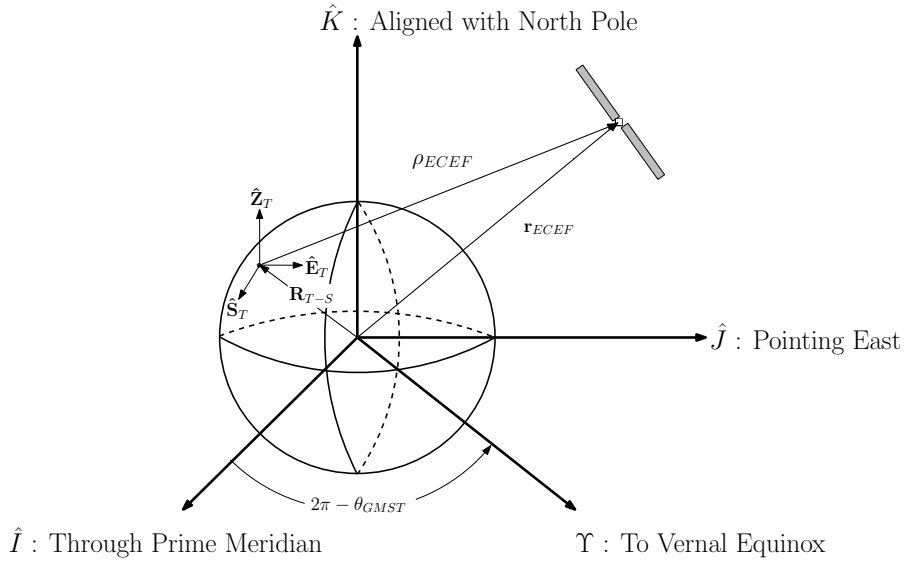

Figure 4.22: Relation of SEZ Frame to ECI Frame

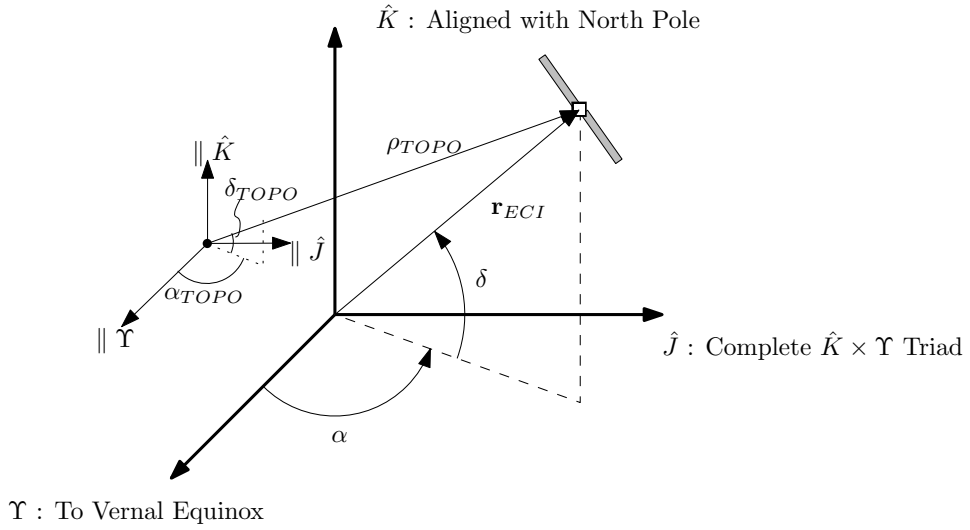

Figure 4.23: Relation of Topocentric Right Ascension and Declination Frame to ECI Frame

4.3.3 Transformation of Variables Analysis of Herrick-Gibbs Initial Orbit Determination

For mapping spherical measurement uncertainties to the Cartesian velocity domain at the second observation, either the first or third position measurement needs to be expressed as a function of the position and velocity vectors at the second observation time. For nomenclature, the first and third measurements are referred to as the bookend measurements of the second measurement. In keeping with the spirit of how the Herrick-Gibbs IOD algorithm is derived, the F and G series solution using the first-order fundamental invariants [72] is utilized and truncated after fourth order. The mapping between the bookend position measurements and the second position and velocity vectors are given by Equation (4.31). The fundamental invariants used by the F and G series solution are shown in Equation (4.32), and are solely

functions of the position and velocity vectors at the second observation time. They are deemed fundamental because they form a closed set under time differentiation and are invariant because they are scalars, thus independent of the coordinate system choice [72].

$$\begin{aligned}
\mathbf{r}_1 &= F_{12}\mathbf{r}_2 + G_{12}\dot{\mathbf{r}}_2 \\
\mathbf{r}_3 &= F_{32}\mathbf{r}_2 + G_{32}\dot{\mathbf{r}}_2 \\
F_{i2} &= 1 - \frac{\tau_{i2}^2}{2}\epsilon + \frac{\tau_{i2}^3}{2}\epsilon\lambda - \frac{\tau_{i2}^4}{24}\left(15\epsilon\lambda^2 - 3\epsilon\psi + 2\epsilon^2\right) + \ldots \\
G_{i2} &= \tau_{i2} - \frac{\tau_{i2}^3}{6}\epsilon + \frac{\tau_{i2}^4}{4}\epsilon\lambda + \ldots
\end{aligned} \tag{4.31}$$

$$\begin{bmatrix} \epsilon \\ \lambda \\ \psi \end{bmatrix} = \begin{bmatrix} \mu\left(\mathbf{r}_2^T\mathbf{r}_2\right)^{-3/2} \\ \left(\mathbf{r}_2^T\mathbf{r}_2\right)^{-1}\left(\mathbf{r}_2^T\dot{\mathbf{r}}_2\right) \\ \left(\mathbf{r}_2^T\mathbf{r}_2\right)^{-1}\left(\dot{\mathbf{r}}_2^T\dot{\mathbf{r}}_2\right) \end{bmatrix} \tag{4.32}$$

The time derivatives of the F and G series are useful when the need arises to propagate the position and velocity vectors in time and are given by Equation (4.33) to first-order in the time rates of change of the fundamental invariants. For higher order expansions of the fundamental invariants time rates of change see Battin [72]. The time rates of change of the fundamental invariants are given by Equation (4.34) [72].

$$\begin{aligned}
\frac{d}{d\tau}\left(F_{i2}\right) &= -\tau_{i2}\epsilon - \frac{\tau_{i2}^2}{2}\dot{\epsilon} + \frac{3}{2}\tau_{i2}^2\epsilon\lambda + \frac{\tau_{i2}^3}{2}\left(\dot{\epsilon}\lambda + \epsilon\dot{\lambda}\right) + \ldots \\
\frac{d}{d\tau}\left(G_{i2}\right) &= 1 - \frac{\tau_{i2}^2}{2}\epsilon - \frac{\tau_{i2}^3}{6}\dot{\epsilon} + \ldots
\end{aligned} \tag{4.33}$$

$$\frac{d}{d\tau}\left(\begin{bmatrix} \epsilon \\ \lambda \\ \psi \end{bmatrix}\right) = \begin{bmatrix} -3\epsilon\lambda \\ \psi - \epsilon - 2\lambda^2 \\ -2\lambda\left(\epsilon + \psi\right) \end{bmatrix} \tag{4.34}$$

4.3.3.1 *Cartesian Position and Velocity Likelihood Probability Density Function Computation*

The Herrick-Gibbs IOD algorithm is an over-constrained smoother since three position vectors are used to form a single velocity vector, whereas a minimal smoother would require only two position vectors. From Equation (4.27), the over-constrained nonlinear system is of the form given by Equation (4.35).

$$\begin{aligned}
\begin{bmatrix} \dot{\mathbf{r}}_2 \\ \mathbf{r}_2 \end{bmatrix} &= \mathbf{h}^{-1}\left(\begin{bmatrix} \mathbf{r}_1 \\ \mathbf{r}_2 \\ \mathbf{r}_3 \end{bmatrix}\right) \\
&= \left[\begin{array}{c:c:c} t_{23}\left(\frac{1}{t_{21}t_{31}} + \frac{\mu}{12r_1^3}\right) & (t_{32}-t_{21})\left(\frac{1}{t_{21}t_{32}} + \frac{\mu}{12r_2^3}\right) & t_{21}\left(\frac{1}{t_{31}t_{32}} + \frac{\mu}{12r_3^3}\right) \\ \hdashline \mathbf{0}_{n\times n} & \mathbf{1}_{n\times n} & \mathbf{0}_{n\times n} \end{array}\right] \\
&\quad \times \begin{bmatrix} \mathbf{r}_1 \\ \mathbf{r}_2 \\ \mathbf{r}_3 \end{bmatrix} \\
r_i &= ||\mathbf{r}_i||
\end{aligned} \tag{4.35}$$

Application of TOV using Equation (4.35) cannot be carried out directly because of solving for the roots of the equation in terms of the desired state variables, $(\dot{\mathbf{r}}_2, \mathbf{r}_2)$, only. Additionally, the transformation of Cartesian position only to position and velocity is not square due to over-constraint, so the determinant of the Jacobian cannot be evaluated. For an approximate solution of the roots, Equations (4.31) and (4.32) provide solutions of $\mathbf{r}_1$ and $\mathbf{r}_3$ in terms of $(\dot{\mathbf{r}}_2, \mathbf{r}_2)$ for small propagation times, error on $\mathcal{O}\left(\mathbf{r}_2^{\mathrm{v}}\right)$, and are given in state-space form by Equation (4.36). However, the

transformation between desired state variables and measurement variables does not lead to a square Jacobian due to over-constraint on the velocity states.

$$\begin{bmatrix} \mathbf{r}_1 \\ \mathbf{r}_2 \\ \mathbf{r}_3 \end{bmatrix} = \mathbf{h}\left(\begin{bmatrix} \dot{\mathbf{r}}_2 \\ \mathbf{r}_2 \end{bmatrix}\right)$$
$$= \left[\begin{array}{c|c} \tau_{12} - \frac{\tau_{12}^3}{6}\epsilon + \frac{\tau_{12}^4}{4}\epsilon\lambda & 1 - \frac{\tau_{12}^2}{2}\epsilon + \frac{\tau_{12}^3}{2}\epsilon\lambda - \frac{\tau_{12}^4}{24}\left(15\epsilon\lambda^2 - 3\epsilon\psi + 2\epsilon^2\right) \\ \hline \mathbf{0}_{n\times n} & \mathbf{1}_{n\times n} \\ \hline \tau_{32} - \frac{\tau_{32}^3}{6}\epsilon + \frac{\tau_{32}^4}{4}\epsilon\lambda & 1 - \frac{\tau_{32}^2}{2}\epsilon + \frac{\tau_{32}^3}{2}\epsilon\lambda - \frac{\tau_{32}^4}{24}\left(15\epsilon\lambda^2 - 3\epsilon\psi + 2\epsilon^2\right) \end{array}\right]$$
$$\times \begin{bmatrix} \dot{\mathbf{r}}_2 \\ \mathbf{r}_2 \end{bmatrix} \tag{4.36}$$

Since the over-constraint of the velocity variable has led to a nonsquare Jacobian of the transformation, application of the Dirac Generalized Function [27] can be used to extract the necessary joint probability density function of $(\dot{\mathbf{r}}_2, \mathbf{r}_2)$. Inspection of the Herrick-Gibbs IOD routine shows that the roots of $\mathbf{r}_1$ or $\mathbf{r}_3$ cannot be written as standalone functions of $\dot{\mathbf{r}}_2$, $\mathbf{r}_2$, and the other bookend position, either $\mathbf{r}_1$ or $\mathbf{r}_3$, due to the existence of the magnitude of the position cubed.

In Equation (4.35), the contribution of the $\mu\left(12\left|\mathbf{r}_i\right|^3\right)^{-1}$ term to the overall time weighting of the position measurement in the velocity smoothing for an object at an altitude of 160 kilometers is on the order of 1.2×10^{-7}. When considering estimation error, if the position vector magnitude error was 10 kilometers when the true magnitude was 160 kilometers, the difference between the true and estimated $\mu\left(12r_i^3\right)^{-1}$ term would be on the order of 5.4×10^{-10}. Keeping these differences in mind, replacing the magnitude of either bookend position vector with its F and G

series expansion solution in terms of the second position and velocity will not significantly affect the outcome of the solution. Equation (4.37) provides the bookend roots of the Herrick-Gibbs IOD solution using the substitution of the F and G series solution. The partial derivatives of the Herrick-Gibbs IOD solution with respect to the bookend measurements are given by Equation (4.38).

$$\mathbf{r}_1 = g_{12}\left(\dot{\mathbf{r}}_2, \mathbf{r}_2, \mathbf{r}_3\right) = \frac{\dot{\mathbf{r}}_2 - \left(t_{32} - t_{21}\right)\left(\frac{1}{t_{21}t_{32}} + \frac{\mu}{12r_2^3}\right)\mathbf{r}_2 - t_{21}\left(\frac{1}{t_{31}t_{32}} + \frac{\mu}{12r_3^3}\right)\mathbf{r}_3}{t_{23}\left(\frac{1}{t_{21}t_{31}} + \frac{\mu}{12}\left|F_{12}\mathbf{r}_2 + G_{12}\dot{\mathbf{r}}_2\right|^{-3}\right)}$$

$$\mathbf{r}_3 = g_{32}\left(\dot{\mathbf{r}}_2, \mathbf{r}_2, \mathbf{r}_1\right) = \frac{\dot{\mathbf{r}}_2 - t_{23}\left(\frac{1}{t_{21}t_{31}} + \frac{\mu}{12r_1^3}\right)\mathbf{r}_1 - \left(t_{32} - t_{21}\right)\left(\frac{1}{t_{21}t_{32}} + \frac{\mu}{12r_2^3}\right)\mathbf{r}_2}{t_{21}\left(\frac{1}{t_{31}t_{32}} + \frac{\mu}{12}\left|F_{32}\mathbf{r}_2 + G_{32}\dot{\mathbf{r}}_2\right|^{-3}\right)} \tag{4.37}$$

$$\frac{\partial \dot{\mathbf{r}}_2}{\partial \mathbf{r}_1} = \begin{bmatrix} \frac{\partial \dot{x}_2}{\partial x_1} & \frac{\partial \dot{x}_2}{\partial y_1} & \frac{\partial \dot{x}_2}{\partial z_1} \\ \frac{\partial \dot{y}_2}{\partial x_1} & \frac{\partial \dot{y}_2}{\partial y_1} & \frac{\partial \dot{y}_2}{\partial z_1} \\ \frac{\partial \dot{z}_2}{\partial x_1} & \frac{\partial \dot{z}_2}{\partial y_1} & \frac{\partial \dot{z}_2}{\partial z_1} \end{bmatrix} = t_{23}\left(\frac{1}{t_{21}t_{31}} + \frac{\mu}{12r_1^3}\right)\mathbf{1}_{3\times 3} - \frac{t_{23}\mu}{4}\left|\mathbf{r}_1\right|^{-5}\mathbf{r}_1\mathbf{r}_1^T$$

$$\frac{\partial \dot{\mathbf{r}}_2}{\partial \mathbf{r}_3} = t_{21}\left(\frac{1}{t_{31}t_{32}} + \frac{\mu}{12r_3^3}\right)\mathbf{1}_{3\times 3} - \frac{t_{21}\mu}{4}\left|\mathbf{r}_3\right|^{-5}\mathbf{r}_3\mathbf{r}_3^T \tag{4.38}$$

Application of the Dirac Generalized function to compute the marginal joint PDF of $(\dot{\mathbf{r}}_2, \mathbf{r}_2)$ from the given joint PDF of $(\mathbf{r}_1, \mathbf{r}_2, \mathbf{r}_3)$ can then be carried out. However, due to the over-constraint of the Herrick-Gibbs smoothing process, the marginal joint PDF can be computed by replacing either the first bookend measurement or the last measurement. Computation of both marginal likelihood PDFs is shown in Equation (4.39). Both joint densities shown in Equation (4.39) are equivalent, but derived two different ways due to the over-constraint on the velocity state vari-

able. Therefore, one could use either solution to compute the joint PDF of the state variables of interest. However, numerical differences could arise since the integral operation is typically reduced to a large sum and the bookend measurements can be different time intervals away from the second observation. If the bookend measurements are symmetrical in time, it would seem that one should use the latter solution of the PDF, i.e. the replacement of the third position in terms of the other three variables, due to the natural progression of measurements.

Replace $\mathbf{r}_1$

$$\begin{aligned} p\left(\dot{\mathbf{r}}_2, \mathbf{r}_2\right) &= \int_{\mathcal{D}_{\mathbf{r}_2}} \int_{\mathcal{D}_{\mathbf{r}_3}} p\left(\mathbf{r}_1, \mathbf{r}_2, \mathbf{r}_3\right) \delta\left(HG\left(\mathbf{r}_1, \mathbf{r}_2, \mathbf{r}_3\right) - \dot{\mathbf{r}}_2\right) \delta\left(\mathbf{r}_2 - \mathbf{r}_2\right) d\mathbf{r}_1 d\mathbf{r}_2 d\mathbf{r}_3 \\ &= \int_{\mathcal{D}_{\mathbf{r}_1}} \int_{\mathcal{D}_{\mathbf{r}_3}} p\left(\mathbf{r}_1, \mathbf{r}_2, \mathbf{r}_3\right) \delta\left(HG\left(\mathbf{r}_1, \mathbf{r}_2, \mathbf{r}_3\right) - \dot{\mathbf{r}}_2\right) d\mathbf{r}_1 d\mathbf{r}_3 \\ &= \int_{\mathcal{D}_{\mathbf{r}_3}} p\left(\mathbf{r}_1 = g_{12}\left(\dot{\mathbf{r}}_2, \mathbf{r}_2, \mathbf{r}_3\right), \mathbf{r}_2, \mathbf{r}_3\right) \left| \frac{\partial \dot{\mathbf{r}}_2}{\partial \mathbf{r}_1} \right|^{-1}_{\mathbf{r}_1 = g_{12}(\dot{\mathbf{r}}_2, \mathbf{r}_2, \mathbf{r}_3)} d\mathbf{r}_3 \end{aligned}$$

Replace $\mathbf{r}_3$

$$p\left(\dot{\mathbf{r}}_2, \mathbf{r}_2\right) = \int_{\mathcal{D}_{\mathbf{r}_1}} p\left(\mathbf{r}_1, \mathbf{r}_2, \mathbf{r}_3 = g_{32}\left(\dot{\mathbf{r}}_2, \mathbf{r}_2, \mathbf{r}_1\right)\right) \left| \frac{\partial \dot{\mathbf{r}}_2}{\partial \mathbf{r}_3} \right|^{-1}_{\mathbf{r}_3 = g_{32}(\dot{\mathbf{r}}_2, \mathbf{r}_2, \mathbf{r}_1)} d\mathbf{r}_1 \tag{4.39}$$

4.3.3.2 Joint Measurement Probability Density Function Computation

In order for Equation (4.39) to be calculated, the joint PDF of the Cartesian positions at the first, second, and third observation times must be computed. Figure 4.24 illustrates this task is not trivial since propagation of the previous measurement PDF requires knowledge of the initial state domain for solution of the differential or difference equations.

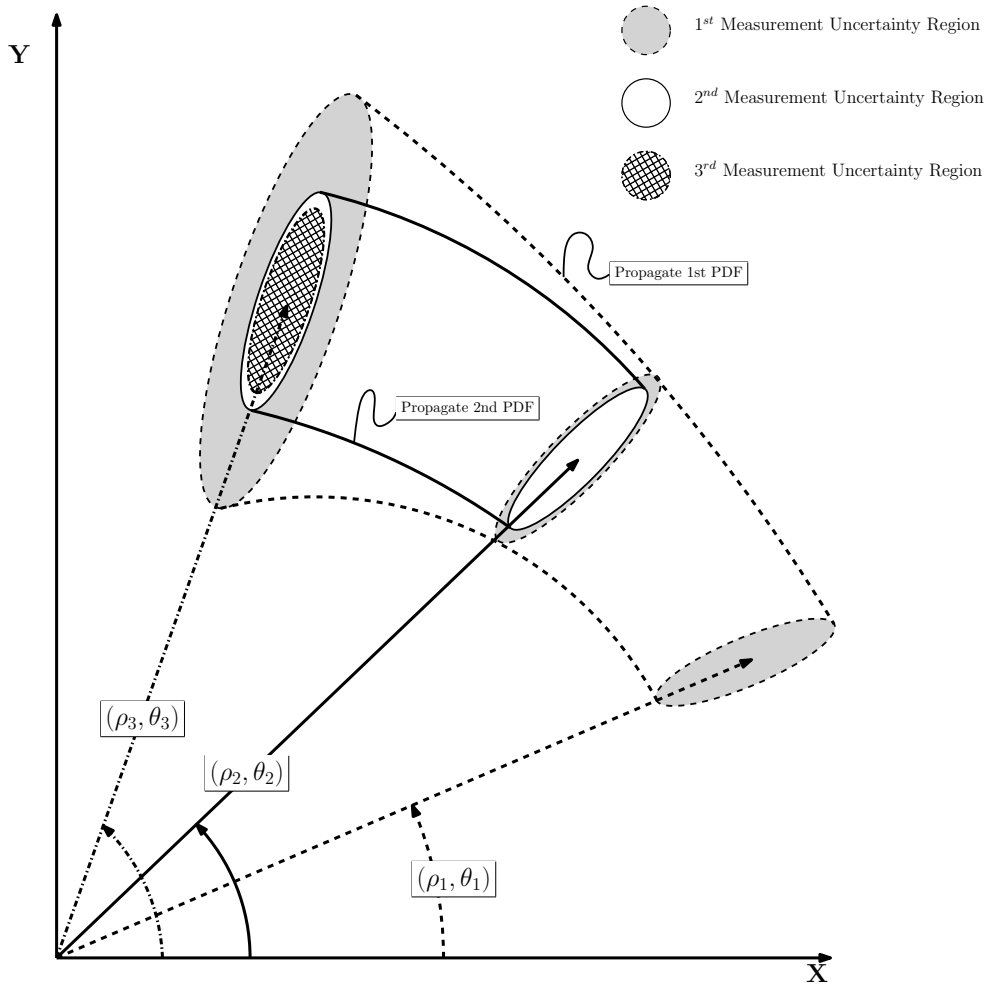

Figure 4.24: Propagated versus Measurement Update State Probability Density Functions

Assuming all initial state domains are accurately known, Figure 4.24 shows that the propagated solution is not only a function of the initial states but also of time via comparison of the propagated PDF solutions at the third measurement time from the first measurement and second measurements. If all initial position state PDFs are known, the computation of the joint PDF is given by carrying out the chain rule of probability [2], Equation (4.40). Computation of the conditional PDFs in Equation (4.40) are dependent upon the dynamic model used in characterizing the

RSO's motion.

$$\begin{aligned} \text{Chain Rule: } p(a_1, \ldots, a_n) &= p(a_n|a_{n-1}, \ldots, a_1) \ldots p(a_2|a_1)\, p(a_1) \\ p(\mathbf{r}_1, \mathbf{r}_2, \mathbf{r}_3) &= p(\mathbf{r}_3|\mathbf{r}_1, \mathbf{r}_2)\, p(\mathbf{r}_1, \mathbf{r}_2) \\ &= p(\mathbf{r}_3|\mathbf{r}_1, \mathbf{r}_2)\, p(\mathbf{r}_2|\mathbf{r}_1)\, p(\mathbf{r}_1) \end{aligned} \tag{4.40}$$

Equation (4.40) can be somewhat simplified if the differential or difference equation(s) dictating the evolution of the state is Markov in nature, i.e. the differential equation is ordinary, whereby the future states are predicated only upon the present states. The solution of the PDF by the chain rule can be a problem for overly constrained solutions using measurements before and after the desired state observation time. For the Herrick-Gibbs IOD algorithm, it was shown through examination of time-weighting contributions that the last bookend measurement could be written as a function of only previous time state variables without significant impact to the solution. As such, the second marginal PDF solution of Equation (4.39) should be utilized.

Before the Cartesian position and velocity marginal PDF at the time of interest can be constructed, the measurement domain PDF must be developed then mapped to the Cartesian position domain at each respective observation time. Using the spatial transformation between coordinate frames, TOV can be carried out to map the position uncertainty of either the SEZ frame or the topocentric frame parallel to ECI into the Cartesian ECI frame. Assuming that the consecutive position measurements are statistically independent of each other, Equation (3.53) can be computed for the measurement domain joint likelihood, shown by Equation (4.41). The measurement domain likelihood can then be mapped into the ECI frame using Equation (3.34), the Jacobians for the different measurement domains are given by Equation (4.42),

resulting in Equation (4.43).

$$\begin{aligned} p\left(\tilde{\mathbf{z}}_1, \tilde{\mathbf{z}}_2, \tilde{\mathbf{z}}_3\right) &= \prod_{i=1}^{3} p\left(\rho_i\right) p\left(el_i\right) p\left(\beta_i\right) \\ &= \prod_{i=1}^{3} p\left(\rho_i\right) p\left(\alpha_{T,i}\right) p\left(\delta_{T,i}\right) \end{aligned} \tag{4.41}$$

$$\begin{aligned} \left|J_i\right| &= \left|\frac{\partial \mathbf{r}_i}{\{\rho, el, \beta\}_i}\right| = \rho^2 \cos(el) \\ &= \left|\frac{\partial \mathbf{r}_i}{\{\rho, \alpha_T, \delta_T\}_i}\right| = \rho^2 \cos(\delta_T) \end{aligned} \tag{4.42}$$

$$p\left(\mathbf{r}_1, \mathbf{r}_2, \mathbf{r}_3\right) = \left[p\left(\tilde{\mathbf{z}}_1, \tilde{\mathbf{z}}_2, \tilde{\mathbf{z}}_3\right) \prod_{i=1}^{3} \left|J_i\right|^{-1}\right]_{\mathbf{z}=f(\mathbf{r}_i)} \tag{4.43}$$

Singularities are present in the Jacobians, $\rho = 0$ or $el = \delta_T = 0$, but these singularities are not due to the TOV procedure, but rather to the geometric limitations of the measurement frames. The range singularity is trivial since one would not be measuring object range if the object were already at the origin. The angle singularity of an overhead observation can only be avoided when velocity measurements are also available so that the cosine of the angle can be estimated [49].

4.3.3.3 Cartesian Position and Velocity Prior Probability Density Function Computation

With computation of the marginal likelihood PDF, if positional measurement data exists prior to the first measurement used in the Herrick-Gibbs algorithm, the F and G series solution given by Equations (4.31) and (4.33) can be applied to map the position-velocity domain to any other time of interest. The conventional F and G solution, see Appendix A.2.5, is not used since it requires transforming into the Keplerian element domain while the series solution remains in the Cartesian domain. The posterior can be computed by using Equation (4.39) for the likelihood PDF and

Equation (4.44) for the prior PDF, where i corresponds to the measurement time to propagate to and j corresponds to the generated Cartesian domain to evaluate.

$$p\left(\dot{\mathbf{r}}_j^-, \mathbf{r}_j^-\right) = p\left(\mathbf{r}_i = F_{ij}\mathbf{r}_j + G_{ij}\dot{\mathbf{r}}_j, \dot{\mathbf{r}}_i = \dot{F}_{ij}\mathbf{r}_j + \dot{G}_{ij}\dot{\mathbf{r}}_j\right)\left|F_{ij}\dot{G}_{ij} - G_{ij}\dot{F}_{ij}\right| \tag{4.44}$$

As noted in Section 3.5.1, application of TOV for the time mapping may not be required if the mapping between time instances yields a constant across the domain, which results from remaining in the same set of basis functions during propagation. For the F and G solution, the determinate should theoretically remain unity, but numerically may diverge from unity, which can indicate that the propagation time is too long for the solution to remain valid.

4.3.4 Transformation of Variables Analysis of Osculating Orbital Element Space

Analysis of the likelihood and prior PDFs in osculating, instantaneous, orbital element space, follows the same approach as the Cartesian space approach. This research uses the Keplerian elements, $(a, e, \Omega, i, \omega, M$ or f or $E)$, with the Cartesian ECI to Keplerian element state mapping equations given in Appendix A.3. The PDF of the measurement domain can be mapped into the Keplerian domain as shown by Equation (4.45), following Equation (3.34). The vector $\mathbf{s}$ represents any state description possessing the same number of basis functions as the Cartesian domain and is related to the Cartesian domain via the transformation function $\boldsymbol{\psi}$.

$$p\left(\mathbf{s}\right) = p\left(\mathbf{r}_i = \boldsymbol{\psi}_{Pos}\left(\mathbf{s}\right), \dot{\mathbf{r}}_i = \boldsymbol{\psi}_{Vel}\left(\mathbf{s}\right)\right)\left|\frac{\partial\ \boldsymbol{\psi}\left(\mathbf{s}\right)}{\partial\ \mathbf{s}}\right| \tag{4.45}$$

The Keplerian orientation parameters are shown in Figure 4.25 and are angles whose 3-1-3 rotation sequence rotates the ECI frame into the local orbit frame whose

origin is at the primary focus of the conic section defining the orbit. The angles in order of rotation from ECI to orbit frame are Right Ascension of Ascending Node, Inclination, and Argument of Perigee, (Ω, i, ω). The Keplerian time parameter is also an angle and is measured from the line connecting the focus of the conic section and point of closest approach, this line dictates the direction of the eccentricity vector, $\hat{\mathbf{e}}$, which is the primary axis of the orbital plane. The tertiary axis is aligned with the direction of the RSO's specific angular momentum vector, $\hat{\mathbf{h}}$, the triad is then completed with the cross product of the tertiary and primary axes. The time parameter shown is true anomaly, f, which is the angle measured when considering angular rotation about the conic section focus.

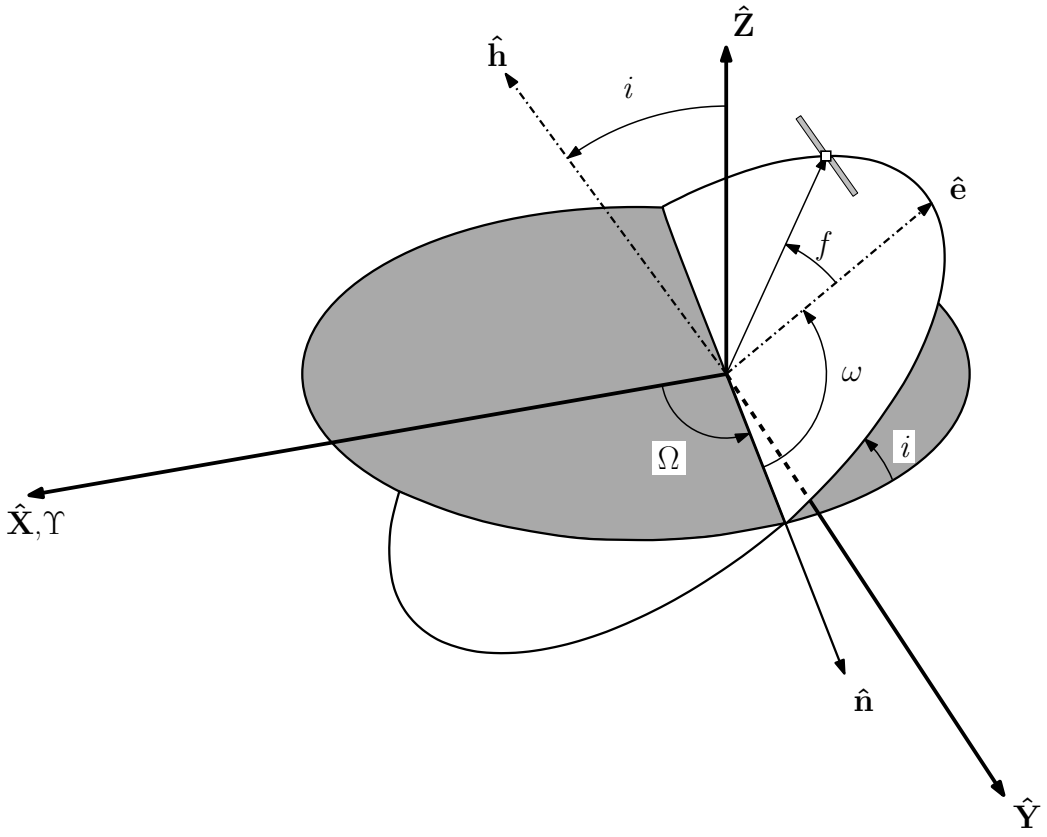

Figure 4.25: Orientation Keplerian Orbital Elements with Respect to Cartesian Earth Centered Inertial Frame

With the orientation and time parameters, only the size and shape of the conic section are left to define. The size parameter is the semi-major axis, a, and is half the distance between the point of closest primary focal approach, periapsis, and point of farthest primary focal approach, apoapsis, as such this parameter is undefined for a parabola. The shape parameter is known as eccentricity, e, and indicates the type of conic section: $e = 0$ for circle, $0 < e < 1$ for ellipse, $e = 1$ for parabola, and $e > 1$ for hyperbola. Figure 4.26 displays the semi-major axis and eccentricity along with two time parameters, true anomaly and eccentric anomaly, E.

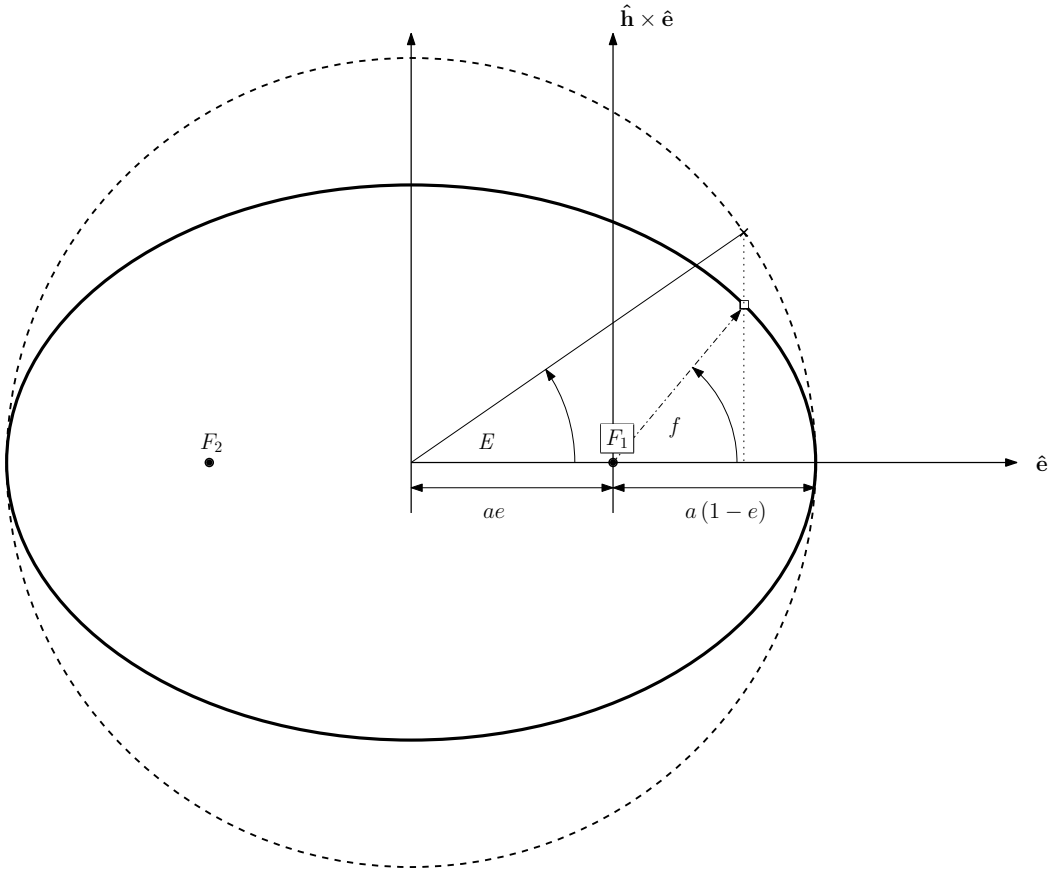

Figure 4.26: Size, Shape, and Time Parameters for Keplerian Elements

As shown by Figure 4.26, in addition to true anomaly there exists what is known as the eccentric anomaly, which is defined with respect to the RSO's position pro-

jected onto a circle with radius equal to the semi-major axis. With the magnitude of the eccentricity vector and true anomaly known, eccentric anomaly is able to be computed from true anomaly but, more importantly, the mean anomaly, M, is able to be calculated. Mean anomaly is often used because it allows for linear propagation of the RSO's motion when undergoing Keplerian(unperturbed Two-Body dynamics) motion. Selection of the time parameter also has an impact on the ease with which one can convert between osculating and Cartesian domains.

As an example of the Jacobian computation for Equation (4.45), consider motion in the ECI frame equatorial plane with the orbit frame axes parallel to those of the ECI frame. The Cartesian position and velocity vectors will only be composed of an x and y component while the Keplerian elements will be composed of only a size, shape, and time parameter since all the orientation angles are zero. True anomaly is chosen as the time variable, in lieu of eccentric or mean anomaly, since it is more easily computed from the Cartesian states. However, a price is paid when partial derivatives of the Cartesian states are computed since eccentric anomaly gives these a nicer form.

For this example, Equation (4.45) is simplified to what is shown in Equation (4.46). Equation (4.47) displays the Jacobian from the Cartesian state domain to the Keplerian domain using the y velocity as the auxiliary variable. This choice allows for the determinant of the Jacobian to be simply the determinant of the upper 3×3 matrix, due to the left most column being all zeroes except for the last element. Note that the x velocity could have been used instead of the y velocity but the y velocity was chosen for a slightly easier reduction.

$$p\left(a,\ e,\ f\right) = \int_{\mathcal{D}_{\dot{y}}} p\left(x, y, \dot{x}, \dot{y}\right) \left|K\left(a,\ e,\ f,\ \dot{y}\right)\right| d\dot{y} \tag{4.46}$$

$$K\left(a,\ e,\ f,\ \dot{y}\right) = \begin{bmatrix} \dfrac{\partial x}{\partial a} & \dfrac{\partial x}{\partial e} & \dfrac{\partial x}{\partial f} & \dfrac{\partial x}{\partial \dot{y}} \\ \dfrac{\partial y}{\partial a} & \dfrac{\partial y}{\partial e} & \dfrac{\partial y}{\partial f} & \dfrac{\partial y}{\partial \dot{y}} \\ \dfrac{\partial \dot{x}}{\partial a} & \dfrac{\partial \dot{x}}{\partial e} & \dfrac{\partial \dot{x}}{\partial f} & \dfrac{\partial \dot{x}}{\partial \dot{y}} \\ \dfrac{\partial \dot{y}}{\partial a} & \dfrac{\partial \dot{y}}{\partial e} & \dfrac{\partial \dot{y}}{\partial f} & \dfrac{\partial \dot{y}}{\partial \dot{y}} \end{bmatrix} \tag{4.47}$$

For the planar orbit considered, the relationships between the Cartesian and Keplerian elements are given by Equation (4.48). The intermediate expressions of radius, radial velocity, and time rate change of true anomaly are given by Equation (4.49).

$$\begin{array}{l|l} x = r\cos(f) & \dot{x} = \dot{r}\cos(f) - r\dot{f}\sin(f) \\ y = r\sin(f) & \dot{y} = \dot{r}\sin(f) + r\dot{f}\cos(f) \end{array} \tag{4.48}$$

$$\begin{aligned} r &= \frac{a\left(1-e^2\right)}{1+e\cos(f)} \\ \dot{r} &= \sqrt{\frac{\mu}{a\left(1-e^2\right)}}e\sin(f) \\ \dot{f} &= \frac{\sqrt{\mu a\left(1-e^2\right)}}{r^2} \end{aligned} \tag{4.49}$$

The partial derivatives needed for the Jacobian are given by Equations (4.50) through (4.52). The existence of the partial derivative of true anomaly with respect to eccentricity arises from the solution of Kepler's equation if true anomaly is computed from the solution of Kepler's equation.

$$\begin{aligned} \frac{\partial r}{\partial a} &= \frac{1-e^2}{1+e\cos(f)} \\ \frac{\partial r}{\partial e} &= \frac{-2ae}{1+e\cos(f)} - \frac{a\left(1-e^2\right)}{\left(1+e\cos(f)\right)^2}\left[\cos(f) - e\sin(f)\frac{\partial f}{\partial e}\right] \\ \frac{\partial r}{\partial f} &= \frac{re\sin(f)}{1+e\cos(f)} \end{aligned} \tag{4.50}$$

$$\begin{aligned}
\frac{\partial \dot{r}}{\partial a} &= -\frac{\dot{r}}{2a} \\
\frac{\partial \dot{r}}{\partial e} &= \sqrt{\frac{\mu}{a\left(1-e^2\right)}}\left[-\frac{e\sin(f)}{2\left(1-e^2\right)} + \sin(f) + e\cos(f)\frac{\partial f}{\partial e}\right] \\
\frac{\partial \dot{r}}{\partial f} &= \sqrt{\frac{\mu}{a\left(1-e^2\right)}}e\cos(f)
\end{aligned} \tag{4.51}$$

$$\begin{aligned}
\frac{\partial\left(r\dot{f}\right)}{\partial a} &= -\frac{r\dot{f}}{2a} \\
\frac{\partial\left(r\dot{f}\right)}{\partial e} &= \sqrt{\frac{\mu}{a\left(1-e^2\right)}}\left[\cos(f) + \frac{1+e\cos(f)}{1-e^2} - e\sin(f)\frac{\partial f}{\partial e}\right] \\
\frac{\partial\left(r\dot{f}\right)}{\partial f} &= -\sqrt{\frac{\mu}{a\left(1-e^2\right)}}e\sin(f)
\end{aligned} \tag{4.52}$$

If true anomaly is computed from mean anomaly or if one possesses true anomaly directly and desires to transform the PDF of semi-major axis, eccentricity, and true anomaly to that of semi-major axis, eccentricity, and mean anomaly for easier propagation in time, Kepler's equation [72] must be solved. Kepler's equation is the most well-known transcendental equation in orbital mechanics, given by Equation (4.53), and relates eccentric anomaly to mean anomaly and true anomaly to mean anomaly.

$$\begin{aligned}
M &= E - e\sin(E) \\
E &= 2\arctan\left[\sqrt{\frac{1-e}{1+e}}\tan\left(\frac{f}{2}\right)\right]
\end{aligned} \tag{4.53}$$

A stand-alone solution of eccentric or true anomaly from mean anomaly without use of previous anomaly data has been classically performed using Newton's Method, but Lagrange's Generalized Expansion Theorem or Bessel Functions can also be applied [72]. For orbits with eccentricity less than approximately 2/3, Lagrange's Generalized Expansion Theorem can be applied to compute the eccentric anomaly as a function of mean anomaly [72] or compute true anomaly as a function of mean anomaly [73], via a power series expansion in eccentricity. For orbits with ec-

centricity greater than 2/3, the series can be reordered in the form of a Fourier series which possesses absolute convergence for all values of eccentricity. The Lagrange expansions [72,73] of eccentric and true anomaly as a function of eccentricity and mean anomaly are given in Equation (4.54) and the Fourier-Bessel series expansions [72] are given by Equation (4.55).

$$\begin{aligned}
E &= M + \left(e - \frac{1}{8}e^3 + \frac{1}{192}e^5\right)\sin(M) + \left(\frac{1}{2}e^2 - \frac{1}{6}e^4 + \frac{1}{48}e^6\right)\sin(2M) \\
&\quad + \left(\frac{3}{8}e^3 - \frac{27}{128}e^5\right)\sin(3M) + \left(\frac{1}{4}e^4 - \frac{4}{15}e^6\right)\sin(4M) \\
&\quad + \frac{125}{384}e^5\sin(5M) + \frac{27}{80}e^6\sin(6M) + \mathcal{O}\left(e^7\right) \\
f &= M + \left(2e - \frac{1}{4}e^3 + \frac{5}{96}e^5\right)\sin(M) + \left(\frac{5}{4}e^2 - \frac{11}{24}e^4 + \frac{17}{192}e^6\right)\sin(2M) \\
&\quad + \left(\frac{13}{12}e^3 - \frac{43}{64}e^5\right)\sin(3M) + \left(\frac{103}{96}e^4 - \frac{451}{480}e^6\right)\sin(4M) \\
&\quad + \frac{1097}{960}e^5\sin(5M) + \frac{1223}{960}e^6\sin(6M) + \mathcal{O}\left(e^7\right)
\end{aligned} \tag{4.54}$$

$$\begin{aligned}
E &= M + 2\sum_{k=1}^{\infty}\frac{1}{k}J_k\left(ke\right)\sin(kM) \\
f &= M + 2\sum_{k=1}^{\infty}\frac{1}{k}\left[\sum_{n=-\infty}^{\infty}J_n\left(-ke\right)\beta^{|k+n|}\right]\sin(kM) \\
\beta &= \frac{1-\sqrt{1-e^2}}{e} \\
J_n\left(x\right) &= \sum_{j=0}^{\infty}(-1)^j\frac{\left(\frac{x}{2}\right)^{n+2j}}{j!\,(n+j)!}
\end{aligned} \tag{4.55}$$

From Equations 4.54 and 4.55, the partial derivatives of eccentric or true anomaly can be computed with respect to eccentricity and mean anomaly. If one were to instead use the iterated solution of Kepler's equation, the partial derivatives would

be those given by Equation (4.56) [46, 74].

$$\begin{array}{l|l} \dfrac{\partial E}{\partial e} = \dfrac{a\sin(E)}{r} & \dfrac{\partial f}{\partial e} = \left(\dfrac{a}{r} - \left(1-e^2\right)^{-1}\right)\sin(f) \\ \dfrac{\partial E}{\partial M} = \dfrac{a}{r} & \dfrac{\partial f}{\partial M} = \left(\dfrac{a}{r}\right)^2\sqrt{1-e^2} \end{array} \tag{4.56}$$

For the equatorial orbit example, only the true anomaly is being traded for mean anomaly, the determinant of the mapping Jacobian from the true anomaly set to the mean anomaly set is simply the partial derivative with respect to mean anomaly of either the series expansions or numerical solution of Kepler's equation. For three-dimensional orbits, see Broucke [75] for the partial derivatives from Cartesian ECI to Keplerian elements as well as other element sets.

4.3.4.1 Propagation of Osculating Orbital Elements and their Uncertainties

Propagation of osculating Keplerian elements can be accomplished by applying TOV as it was used for the construction of the prior in the previous section. However, instead of using the F and G power series solution, the Mean Anomaly is linearly updated, Equation (4.57), while the rest of the osculating elements are held constant. Since the orbital elements are curvilinear elements instead of rectilinear elements, their propagated solution will more accurately describe the behavior of the PDF which is undergoing curvilinear motion. For Two-Body unperturbed motion, the determinant of the Jacobian required for time propagation will be unity since the all other elements are considered constant with respect to mean anomaly.

$$M(t) = M(t_0) + \sqrt{\frac{\mu}{a^3}}(t - t_0) \tag{4.57}$$

4.3.5 Transformation of Variables Analysis of Mean Orbital Element Space

Brouwer [47] derived the secular drift of a RSO to the second-order and the long-period motion to first-order of the dominant geopotential perturbation source. The dominant geopotential perturbation source is from the J_2 zonal harmonic and results from the Earth's bulge around the equator which causes rotation of perigee, rotation of the orbit plane about the ECI tertiary axis, and a change in mean motion [76]. The value of J_2 is $1.0826266835\times10^{-3}$ and due to its relatively high value, inclusion of higher order zonal harmonic effects requires inclusion of the J_2^2 contribution since the second-order effect of J_2 is on the order of the higher zonals' first-order effects, namely $\mathcal{O}\left(J_2^2\right) \approx \mathcal{O}\left(J_3\right), \ldots, \mathcal{O}\left(J_7\right)$. Since consideration of only the J_2 zonal harmonic is a good approximation for a RSO's geopotential perturbed Two-Body motion, the osculating Hamiltonian of the geopotential perturbed Two-Body motion takes a more simplified form than Equation (2.22), shown by Equation (4.58) with the Delaunay elements used by Brouwer given by Equation (4.59).

$$\begin{aligned}\mathscr{H}\left(\mathbf{q},\mathbf{p},J_2\right) &= \sum_{i=0}^{N} \mathscr{H}_i\left(\mathbf{q},\mathbf{p}\right)\frac{J_2^i}{i!} + \mathcal{O}\left(J_2^{N+1}\right) \\ &= -\frac{\mu}{2a} - \frac{\mu J_2 R_\oplus^2}{4r^3}\Big[3\cos^2(i) - 1 \\ &\qquad +3\left(1-\cos^2(i)\right)\cos(2\omega+2f)\Big] + \mathcal{O}\left(J_2^2\right)\end{aligned} \tag{4.58}$$

$$\begin{aligned}\mathbf{q} &= [l,\ g,\ h] = [M,\ \omega,\ \Omega] \\ \mathbf{p} &= [L,\ G,\ H] = \left[\sqrt{\mu a},\ L\sqrt{1-e^2},\ G\cos(i)\right]\end{aligned} \tag{4.59}$$

Brouwer's approach used two canonical transformations with generating functions chosen to eliminate mean anomaly and argument of perigee, the "doubly-averaged" Hamiltonian is free of the Delaunay coordinates. The mean or secular, i.e. free

of short-period and long-period effects, Hamiltonian to first-order of J_2 is given by Equation (4.60) in terms of momenta, denoted by double primes, with the equations of motion derived using Equation (2.18). Since the Delaunay momenta are constant for the secular Hamiltonian, the mean coordinates are denoted with an underscore in the mean Hamiltonian to show they are cyclic.

$$\mathscr{H}''\left(\_, \mathbf{p}, J_2\right) = -\frac{\mu^2}{2L''^2} - \frac{\mu^4 J_2^4}{L''^3 G''^3}\left(-\frac{1}{2} + \frac{3}{2}\frac{H''^2}{G''^2}\right) \tag{4.60}$$

Use of the first-order doubly-averaged, double canonical transformations, Hamiltonian for mapping between osculating and mean orbital elements requires only a change in sign [66, 77], which alleviates the need for solution iteration when converting from osculating to mean elements [78, 79]. One can add numerical stability to the transformation between osculating and mean elements by using an orbital element set similar to the equinoctial elements which replaces eccentricity, mean anomaly, and argument of perigee with $q_1 = e\cos(\omega)$, $q_2 = e\sin(\omega)$, and $\lambda = \omega + M$, then reformulate Brouwer's equations [77]. However, this would require additional applications TOV to produce the PDF for Keplerian elements, so the traditional Keplerian element set is kept with Lyddane's modification of Brouwer's theory to the first-order of J_2 utilized to study the effect of the canonical transformations into mean element space from osculating elements.

This research utilizes the first-order of J_2 solution of Lyddane's modification of Brouwer's theory to convert between osculating and mean Keplerian orbital elements, which is given in Appendix B. As was done for the example in Section 4.3.4, if one considers equatorial orbital motion, the PDF of the mean Keplerian orbital elements can be computed through use of TOV with the mapping Jacobian given by Equation (4.61). Using convention, unprimed elements denote osculating, single

primed elements denote long-period elements, and double primed elements denote mean elements.

$$K\left(a'',\ e'',\ M''\right) = \begin{bmatrix} \dfrac{\partial a}{\partial a''} & \dfrac{\partial a}{\partial e''} & \dfrac{\partial a}{\partial M''} \\ \dfrac{\partial e}{\partial a''} & \dfrac{\partial e}{\partial e''} & \dfrac{\partial e}{\partial M''} \\ \dfrac{\partial M}{\partial a''} & \dfrac{\partial M}{\partial e''} & \dfrac{\partial M}{\partial M''} \end{bmatrix} \tag{4.61}$$

Using the first-order of J_2 the transformation procedure given in Appendix B, the partial derivatives required for Equation (4.61) are derived in Appendix C. From the osculating orbital solution of Equation (4.46), one can transform the solution into the mean orbital space as shown by Equation (4.62). The function **O2M**() is taken to represent the mapping from osculating to mean orbital element space with the partial of true anomaly with respect to mean anomaly computed from Equations (4.54), (4.55), or (4.56).

$$p\left(a\text{”},\ e\text{”},\ M\text{”}\right) = p\left(\{a, e, f\} = \mathbf{O2M}\left\{a\text{”}, e\text{”}, M\text{”}\right\}\right) \left|\frac{\partial f}{\partial M}\right| \left|K\left(a\text{”},\ e\text{”},\ M\text{”}\right)\right| \tag{4.62}$$

4.3.5.1 Propagation of Mean Orbital Elements and their Uncertainties

Brouwer's application of canonical transforms to the Delaunay element set resulted in only the coordinates of mean mean anomaly, mean argument of perigee, and mean right ascension of ascending node possessing equations of motion since their conjugate momenta were constant. Since the mean conjugate momenta were found to be constant, their respective composition variables of mean semi-major axis, mean eccentricity, and mean inclination were also constant. The propagation of the mean elements to first-order of J_2 is given by Equation (4.63), $R_\oplus$ is the radius of the

Earth and n_0 is the mean motion corresponding to the osculating semi-major axis.

$$\begin{aligned} M''(t) &= M''(t_0) + n_0 \Delta t \left(1 + \frac{3}{2}\gamma_2' \eta \left(3\cos^2(i) - 1\right)\right) \\ \omega''(t) &= \omega''(t_0) + \frac{3}{2}\gamma_2' \left(5\cos^2(i) - 1\right) n_0 \Delta t \\ \Omega''(t) &= \Omega''(t_0) - \frac{3}{2}\gamma_2' \cos(i) n_0 \Delta t \\ \Delta t = t - t_0 \ , \ \gamma_2' &= \frac{J_2}{2}\left(\frac{R_\oplus}{a}\right)^2 \frac{1}{\eta^4} \ , \ \eta = \sqrt{1-e^2} \end{aligned} \tag{4.63}$$

4.3.6 Equatorial Plane Keplerian Motion Orbit Determination and Tracking Results

Initial illustration of the application of the TOV technique for RSO orbit determination and sequential tracking is demonstrated via planar Two-Body dynamics for a circular low Earth orbit with position and velocity observations and position only observations. The ECEF frame is assumed to be aligned with the ECI frame so that all orientation parameters can be assumed to be zero. Figure 4.27 displays the geometry of the problem with the inertial frame denoted by $(\mathbf{X}, \mathbf{Y})$ and referred to as ECI and the local topocentric measurement frame denoted by $(\mathbf{x}', \mathbf{y}')$.

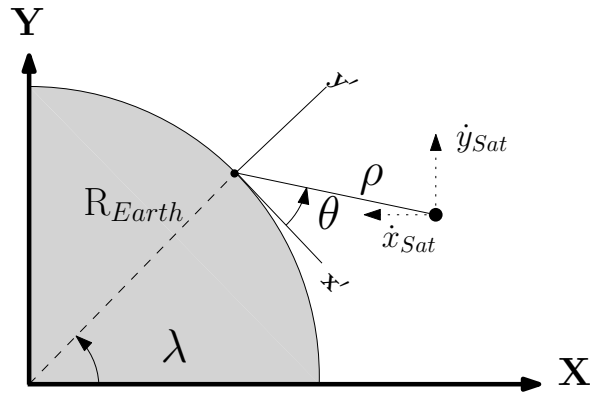

Figure 4.27: Geometry of Planar Space Surveillance Example

The measurements of the true trajectory by the tracking station are corrupted by a zero mean and Gaussian distributed process with standard deviation values representative of typical tracking installations [5]. The standard deviations of the range-rate and elevation angle rate were taken to be ten percent of their respective position standard deviations. Table 4.4 gives the reference values used to simulate the Two-Body orbital motion and the tracking station observations of the motion.

Table 4.4: Simulation Conditions for Space Surveillance Example

Parameter	Value
μ (km^3/sec^2)	3.986004415e5
$R_\oplus$ (km)	6378.1363
Tracking Station Longitude (Deg)	72
Range Noise 1σ (km)	0.030
Range-Rate Noise 1σ (km/sec)	0.003
Elevation Noise 1σ (Deg)	0.015
Elevation-Rate Noise 1σ (Deg/sec)	0.0015
Sampling Time (sec)	20

For TOV domain construction, the range of the measurement domain variables was set to four times their respective standard deviations. For all cases, a sequential Bayes' filter using the TOV approach was compared to a conventional EKF and UKF. For user-initialization, the EKF and UKF were given state covariance matrices of diag[10 10 1 1]^T for the $\left(X, Y, \dot{X}, \dot{Y}\right)$ states respectively. Initialization of state estimates by the user was done by taking the raw measurements and simply transforming them into the state domain. Additionally, the integration routines used by the Kalman filters possessed set time steps of one second. The Cholesky Decomposition of the covariance matrix computed by the TOV Bayes' filter was carried out as a check to ensure that the matrix was positive definite.

4.3.6.1 Equatorial Plane Two-Body Dynamics Full Sensing

To show the TOV technique allows for effective PDF mapping between frames, a test case of only spatial differences between domains is considered, this case repeats a prior one explored by Weisman et al. [36], except with different noise values to reproduce more realistic observation data. The RSO being tracked resides in a circular orbit with the tracking station reporting range, elevation, range-rate, and elevation rate observations every 20 seconds, resulting in eight observations per object pass. The initial conditions for the object were set to $[x, y] = [6.9681, 0]^T$km and $[\dot{x}, \dot{y}] = [0, 7.5633]^T$km/sec, corresponding to a semi-major axis of 1.0925 Earth radii with all other Keplerian orbital element parameters set to zero.

Figure 4.28 displays the position tracking performance for the EKF and UKF with user-tuned initial state estimates and state covariance compared with the TOV computed likelihood PDF results. The TOV likelihood solution is analogous to assuming a uniform prior PDF in the Bayes' filter and computes the maximum uncertainty bounds at each measurement time. The initial estimates for the EKF and UKF were simply the polar observations transformed into ECI space, the initial covariance was the same for each filter and was tuned by the user to keep the EKF state error within three standard deviations.

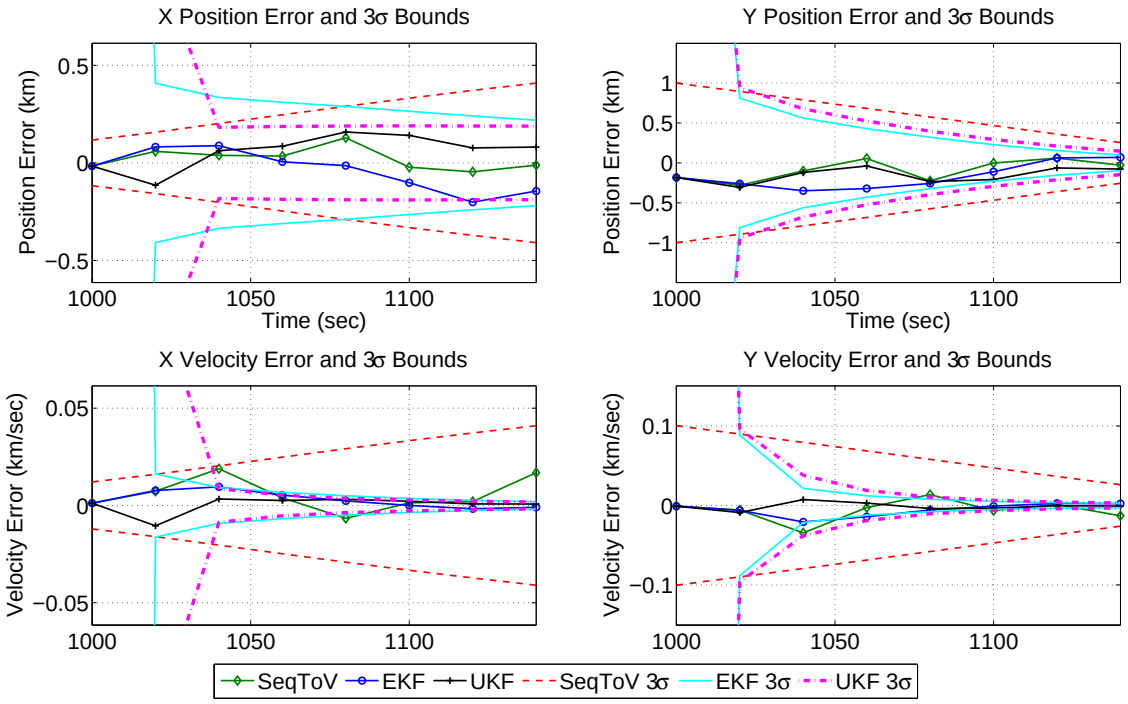

Figure 4.28: Full Observation LEO: Sequential Filters State Tracking Performance

Figure 4.28 shows an increase in uncertainty in the primary ECI direction as the RSO moves through its orbit, which is to be expected due to the value of the cosine function near a local elevation of 90 degrees. The cosine function increases in sensitivity to angle changes as the elevation angle nears 90 degrees, thus becoming more sensitive to angle noise resulting in increasing uncertainty. This same behavior is shown in the secondary ECI direction error plot where the error decreases as the local elevation angle nears 90 degrees due to the sine function being insensitive to angle changes around 90 degrees, but extremely sensitive to angle changes about zero degrees elevation. These results are simply the reverse of those seen for the arcing mass example in Section 4.1, the reason for the reversal is that the RSO is traveling counter-clockwise while the arcing mass was traveling clockwise.

For comparison with the uncertainty bounds computed by the TOV likelihood at every measurement time, a Monte Carlo analysis of the measurement errors was

performed with the numerical covariance, Equation (4.1), computed at every measurement time using 100,000 simulated measurements. Figure 4.29 compares the TOV likelihood state uncertainty and correlation error with the EKF and UKF uncertainty errors.

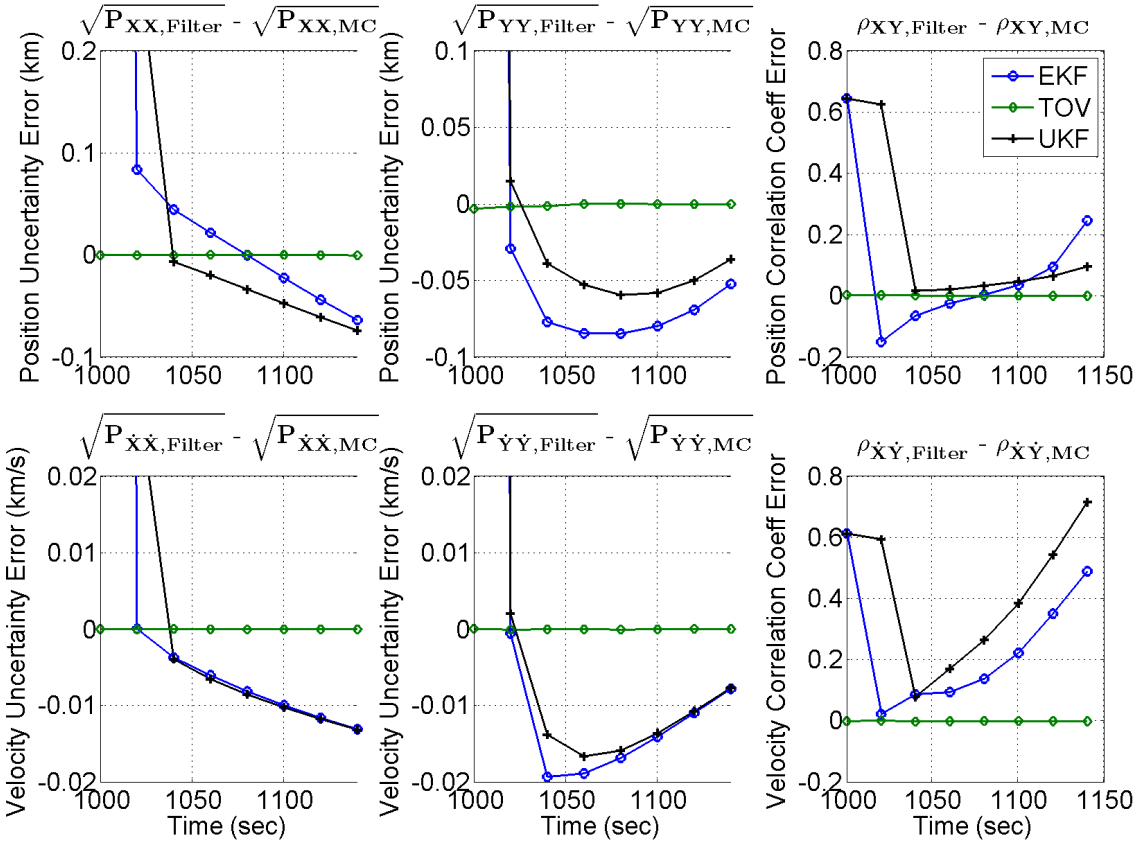

Figure 4.29: Full Observation LEO: Sequential Filters State Uncertainty and Correlation Tracking Error

The numerical mean was compared with the true solution and the error was found to be on the order of decimeters for position and centimeters per second for velocity, so no significant bias was inserted into the numerical covariance computation. The numerical covariance was held to be the truth with respect to state error uncertainty as well as state correlation. The other correlation coefficient errors of the TOV

likelihood are similar to those in Figure 4.29, where the Monte Carlo correlation is tracked well while the EKF and UKF overestimate the correlations. The behavior of the EKF and UKF is to be expected because they utilize previous data via the covariance and the Kalman gain seeks to minimize the trace of the covariance at each update time. A comparison of the TOV Bayes' filter incorporating different amounts of prior information, zero to two previous measurements measurements, to the EKF and UKF was performed and is shown by Figure 4.30.

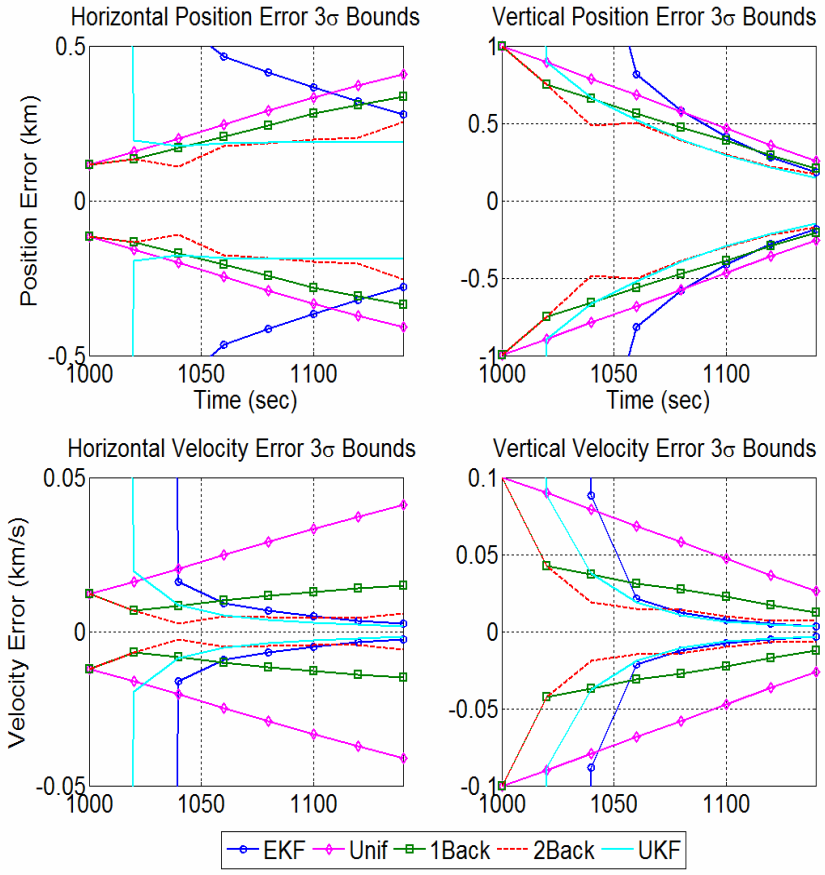

Figure 4.30: Full Observation LEO: Bayes' Filter Uncertainty Bounds Using Prior Data

Figure 4.30 illustrates how incorporation of previous data affects the uncertainty bounds generated by the TOV Bayes' filter. As the amount of previous information

is increased for computation of the prior, Equation (3.56), the uncertainty bounds for the Bayes' filter begin to mimic those produced by the UKF and EKF, which should be expected since the state estimates of the UKF and EKF are conditioned on all previous measurements. Figure 4.31 shows how the incorporation of previous measurement data into the prior PDF allows for the state estimate error of the Bayes' filter to diminish.

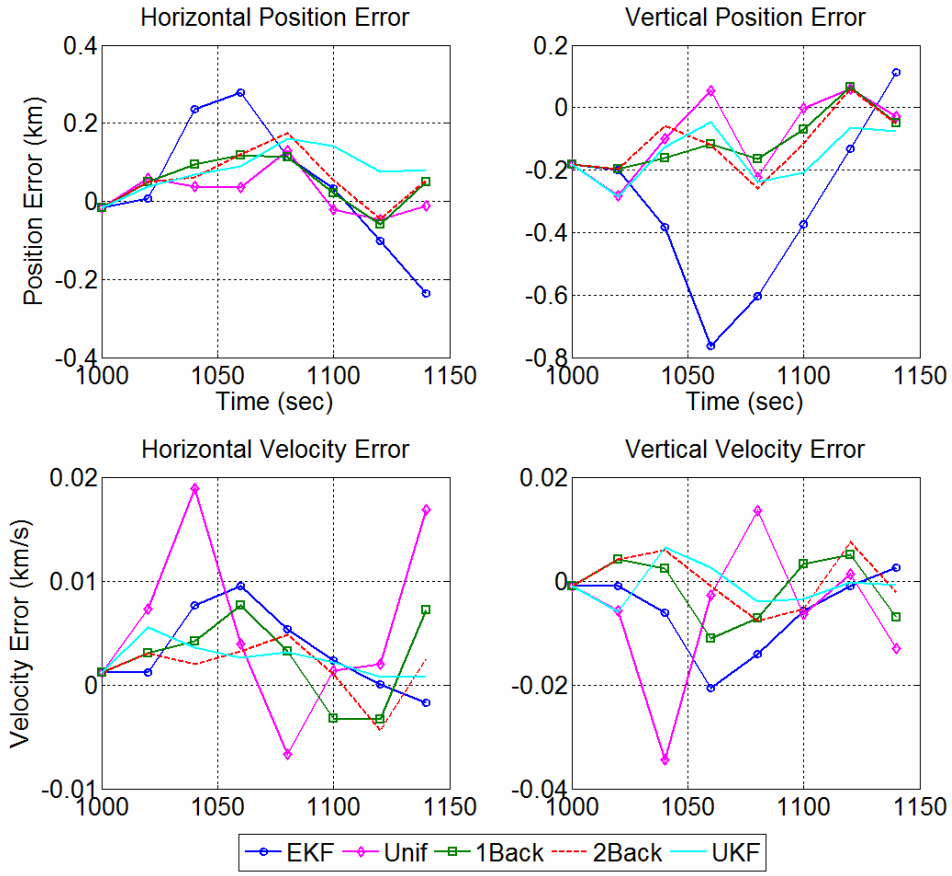

Figure 4.31: Full Observation LEO: Bayes' Filter State Error Using Prior Data

Since application of TOV for generation of the likelihood PDF allows for the accurate tracking of the Monte Carlo solution, the EKF and UKF were initialized with the output of the TOV approach which provided not only initial state uncertainty but also state correlation information. Figure 4.32 compares the state error results

of the user-tuned conventional filters with automated initialization of the filters by the TOV approach and shows that the automation process allows for the EKF state error to be significantly reduced while the UKF operation is slightly improved.

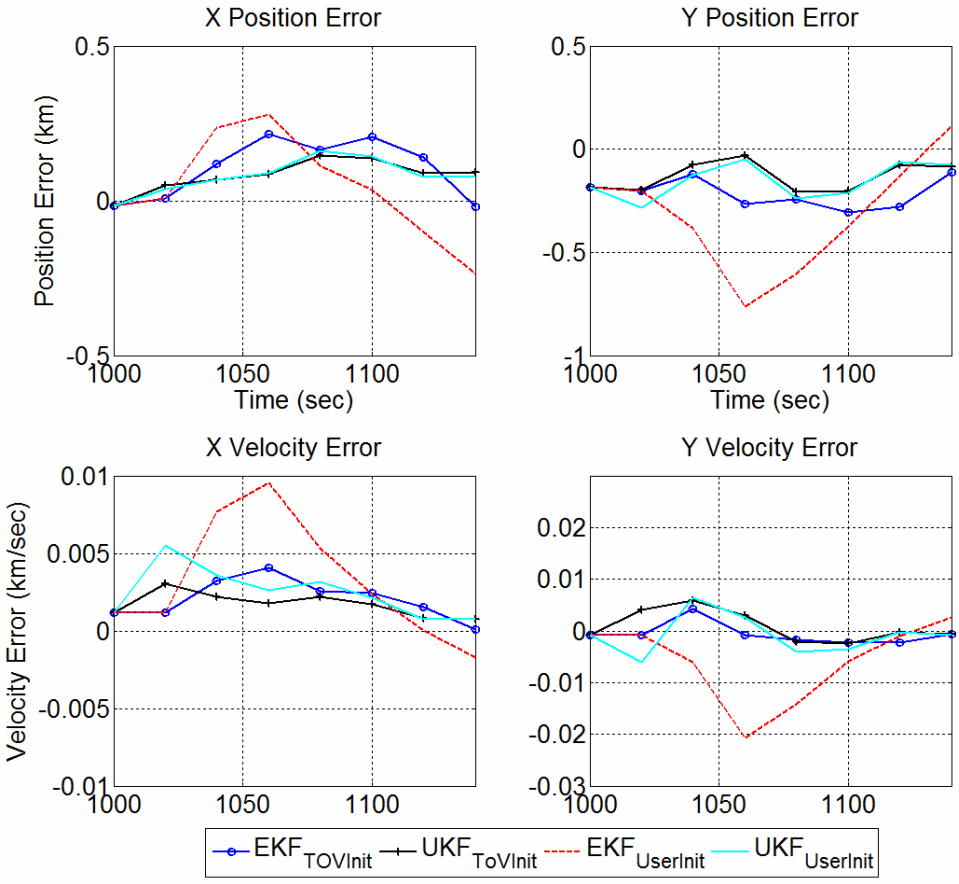

Figure 4.32: Full Observation LEO: User vs. Automated Conventional Filter State Errors

4.3.6.2 Equatorial Plane Two-Body Dynamics Reduced Sensing

Performance assessment of TOV for uncertainty estimation of the Herrick-Gibbs IOD routine was conducted using range and elevation angle measurements of the previous example's circular equatorial orbit. After initialization of a full state estimate, the Herrick-Gibbs solution was utilized to estimate smoothed velocity states via a moving window of three sequential range and angle measurements transformed to

ECI frame. The F and G series solutions were used as to map between the bookend position measurements and the position and velocity states at the second measurement time. In lieu of solving Kepler's equation to compute the F and G coefficients, the power series expansion solutions utilizing fundamental invariants [72] were used.

Orbit Initialization and Tracking This example repeats the circular orbit with full sensing example but, using only position measurements. A Monte Carlo analysis of the Herrick-Gibbs IOD algorithm was performed to numerically compute the covariance for assessment of state uncertainty and correlation at the second measurement time utilizing position only measurements. For the Monte Carlo solution, 100,000 simulated measurements at each observation time were produced from the true trajectory corrupted by sensor noise for each of the measurements then Herrick-Gibbs was applied. The Monte Carlo numerical mean and covariance solutions, Equation (4.1), were used as the true solutions and utilized to assess the error of the state estimates, uncertainty estimates, and correlation estimates computed by the EKF, UKF and TOV Bayes' filter.

Figures 4.33 and 4.34 compare the marginalized joint state PDF results of the Monte Carlo analysis and TOV for initialization of the RSO track. For plotting of the Monte Carlo results, a 50 x 50 bin histogram was applied to the numerical results of the analysis to provide the marginalized joint PDF plots. This is appropriate because PDFs are measures of the frequency of occurrences of particular events. To be completely comparable to the TOV marginal joint PDF results, a 14 x 14 bin histogram(15 x 15 grid points) analysis was performed on the Monte Carlo data. This produced the same results as the higher resolution analysis, namely the TOV marginal joint PDF shows a positive bias in the ECI X direction of the ECI X-Y and ECI $\dot{X}$-X PDFs.

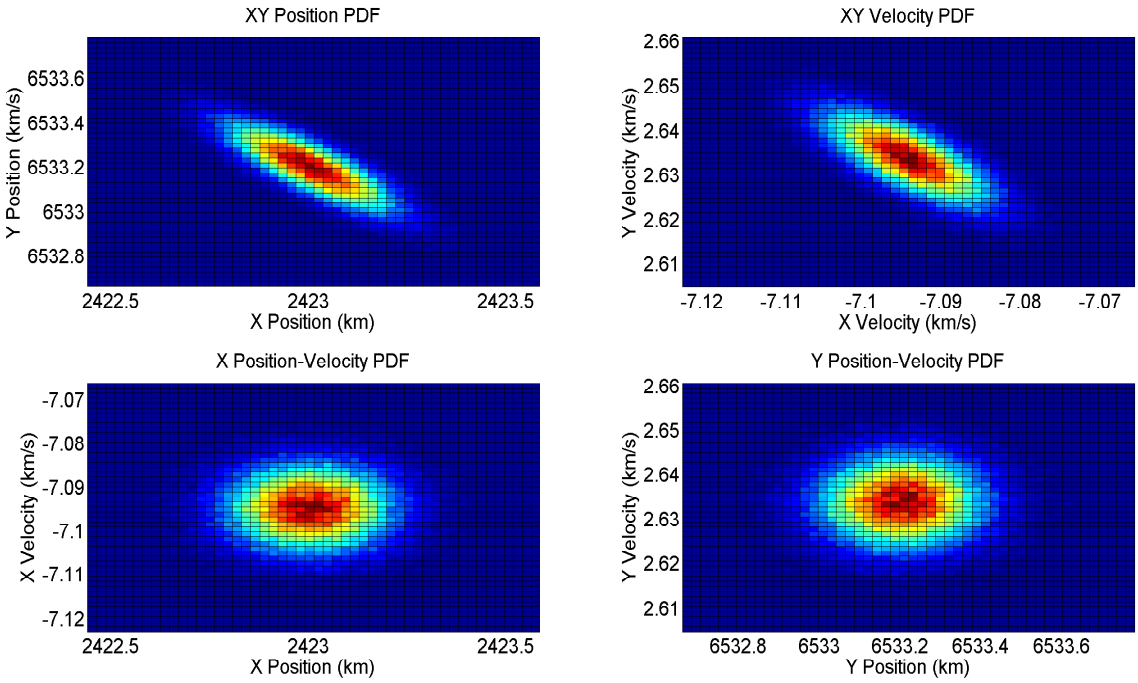

Figure 4.33: ECI State Joint PDFs from Monte Carlo Analysis using Herrick-Gibbs Routine for ECI velocity estimation

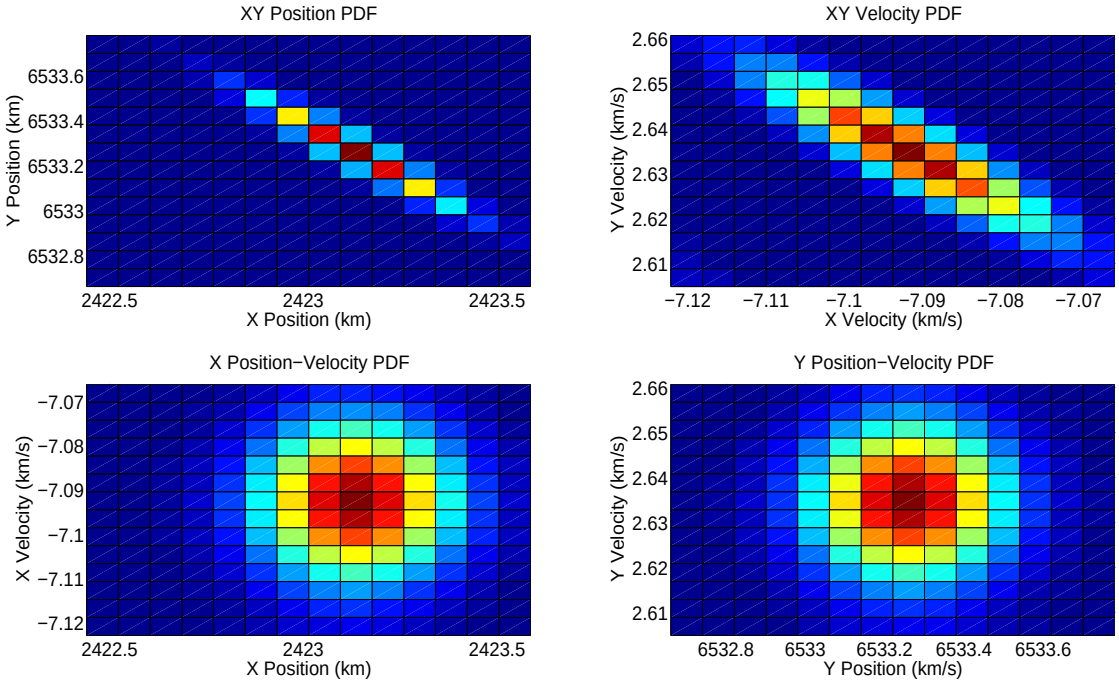

Figure 4.34: ECI State Joint PDFs from TOV using Herrick-Gibbs Routine for ECI Velocity Estimation

The TOV technique was applied to compute the likelihood PDF results of the Herrick-Gibbs IOD algorithm and compared with an EKF and UKF using user-tuned initial estimates and covariance with the results shown in Figure 4.35. For performance of the EKF, the integration timestep was set to one second to allow convergence from user-tuned initialization. Comparison of Figures 4.35 and 4.28 show a different behavior in the velocity error bounds. This behavior difference is due to the Herrick-Gibbs smoothing process used to compute the velocity estimate domain as well as the F and G power series solution used in the application of TOV to map the measurement PDF to the desired state domain. The TOV likelihood solution was used to automate initialization of the EKF and UKF for the tracking interval. Figure 4.36 plots the error performance of the user and TOV tuned filters and Figure 4.37 plots the state error and covariance bound histories.

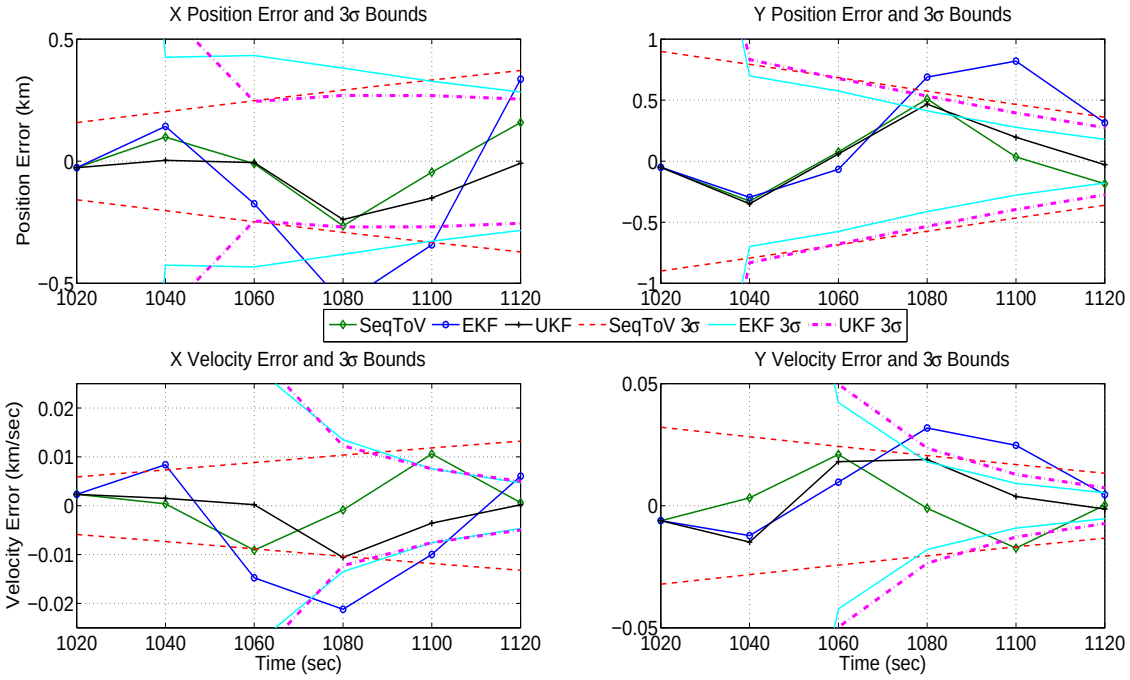

Figure 4.35: Reduced Observation LEO: Sequential Filter State Tracking Performance

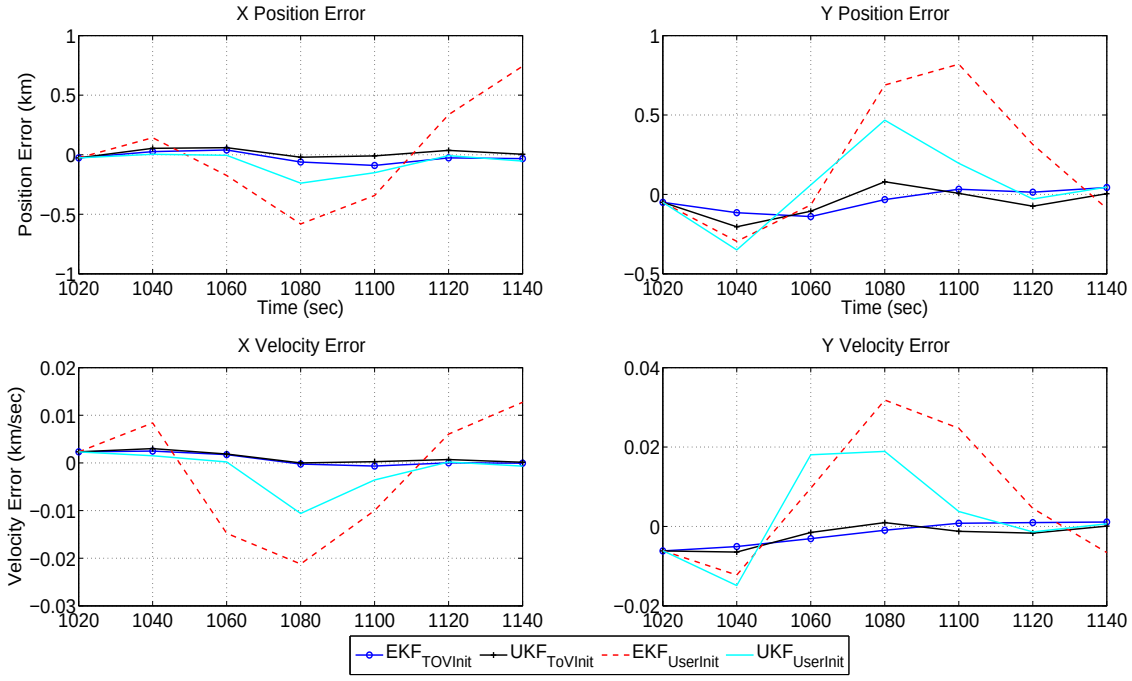

Figure 4.36: Reduced Observation LEO: Conventional Filter State Errors (User-defined vs. TOV Automated)

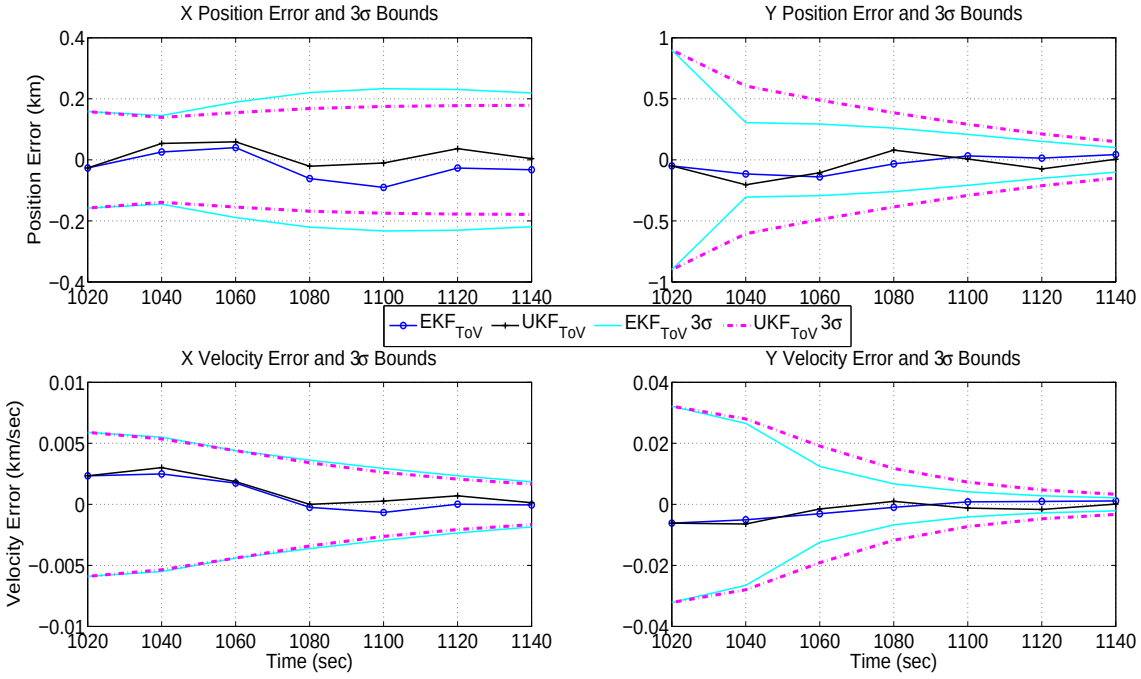

Figure 4.37: Reduced Observation LEO: TOV Tuned Filter Error and Uncertainy Performance

Figures 4.36 and 4.37 demonstrate that the TOV reduced sensing procedure allows for automation of the initial state estimate and, more importantly, covariance. This automation allows for a significant reduction in the amount of state error accrued by the EKF and even helps to provide more consistent operation of the EKF and UKF. The Monte Carlo computed state uncertainty and correlation tracking performance of the TOV likelihood and EKF and UKF using TOV initialization over the simulation time are shown by Figures 4.38 and 4.39. The figures plot the ratio of the error between the filter and Monte Carlo results normalized by the Monte Carlo results. As should be expected, the TOV likelihood solution best agrees with the Monte Carlo uncertainty and correlation solutions because it does not consider any additional data except what was used for the IOD.

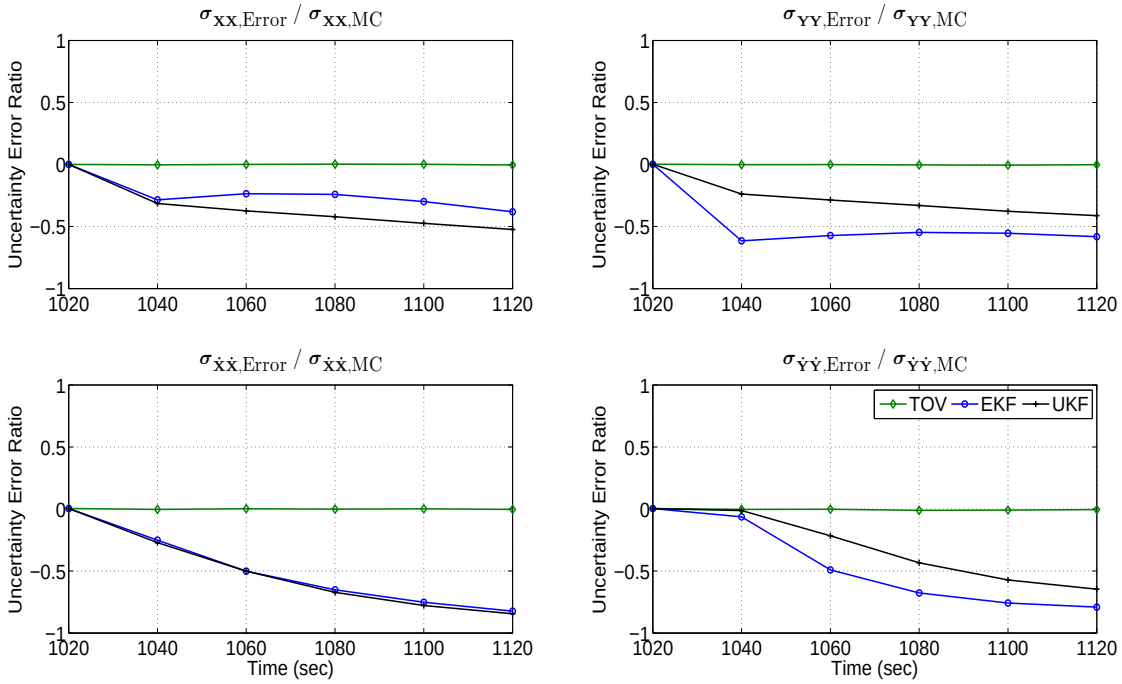

Figure 4.38: Reduced Observation LEO: Sequential Filters State Uncertainty Tracking Error Ratio

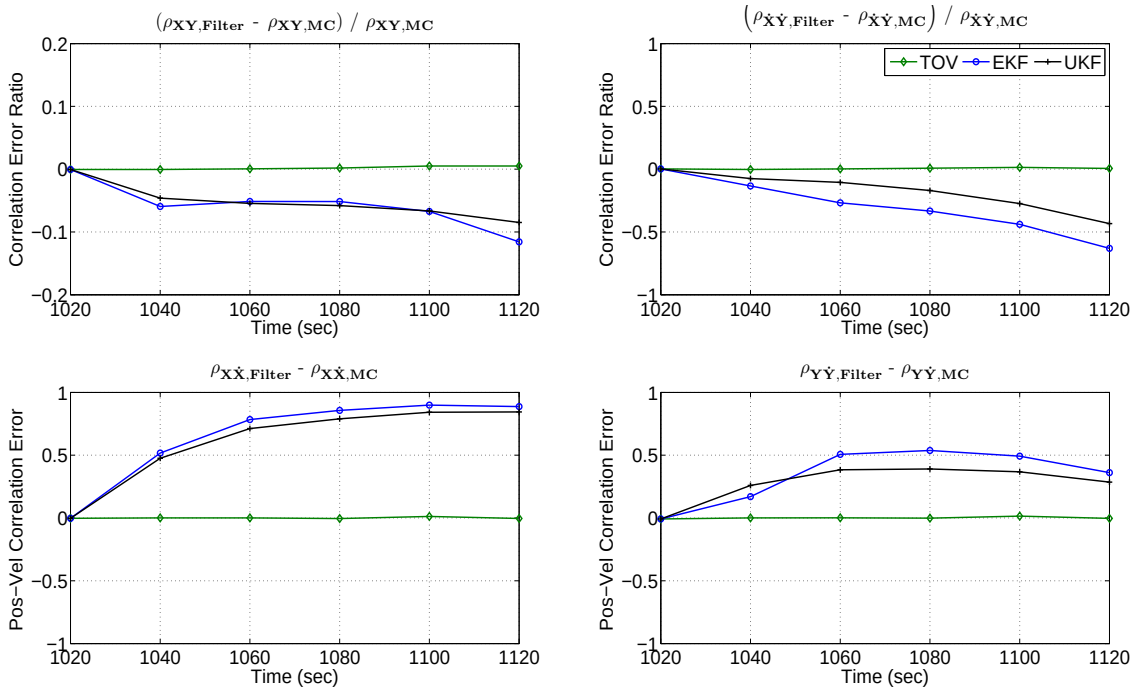

Figure 4.39: Reduced Observation LEO: Sequential Filters State Correlation Tracking Error

Figures 4.40 and 4.41 compare the performance of the TOV Bayes' filter utilizing prior information to the TOV likelihood and the EKF and UKF solutions. The prior density is computed using the approach in Section 4.3.3.1. The maximum amount of previous data considered in the prior PDF computation was set to the five most recent data points not utilized for IOD. Figure 4.40 compares the state tracking results of the TOV Bayes' filter versus the TOV likelihood density and demonstrates that introduction of prior information allows for increased estimation accuracy and reduced state uncertainty. Figure 4.41 reproduces Figure 4.38 but adds the performance of the TOV Bayes' filter. The figures show that as previous data is added for computation of the prior, the uncertainty predictions begin to mimic those of the conventional nonlinear filters, which was also shown by Figure 4.5 for the arcing mass results.

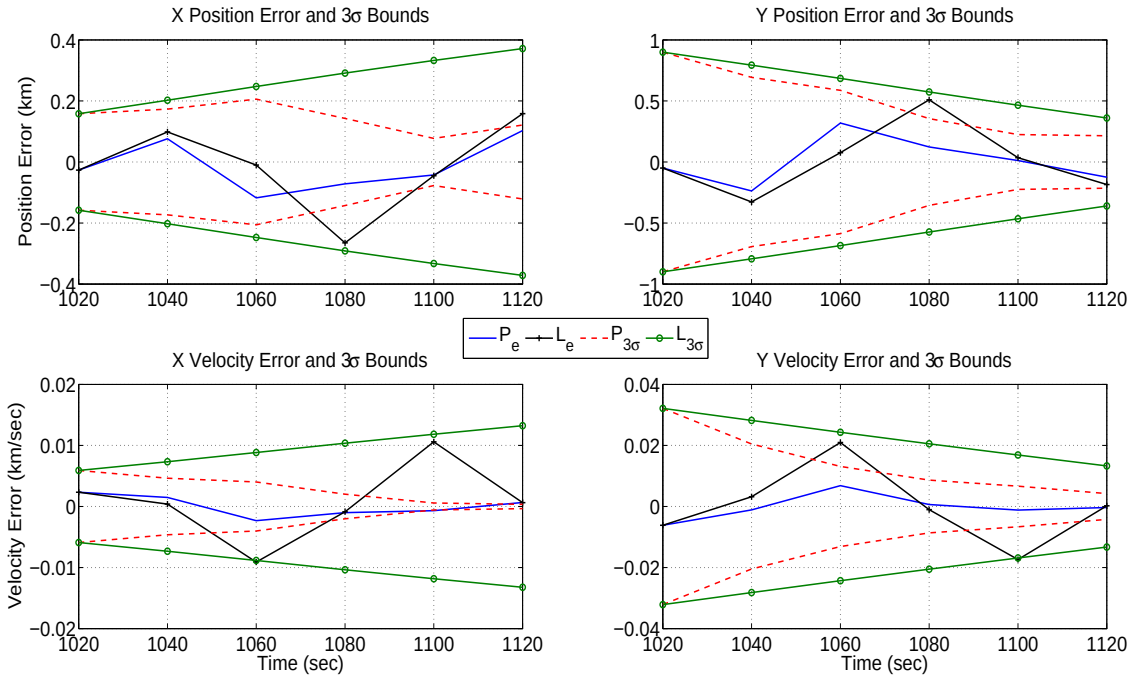

Figure 4.40: Reduced Observation LEO: TOV Bayes' Filter Likelihood vs. Posterior State Error and Uncertainty Comparison

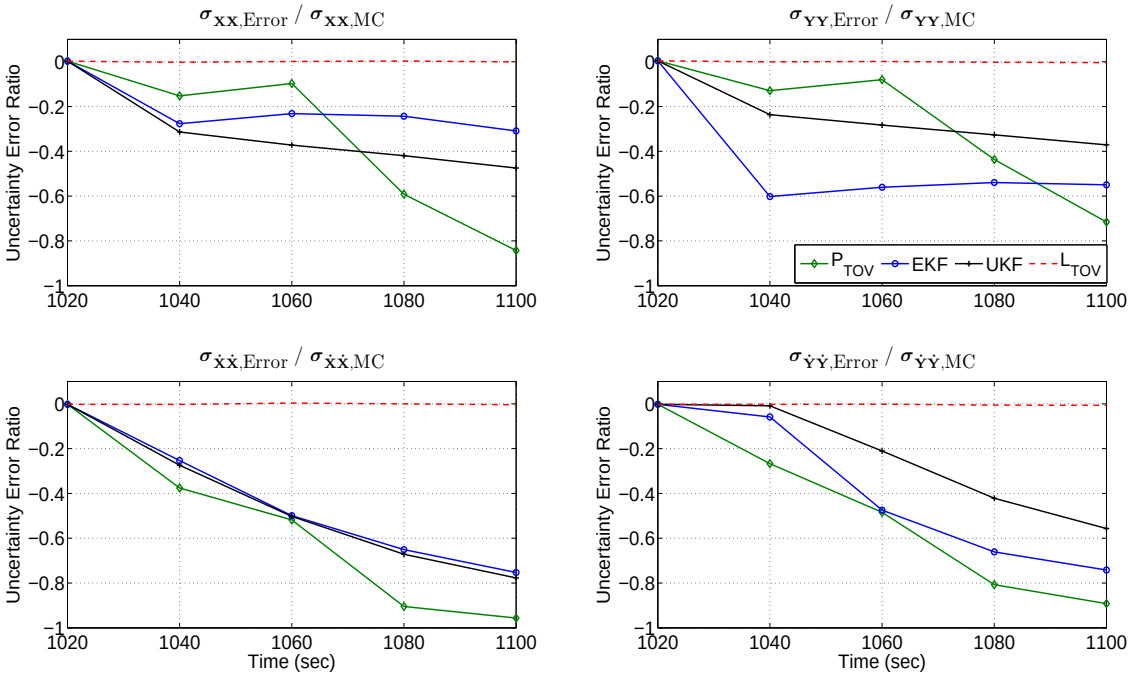

Figure 4.41: Reduced Observation LEO: Posterior TOV Bayes' Filter and Conventional Sequential Filters State Uncertainty Tracking Error Ratio

4.3.7 Equatorial Plane Geopotential Perturbed Motion Orbit Determination and Tracking Results

The results of applying TOV for estimation of Cartesian, osculating orbital element, and first-order mean orbital element state vectors with corresponding uncertainties are shown in the following sections for more realistic LEO RSOs. In the fashion of increasing problem complexity, two equatorial orbits with conservative perturbations are considered: (1) equatorial LEO RSO and (2) equatorial HEO RSO that has just passed perigee. The orbits are subjected to the J_2 zonal geopotential perturbation, which is the dominant conservative perturbation for low earth orbits [66].

The LEO RSO's orbital parameters are changed from the previous example to allow for analysis near the limit of the first-order expansion, e.g. eccentricity on the order of J_2, used for computing mean elements from osculating elements. The Monte Carlo state and covariance solution for the geopotential perturbed orbits was computed in the same manner as the unperturbed case using 250,000 measurement trials of the true trajectory, then computing their statistical moments according to the spread of points in the state domain of interest.

The LEO RSO's initial osculating orbital elements were chosen as $(a, e, \Omega, i, \omega, M)$ = (6937.3 km, 0.00145,0 rad ,0 rad ,0 rad ,0 rad) where the semi-major axis and eccentricity are close to that of Hubble Space Telescope and the eccentricity is also representative of the lower limit of LEO eccentricities. The eccentricity is on the same order of J_2, so this case allows for analysis near the limit of the first-order mean element transformation. The HEO RSO's initial orbital elements were chosen as $(a, e, \Omega, i, \omega, M)$ = (23.26$\times$ 10^3km, 0.7, 0 rad, 0 rad, 0 rad, 0 rad) where the semi-major axis and eccentricity are representative of some communications satellites. The

HEO RSO's trajectory was chosen such that its perigee altitude is approximately 600 kilometers and it just passed out of perigee as it entered the tracking station window. The tracking station parameters are the same as those used for the circular unperturbed LEO RSO with only position and angle measurements utilized, so IOD must be carried out.

For the TOV Bayes' filter, the likelihood density is computed by transforming the current measurement space into the state-space of interest and the prior density is computed by transforming the current state-space of interest to a previous measurement time. The prior and likelihood densities for the Cartesian domain due to the Herrick-Gibbs IOD algorithm were derived in Section 4.3.3 while the results for the osculating and mean element domains were derived in Sections 4.3.4 and 4.3.5 respectively. For computation of the prior PDF, the number of previous data points for the LEO RSO was the same as the circular LEO RSO, five, while the number of previous data points for the HEO RSO was set to three. For the propagation phases of the TOV Bayes' filter, the Cartesian states were propagated using the F and G series solution, the osculating orbital elements were propagated using the linear time update of mean anomaly, and the mean orbital elements were propagated according to the Brouwer theory. As with the previous surveillance results, the Cholesky decomposition of the computed covariance matrix was applied as a check to ensure positive definiteness.

To reduce the domain computation burden, not all combinations of the perturbed measurement domains were mapped into the desired state domains because this would require N^4 points for each state vector for the Cartesian domain. Instead, all possible combinations were evaluated in the measurement domain for each observation time, then permutations with the other observation times were generated by uniformly selecting a measurement combination in each domain. In this man-

ner, only N^2 points are generated for each observation time and from these points N_{Select} are selected to generate the desired state domain. The following results were produced using this sampling technique for permutation generation and were found to coincide with the solutions produced by evaluating all permutations. This permutation sampling technique allowed for the state domain size to be reduced from approximately 2×10^6 to 1×10^4.

For user-tuned initialization of the EKF and UKF, the initial state estimate was computed by direct application of the Herrick-Gibbs IOD algorithm while the Cartesian state covariance was initialized differently depending on the type of orbit. For the LEO RSO, the covariance was initialized on the diagonal with variances of 2 km^2 and 0.5 km^2/sec^2 and off-diagonal elements equal to zero. For the HEO RSO, the covariance was initialized on the diagonal with variances of 5 km^2 and 0.5 km^2/sec^2 and off-diagonal elements equal to zero. For the UKF and EKF propagation phases, the equations were modified to account for the J_2 perturbation.

4.3.7.1 Cartesian State Vector from Herrick-Gibbs Initial Orbit Determination

Figures 4.42 through 4.45 plot the results for the Cartesian estimation of the eccentric LEO RSO, index entries of "L" and "P" represent the TOV likelihood and TOV Bayes' posterior PDF solutions. The LEO geopotential perturbed results are similar to those of the circular LEO RSO since the geopotential perturbation will only present large differences over the period of the orbit, approximately 5700 seconds, not over the period of the tracking window, 100 seconds. Figure 4.46 plots the Cartesian state differences between the perturbed and Keplerian motion, the epoch time is at the second observation time and the final time is with respect to the second to last observation. The figure shows that the J_2 perturbation causes differences on the order of meters, within the Cartesian domain 1σ uncertainty bounds, Figure 4.43.

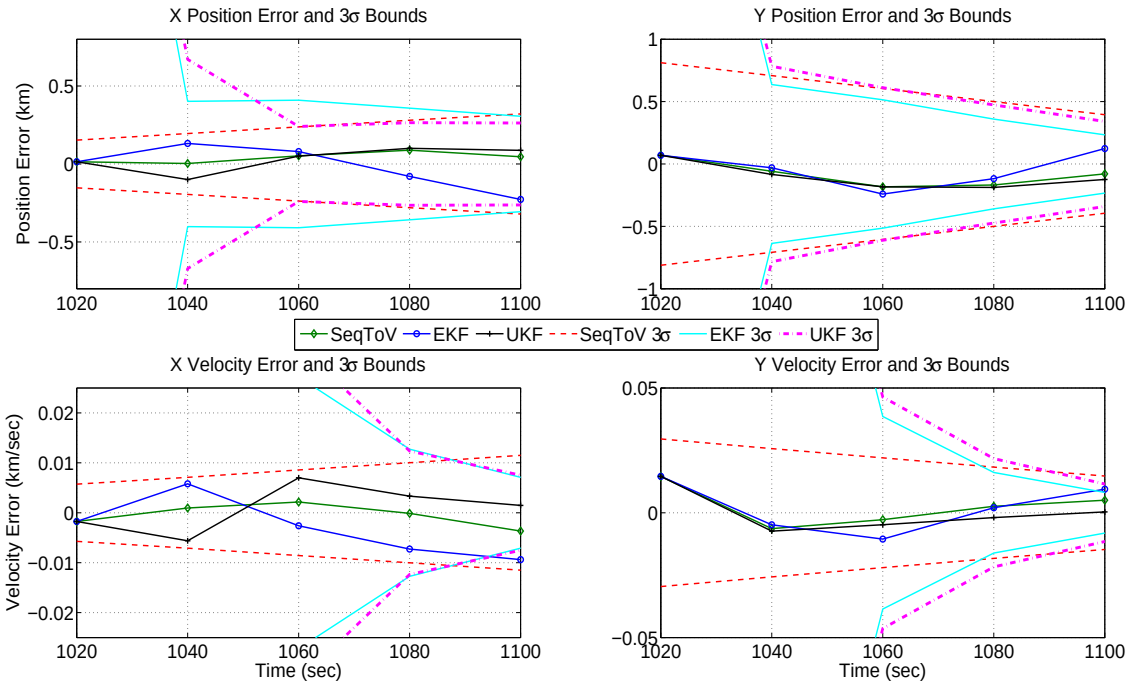

Figure 4.42: LEO RSO TOV Likelihood Cartesian State Error and 3σ Covariance Bounds Results vs. EKF and UKF

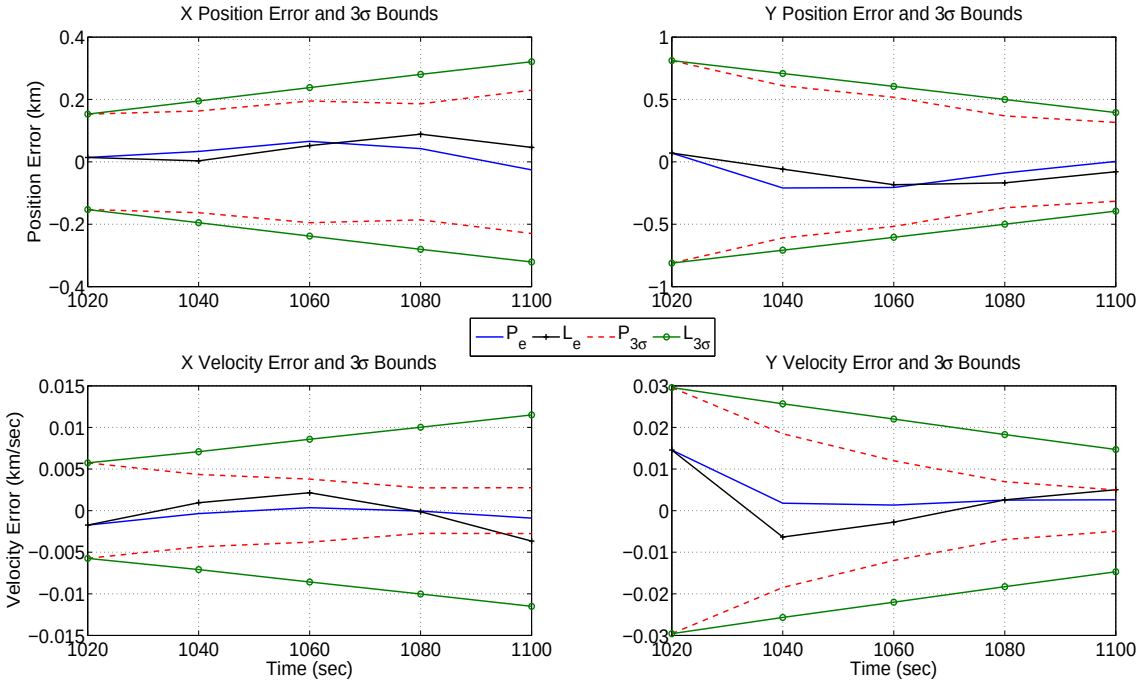

Figure 4.43: LEO RSO TOV Likelihood and Posterior Cartesian State Error and 3σ Covariance Bounds Results

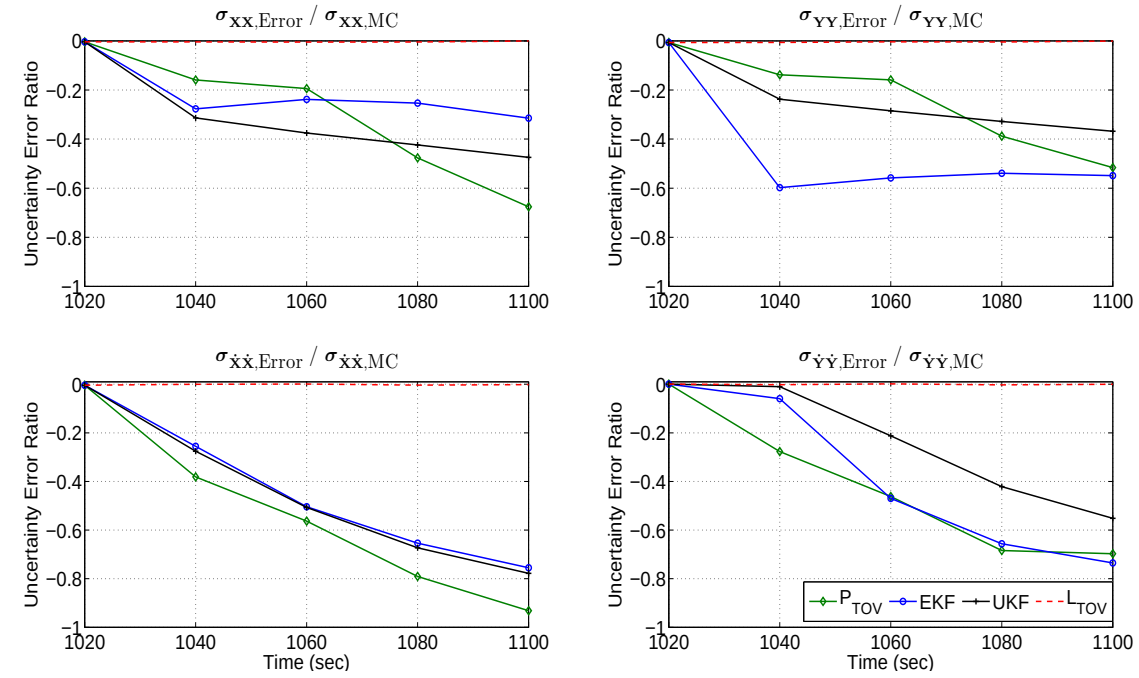

Figure 4.44: LEO RSO TOV Likelihood and Posterior Cartesian State Uncertainty Tracking Results vs. EKF and UKF

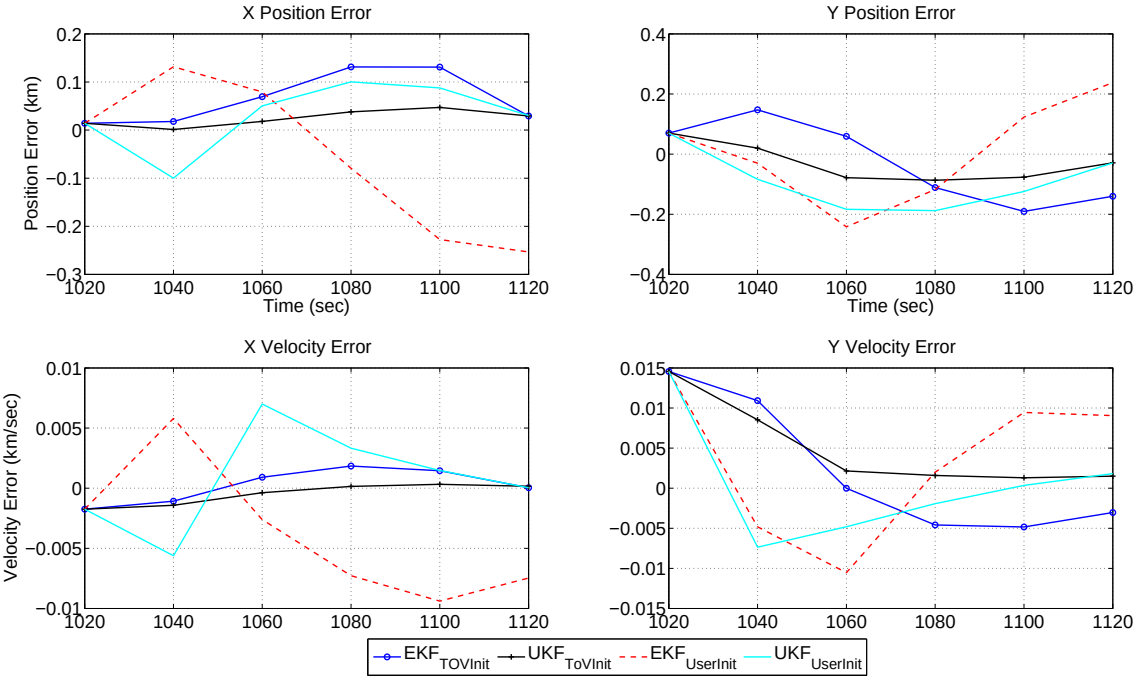

Figure 4.45: LEO RSO TOV Likelihood Cartesian State Error Initialization Results of EKF and UKF vs. User-Tuned

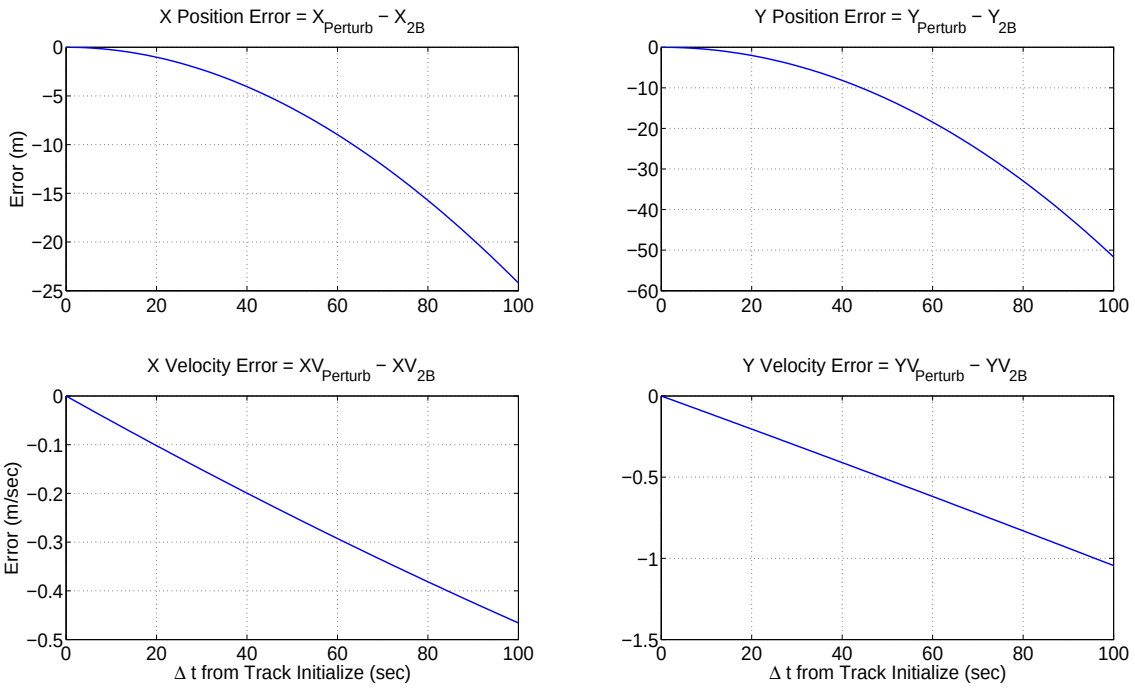

Figure 4.46: LEO RSO Cartesian Element Differences Over Tracking Window from Herrick-Gibbs Initialization

Figure 4.44 demonstrates that the TOV likelihood is able to effectively track the Monte Carlo computed uncertainties. In Figure 4.44, the TOV likelihood PDF solution slightly underestimates the position state solution of the Monte Carlo analysis , approximately 1%, while the behavior of the posterior with respect to the EKF and UKF is less erratic than the circular LEO results. Figure 4.45 shows the merit of using TOV for initialization of the EKF and UKF initial state estimate and covariance where the initialized solutions possessed less fluctuation and higher accuracy compared with user tuning.

Figures 4.47 through 4.50 plot the Cartesian estimation results of the HEO RSO. Figure 4.47 shows the EKF diverging approximately 50 seconds after the track is initialized, while the UKF and TOV Bayes filter results possess a behavior similar to the LEO RSO results. Figures 4.48 and 4.49 show that the initialization of the

EKF and UKF by the TOV Bayes' filter allows for less erratic state error histories as well as the ability to extend the convergence behavior of the EKF.

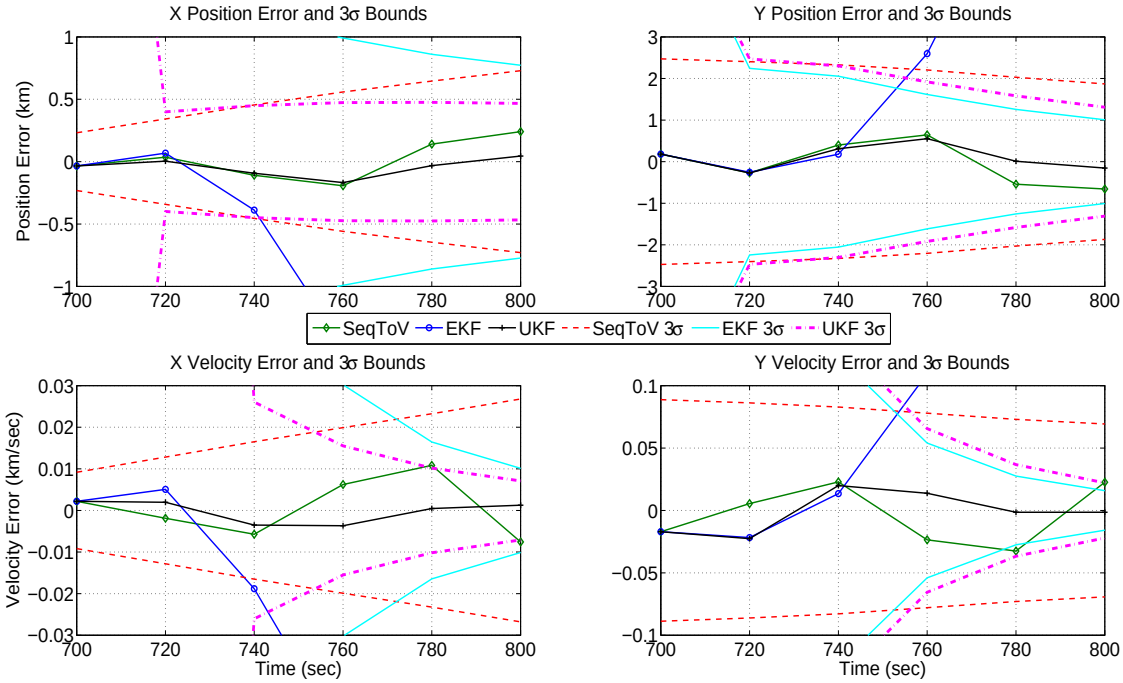

Figure 4.47: HEO RSO TOV Likelihood Cartesian State Error and 3σ Covariance Bounds Results vs. EKF and UKF

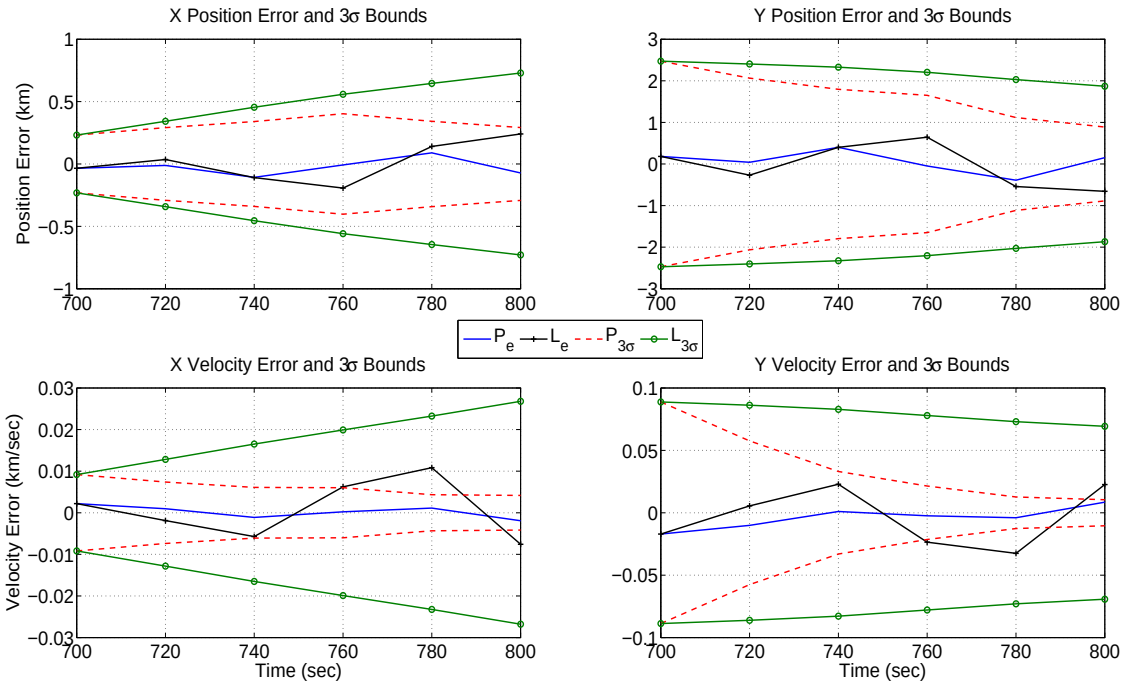

Figure 4.48: HEO RSO TOV Likelihood and Posterior Cartesian State Error and 3σ Covariance Bounds Results

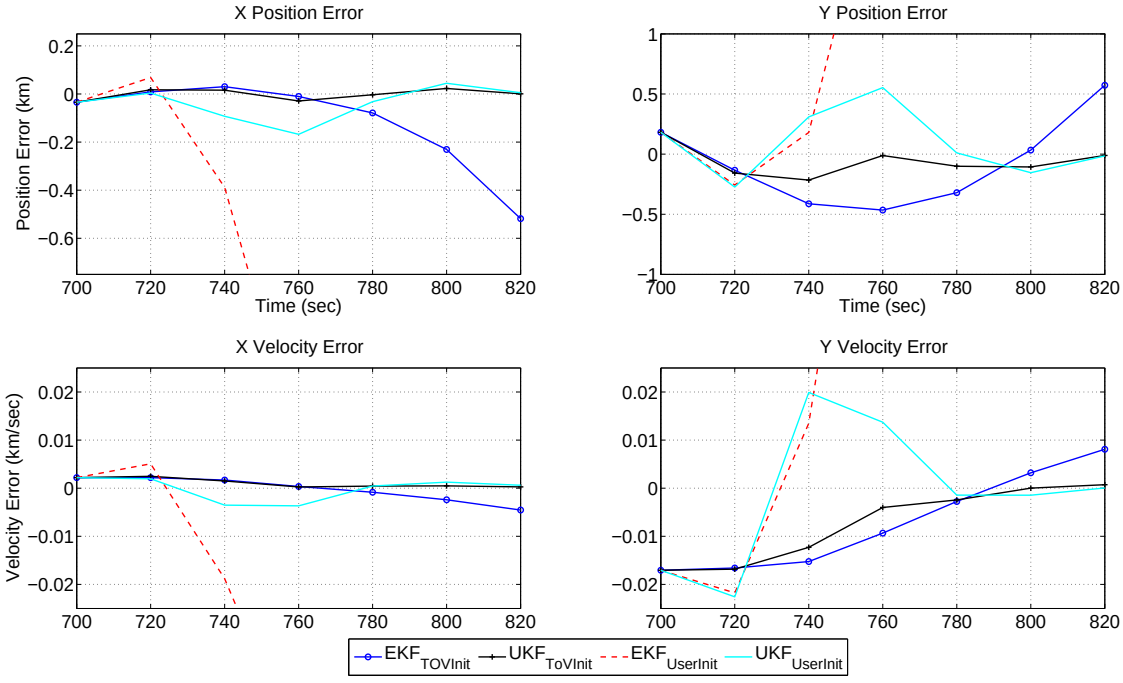

Figure 4.49: HEO RSO TOV Likelihood Cartesian State Error Initialization Results of EKF and UKF vs. User-Tuned

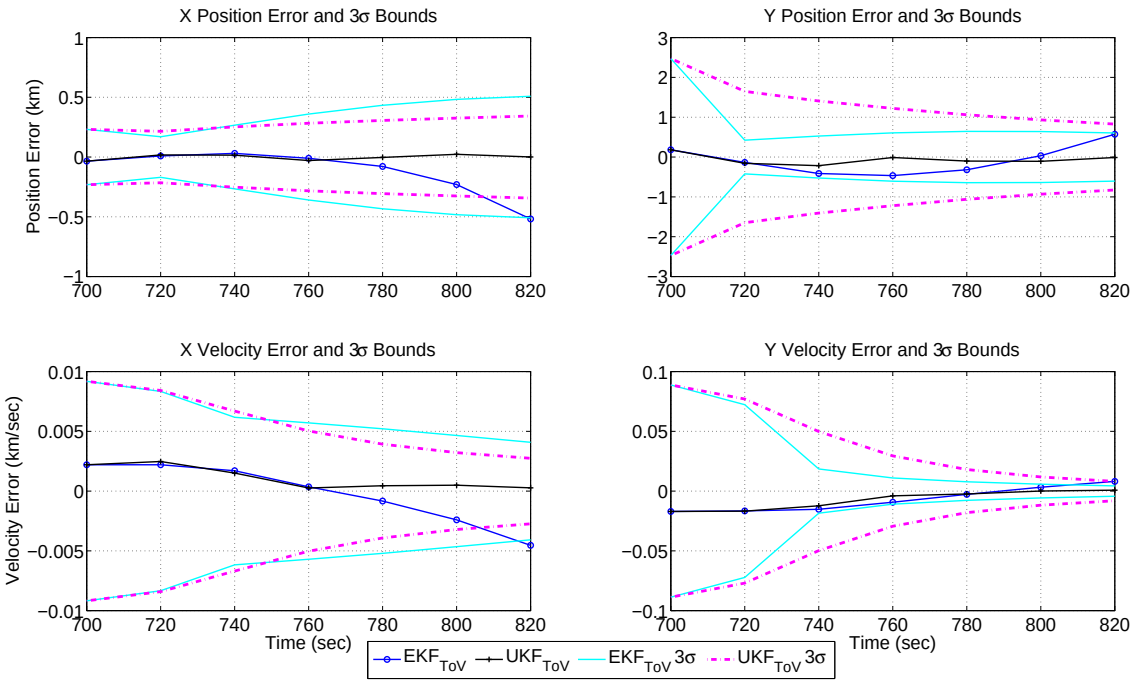

Figure 4.50: HEO RSO TOV Likelihood Cartesian State Error and 3σ Covariance Bounds Results of TOV Initialized EKF and UKF

4.3.7.2 Osculating Orbital Element State Vector from Herrick-Gibbs Initial Orbit Determination Results

Figures 4.51 and 4.52 plot the state error and covariance bounds computed by the TOV Bayes' filter for the osculating orbital elements of the LEO and HEO RSOs respectively. Comparison of the likelihood and posterior PDF results characterize the effectiveness of using prior information for state estimation. For the figures, the semi-major axis and eccentricity results use the set of semi-major axis, eccentricity, and true anomaly, (a, e, f), however the results using mean anomaly are similar. Figure 4.53 compares the posterior result accuracy of the two sets for the LEO RSO, the maximum differences in semi-major axis and eccentricity were approximately 3 kilometers and 6×10^{-4}, the HEO RSO results possessed even less difference.

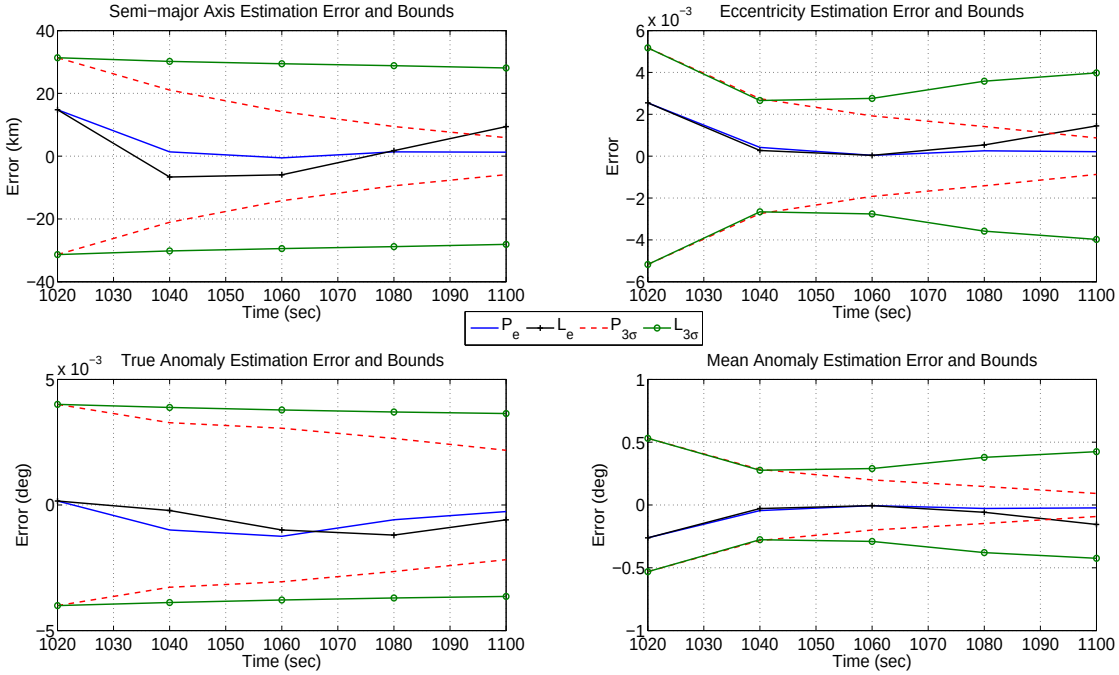

Figure 4.51: LEO RSO TOV Likelihood and Posterior Osculating Orbital State Error and 3σ Covariance Bounds Results

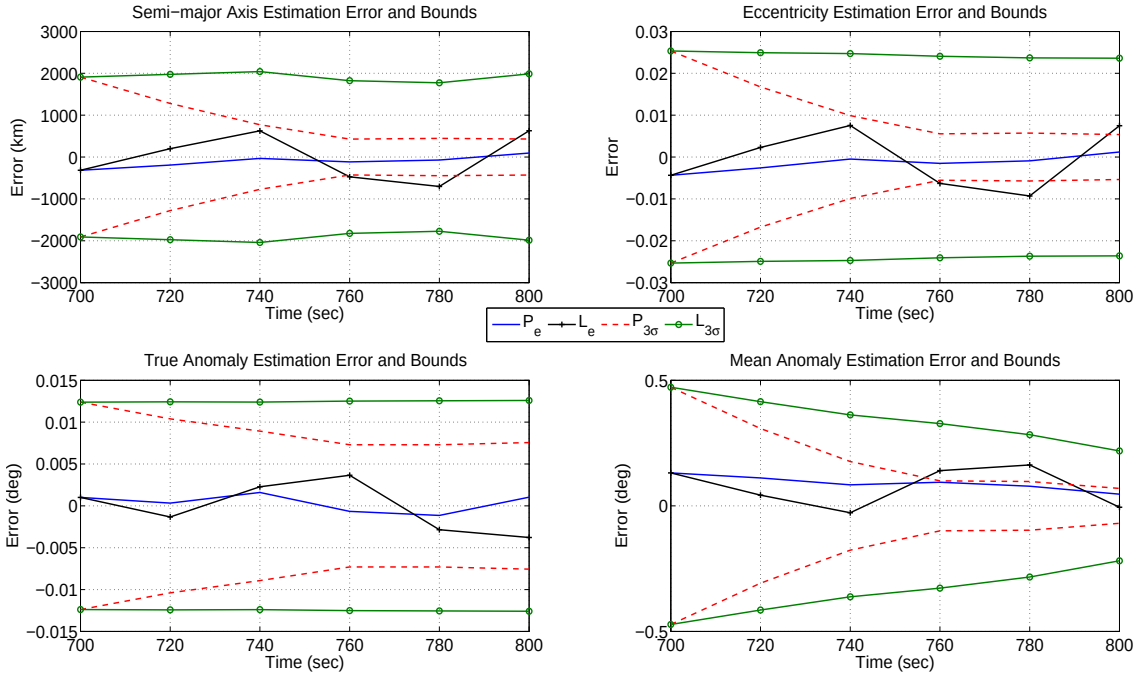

Figure 4.52: HEO RSO TOV Likelihood and Posterior Osculating Orbital State Error and 3σ Covariance Bounds Results

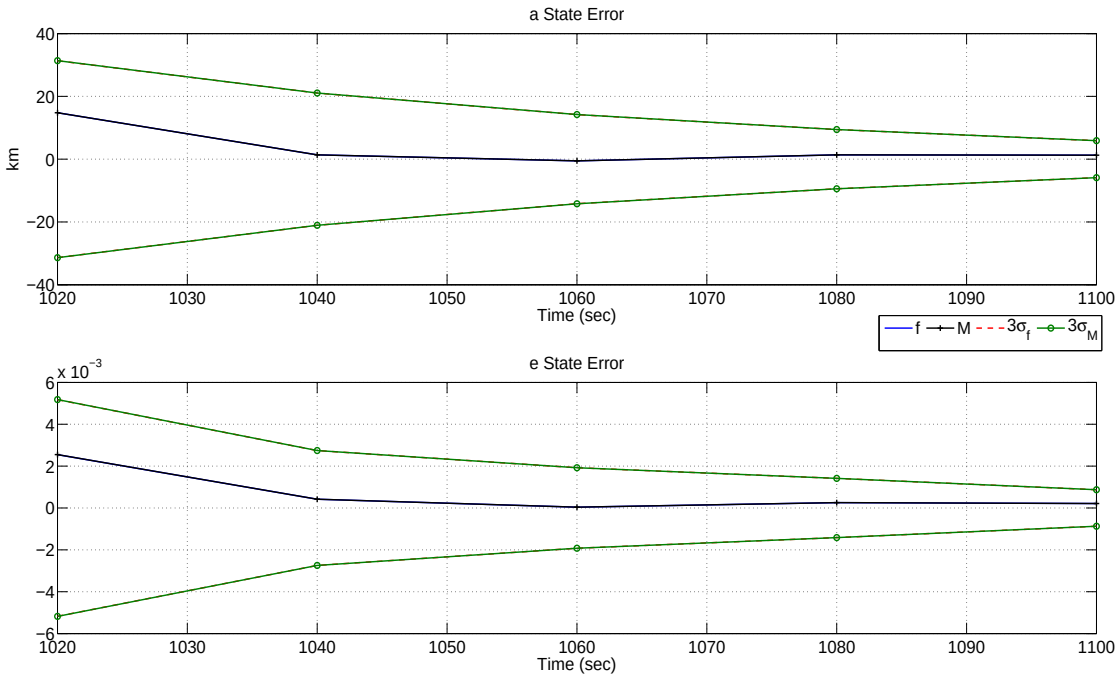

Figure 4.53: LEO RSO TOV Posterior Osculating Orbital Element Error of $(a,\ e,\ f)$ vs $(a,\ e,\ M)$

The scale differences of the orbital element errors and uncertainties stand out when comparing Figures 4.51 and 4.52, especially for the semi-major axis. For the eccentricity state, the LEO RSO possesses error and uncertainty on the order of the actual value of eccentricity, approximately 1.45×10^{-3}, while for the HEO RSO, the error and uncertainty are approximately an order of magnitude less than the actual value, approximately 0.7. For true anomaly, the state error and uncertainty for the LEO RSO are five orders of magnitude less than true, $f \in [62, 70]$deg, while the mean anomaly error is two orders of magnitude less for approximately the same angular range. For the HEO RSO, the true anomaly error and uncertainty are four orders of magnitude less than the truth. An interesting result when comparing the two scenarios is that the mean anomaly likelihoods are of the same of order magnitude while the true anomaly likelihoods differ by an order of magnitude.

Figures 4.54 and 4.55 plot the Marginal PDF contours of osculating state pairings from the likelihood generated by the TOV likelihood PDF and the Monte Carlo analysis at first time the Herrick-Gibbs IOD was able to be applied. The likelihood PDF contours are computed by (1) evaluation of the entire likelihood PDF, (2) marginalizing over the unwanted variable, (3) applying a binned mesh to the resulting domain, then (4) summing all likelihood values that reside within each bin to create a matrix which enabled contour plotting. For the TOV likelihood PDF figures, the top row presents results of the $(a,\ e,\ f)$ state variable set while the bottom row presents the results of the $(a,\ e,\ M)$ state variable set. Figure 4.56 presents the scatter plots of the marginal PDFs which were used to generate the contour plots, red represents a high function value and blue represents a low function value. The scatter plot domain evaluation points were generated from the selected measurement domain points which were then mapped into the osculating orbital element domain.

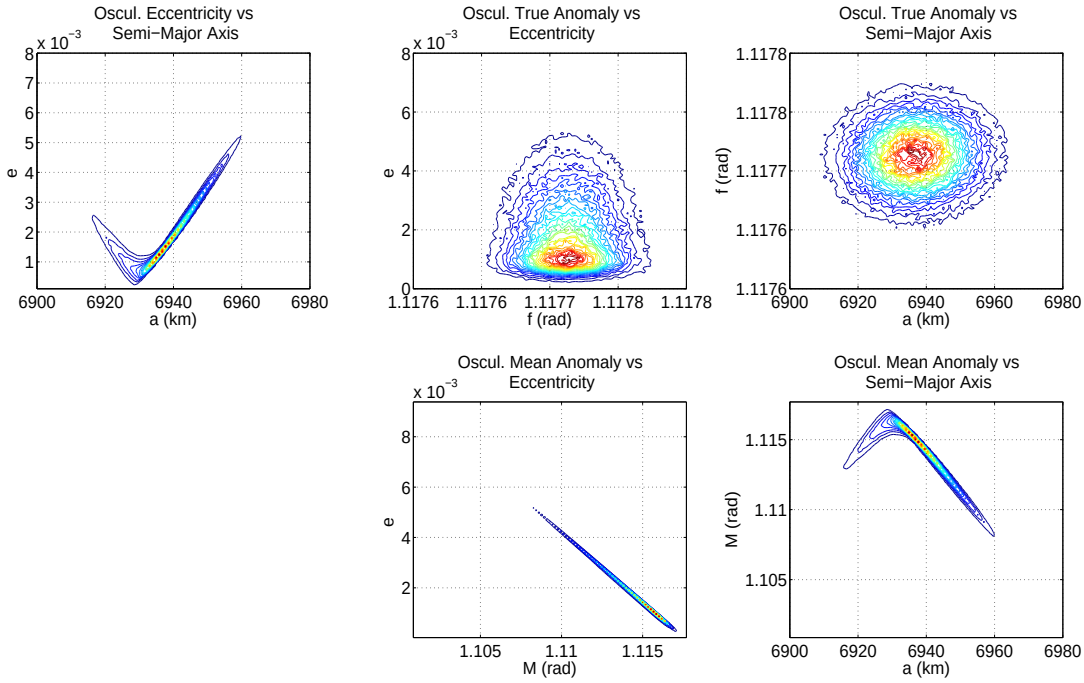

Figure 4.54: LEO RSO Monte Carlo Osculating Orbital Element Marginal PDF Contour Results

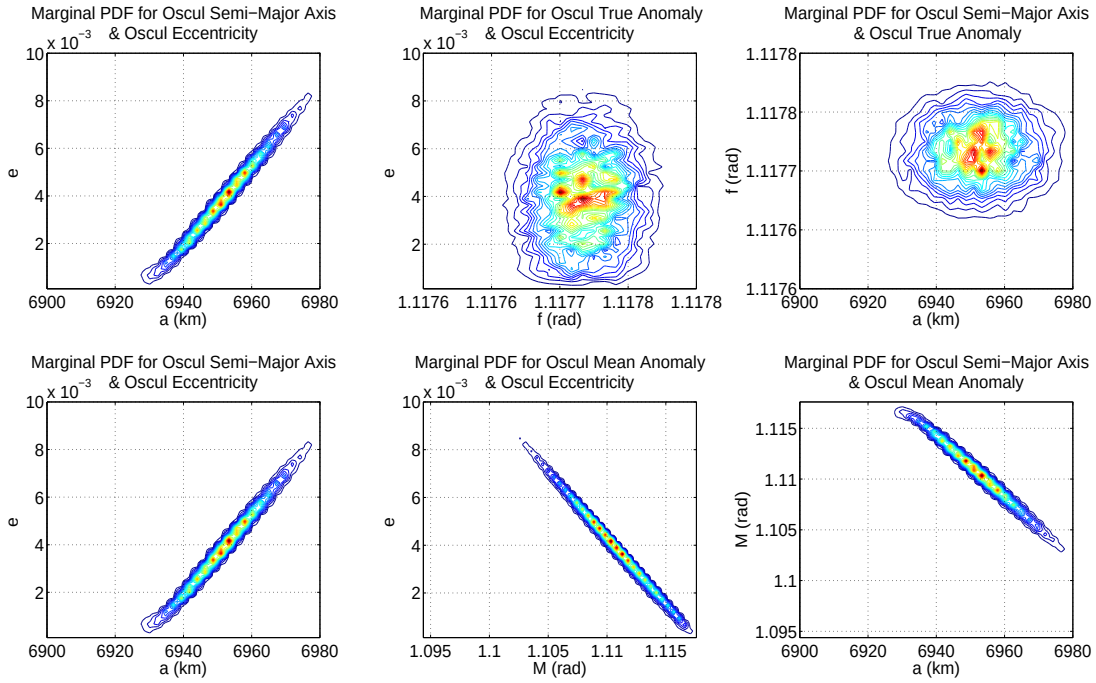

Figure 4.55: LEO RSO TOV Likelihood Osculating Orbital Element Marginal PDF Contour Results

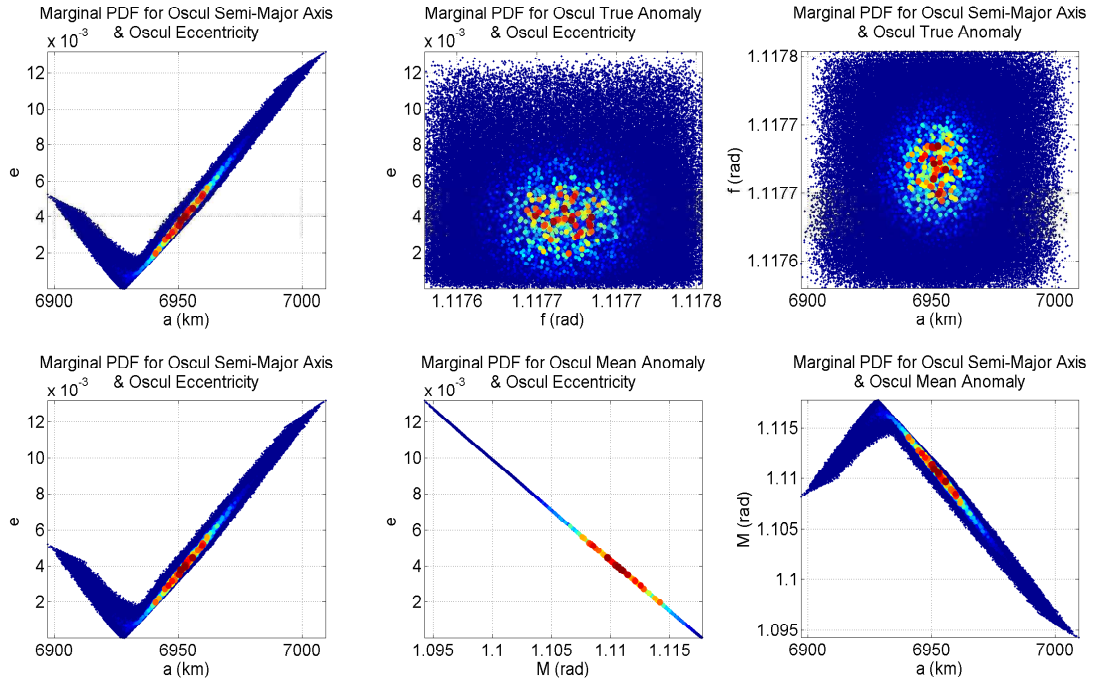

Figure 4.56: LEO RSO TOV Likelihood Osculating Orbital Element Marginal PDF Color-Coded Scatter Results

Comparing Figure 4.54 to Figures 4.55 and 4.56, one sees (1) the marginalized likelihood PDF occupies a larger amount of the two-dimensional domain than the Monte Carlo analysis for the osculating pairs and (2) a bias is apparent in the TOV likelihood PDF whose minimum variance solution is $\hat{\mathbf{s}} = (6952.1km\ ,\ 4.0 \times 10^{-3},$ $1.1177rad,\ \ 1.1106rad)$ while the true solution is a semi-major axis of 6937.3km, eccentricity of 0.0014, and values of 1.1177rad and 1.1152rad for true anomaly and mean anomaly respectively. The check-mark behavior of the (a, e) and (a, M) domains for the TOV analysis was also seen in the histogram analysis of the Monte Carlo results. The behavior is due to the low value of eccentricity considered, which is causing the direction of the eccentricity vector to be not so well-defined. The behavior is not seen in the true anomaly results because true anomaly can be calculated without the use of the eccentricity vector due to the equatorial orbit, which is not true for the mean anomaly.

Figure 4.57 plots the PDF scatter plot for the TOV likelihood for the HEO RSO and shows that a better defined eccentricity vector location produces a more well defined state domain. The marginalized PDF contours for the HEO RSO are shown in Appendix D and show good agreement between the Monte Carlo and TOV likelihood solutions. Figures 4.58 and 4.59 compare the state errors for the TOV likelihood, TOV Bayes' filter, and Monte Carlo analysis for the LEO and HEO RSOs respectively. In Figure 4.58, the first moment of the Monte Carlo analysis for the LEO RSO can no longer be considered a zero mean process since there is a relatively constant bias present in eccentricity and the anomalies. The biases for the HEO RSO were approximately 18 kilometers in semi-major axis and 1×10^{-4} for eccentricity. However, the biased numerical first moment will not bias the second numerical moment computation because of a cancellation of the first moments when computing the second moment.

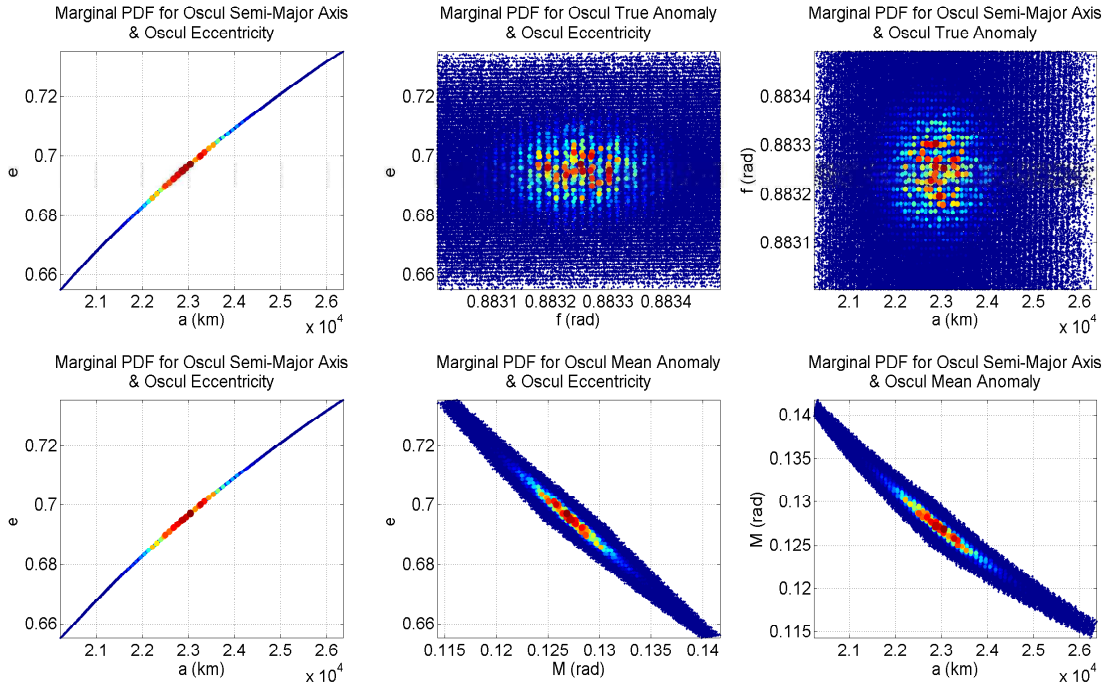

Figure 4.57: HEO RSO TOV Likelihood Osculating Orbital Element Marginal PDF Color-Coded Scatter Results

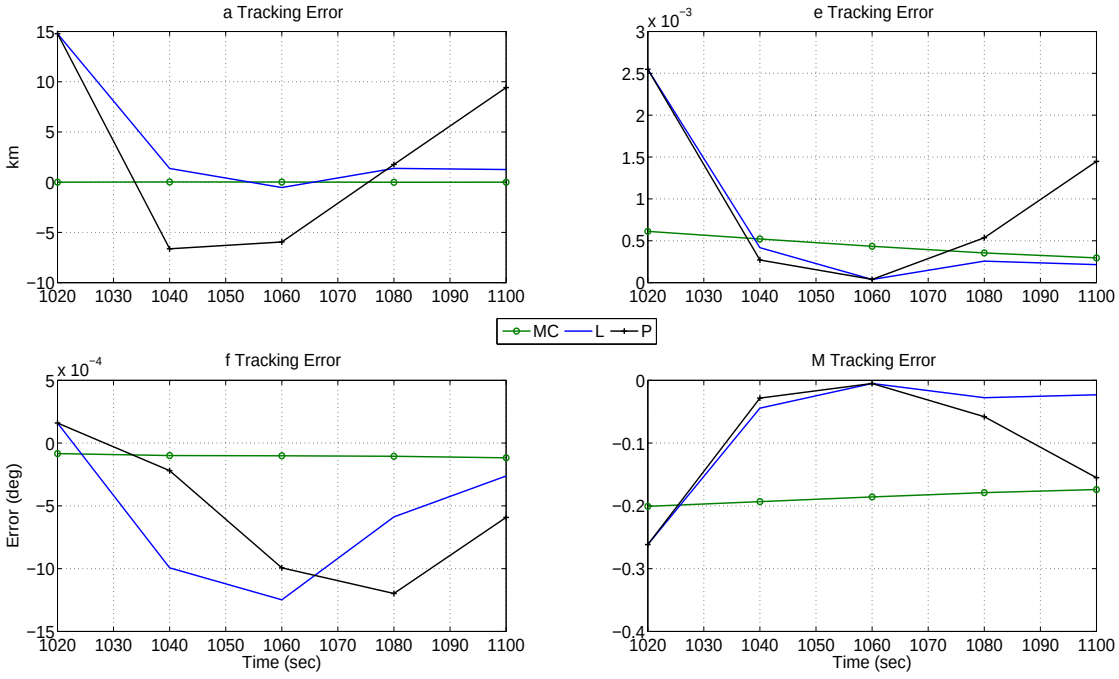

Figure 4.58: LEO RSO Osculating Orbital Element Tracking for TOV Bayes' filter and Monte Carlo vs. True

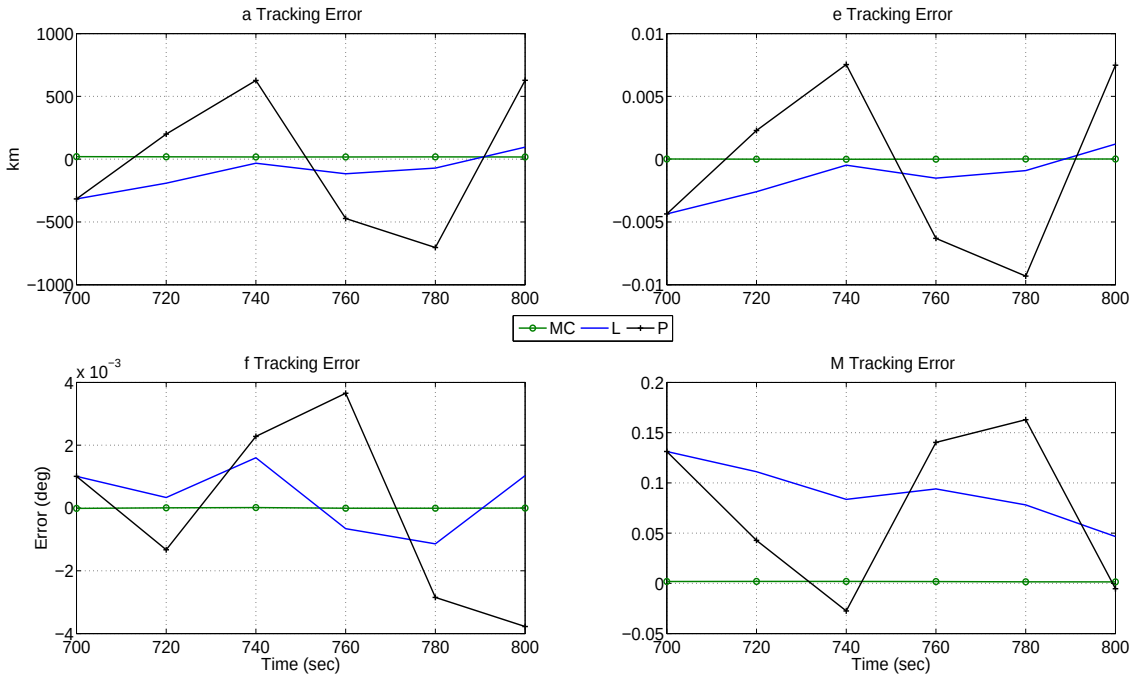

Figure 4.59: HEO RSO Osculating Orbital Element Tracking for TOV Bayes' filter and Monte Carlo vs. True

Figures 4.60 and 4.61 plot the uncertainty tracking comparison between the TOV likelihood and Monte Carlo, the first row corresponds to using the true anomaly as the time coordinate while the second row uses the mean anomaly as the time parameter. For the orbital elements not requiring eccentricity to be computed, semi-major axis and true anomaly for an equatorial orbit with node known, Figure 4.60 shows that the TOV likelihood and Monte Carlo solutions are in good agreement. For the LEO RSO when an eccentricity estimate is required to be computed, both the Monte Carlo and TOV likelihood solutions yield uncertainty answers which are on the same order of magnitude as the true eccentricity value, so one can only make claims as to the order of magnitude of the uncertainty and not the uncertainty value.

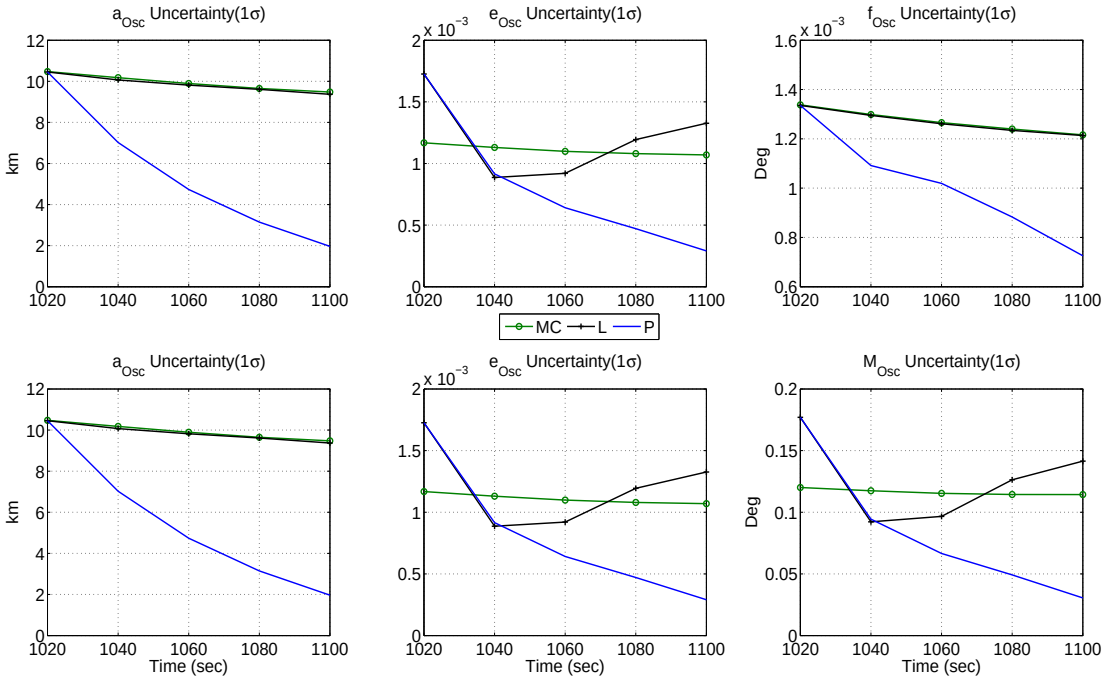

Figure 4.60: LEO RSO Osculating Orbital Element Uncertainty vs. Monte Carlo

The LEO RSO eccentricity Monte Carlo results possess a more well-behaved trend but, the TOV likelihood solution does mimic the same downward trend as the tracking interval proceeds. The effect of the eccentricity uncertainty on the mean anomaly uncertainty is directly apparent when comparing the LEO and HEO RSO results.

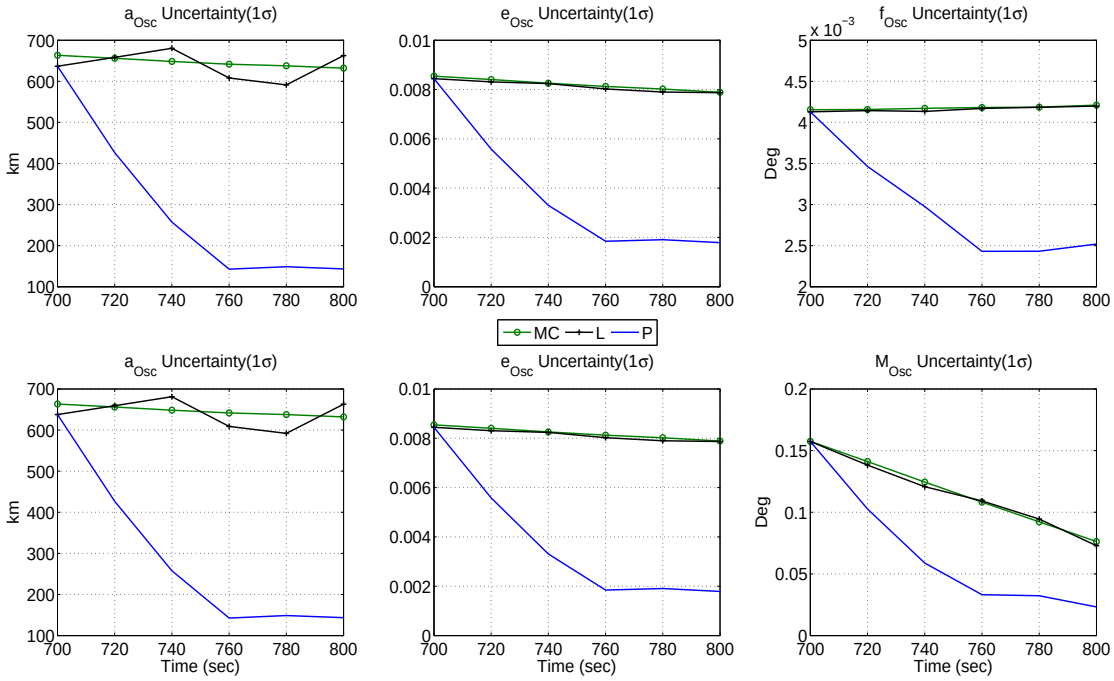

Figure 4.61: HEO RSO Osculating Orbital Element Uncertainty vs. Monte Carlo

4.3.7.3 Mean Orbital Element State Vector from Herrick-Gibbs Initial Orbit Determination Results

Application of the results of Section 4.3.5 allows for a first-order J_2 transformation of the osculating orbital element PDF to the mean element PDF through the use of Lyddane's modification of Brouwer's theory [55], the conversion error between domains will be on the order of J_2 [66] and is shown in Appendix B. Figures 4.62 and 4.63 plot the state error and covariance bounds computed by the TOV Bayes' filter for the mean orbital elements of the LEO and HEO RSOs respectively. For the LEO RSO considered, when the osculating eccentricity is converted to the mean domain the value of the true mean eccentricity is 7.4×10^{-5} while the mean semi-major axis is approximately the same as its osculating counterpart. For the HEO RSO, the mean domain parameters are approximately equal to their osculating domain counterparts.

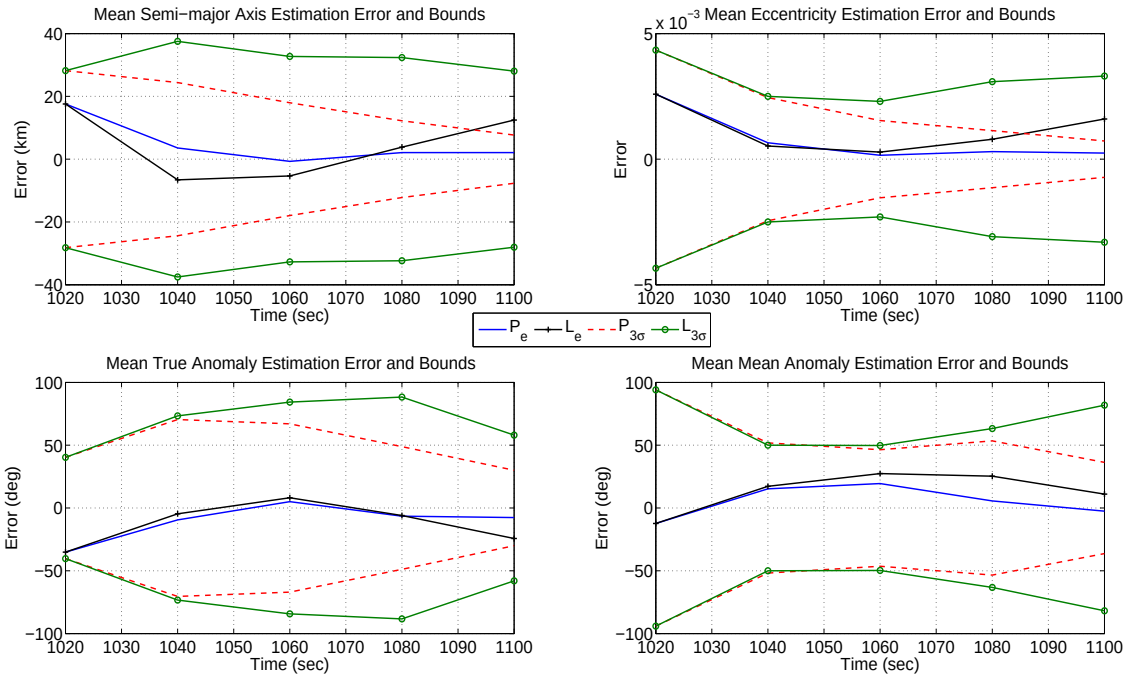

Figure 4.62: LEO RSO TOV Likelihood and Posterior Mean Orbital State Error and 3σ Covariance Bounds Results

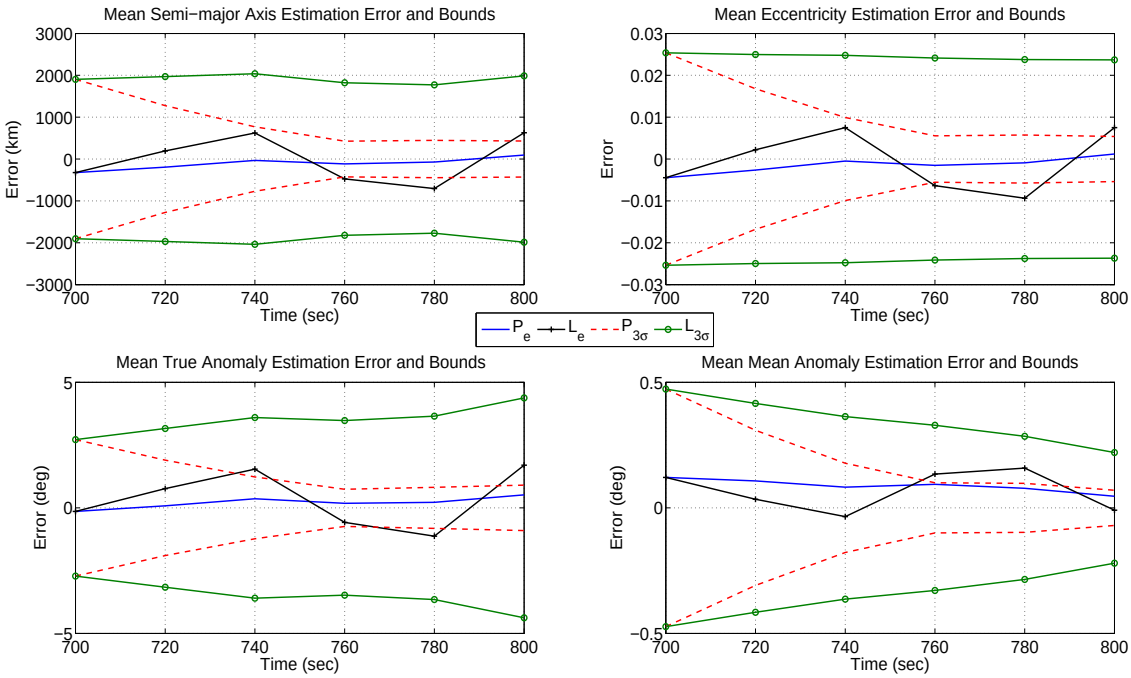

Figure 4.63: HEO RSO TOV Likelihood and Posterior Mean Orbital State Error and 3σ Covariance Bounds Results

The results for the semi-major axis and eccentricity are approximately the same as with their osculating counterparts except that the scale of the results for the anomalies has increased drastically for the LEO RSO. The reason for the anomalies' scale increase for the LEO RSO is due to the uncertainty of the osculating eccentricity being on the order of the true osculating eccentricity, which causes the mean eccentricity uncertainty to be on the same order as the osculating uncertainty. Figure 4.64 plots the mapping of the true osculating eccentricity to mean eccentricity on the interval of e_{Osc}=0.00145$\pm 1 \times 10^{-3}$ with the semi-major axis is set to the true osculating semi-major axis and all other osculating elements are set to zero.

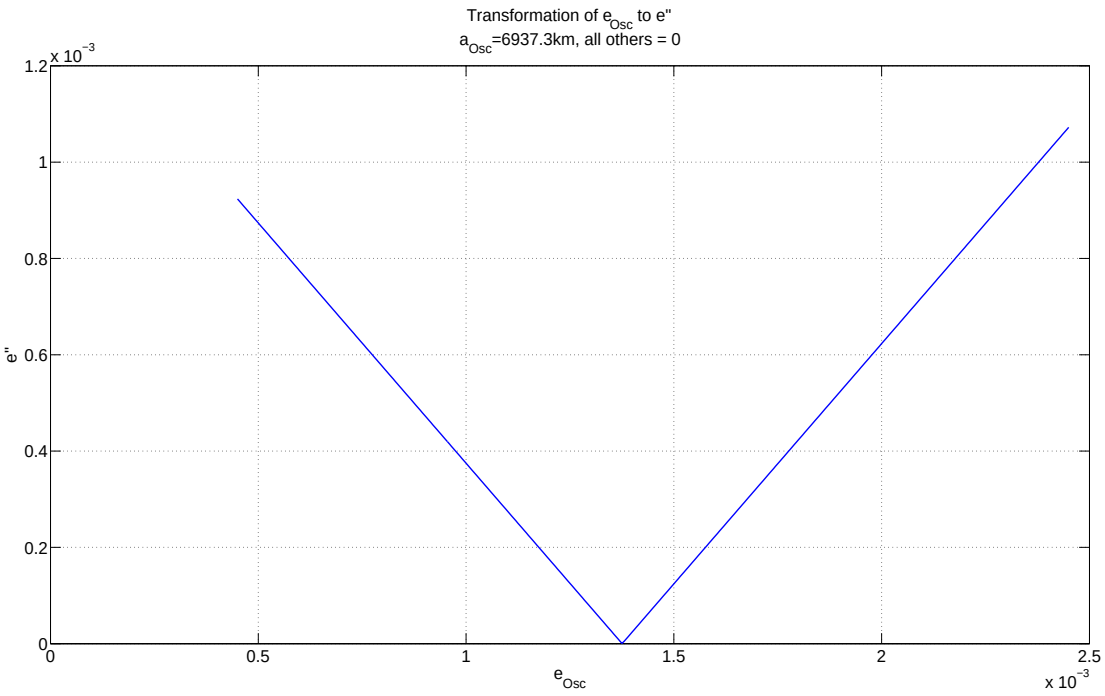

Figure 4.64: LEO RSO Osculating Eccentricity to Mean Eccentricity Mapping

Besides the figure showing how the osculating eccentricity uncertainty directly impacts the mean eccentricity uncertainty, if one were to take the true osculating values of semi-major axis and mean anomaly but add 0.001 to the true osculating eccentricity value, 0.00145, the resulting converted mean true anomaly, f'', would

be 1.7190 radians while the true mean true anomaly is 2.1091 radians. Since the uncertainty of the osculating eccentricity for the HEO RSO is an order of magnitude less than the true value, there is only a slight increase in the mean true anomaly and mean mean anomaly uncertainty bounds and error as shown in Figure 4.63.

Figures 4.65 and 4.66 plot the mean orbital element marginal PDF contours for the Monte Carlo and TOV likelihood solutions for the LEO RSO. The scatter plot used to generate Figure 4.66 over the nonuniform domain is shown in Figure 4.67. The shape of the HEO RSO marginal PDF scatter plot from the likelihood solution mimics its osculating counterpart which again shows that the domain shape is heavily dependent upon ability to correctly estimate the eccentricity vector direction, the contour results for the HEO RSO are again included in Appendix D.

Comparison of the mean element PDF figures with the osculating element figures show that the solution domain has been warped from an ellipse-like shape to more like a banana shape. This banana-like or concave shape has been encountered previously when propagating osculating orbital elements using TOV in time [40]. The lure of mean elements is that their secular momenta are constant, allowing for their coordinates to vary linearly in time. Thus, the mean element PDF representation will be less susceptible to information loss over propagation time, whereas other state representations, e.g. Cartesian, will lose information due to their nonlinear differential equations of motion. Once the measurement PDF is effectively transformed into mean element space, propagation can easily be carried out to any time of particular interest, then the solution can be transformed into another state representation via the TOV technique.

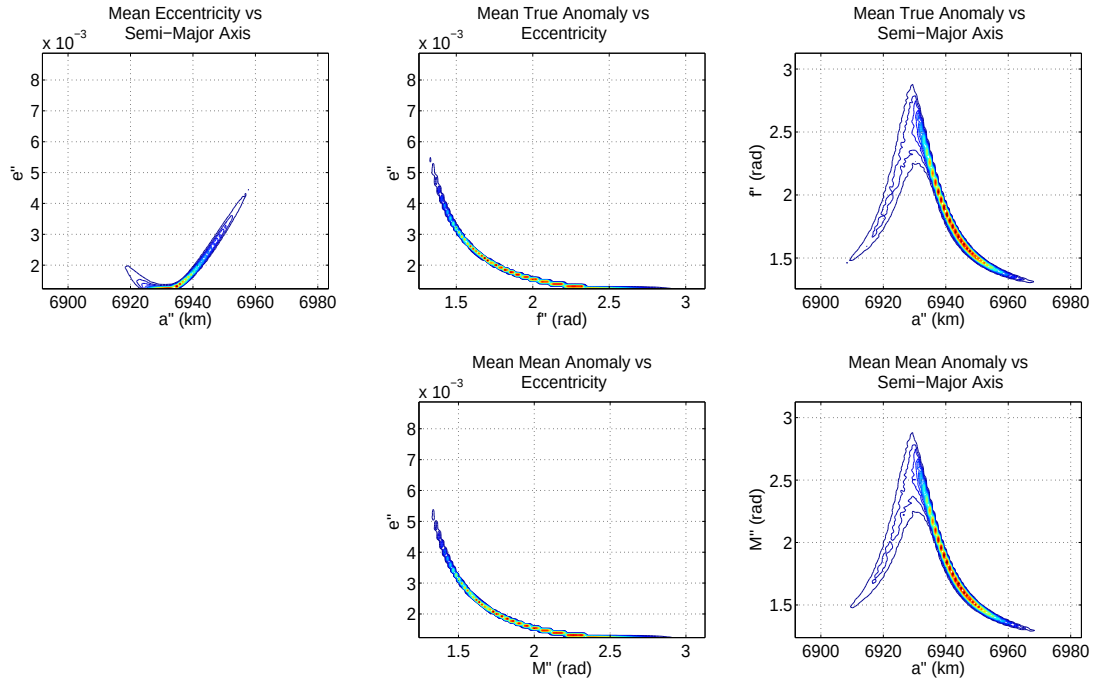

Figure 4.65: LEO RSO Monte Carlo Mean Orbital Element Marginal PDF Contour Results

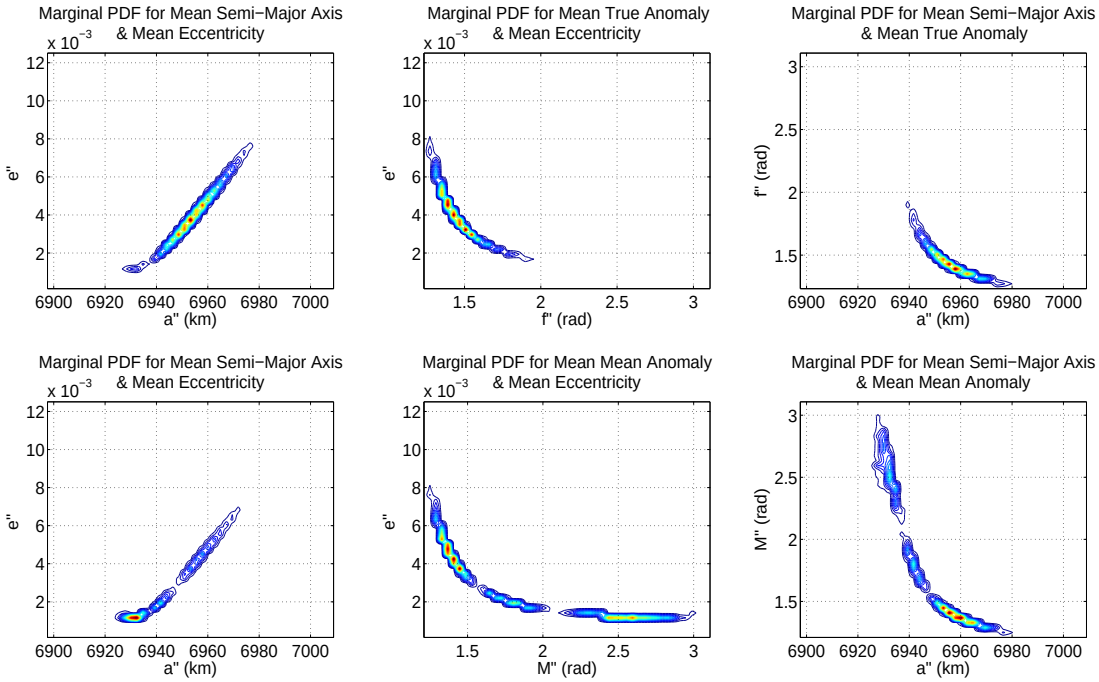

Figure 4.66: LEO RSO TOV Likelihood Mean Orbital Element Marginal PDF Contour Results

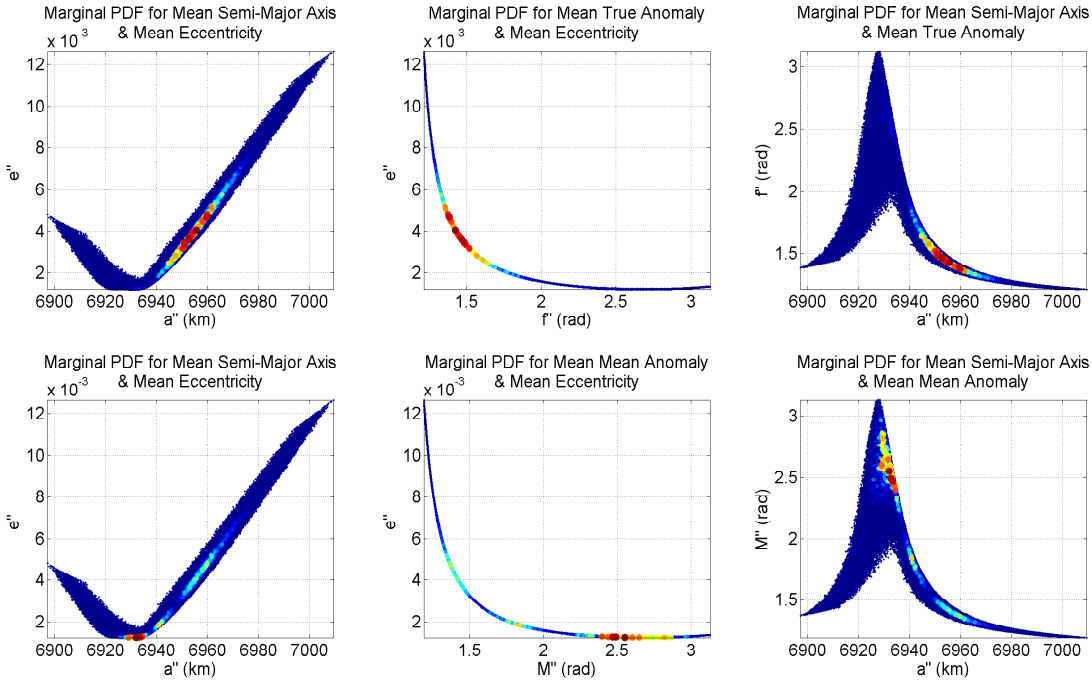

Figure 4.67: LEO RSO TOV Likelihood Mean Orbital Element Marginal PDF Color-Coded Scatter Results

Figure 4.68 compares the mean semi-major axis and eccentricity error of the TOV Bayes' filter posterior for the LEO RSO using different anomalies. The figure shows use of the mean anomaly allows for more accurate estimation of the mean eccentricity. Unlike the osculating results where the state estimate differences were negligible, the difference in the estimated mean semi-major axis was approximately 8 kilometers, while the estimated eccentricity difference was approximately 1×10^{-3} with the (a'', e'', M'') coordinate set being the more accurate with respect to eccentricity estimation. Figure 4.69 displays the same analysis for the HEO RSO and shows there is very little difference between using either anomaly but, the use of the mean mean anomaly is much better for estimating the mean eccentricity.

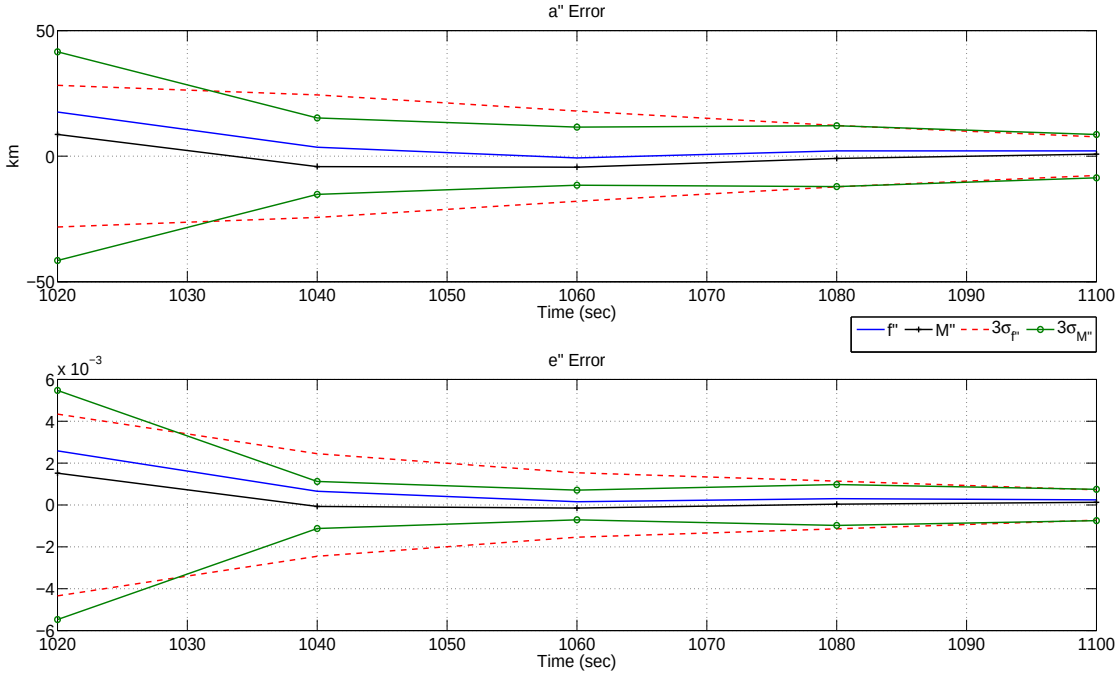

Figure 4.68: LEO RSO TOV Posterior Mean Orbital Element Error of (a'', e'', f'') vs (a'', e'', M'')

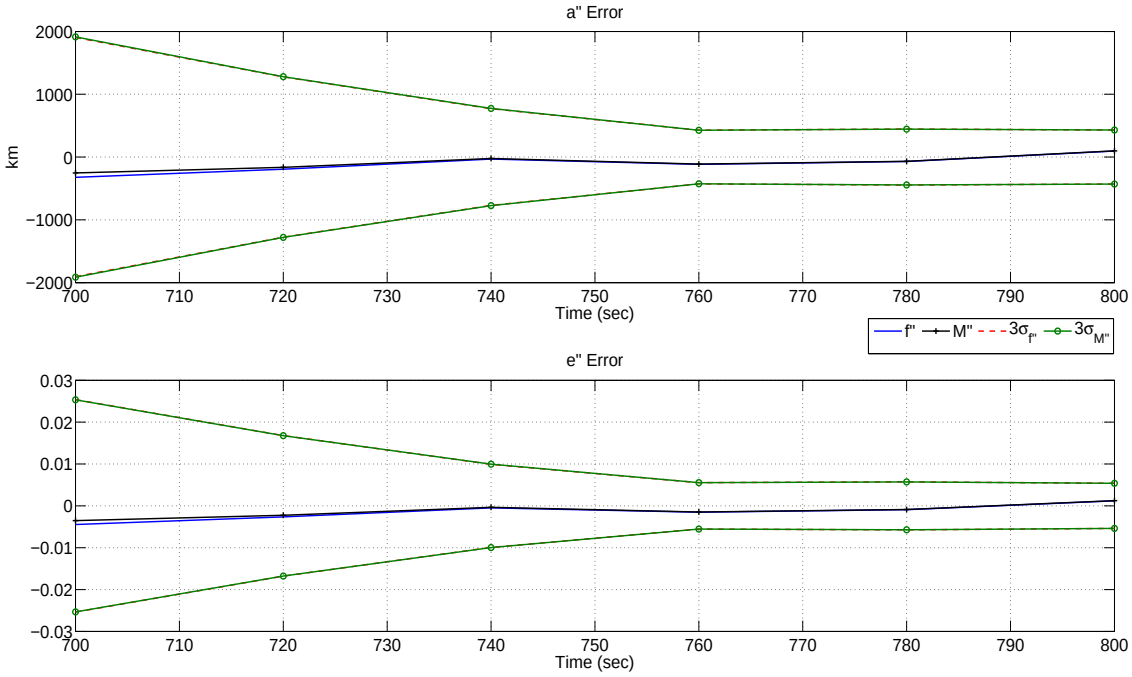

Figure 4.69: HEO RSO TOV Posterior Mean Orbital Element Error of (a'', e'', f'') vs (a'', e'', M'')

Figures 4.70 and 4.71 plot the state tracking results of the TOV likelihood and posterior versus the Monte Carlo analysis. The semi-major axis and eccentricity likelihood and posterior results are computed from the (a'', e'', f'') coordinate set but the results of Figures 4.68 and 4.69 are kept in mind. The results for the LEO mean element case are similar to its osculating counterpart for eccentricity in that the posterior allowed for better state estimation than the Monte Carlo analysis. Again the Monte Carlo analysis is biased for the mean eccentricity and anomalies due to the osculating eccentricity uncertainty being on the order of the truth. The TOV likelihood and posterior uncertainties for the mean elements of the HEO RSO are similar to the osculating HEO results, both oscillate around the truth with the posterior reducing the magnitude of the error oscillation. Figures 4.72 and 4.73 compare the TOV likelihood and Monte Carlo uncertainty analysis which show, as could be intuited from osculating results, that the magnitude of the true eccentricity has a large impact on the uncertainty tracking.

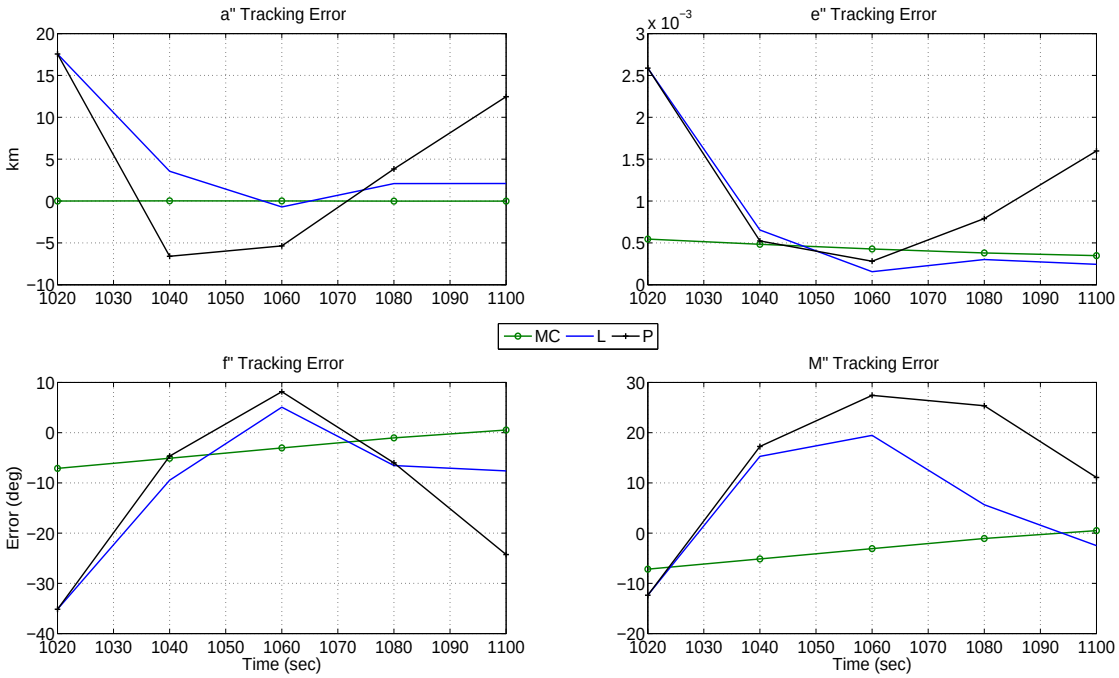

Figure 4.70: LEO RSO Mean Orbital Element Error vs. Monte Carlo

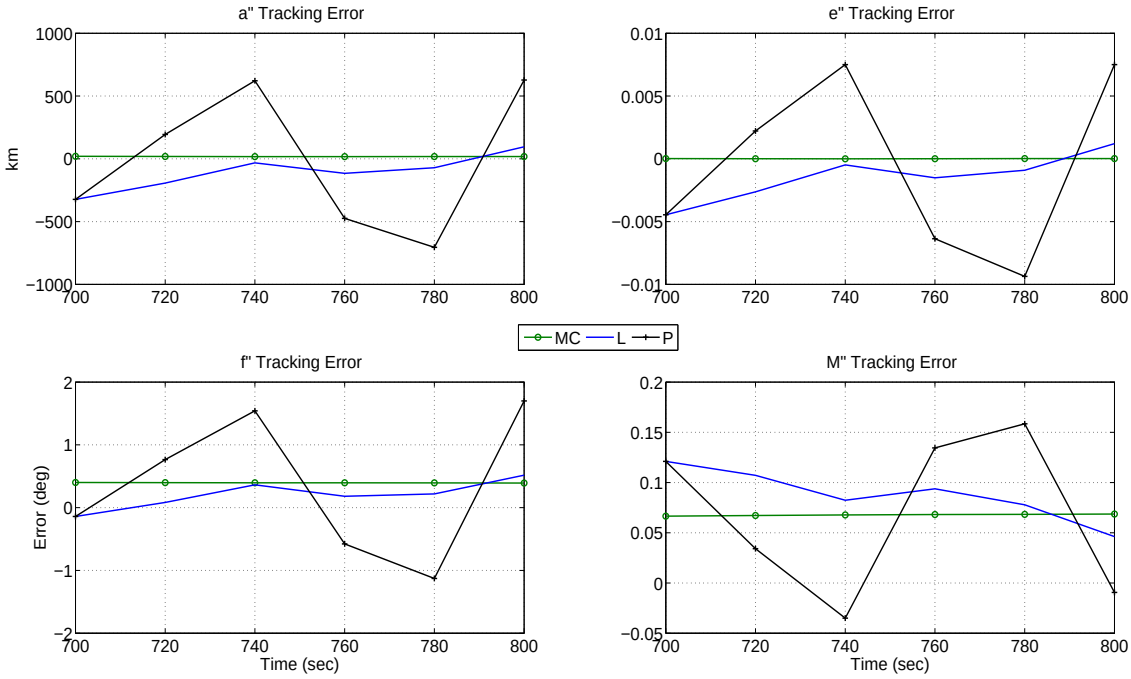

Figure 4.71: HEO RSO Mean Orbital Element Error vs. Monte Carlo

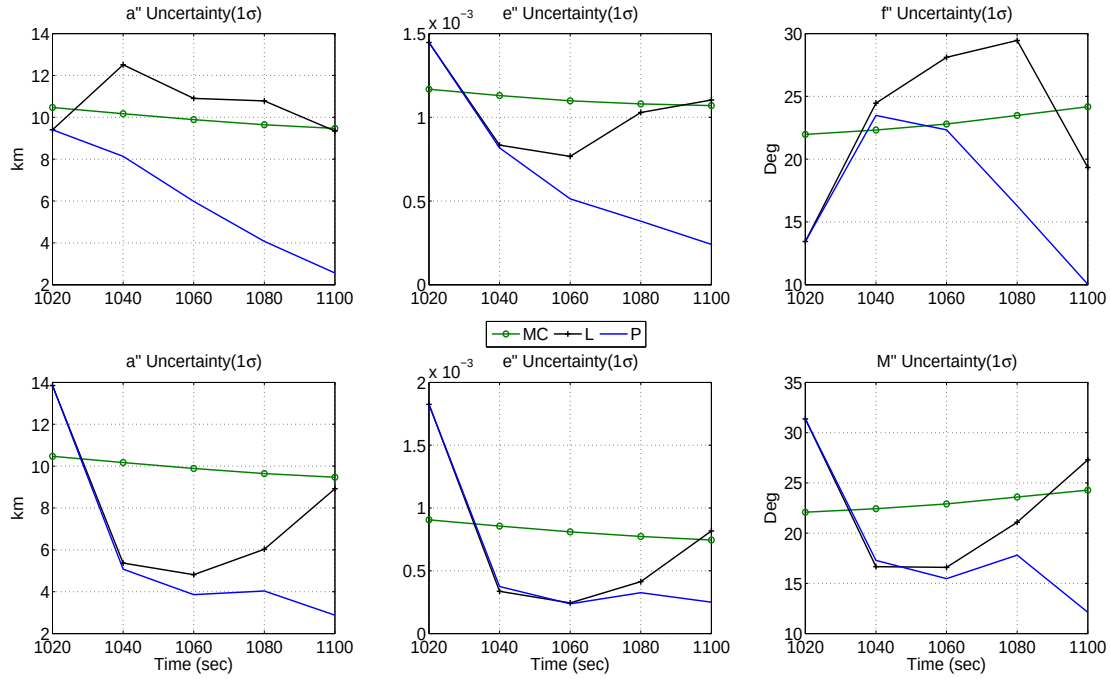

Figure 4.72: LEO RSO Mean Orbital Element Uncertainty vs. Monte Carlo

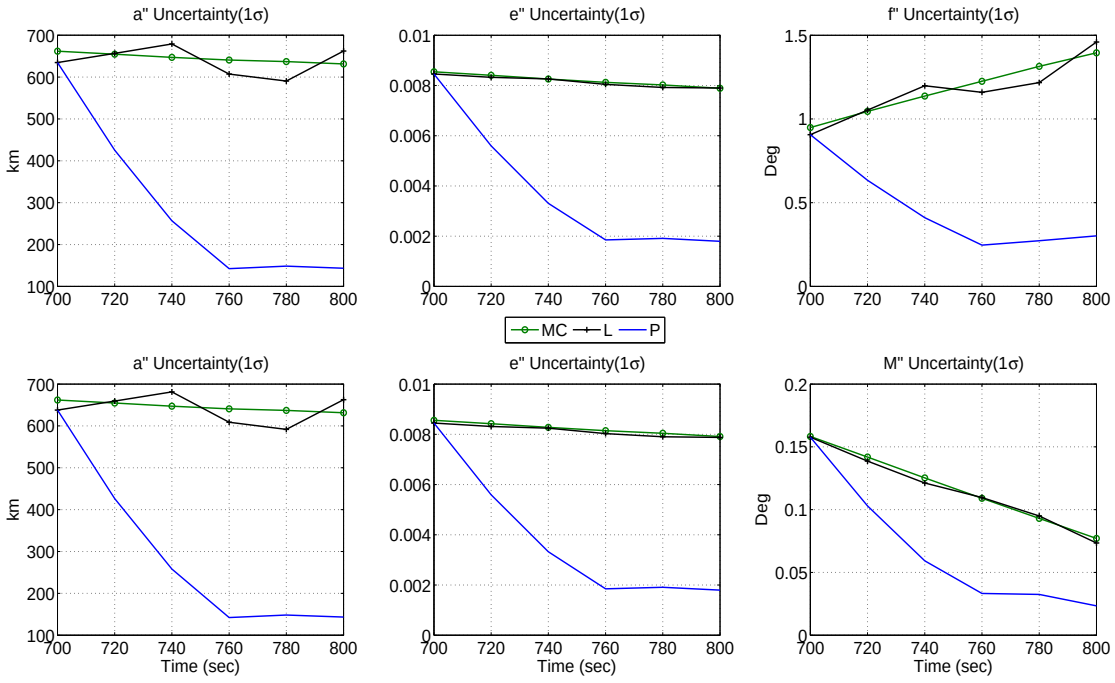

Figure 4.73: HEO RSO Mean Orbital Element Uncertainty vs. Monte Carlo

4.3.8 Three-Dimensional Geopotential Perturbed Motion

As a final space surveillance example, state and uncertainty estimation in the Cartesian, osculating orbital element, and mean orbital element domains via the TOV Bayes' filter is carried out using topocentric measurements of a simulated J_2 perturbed LEO RSO. The three-dimensional motion will be greater affected than the two-dimensional motion since the J_2 effect will be more pronounced due to changes in latitude from the equator. The true trajectory is computed by using the Two-Line Element(TLE) set of Hubble Space Telescope(HST) for day 23 of 2011. Only topocentric measurements of range, azimuth, and elevation angle are recorded so that the Herrick-Gibbs IOD algorithm is required to be carried out.

The likelihood for the osculating and mean domains is computed from the TOV solution of the IOD process. Computation of the prior for each domain is carried out using the linear equations native to each domain for propagation, i.e. F and G solution for Cartesian, mean anomaly for osculating elements, and Brouwer's theory for mean elements. The Monte Carlo solution utilized 2.5×10^6 corrupted measurements of the true trajectory for computation of the numerical first and second moments. The TOV likelihood solution utilized only the three noise corrupted measurements to construct the PDF and approximately 1×10^6 evaluation points while the TOV Bayes' filter posterior utilized up to nine corrupted measurement points, three for the likelihood construction and six for the prior construction, with the same amount of evaluation points.

Since the TLE is given in mean orbital elements, it is converted to osculating elements, shown in Table 4.5, using the first-order J_2 conversion given in Appendix B. The osculating elements are then converted to rectilinear coordinates which are used as the initial conditions for the Two-Body J_2 perturbed differential equations. The

Cartesian solution of the motion was checked against the solution computed from Gauss' Variational Equations [66].

Table 4.5: Initial Conditions of HST TLE for Day 23 of Year 2011

Parameter	Original Mean	Converted Osculating
Semi-Major Axis (km)	6941.499	6943.690
Eccentricity	3.35×10^{-4}	1.45×10^{-3}
RAAN (Deg)	238.23	237.79
Inclination (Deg)	28.47	28.48
Argument of Perigee (Deg)	30.04	6.530
True Anomaly (Deg)	330.02	354.46
Mean Anomaly (Deg)	330.04	354.47

Due to the relatively low eccentricity of HST, the equinoctial form of Gauss' Varitional Equations [72] was used to maintain numerical stability. The format of the TLE is given in Vallado [49] as well as on the website maintained by Kelso [80] which reports the TLEs for many different satellites from NORAD.

From the results of Section 4.3.7 and closely examining Table 4.5, the initial osculating eccentricity of HST will prove to be a problem in reliably estimating the eccentricity vector location and its dependent elements in the osculating domain. Additionally, one can expect that the mean eccentricity uncertainty will be on the order of the osculating eccentricity uncertainty due to the mapping effect already shown and the mean argument of perigee and mean mean anomaly will be directly affected by this mapping. However, this orbit type must still be considered since low eccentricity is characteristic of LEO RSOs and the 28 degree inclination possesses a rather large population of space debris [76] and is typical of launch vehicle insertions from Cape Canaveral for geosynchronous orbits.

The location of the tracking station was set to be Socorro, NM, using sensor pa-

rameters similar to Eglin, FL [49]. The tracking station location and sensor parameters are reported in Table 4.6. For this simulation, the position of the vernal equinox is able to calculated since the TLE reports the Universal Coordinated Time(UTC). The trajectory of HST was simulated for a 24 hour period during which the tracking station was able to observe HST over three different time spans separated by approximately 97 minutes which occurred near the end of the simulation time. The respective lengths of the time spans were 250, 270, and 115 seconds. The results presented are for the first track, but the results of the second and third track and conclusions drawn from them are the same.

Table 4.6: Tracking Station Parameters for Three-Dimensional Simulation

Parameter	Value
Altitude Above Sea-Level (km)	1.5102
Longitude (Deg)	-106.66
Latitude (Deg)	33.82
Range Noise 1σ (km)	0.030
Azimuth Noise 1σ (Deg)	0.015
Azimuth Observation Window (Deg)	[0,360]
Elevation Noise 1σ (Deg)	0.015
Elevation Observation Window (Deg)	[20,90]
Measurement Frequency (sec)	19.2

4.3.8.1 Cartesian Domain Results

Figure 4.74 plots the Cartesian domain state error and uncertainty bound results of the TOV Bayes' filter for the first track of the J_2 perturbed trajectory of HST. The uncertainty bounds reported from the covariance analysis are four times the standard deviation because the system is six dimensional. Figures 4.75 and 4.76 compare the estimated state error and uncertainty of the TOV likelihood and Bayes' filter posterior PDF versus the numerical moments computed from Monte Carlo analysis.

The Monte Carlo and TOV likelihood solutions for the IOD uncertainty are shown to agree extremely well so TOV serves as a viable way to initialize either an EKF or UKF. Figure 4.77 shows that, just as with the planar example, the TOV approach allows for an efficient and accurate way to automate initialization of conventional filtering algorithms.

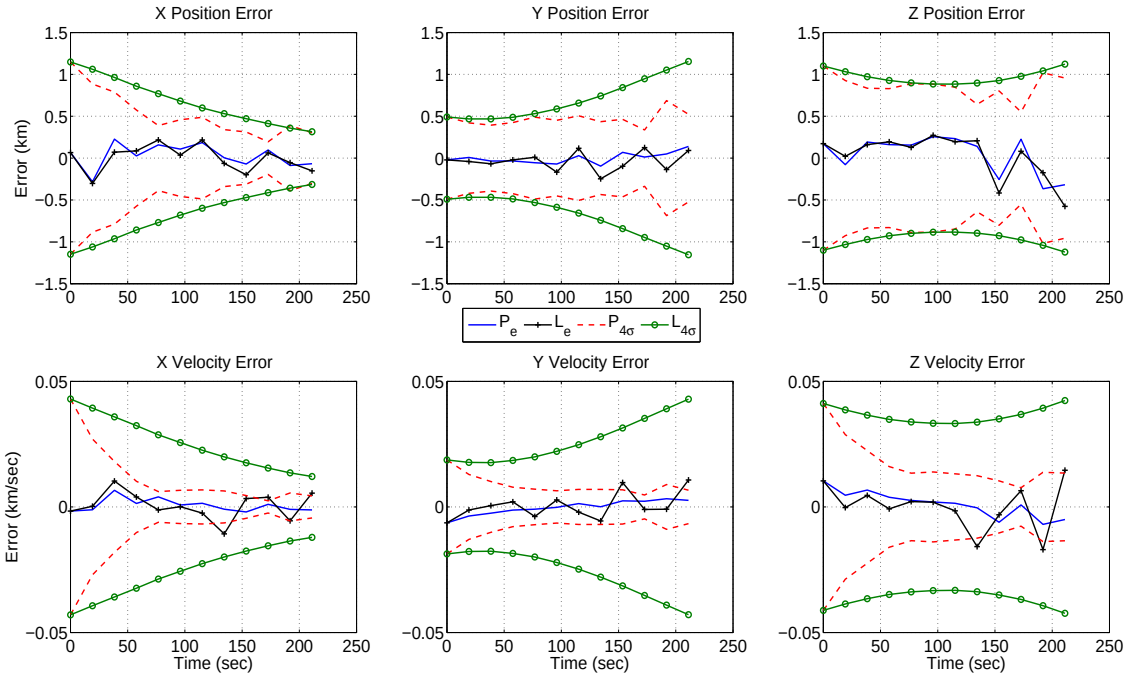

Figure 4.74: TOV Bayes' Filter Operation for Track 1 Cartesian States

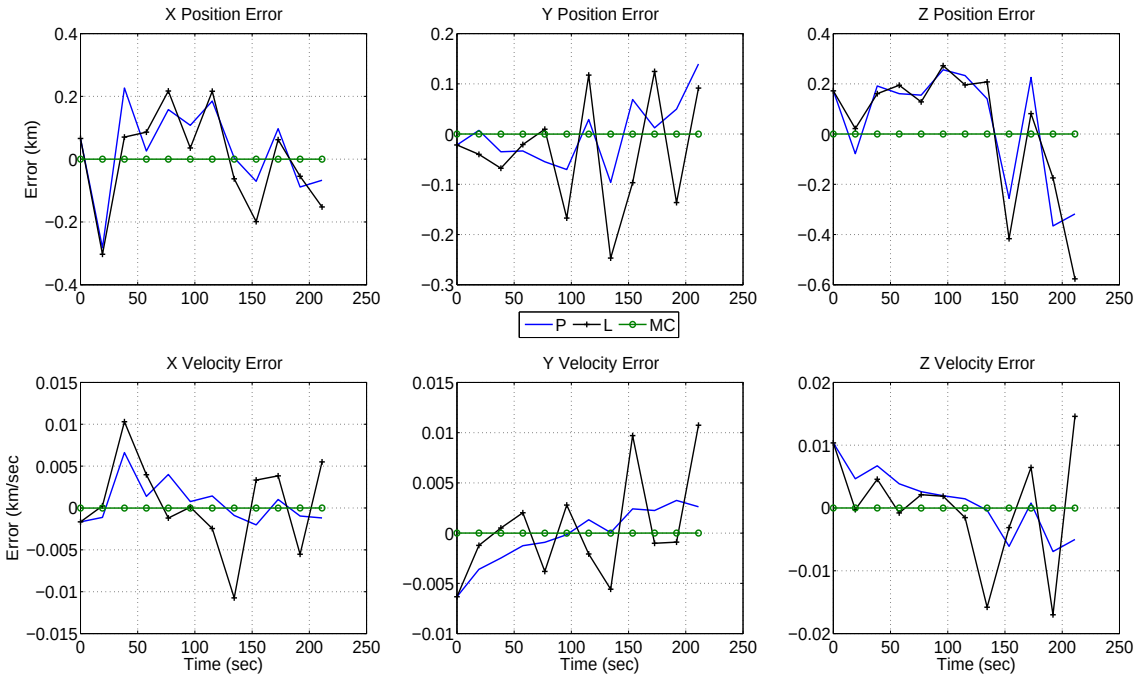

Figure 4.75: TOV Likelihood and Bayes' Filter Posterior State Error Comparison with Monte Carlo for Track 1 Cartesian States

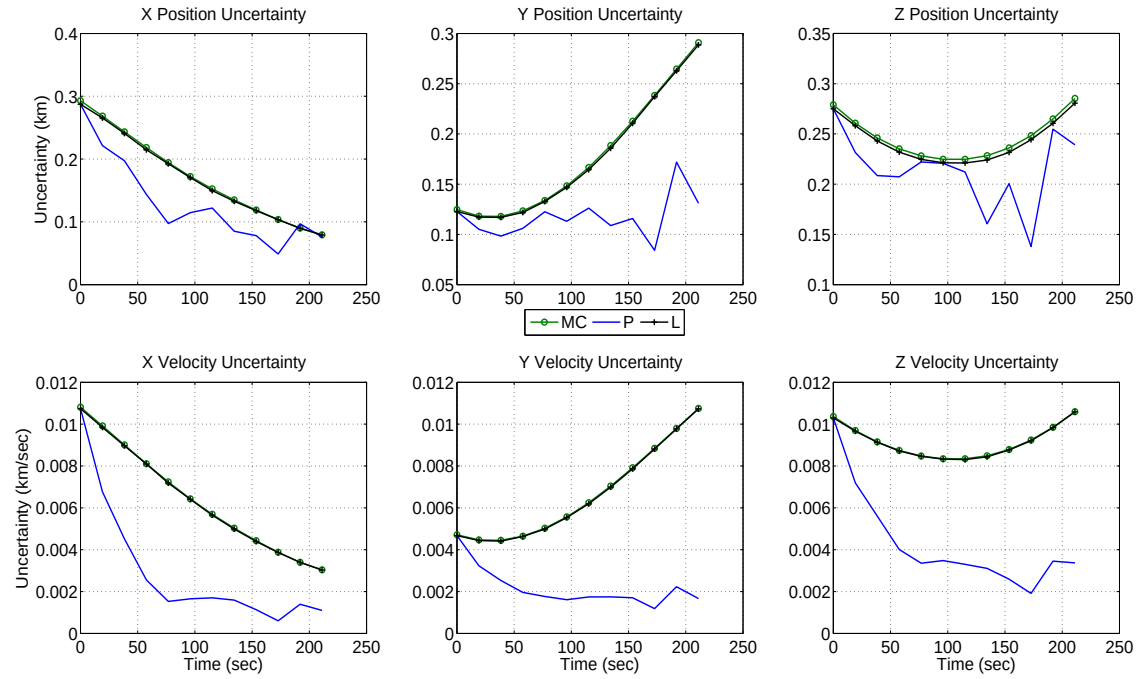

Figure 4.76: TOV Likelihood and Bayes' Filter Posterior Uncertainty Comparison with Monte Carlo for Track 1 Cartesian States

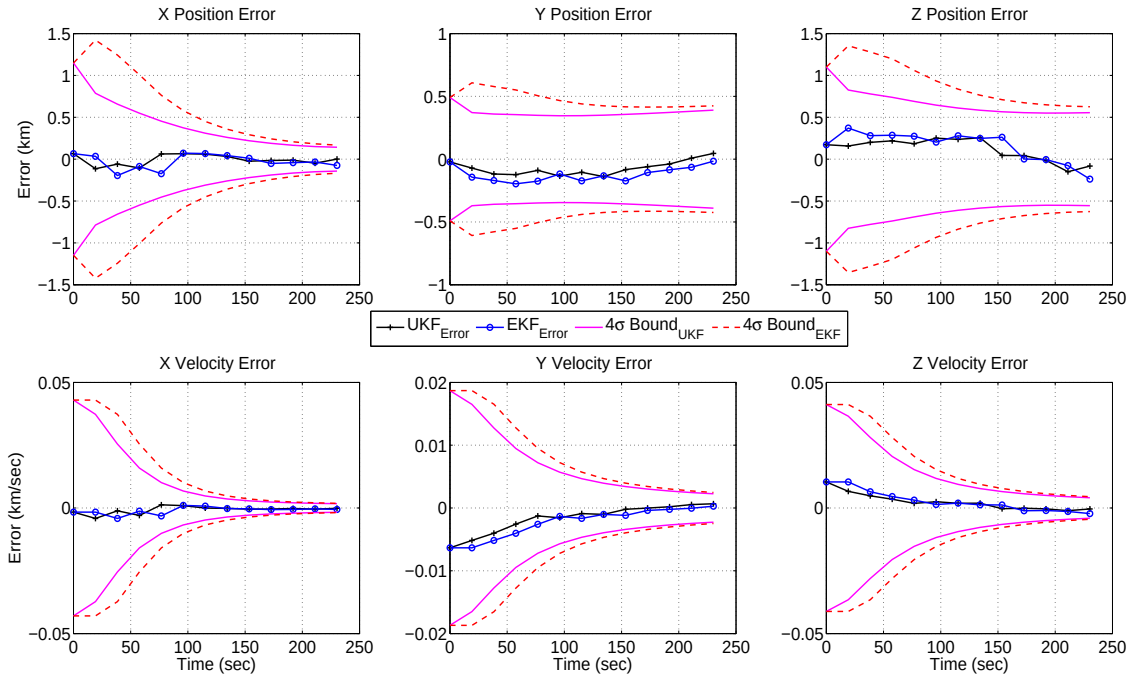

Figure 4.77: TOV Initialization of EKF and UKF for Track 1 Cartesian States

4.3.8.2 Osculating Keplerian Domain Results

Figure 4.78 plots the osculating orbital element domain results with four standard deviation uncertainty bounds of the TOV likelihood and Bayes' filter posterior solutions for the first track of the J_2 perturbed trajectory of HST. The results are similar to the low eccentricity planar example where the eccentricity uncertainty is on the order of the true uncertainty, which causes the uncertainty in argument of perigee and mean anomaly to be significant. The low value of eccentricity leads to the eccentricity vector direction to be not easily located, which directly impacts the argument of perigee and true anomaly computations. The semi-major axis, right ascension of ascending node, and inclination are not affected by the eccentricity, whereas the argument of perigee and anomalies rely upon accurate computation of the eccentricity vector.

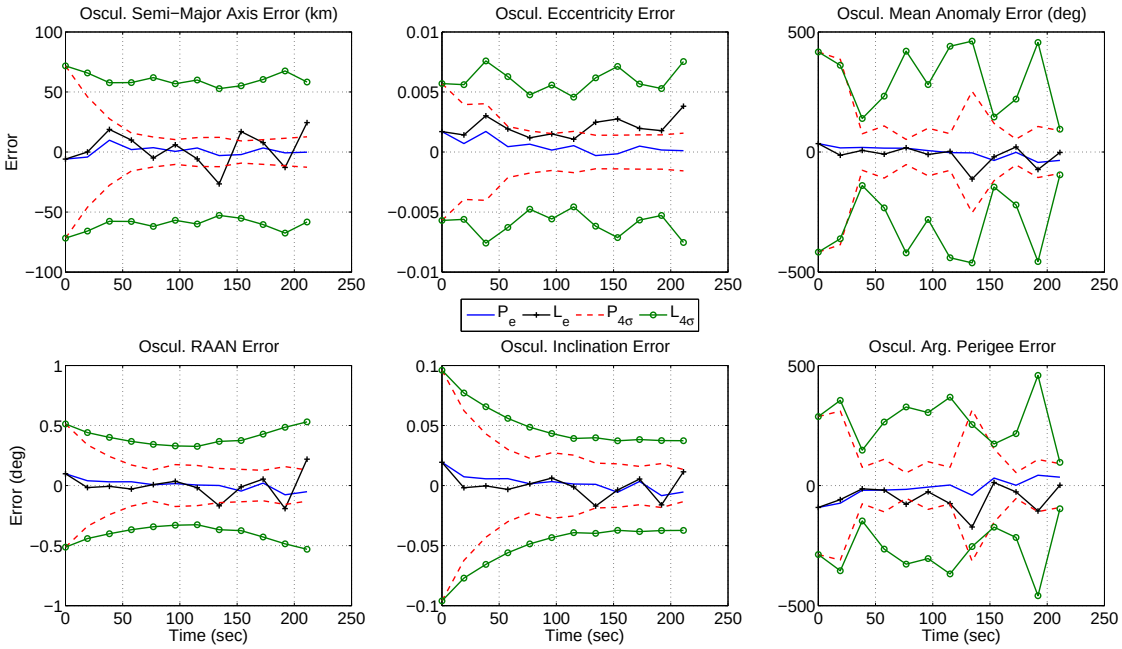

Figure 4.78: TOV Bayes' Filter Operation for Track 1 Osculating Orbital Elements

Figure 4.78 shows that the angular momentum and node vectors are well defined while the eccentricity vector is not, so the orbit plane and orbit size are well defined but significant shape ambiguity exists due to the eccentricity vector not being well defined. Figures 4.79 and 4.80 plot the state error and uncertainty results of the TOV likelihood and Bayes' filter versus the Monte Carlo results and the similarity transform solution, Equation 3.45. The similarity transform is applied to the TOV likelihood and Bayes' posterior Cartesian solutions with the resulting solutions denoted as SP and SL respectively. The similarity transform state error solution corresponds to the state error that would be observed if one simply transformed the Cartesian TOV solutions into the osculating domain. The partial derivatives required by the similarity transform were already computed because they were needed for the TOV solutions, the derivatives were derived by hand, checked with previous references, e.g. Broucke [75], and also checked symbolically using MATLAB®.

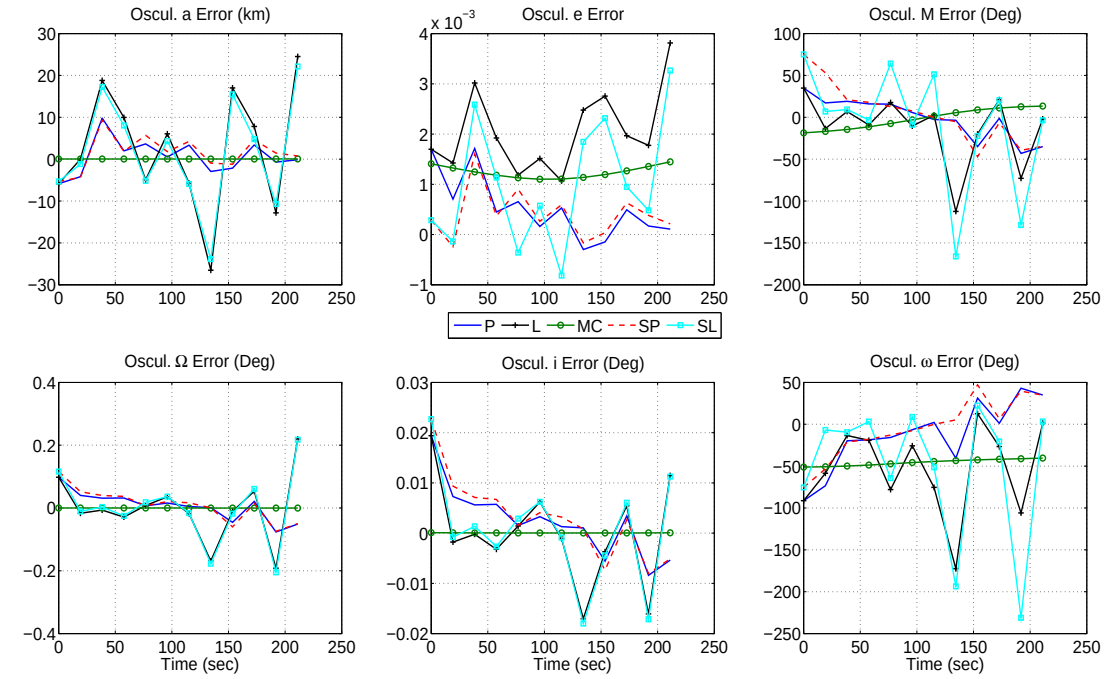

Figure 4.79: Track 1 Osculating Orbital Element Error for TOV Bayes', Monte Carlo, and Similarity Transform

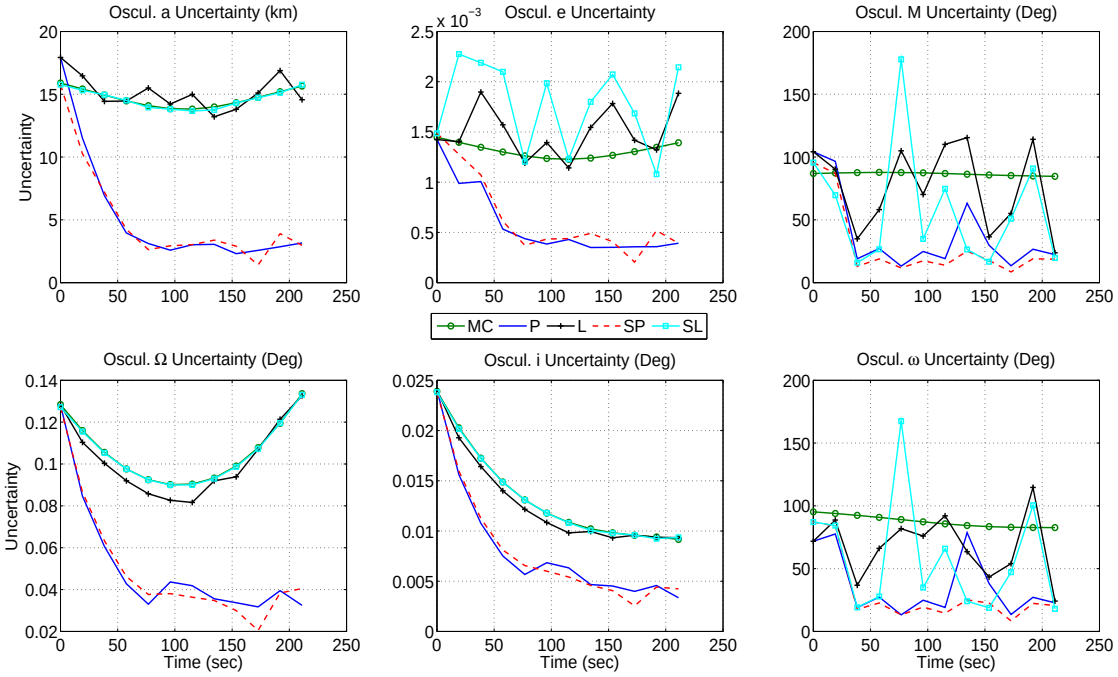

Figure 4.80: Track 1 Osculating Orbital Element Uncertainty for TOV Bayes', Monte Carlo, and Similarity Transform

Figures 4.79 and 4.80 show that the similarity transform is able to track the TOV state and uncertainty solutions for semi-major axis, right ascension of ascending node, and inclination, but possesses large fluctuations in eccentricity, argument of perigee and mean anomaly. It is worth noting that simply transforming the TOV Cartesian solutions allowed for better estimation of the eccentricity, but this still did not help to accurately estimate the argument of perigee or mean anomaly due to inconsistency. The inability to accurately pin down the eccentricity vector led to rather large state and uncertainty errors for all estimators for the mean anomaly and argument of perigee states. For the argument of perigee state error, all solutions which did not utilize previous data possessed a large constant bias of approximately 50 degrees. It is only by utilizing additional data that the TOV Bayes' filter was able to reduce the amount of error in the eccentricity estimate, this helped to reduce, but did not eliminate, the estimation error of mean anomaly and argument of perigee.

Due to the uncertainty computation results of the eccentricity, mean anomaly, and argument of perigee parameters, the marginal PDF contours of the TOV likelihood solution and the Monte Carlo solution for the second observation time of the first track are considered for analysis. Figures 4.81 and 4.82 plot the marginal PDF contours of the TOV likelihood and Monte Carlo solutions for the semi-major axis at track initialization. The TOV likelihood solution is bifurcated for the eccentricity, argument of perigee, and mean anomaly states because it cannot accurately pin down the eccentricity vector, but it can estimate the node vector relatively well. For the Monte Carlo solution, the bifurcation is apparent and the solution area is better defined since the Monte Carlo solution samples about the true trajectory and utilizes six orders of magnitude more points than the TOV solution. The TOV solution possesses a shorter "flow" of uncertainty in the mean anomaly and argument of perigee domains, however the contour shapes are relatively the same with respect to the

semi-major axis. The shorter flow is also repeated in the TOV likelihood marginal PDF solutions with respect to eccentricity as shown by comparing Figure 4.83 to Figure 4.84. For completeness, the remaining six marginal PDF solutions with respect to the orientation parameters are shown in Appendix D, which also show the bifurcation behavior in mean anomaly and argument of perigee.

From Figures 4.81 through 4.84, it is apparent that the Gaussian assumption of the similarity transform is not actually valid for the osculating Keplerian variables for this type of low Earth orbit but, it can be stretched to work for the uncertainty bounds for the semi-major axis, eccentricity, right ascension of ascending node, and inclination. However, in no way can the Gaussian distribution assumption be applied to the mean anomaly or argument of perigee domains due to the shape of their PDF solutions and would be a misguided application of the technique.

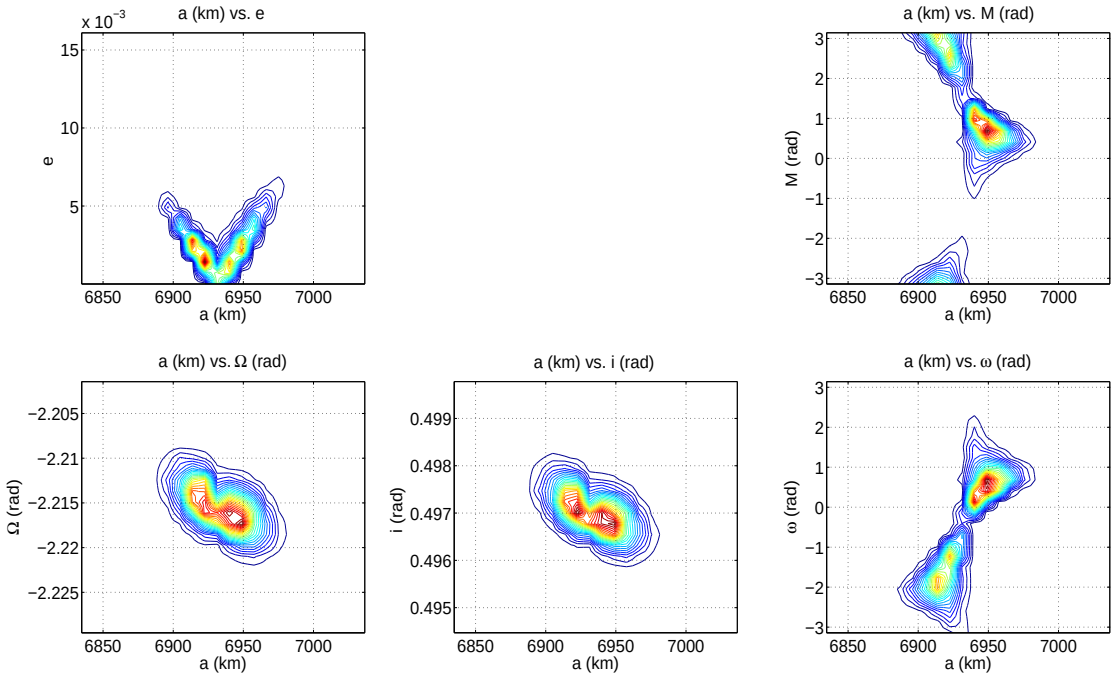

Figure 4.81: Track 1 Osculating Orbital Element Marginal PDFs with respect to Semi-Major Axis from TOV Likelihood Solution

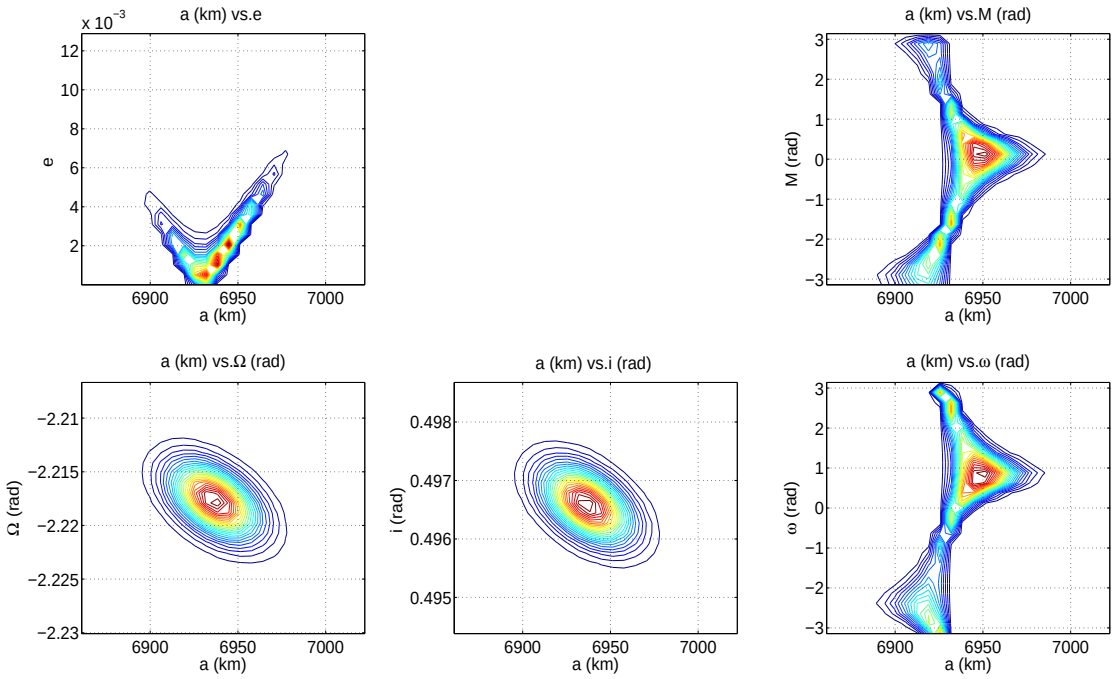

Figure 4.82: Track 1 Osculating Orbital Element Marginal PDFs with respect to Semi-Major Axis from Monte Carlo Solution

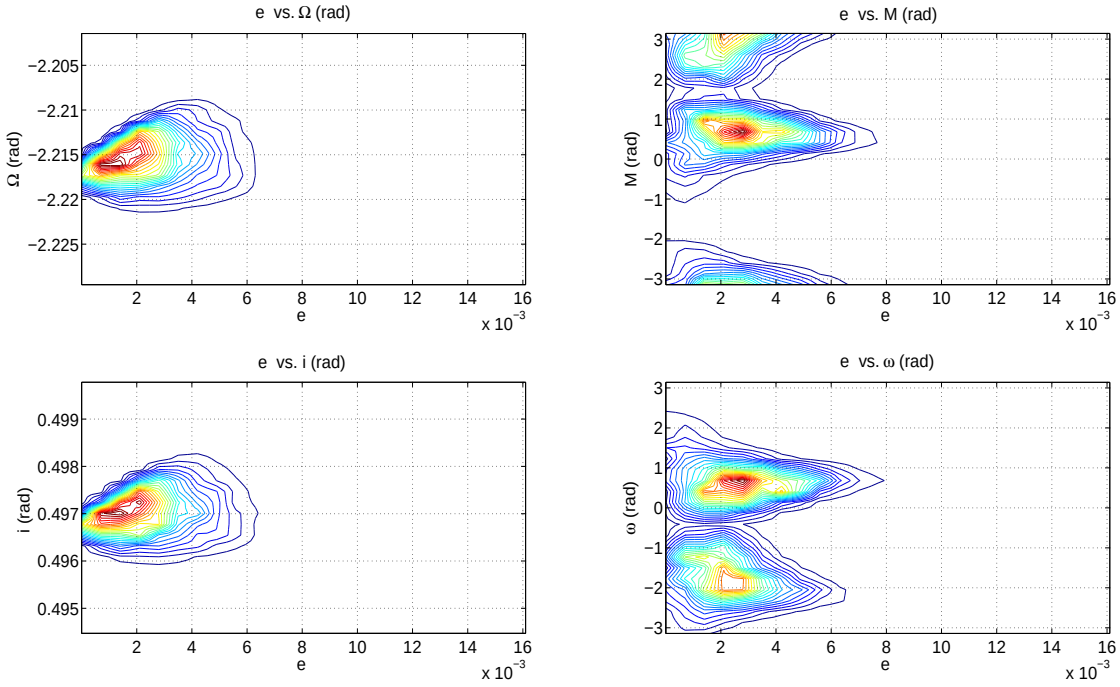

Figure 4.83: Track 1 Osculating Orbital Element Marginal PDFs with respect to Eccentricity from TOV Likelihood Solution

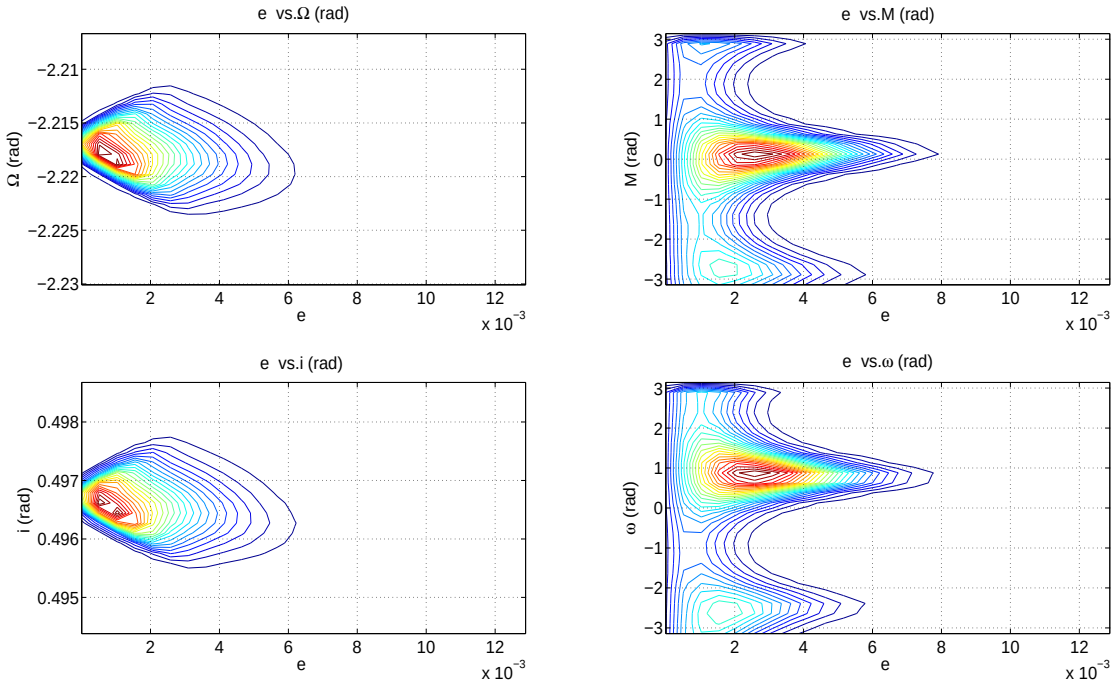

Figure 4.84: Track 1 Osculating Orbital Element Marginal PDFs with respect to Eccentricity from Monte Carlo Solution

4.3.8.3 Mean Keplerian Domain Results

From the results of the equatorial orbit analysis, one already knows that because the uncertainty in osculating eccentricity is on the order of the true eccentricity, conversion of the osculating domain solutions to the mean domain for the eccentricity, argument of perigee, and mean anomaly will provide little insight into the problem. However, they are presented in order to show the effect of the significant eccentricity uncertainty in the mean domain, as well as assess the behavior of a second application of the similarity transform. Figure 4.85 plots the mean orbital element domain results with four standard deviation uncertainty bounds of the TOV Bayes' filter for the first track of the J_2 perturbed trajectory of HST with the tracking accuracy results similar to the osculating results.

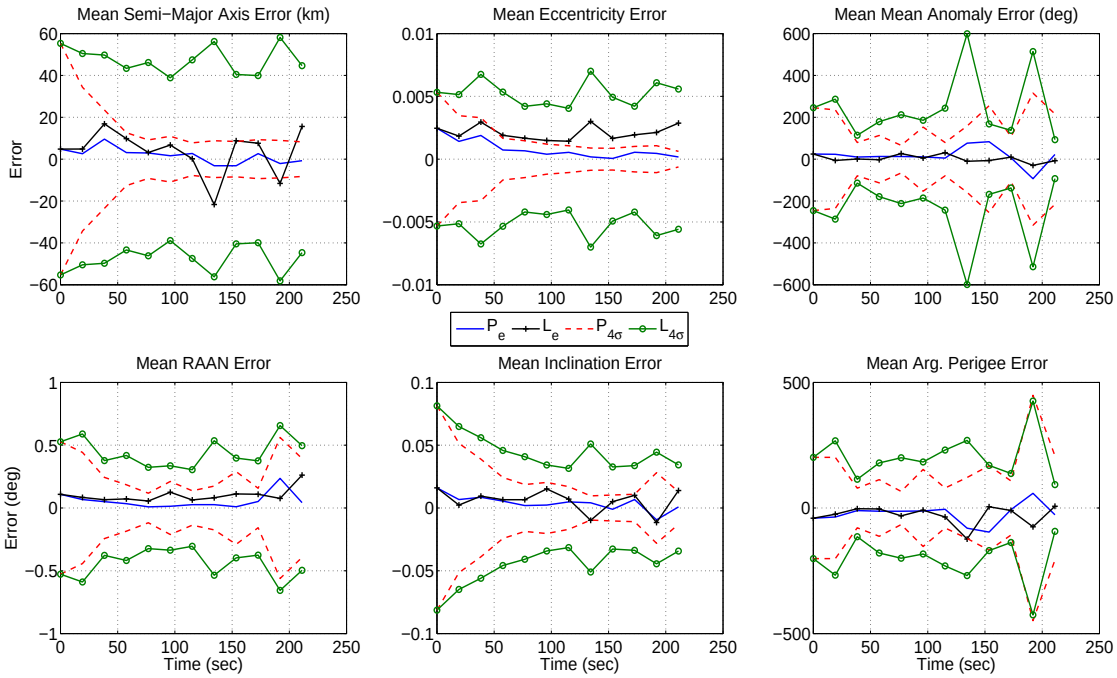

Figure 4.85: TOV Bayes' Filter Operation for Track 1 Mean Orbital Elements

Figures 4.86 and 4.87 compare the state error and uncertainty of the TOV likelihood and posterior solutions versus the Monte Carlo results and the similarity transform of the osculating similarity transform solution. The similarity transform for mean elements is computed by applying Equation 3.45 twice to the Cartesian TOV solutions since it is assumed that the osculating TOV results would not be available. Figure 4.86 shows the Monte Carlo state solution possesses not only strong bias in the mean eccentricity, mean anomaly, and argument of perigee coordinates, but also a bias in mean right ascension of ascending node is apparent. Figure 4.87 shows that the similarity transform solution for mean element uncertainty possesses much higher fluctuations than the Monte Carlo or TOV solutions and does not behave in a consistent manner for any of the states.

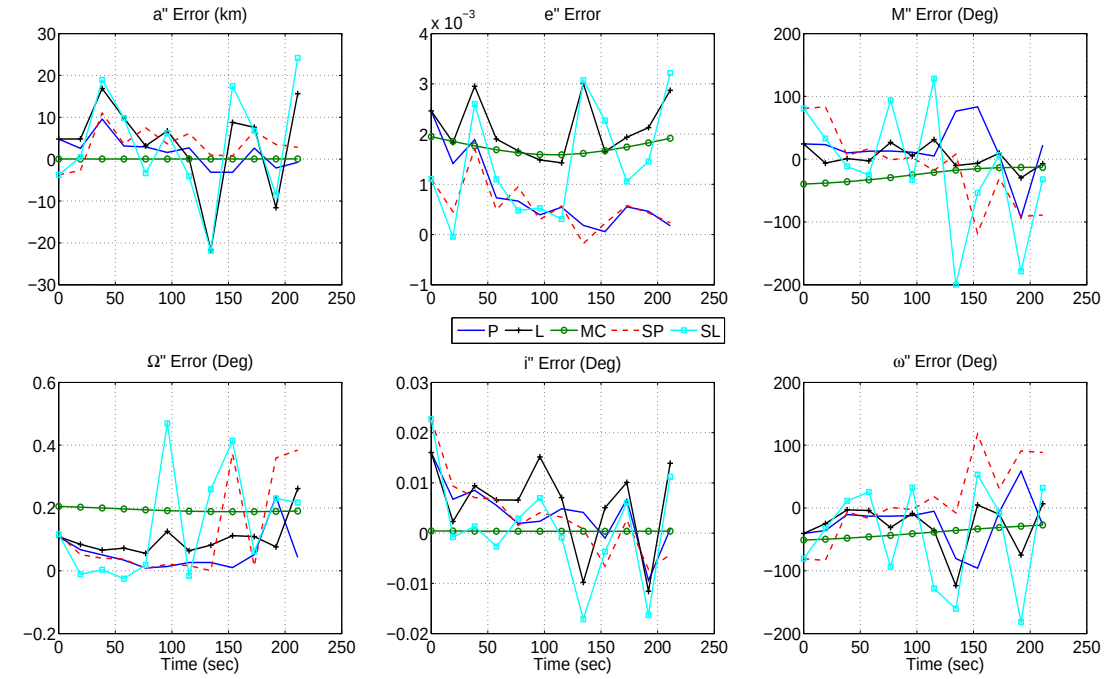

Figure 4.86: Track 1 Mean Orbital Element Error for TOV Bayes', Monte Carlo, and Similarity Transform

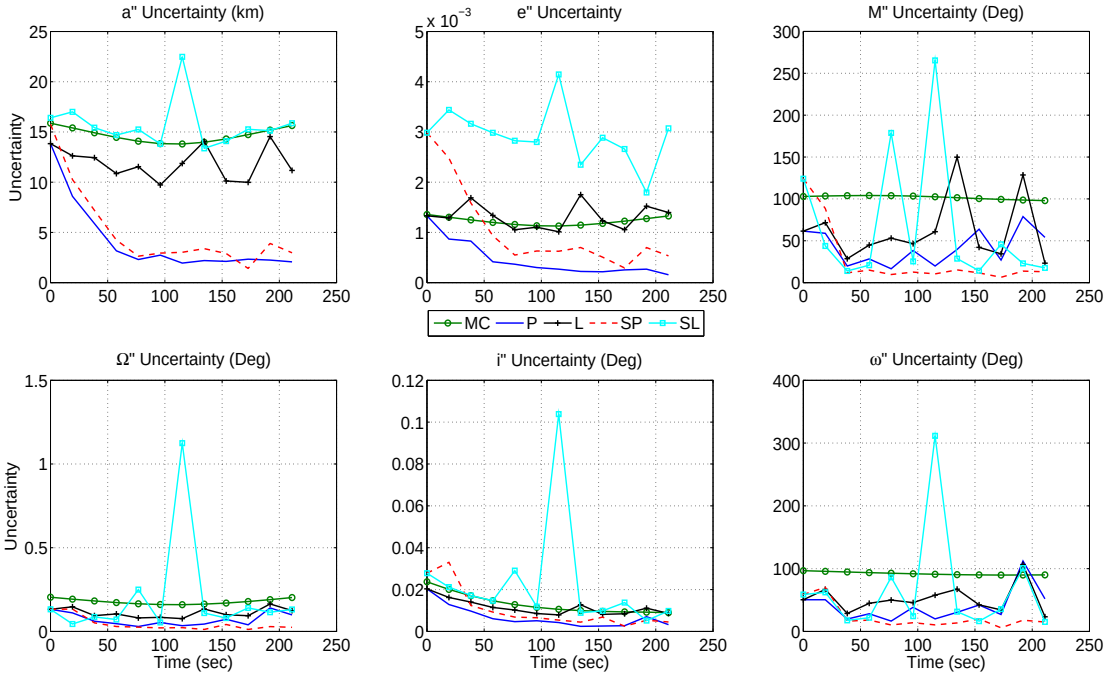

Figure 4.87: Track 1 Mean Orbital Element Uncertainty for TOV Bayes', Monte Carlo, and Similarity Transform

The marginal PDF contour results are presented in Appendix D and are similar to their counterparts in the osculating domain. The TOV mean solution hints at bifurcated behavior for the mean mean anomaly and argument of perigee, but the Monte Carlo solution shows stronger evidence of a bifurcated solution in the two coordinates. Additionally, the Monte Carlo mean right ascension of ascending node solution starts to show a bifurcated solution with relatively equal likelihoods, unlike the mean anomaly and argument of perigee where the likelihood is much stronger for one than the other. However, the bifurcated mean right ascension of ascending node solution only occupies a small angular region, approximately 1 degree instead of 360 degrees for the its coordinate counterparts, so the location of the node vector is still well known in mean element space. The results of the second and third track follow closely the preceding results so they are not shown.

4.3.8.4 Increased Initial Osculating Eccentricity Results

As could be intuited from the planar perturbed Keplerian motion example in Section 4.3.7, having the estimation uncertainty of the osculating eccentricity be on the order of the true eccentricity renders the orientation of the eccentricity vector ill-observed. This introduces significant uncertainty in the computation of mean anomaly and argument of perigee because they are directly dependent upon the eccentricity estimate and its uncertainty, which impact the mean element domain uncertainty computation. In the same spirit as the results presented for equatorial motion, the initial osculating eccentricity of the HST orbit is increased by an order of magnitude to 1.45×10^{-2} while holding the other parameters constant. This increase in eccentricity changes the orbit's perigee and apogee altitudes from (555.485,575.622)kilometers to (464.870, 666.237)kilometers. From Figure 4.80, the large difference between apogee and perigee is well outside the one standard devia-

tion of the semi-major axis from the TOV likelihood so the eccentricity vector should be well observed.

Figure 4.88 plots the Cartesian domain state error and uncertainty bound results of the TOV Bayes' filter for the first track of the J_2 perturbed trajectory of the HST TLE using the osculating eccentricity increased by an order of magnitude. Figure 4.89 compares the estimated uncertainty of the TOV likelihood PDF and the TOV Bayes' filter posterior PDF versus the numerical uncertainties computed from Monte Carlo analysis. The initialization results of the EKF and UKF are not shown because their convergent behavior is similar to that of the original osculating eccentricity results.

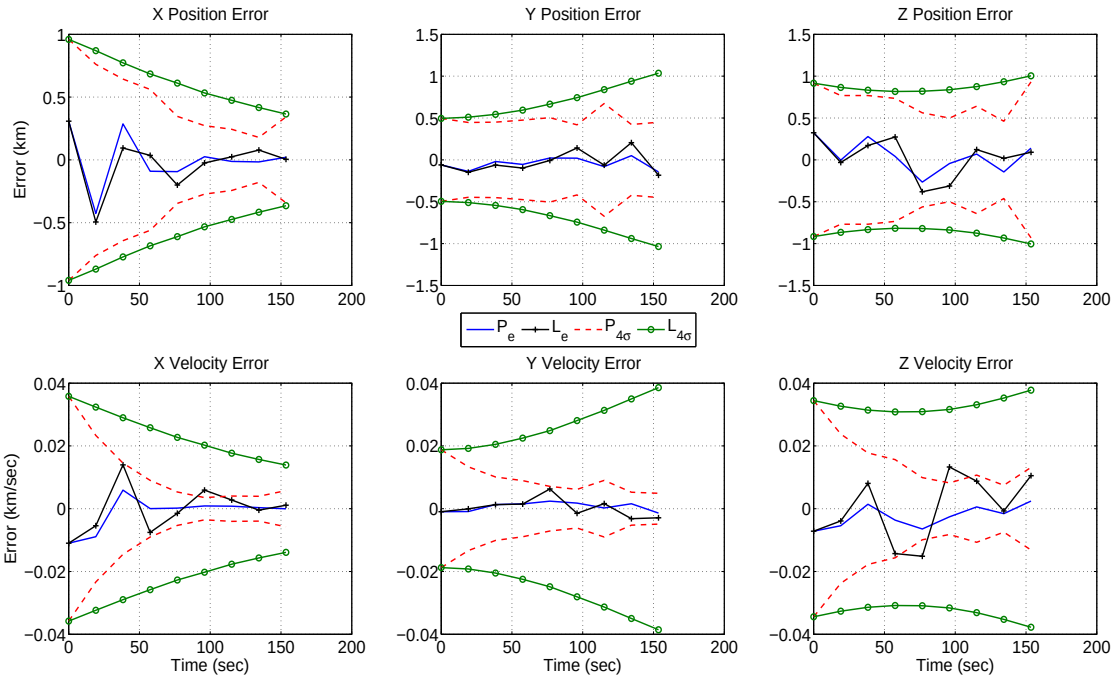

Figure 4.88: Increased Eccentricity TOV Bayes' Filter Operation for Track 1 Cartesian States

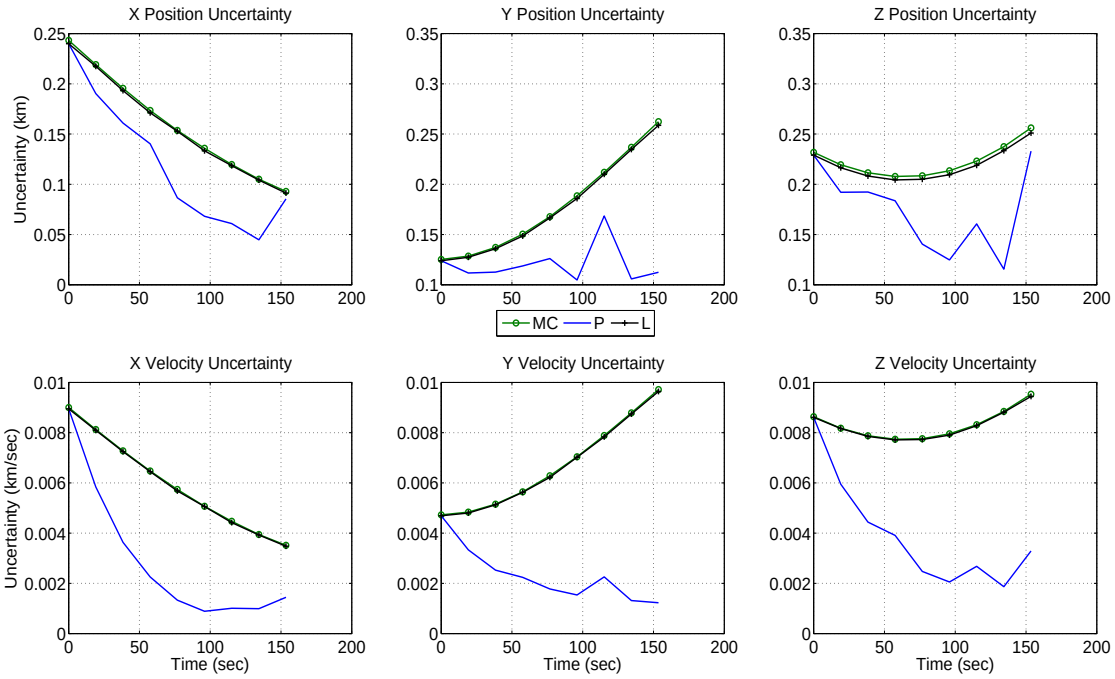

Figure 4.89: Increased Eccentricity TOV Likelihood and Bayes' Filter Posterior Uncertainty Comparison with Monte Carlo for Track 1 Cartesian States

Figure 4.90 plots the osculating element error and uncertainty results of the TOV Bayes' filter for the first track of the J_2 perturbed trajectory of the altered TLE. Increasing the eccentricity by an order of magnitude drastically improved the state estimation results and significantly reduced the uncertainty bounds for the mean anomaly and argument of perigee. The standard deviation of eccentricity error is an order of magnitude less than the true osculating eccentricity magnitude, which could not be said for original eccentricity case. Note that the uncertainty bounds for semi-major axis, eccentricity, right ascension of ascending node, and inclination are only slightly less than the original eccentricity case but the argument of perigee and mean anomaly uncertainty bounds are smaller by approximately an order of magnitude.

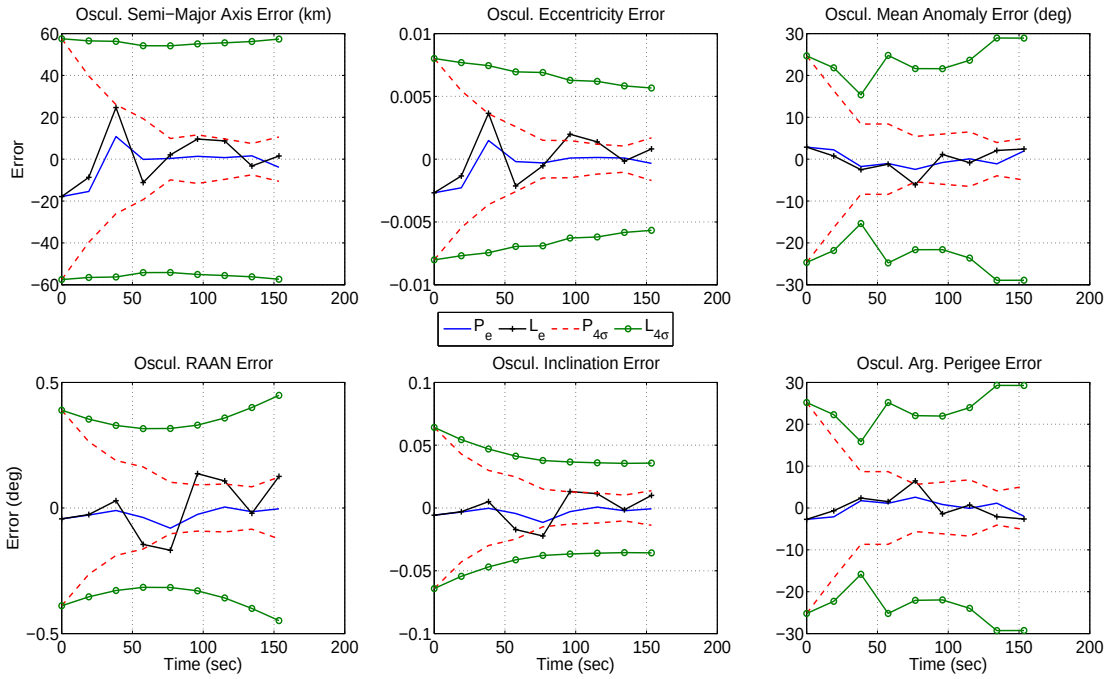

Figure 4.90: Increased Eccentricity TOV Bayes' Filter Operation for Track 1 Osculating Orbital Elements

Figure 4.91 plots the state error of the TOV solutions, similarity transform, and Monte Carlo results. The figure shows that with the increase in magnitude of the eccentricity, the Monte Carlo results no longer possess any significant bias in any of the states, which could not be said for the original eccentricity case.

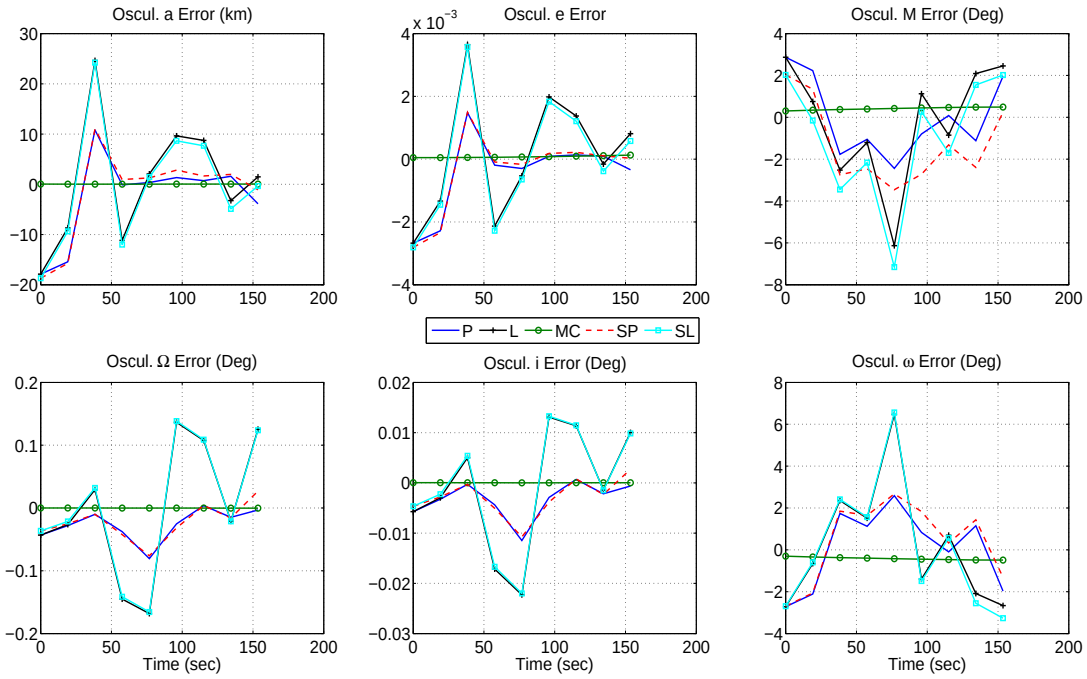

Figure 4.91: Increased Eccentricity Track 1 Osculating Orbital Element Error for TOV Bayes', Monte Carlo, and Similarity Transform

Figure 4.92 plots the osculating state domain uncertainty results of the TOV, similarity transform, and Monte Carlo analysis. The figure demonstrates that all three solutions are in good agreement with one another. The reason why the similarity transform closely tracks the TOV solutions is shown in Figure 4.93, which displays that the marginal PDFs of the TOV likelihood solution, for the first time in the track where the Herrick-Gibbs IOD algorithm could be applied then mapped to the osculating domain, can be approximated by a Gaussian so the similarity transform could be applied. Figure 4.93 matches very well with the Monte Carlo generated PDF contour plot as shown in Figure 4.94. The other marginal PDFs from the TOV likelihood analysis closely mimic their Monte Carlo counterparts and are shown in Appendix D.

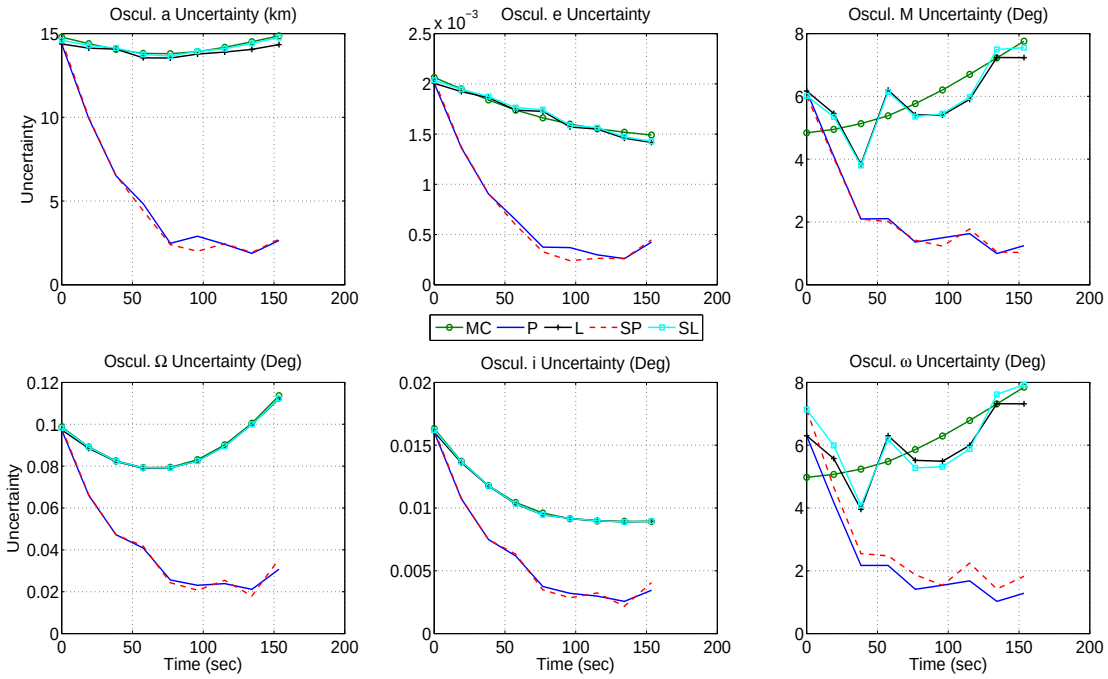

Figure 4.92: Increased Eccentricity Track 1 Osculating Orbital Element Uncertainty for TOV Bayes', Monte Carlo, and Similarity Transform

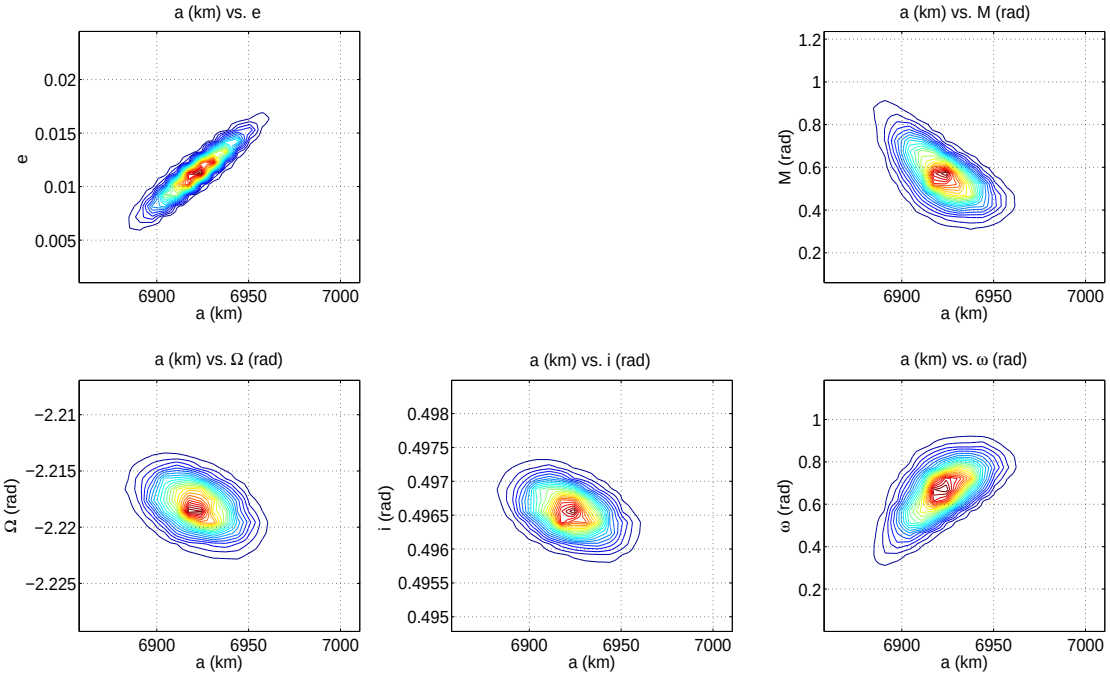

Figure 4.93: Increased Eccentricity Track 1 Osculating Orbital Element Marginal PDFs with respect to Semi-Major Axis from TOV Likelihood Solution

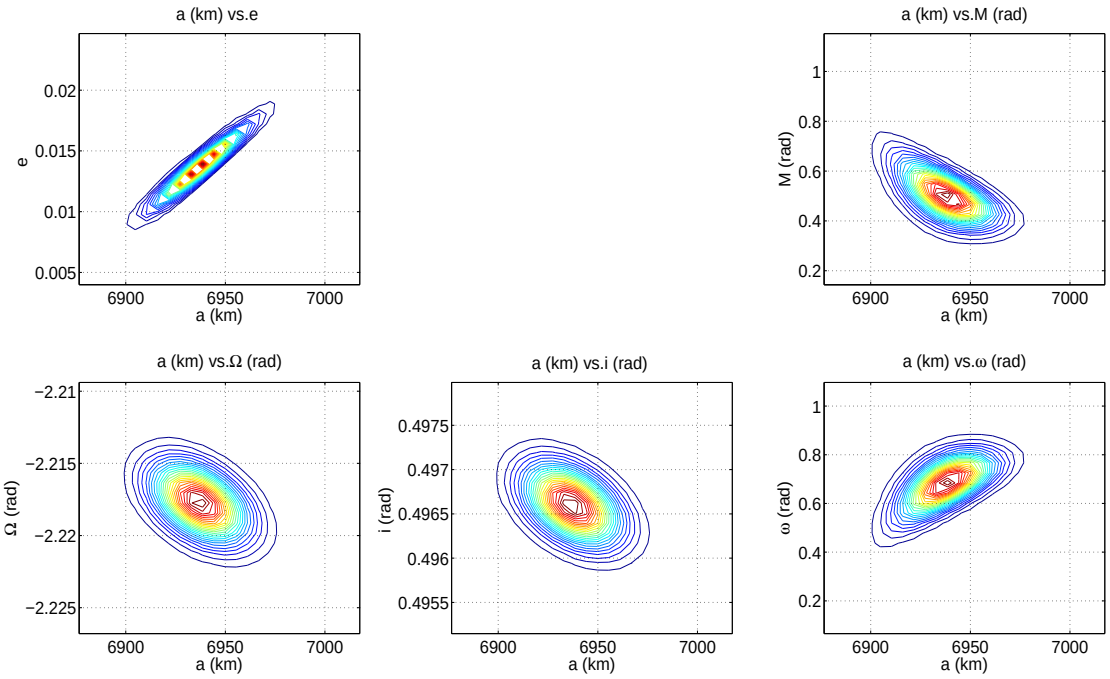

Figure 4.94: Increased Eccentricity Track 1 Osculating Orbital Element Marginal PDFs with respect to Semi-Major Axis from Monte Carlo Solution

The uncertainty bounds in Figure 4.93 for semi-major axis, eccentricity, right ascension of ascending node, and inclination are only slightly less than the original eccentricity case, but the argument of perigee and mean anomaly uncertainty bounds are smaller by approximately an order of magnitude compared with Figure 4.81. With this much improved PDF behavior, Figure 4.95 displays the state error and covariance bounds results for the TOV likelihood and Bayes' filter solutions. When compared with the original eccentricity solution, shown in Figure 4.85, the increased observability of perigee allows for the mean argument of perigee and mean mean anomaly solutions to be better defined.

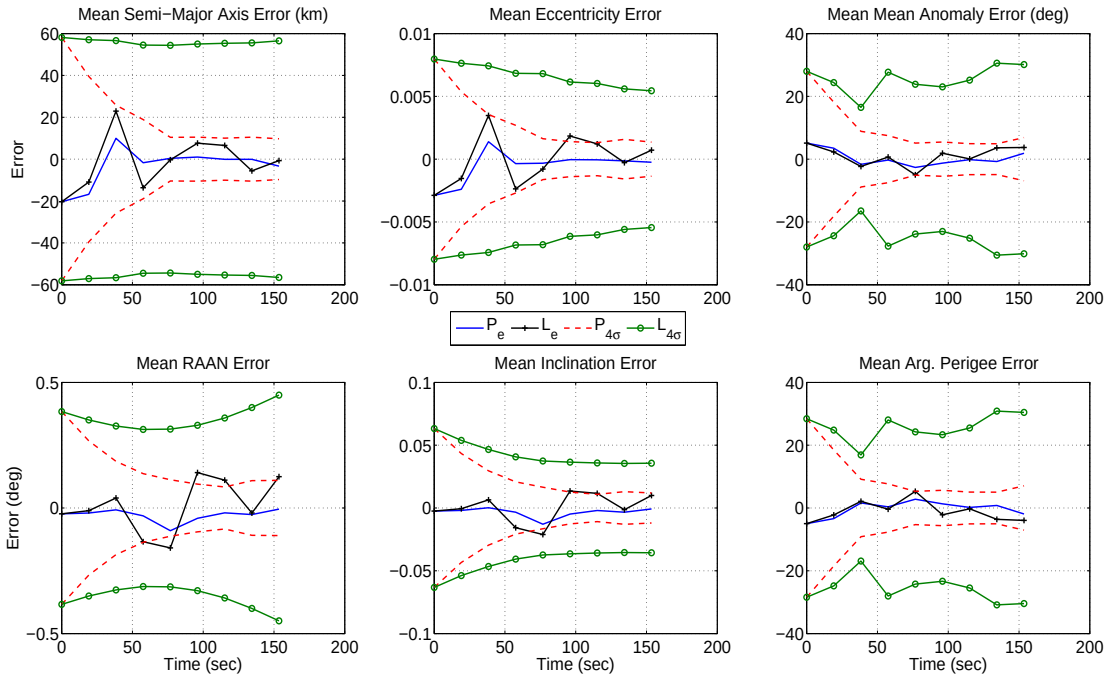

Figure 4.95: Increased Eccentricity TOV Bayes' Filter Operation for Track 1 Mean Orbital Elements

Figure 4.96 plots the state error for the TOV solutions, similarity transform, and Monte Carlo analysis. The figure shows no significant bias is present for the Monte Carlo solution, and the similarity transform of the Herrick-Gibbs solution to the mean element domain closely follows that of the TOV solutions. Figure 4.97 shows that the similarity transform solution for the mean domain does an acceptable job of tracking the TOV and Monte Carlo solutions for the mean semi-major axis, right ascension of ascending node, and inclination, but overestimates the eccentricity uncertainty by approximately 50%. The mean element marginal PDFs closely follow the shape of the osculating marginal PDFs, with the TOV likelihood analysis closely mimicking the Monte Carlo analysis, the results are shown in Appendix D

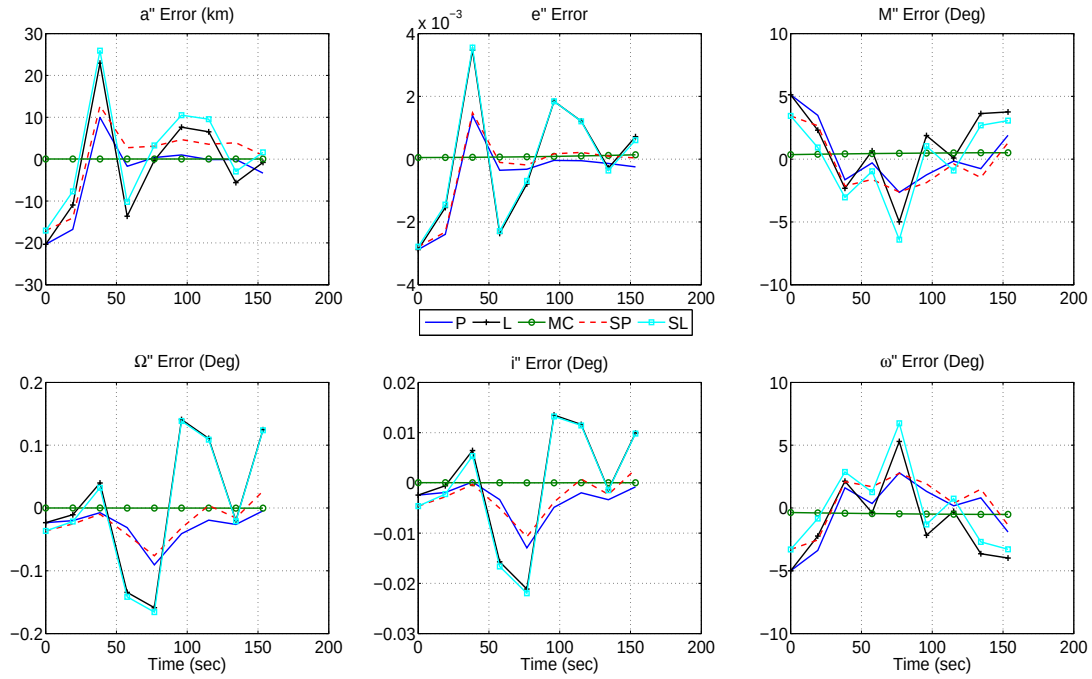

Figure 4.96: Increased Eccentricity Track 1 Mean Orbital Element Error for TOV Bayes', Monte Carlo, and Similarity Transform

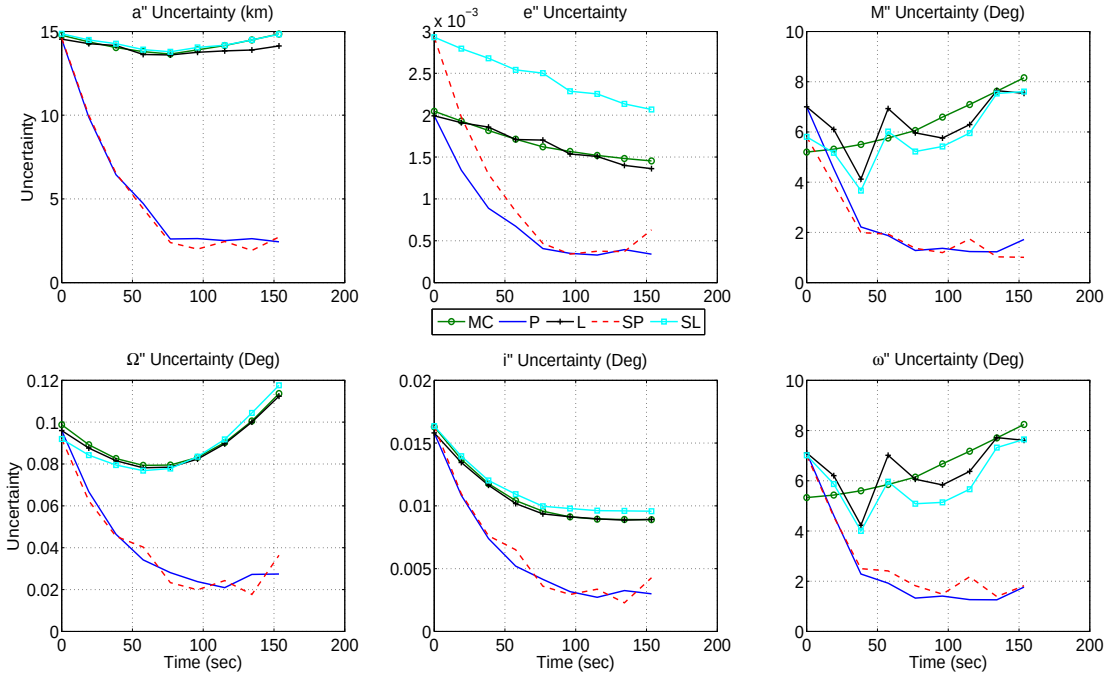

Figure 4.97: Increased Eccentricity Track 1 Mean Orbital Element Uncertainty for TOV Bayes', Monte Carlo, and Similarity Transform

From the mean anomaly and argument of perigee results, the magnitude of eccentricity plays a critical role in the estimation of a RSO's location in the orbit plane with respect to perigee. An alternative could be to use the equinoctial elements [72] or another nonsingular element set such as that used by Alfriend et al. [77]. Alternatively, instead of osculating mean anomaly one could use argument of latitude, $u = \omega + f$, which is computed from angular momentum and the ECI Cartesian position vector but, argument of perigee is still required so that the Cartesian velocity vector can be computed from the orbital element set. Assuming one were to proceed down this path, Figure 4.98 plots the TOV Bayes' filter and Monte Carlo uncertainty results using the original osculating elements of HST and using argument of latitude instead of mean anomaly.

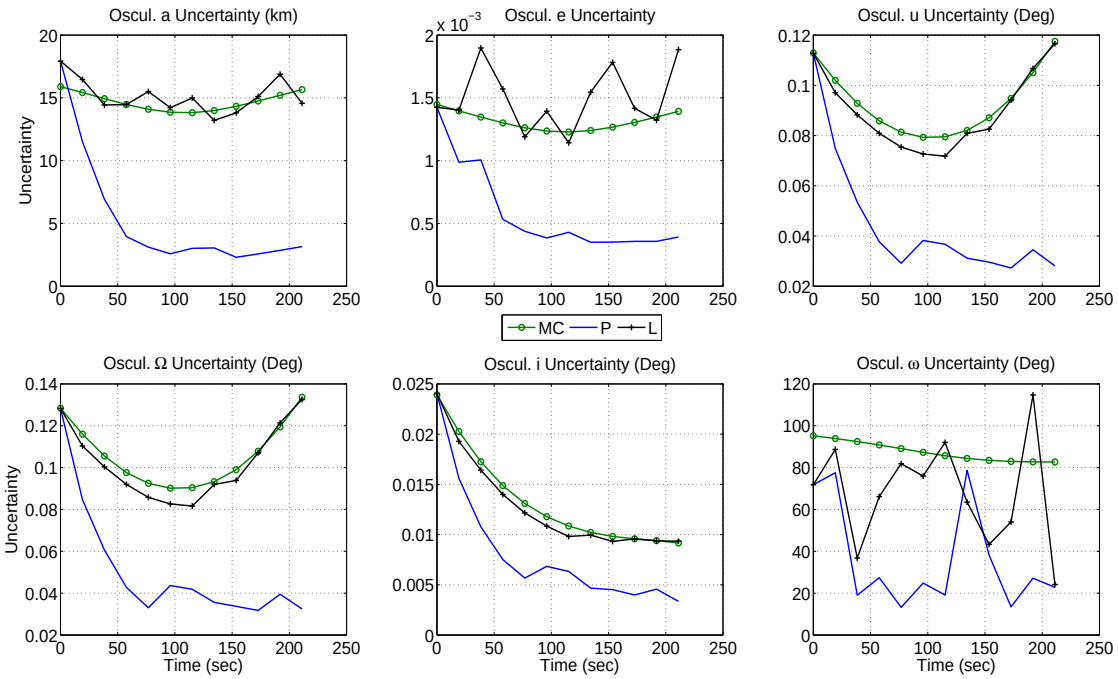

Figure 4.98: HST Track 1 Osculating Orbital Element Uncertainty for TOV Bayes' and Monte Carlo using Argument of Latitude instead of Mean Anomaly

Figure 4.98 shows that good Monte Carlo uncertainty tracking can be achieved

by using Keplerian states that do not require eccentricity directly in their calculation, however the argument of perigee uncertainty is still poor. One could take the approach of Izsak [57] and adopt the Hill set of range, argument of latitude, and right ascension of ascending node as the coordinates with the conjugate momenta given by range-rate, $G = \sqrt{\mu a(1-e^2)}$, and $H = G\cos(i)$ but, this set requires range-rate to be either directly measured or determined via smoothing. More importantly, by getting rid of the mean anomaly variable, one loses the ability to propagate linearly in time and one must convert to mean anomaly in order to use mean element theory. The nonsingular equinoctial-like elements which use a composite longitude, $\lambda = \omega + \Omega + M$, are an enticing set to explore along with the fact that Alfriend et al. [77] have derived the first-order transformation between mean and osculating domains as well as the mean element propagation equations.

4.4 Spacecraft Attitude Filtering

This section compares the state differential correction results of the MEKF and TOV Bayes' filter for attitude estimation of a slow-spinning spacecraft using a noise corrupted body frame measurements of reference stars and a rate gyro. Different sampling frequencies are examined to show filter sensitivity to measurement sparsity and the filters are also compared against the q-Method [60, 61] attitude determination algorithm with respect to principal angle of the attitude error matrix. The q-Method, Appendix E, is used for comparison since it computes the attitude estimate in quaternion form, which is also the basis of many modern attitude determination methods. The simulation was run for 300 seconds with the simulation constants given in Table 4.7.

Table 4.7: Simulation Conditions for Slow Spinning Spacecraft

Parameter	Value
Initial Attitude (True: $\hat{\mathbf{q}}_{True,0}$)	$[0.4020\ 0.0886\ -0.8546\ 0.3165]^T$
Initial Attitude Estimate ($\hat{\mathbf{q}}_{Estim,0}$)	$[0.4028\ 0.0888\ -0.8543\ 0.3164]^T$
Vehicle Angular Velocity	$[0.0\ 0.1\ 0.0]^T$ Rad/Sec
Measurement Noise ($\mathbf{v}_K \sim \mathcal{N}(\mathbf{0}_{3\times3}, \sigma^2_{Meas} I_{3\times3})$)	$\sigma_{Meas} = 20\ (9.7 \times 10^{-5})$ Arseconds (Rad)
Field of View $[\theta_X,\ \theta_Y]$	[10, 12] Deg x Deg
Max Star Visual Magnitude	6

The initial state estimate, which is used by both the MEKF and Bayes' filter, is computed by taking the true attitude and corrupting it with a multiplicative error model assuming a zero mean Gaussian angle error with standard deviation of 0.1 degrees. However, the initial estimate for the filters could also be computed from the q-Method then sequential iterated upon.

Five different sampling, propagation, intervals were examined: [1, 5, 10, 20, 25] seconds. The measurements from the rate gyro were assumed to be uncorrupted to evaluate the utility of the construction of the prior without considering the effects of process noise. The attitude error for the filters and q-Method is defined as the principal angle of rotation resulting from the the product of the true attitude direction cosine matrix and the transpose of the direction cosine matrix computed from the attitude determination routine, Equation (4.64), at evaluation time K.

$$\begin{aligned} \Delta &= C_{True,K} C^T_{Est,K} = C\left(\hat{\mathbf{q}}_{True,K}\right) C\left(\hat{\mathbf{q}}_{Estim,K}\right)^T \\ \phi &= \arccos\left\{\frac{1}{2}\left(\text{trace}\left(\Delta\right) - 1\right)\right\} \end{aligned} \tag{4.64}$$

In keeping in the same spirit as previous examples, a Monte Carlo solution for the differential corrections was computed for comparison with the TOV Bayes' filter. The solution was computed by computing N_{Trials} =1000 corrupted body frame measurements for each star that was in the Field-of-View then computing the direction cosine matrix corresponding to each corrupted measurement by applying Equation (3.72) using the propagated previous quaternion estimate. This yielded a matrix of size $[3 \times (1000 n_{Meas})]$, n_{Meas}= total number of stars in the Field-of-View. Using this Monte Carlo resultant matrix, a solution of the estimated update and corresponding covariance were computed using the numerical representations of the first and second moments of a random vector, Equation (4.65).

$$\begin{aligned} \bar{\delta\mathbf{q}}_K &= \frac{1}{N_{Trials} \times n_{Meas}} \sum_{i=1}^{N_{Trials} \times n_{Meas}} \left(C\left(\delta\mathbf{q}\right) \rightarrow \delta\mathbf{q}\right)_{i,K} \\ P_K &= \frac{1}{N_{Trials} \times n_{Meas} - 1} \sum_{i=1}^{N_{Trials} \times n_{Meas}} \left(\mathbf{resid}_{i,K}\ \mathbf{resid}_{i,K}^T\right) \\ \mathbf{resid}_{i,K} &= \left(C\left(\delta\mathbf{q}\right) \rightarrow \delta\mathbf{q}\right)_{i,K} - \bar{\delta\mathbf{q}} \end{aligned} \tag{4.65}$$

4.4.1 Principal Angle of Attitude Error Matrix Results

Figures 4.99 through 4.103 plot the principal angle of the attitude error for the MEKF, q-Method, and TOV Bayes' filter for the different measurement time intervals. Two different results of the Bayes' filter are plotted, one showing the results of TOV likelihood, TOV_L, and the second showing the results of using the previous measurement time's observations, TOV_1, to compute a prior density for the domain of the differential corrections for the vector part of the quaternion.

From the figures, it is apparent that the TOV Bayes' filter has better performance with respect to error compared to the MEKF for approximately the first 50 seconds. Around 50 seconds, the MEKF is able to converge to a steady-state

covariance solution for the differential correction estimate. Additionally, the TOV likelihood solution at the initial measurement time possesses much less error than the MEKF or q-Method. Comparison of the TOV likelihood solution to the TOV Bayes' posterior shows that consideration of measurements at the previous measurement time has a smoothing effect on the differential state estimate and reduces the variance of the solution time history. This smoothing effect reduces the amount of overall attitude error accrued over the simulation time.

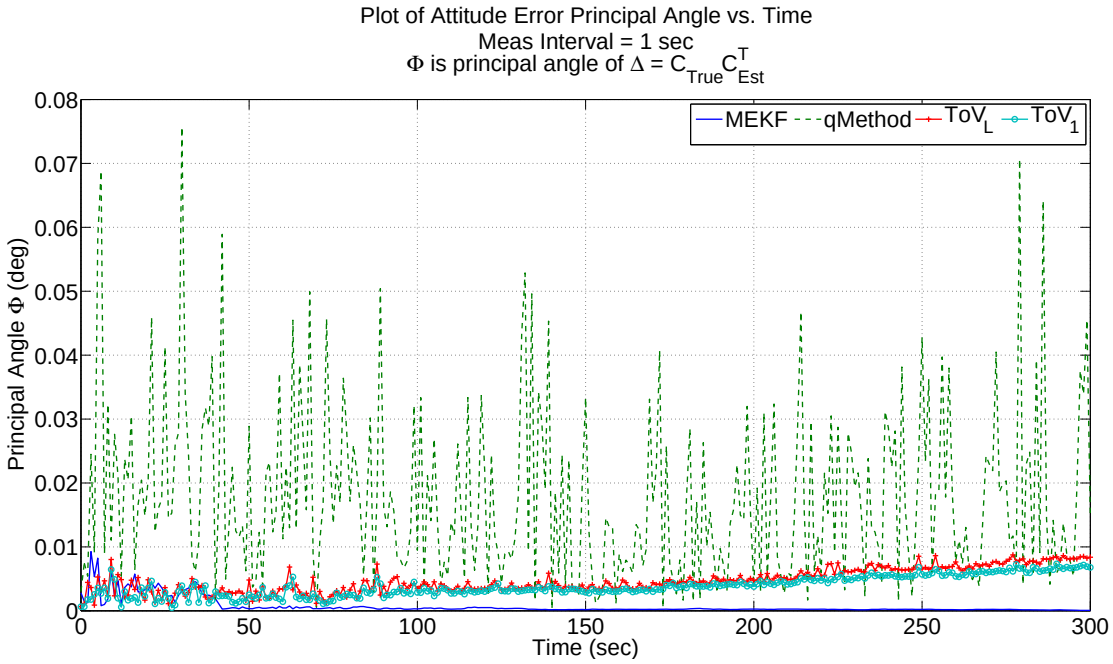

Figure 4.99: Attitude Error Time History with Measurements Every 1 Second

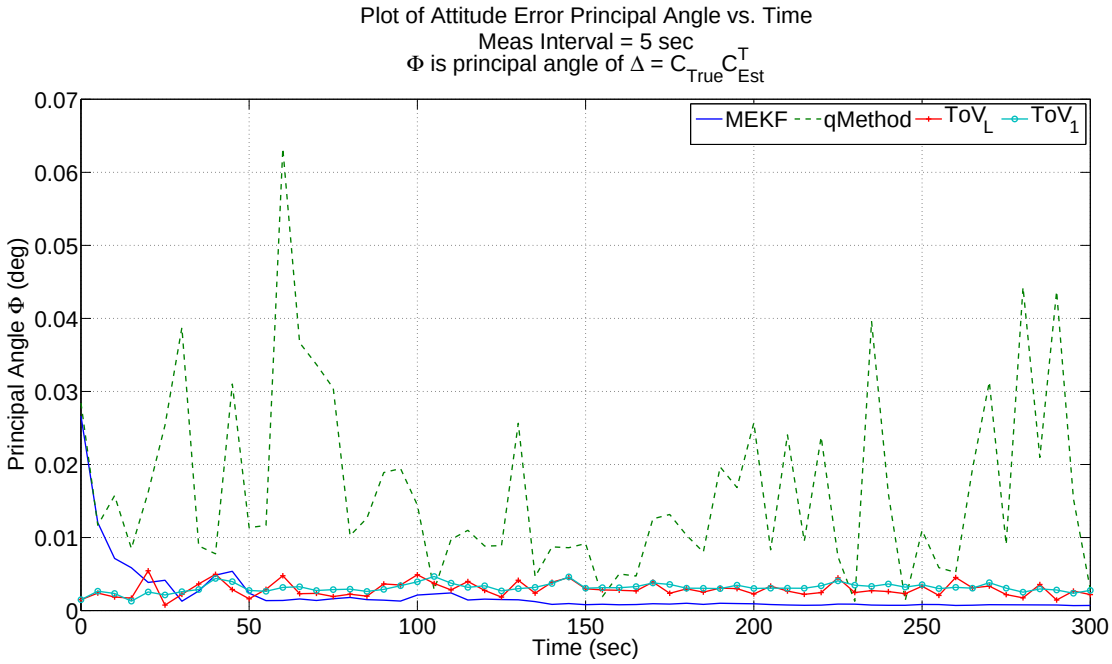

Figure 4.100: Attitude Error Time History with Measurements Every 5 Seconds

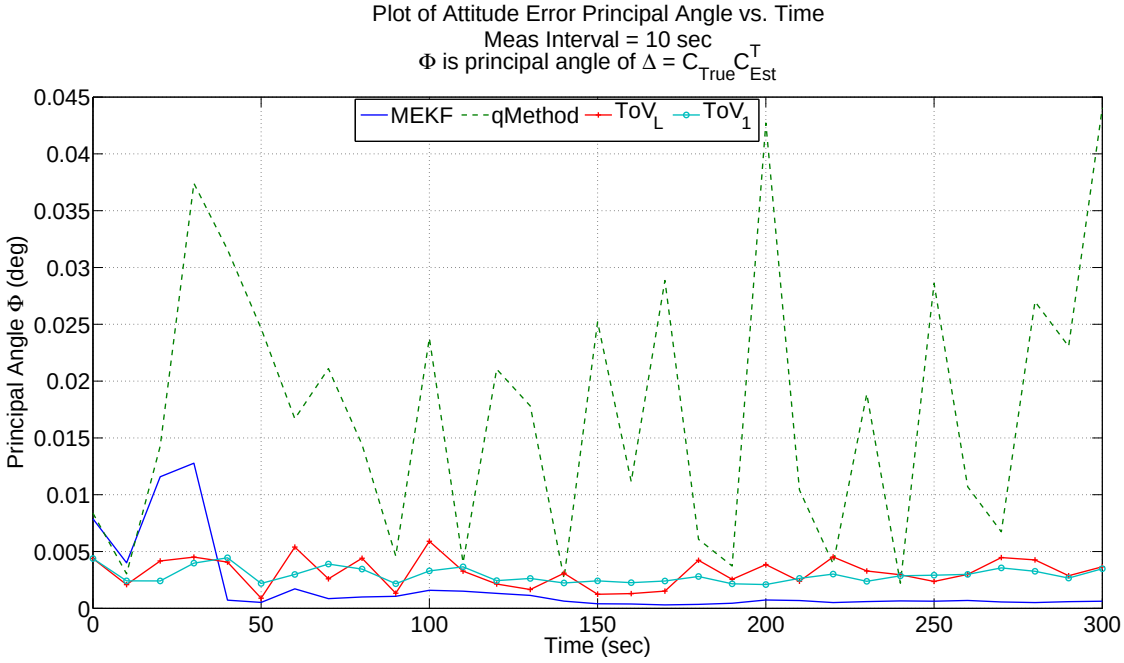

Figure 4.101: Attitude Error Time History with Measurements Every 10 Seconds

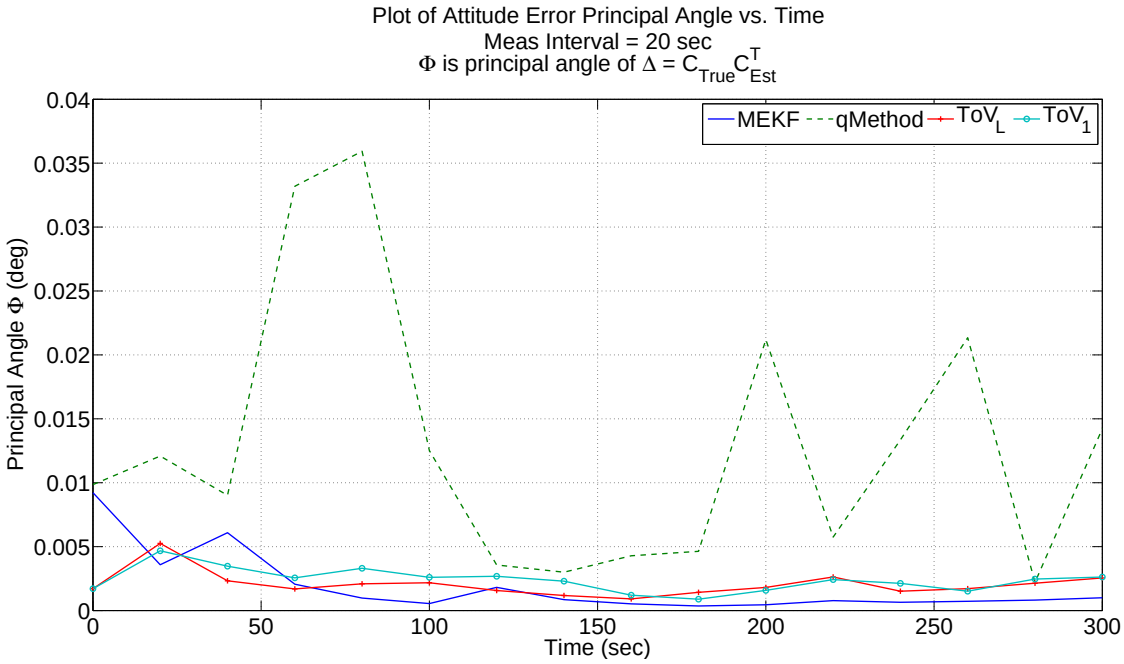

Figure 4.102: Attitude Error Time History with Measurements Every 20 Seconds

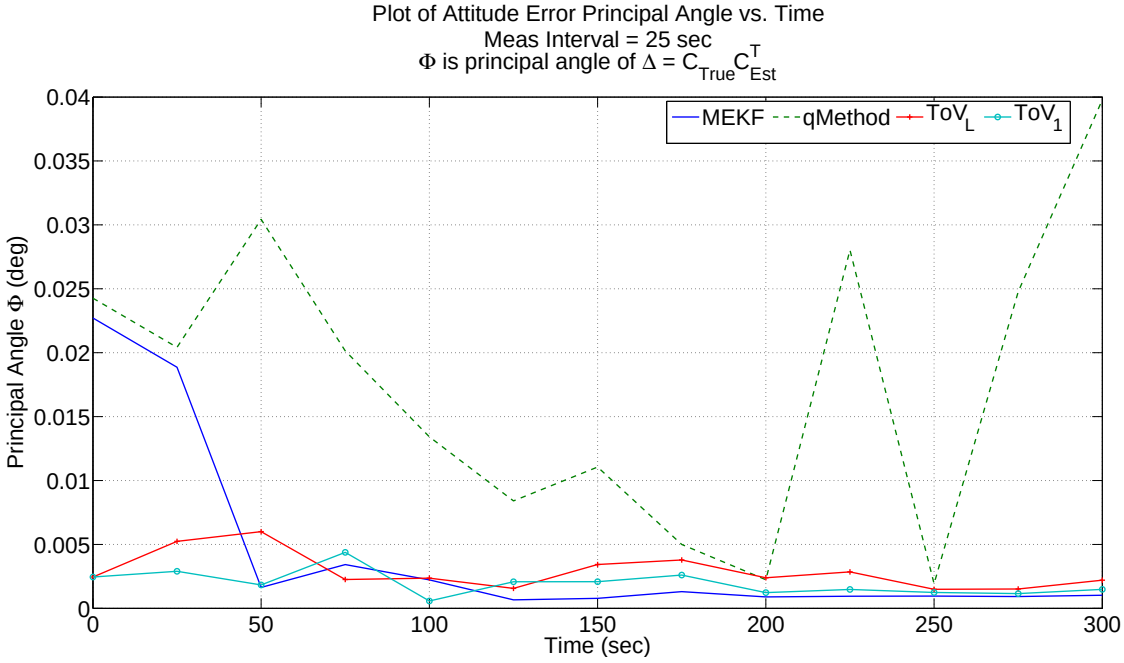

Figure 4.103: Attitude Error Time History with Measurements Every 25 Seconds

4.4.2 Error and Covariance Performance of MEKF and TOV Bayes' Filter Results

Figures 4.104 through 4.105 plot the error and covariance results for the MEKF for all three differential correction angles. The covariance bounds plotted are the 3σ bounds from the square root of the diagonal of the covariance matrix produced by the filter. Only the 1 second sampling and 25 second sampling instances are shown because the behavior for the other three trials follows suit. Examination of the diagonal element behavior of the MEKF covariance shows that at approximately 50 seconds the variance stops changing which coincides with the principal angle of attitude error results.

Figures 4.106 through 4.110 plot the error and covariance results for the TOV Bayes' filter for all three differential correction angles. For the TOV Bayes' filter, the results had to be multiplied by an additional factor of two since the filter dealt with the quaternion corrections directly and not the differential angles as the MEKF did. Examination of the TOV Bayes' filter uncertainty bounds verifies the results of the principal angle of attitude error results in that the variance of the nonuniform prior density reduced the uncertainty bounds for the primary and second angles, while the tertiary angle differential correction bounds remained relatively unchanged. Comparison of the magnitude of the bounds between the TOV Bayes' filters and the MEKF show that the MEKF possesses tighter bounds, which is to be expected because of the pole shifting nature of the covariance update in the Kalman filter which minimizes the trace of the updated covariance. However, increasing the number of prior data used in construction of the nonuniform prior density will cause the same effect so long as the filter is converging.

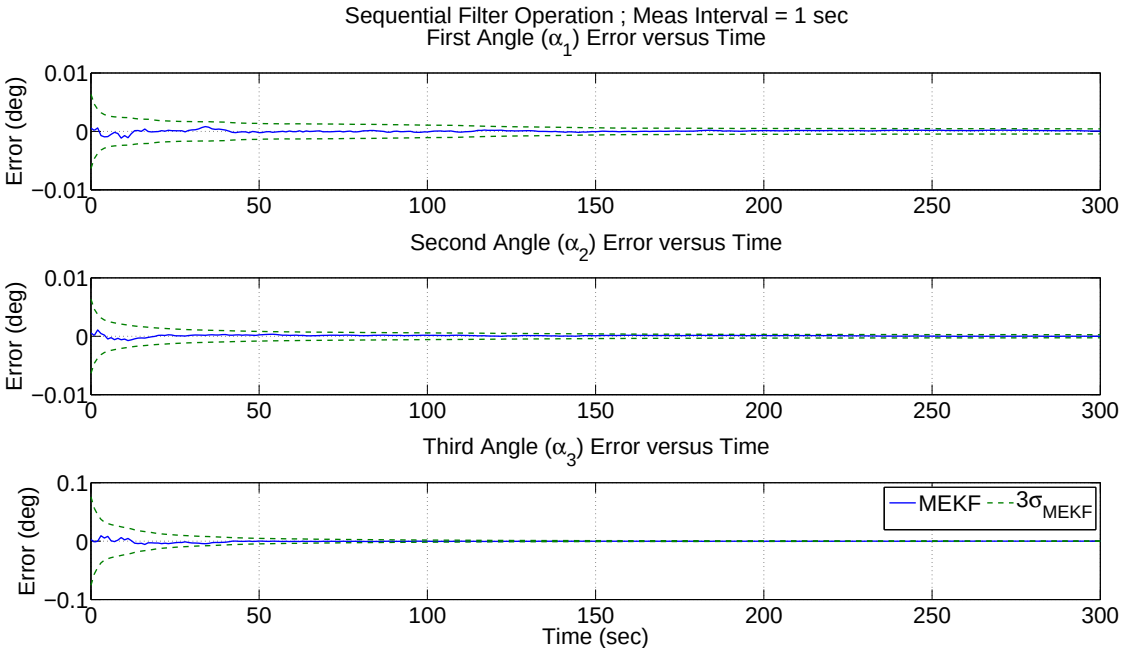

Figure 4.104: MEKF Quaternion Vector Correction Error and 3σ Bounds with Measurements Every 1 Second

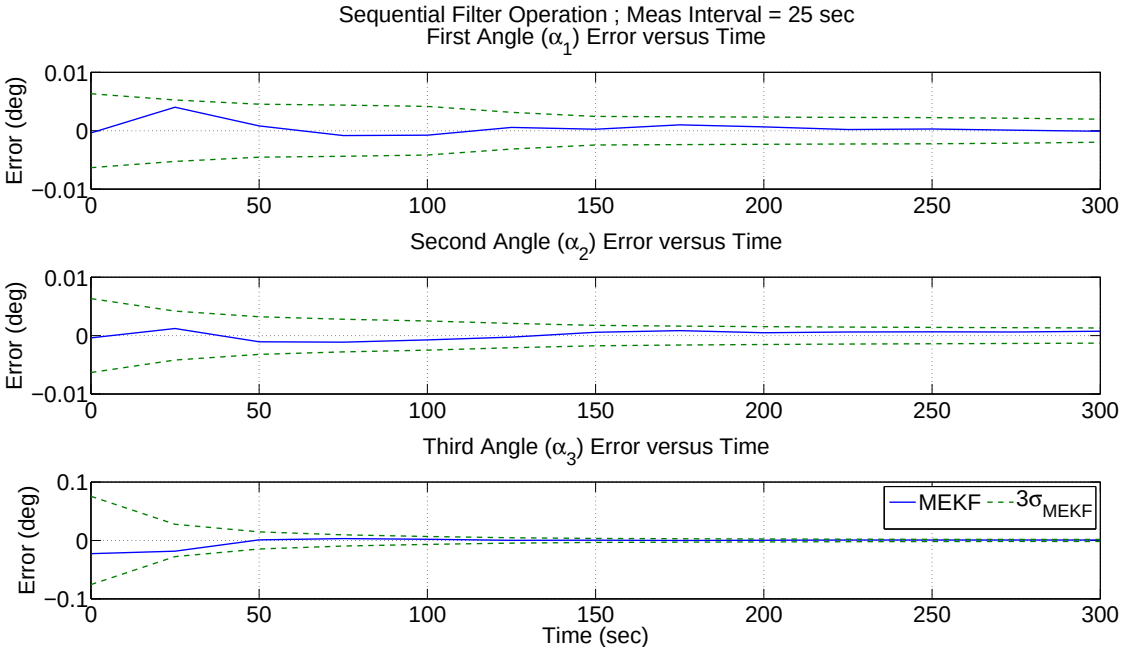

Figure 4.105: MEKF Quaternion Vector Correction Error and 3σ Bounds with Measurements Every 25 Seconds

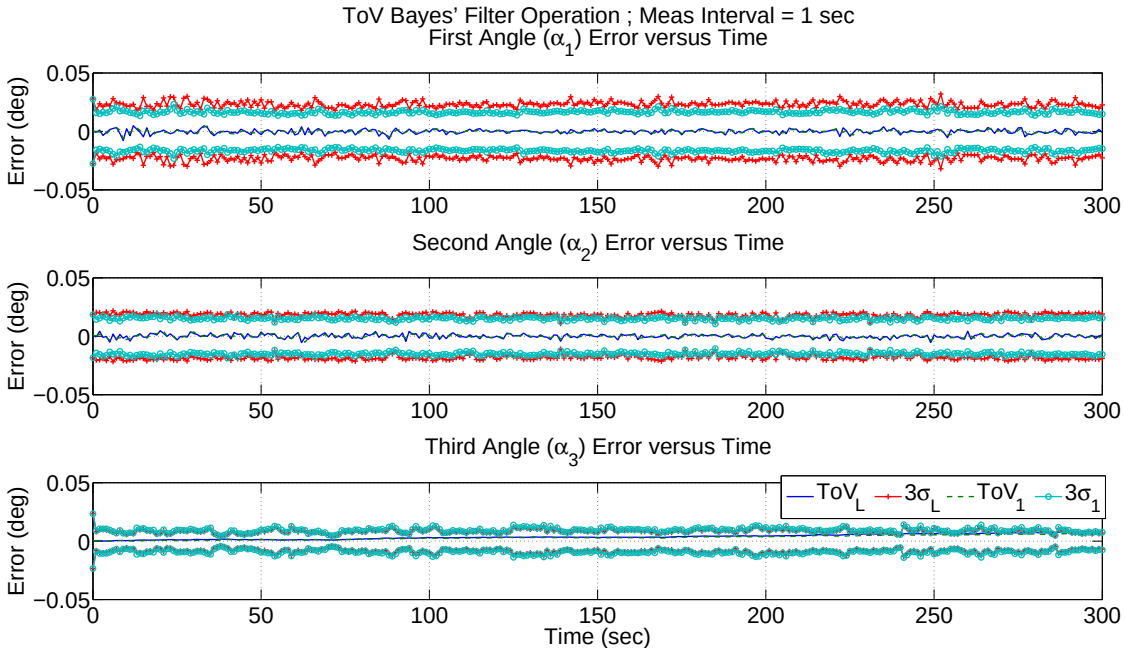

Figure 4.106: TOV Bayes' Filter Quaternion Vector Correction Error and 3σ Bounds with Measurements Every 1 Second

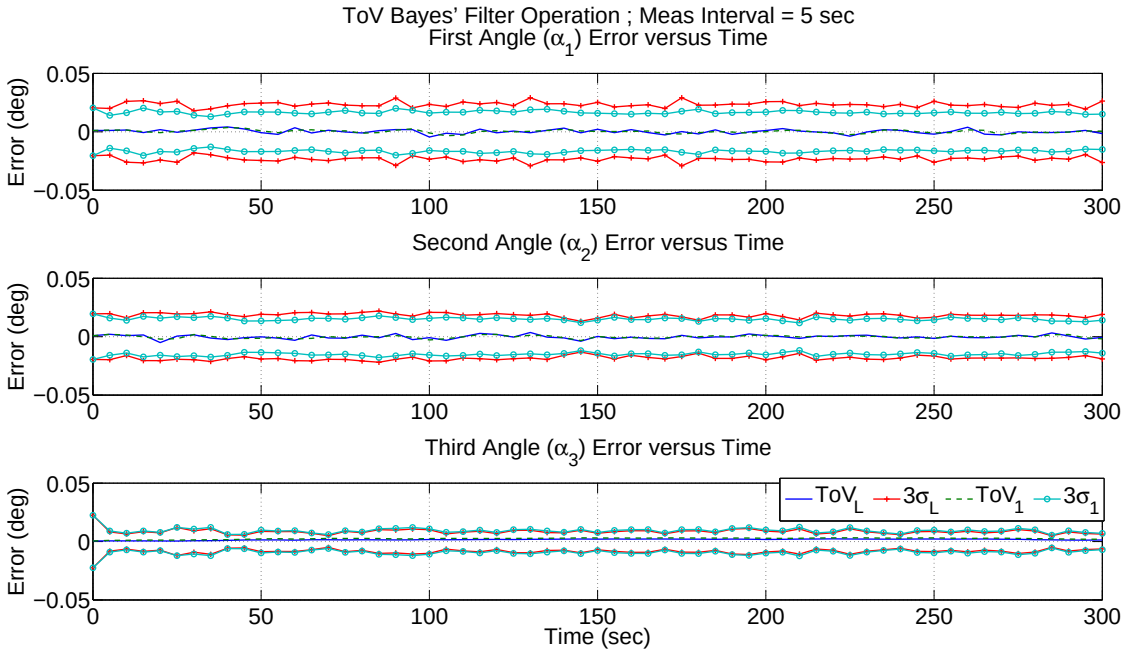

Figure 4.107: TOV Bayes' Filter Quaternion Vector Correction Error and 3σ Bounds with Measurements Every 5 Seconds

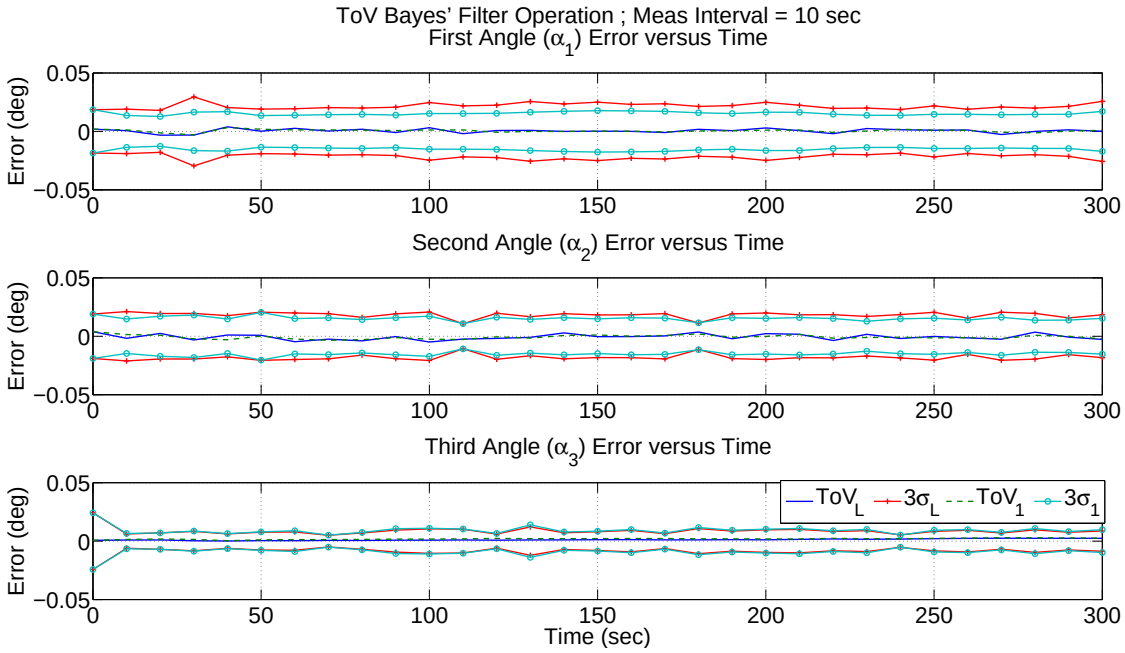

Figure 4.108: TOV Bayes' Filter Quaternion Vector Correction Error and 3σ Bounds with Measurements Every 10 Seconds

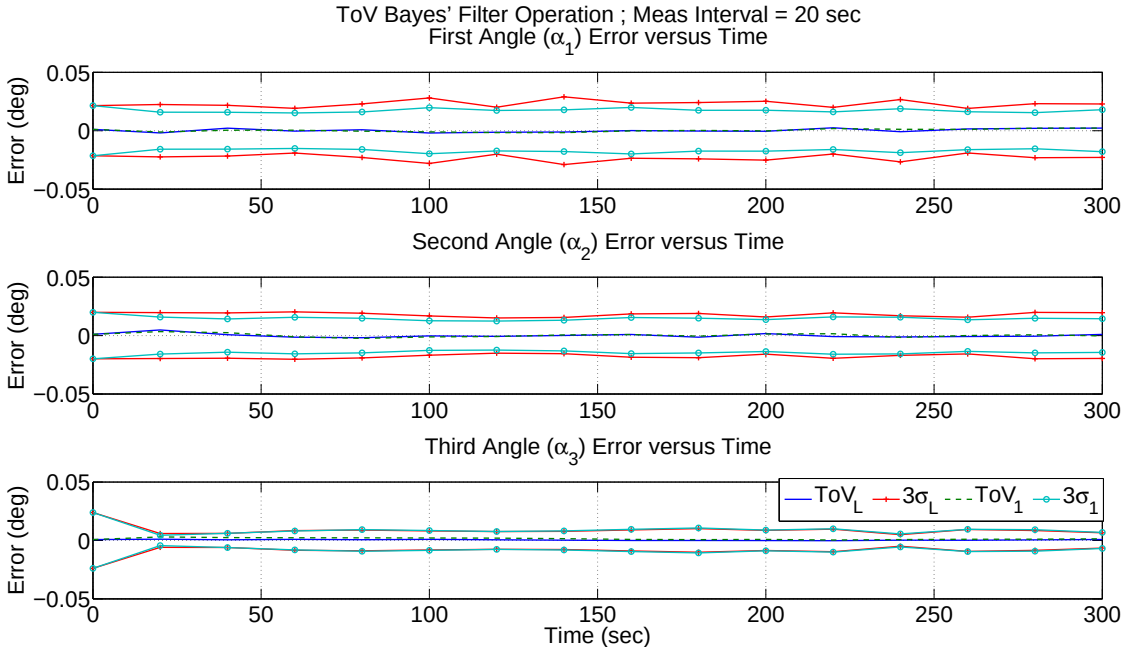

Figure 4.109: TOV Bayes' Filter Quaternion Vector Correction Error and 3σ Bounds with Measurements Every 20 Seconds

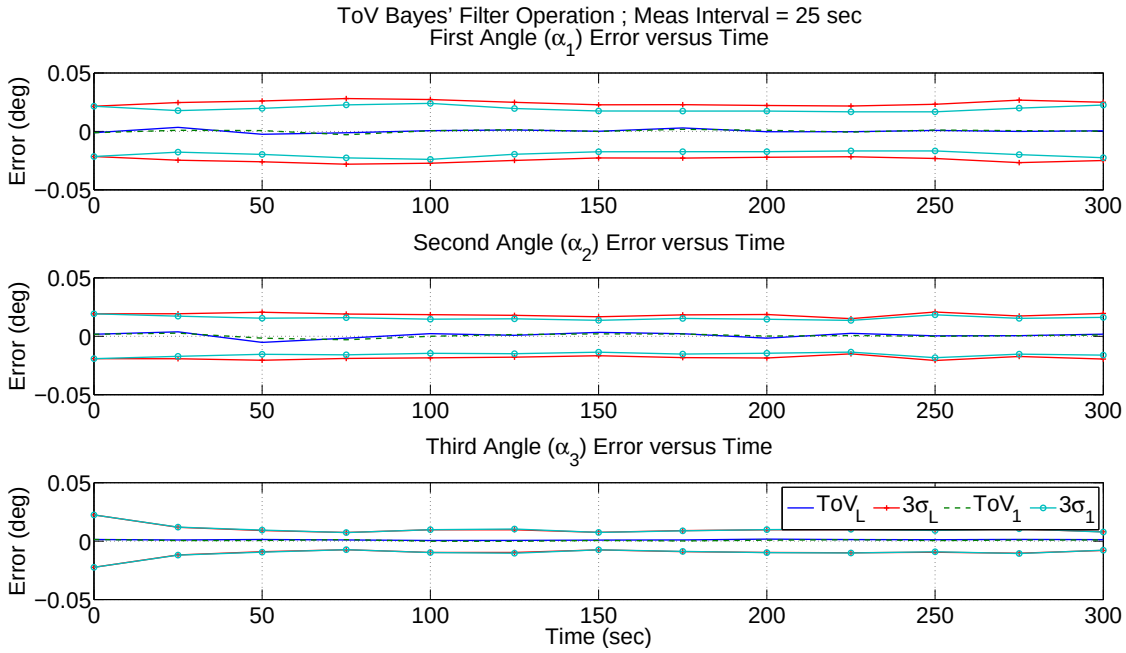

Figure 4.110: TOV Bayes' Filter Quaternion Vector Correction Error and 3σ Bounds with Measurements Every 25 Seconds

4.4.3 Monte Carlo State Error and Covariance Tracking Performance of TOV Bayes' Filter Results

Figures 4.111 through 4.120 compare the state error and covariance results of the Monte Carlo analysis and the TOV likelihood and TOV Bayes' filter using a prior PDF generated from the previous measurement time. On average, the likelihood state solution was better able to track the Monte Carlo solution, but both TOV solutions possessed biases, which was also encountered in previous examples. The figures show that the TOV likelihood was better able to track the Monte Carlo covariance solution in some instances while in others the reverse was true but, construction of a prior density allowed for better tracking of the Monte Carlo covariance and reduced the amount of oscillation in attitude error, as alluded to before. The former result is to be expected since using only the likelihood solution allows for less incursion of a biased solution due to propagation in a biased previous solution.

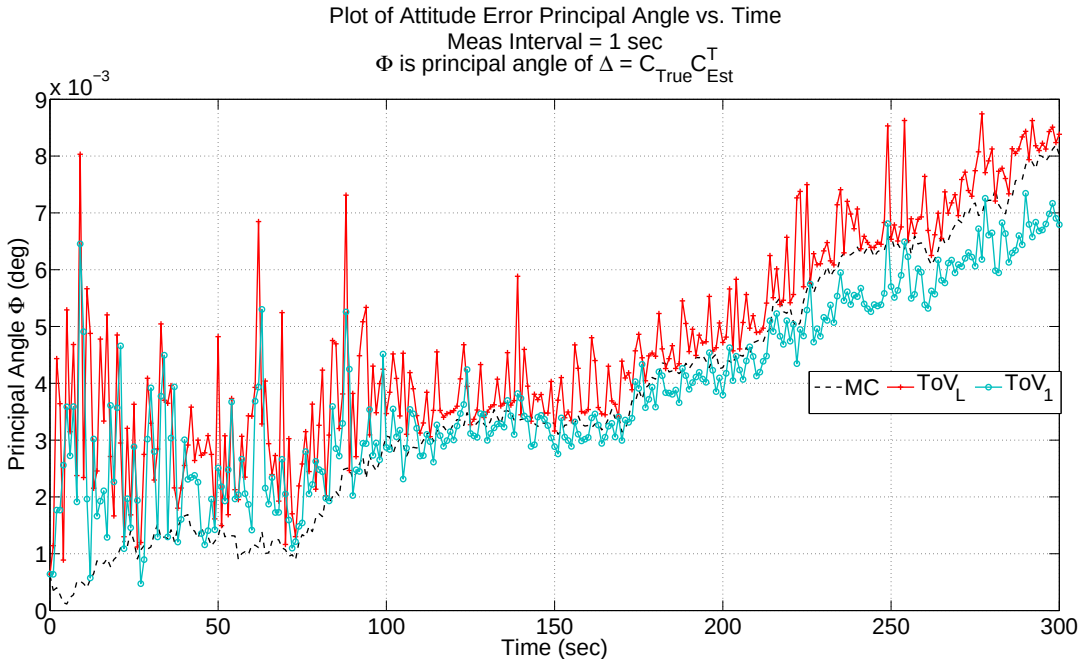

Figure 4.111: TOV Bayes' Filter Error Angle Tracking of Monte Carlo Solution with Measurements Every 1 Second

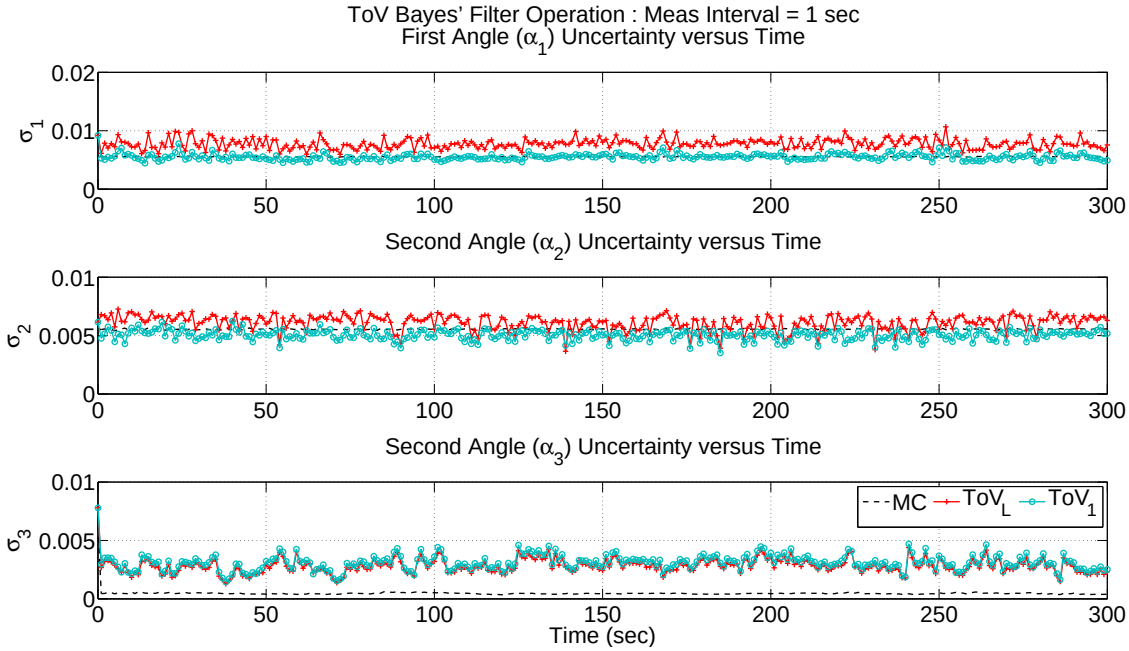

Figure 4.112: TOV Bayes' Filter Standard Deviation Tracking of Monte Carlo Solution with Measurements Every 1 Second

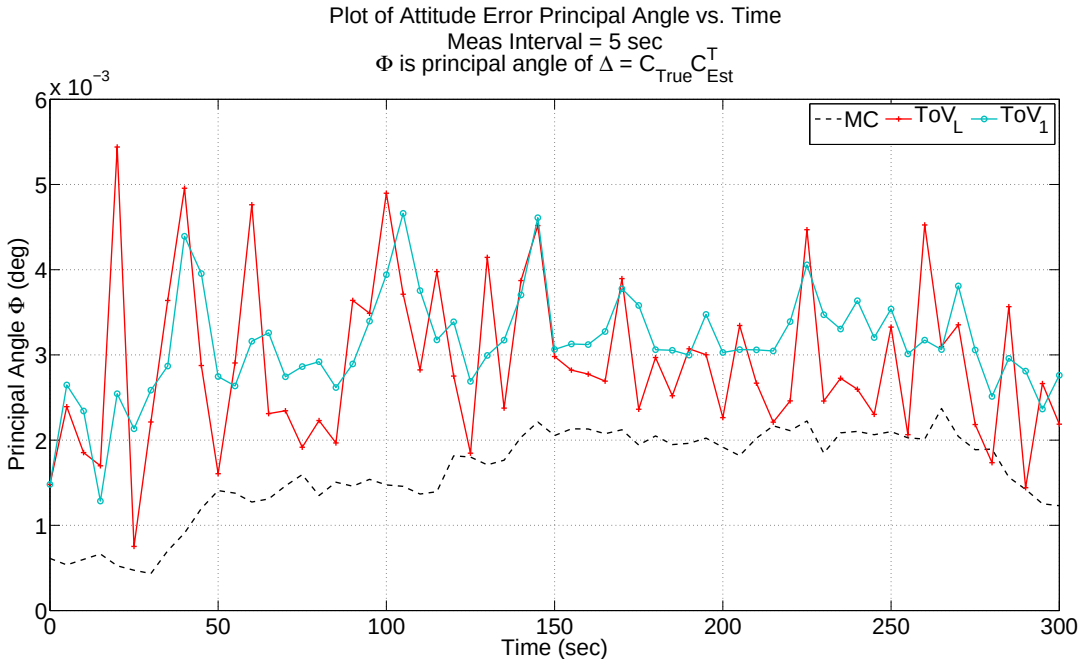

Figure 4.113: TOV Bayes' Filter Error Angle Tracking of Monte Carlo Solution with Measurements Every 5 Seconds

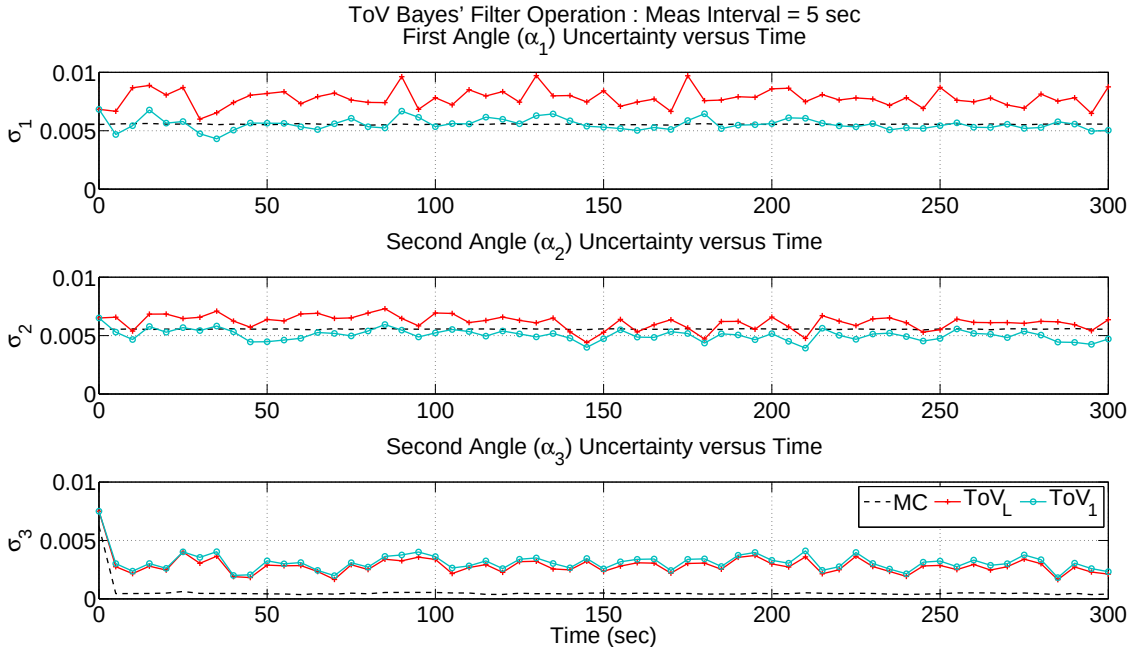

Figure 4.114: TOV Bayes' Filter Standard Deviation Tracking of Monte Carlo Solution with Measurements Every 5 Seconds

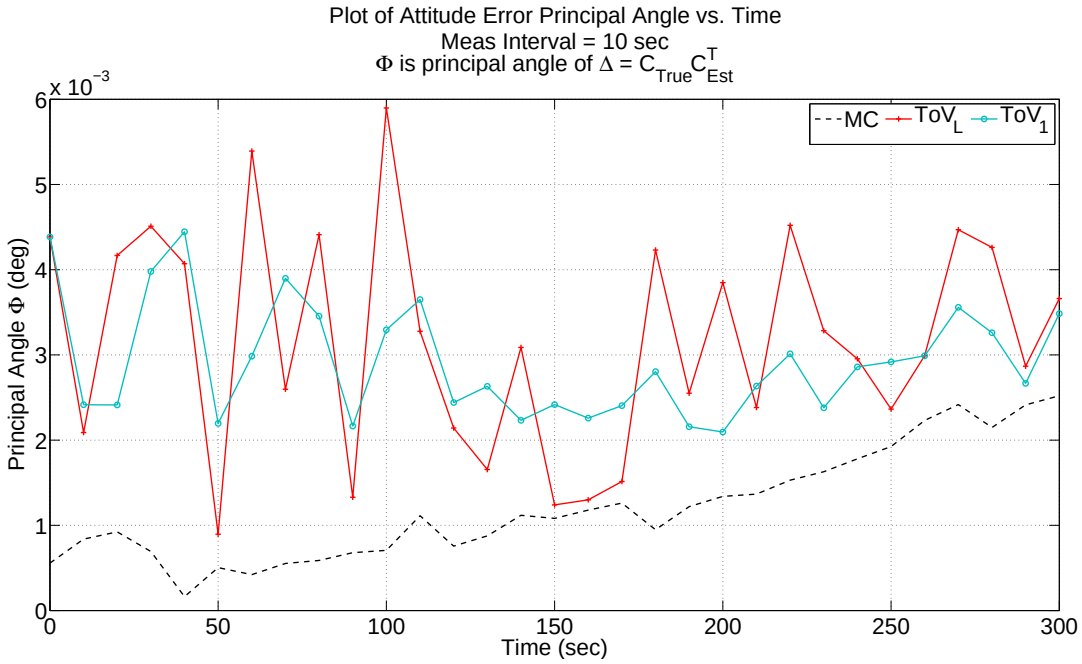

Figure 4.115: TOV Bayes' Filter Error Angle Tracking of Monte Carlo Solution with Measurements Every 10 Seconds

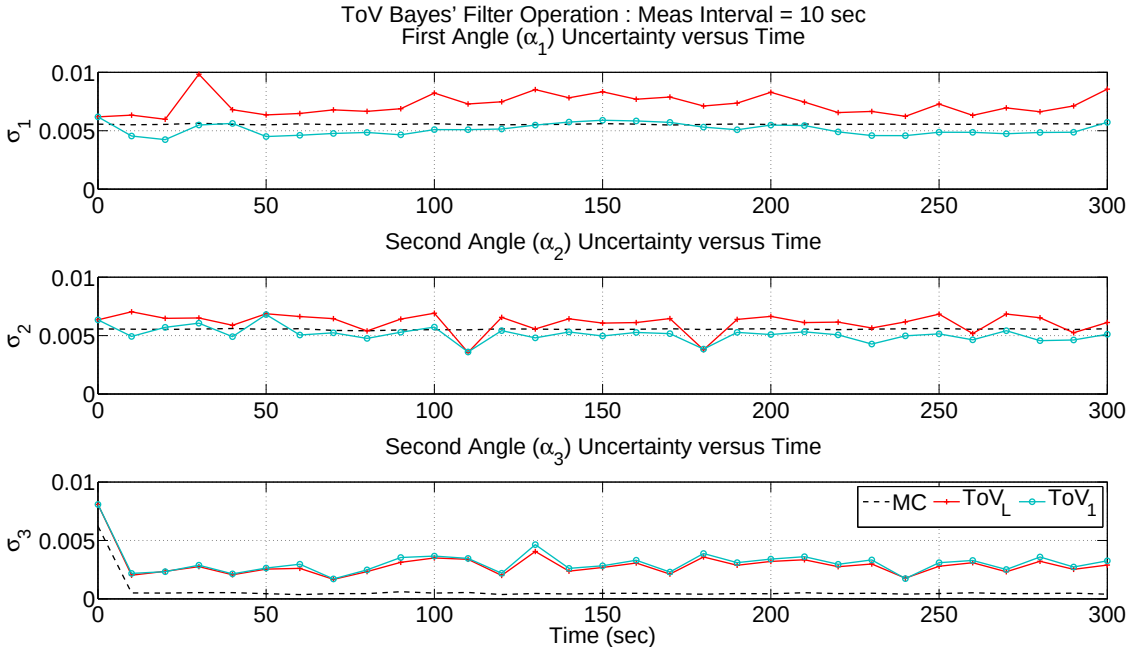

Figure 4.116: TOV Bayes' Filter Standard Deviation Tracking of Monte Carlo Solution with Measurements Every 10 Seconds

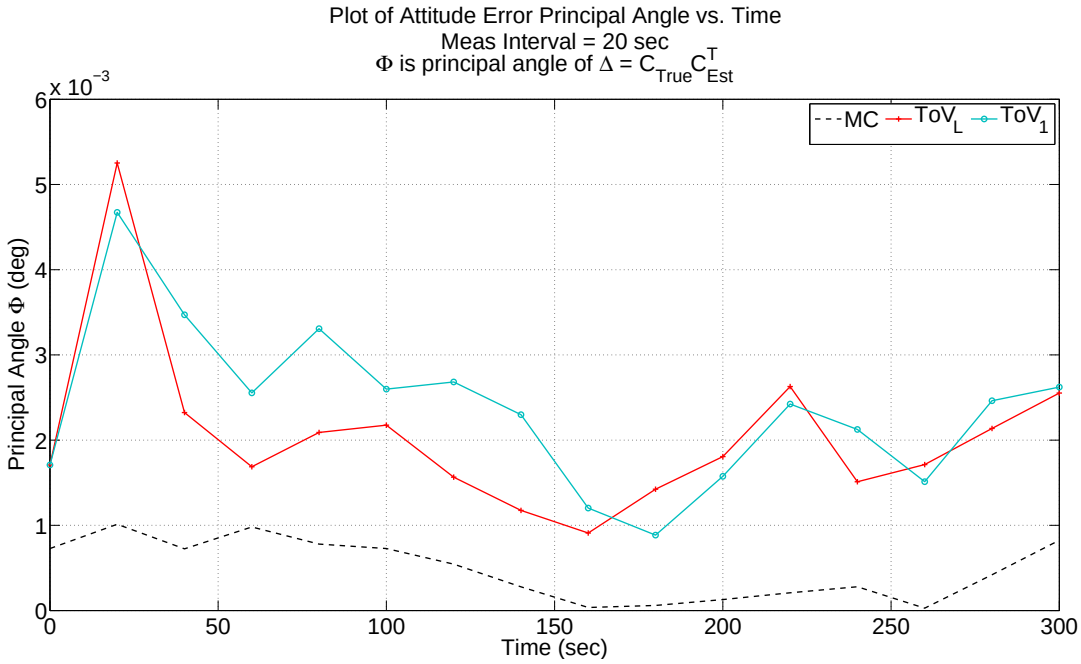

Figure 4.117: TOV Bayes' Filter Error Angle Tracking of Monte Carlo Solution with Measurements Every 20 Seconds

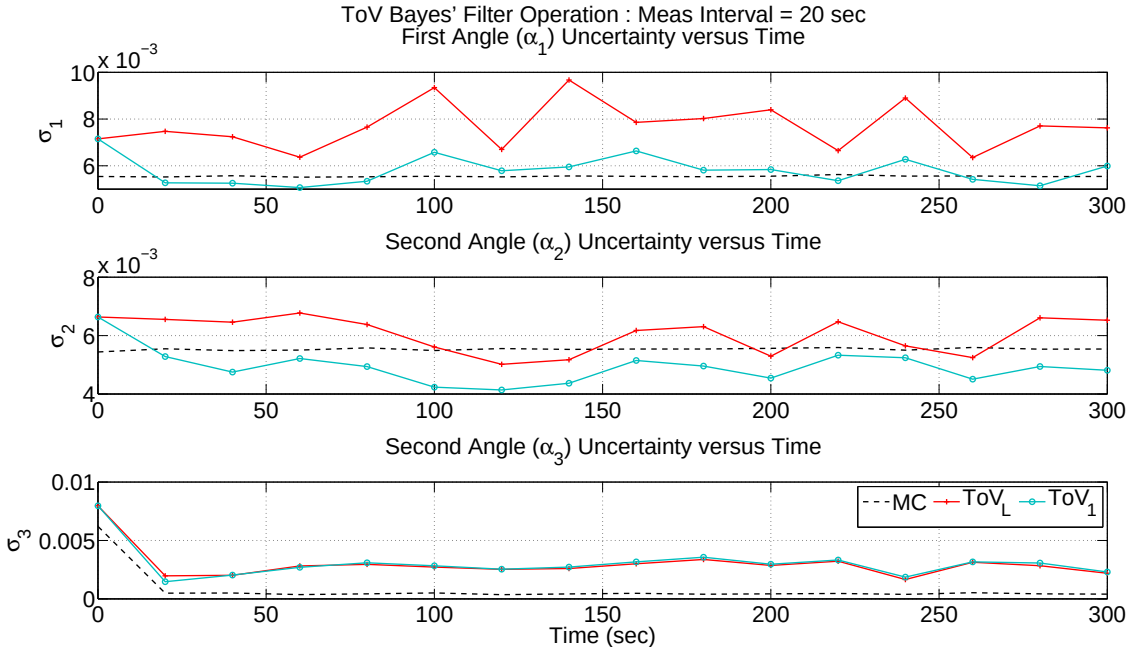

Figure 4.118: TOV Bayes' Filter Standard Deviation Tracking of Monte Carlo Solution with Measurements Every 20 Seconds

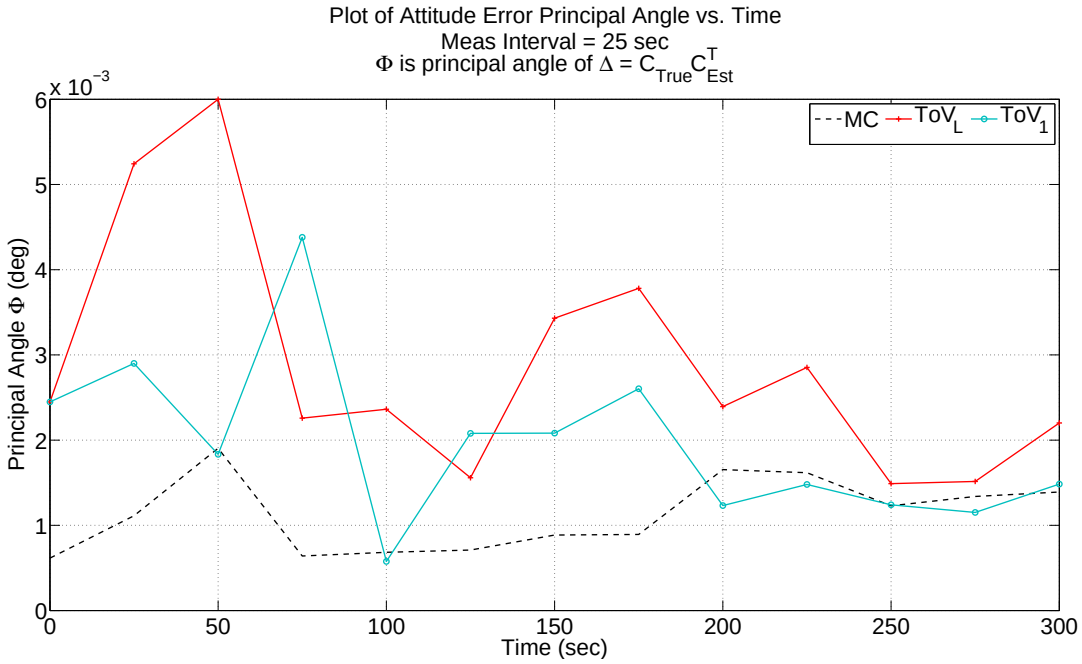

Figure 4.119: TOV Bayes' Filter Error Angle Tracking of Monte Carlo Solution with Measurements Every 25 Seconds

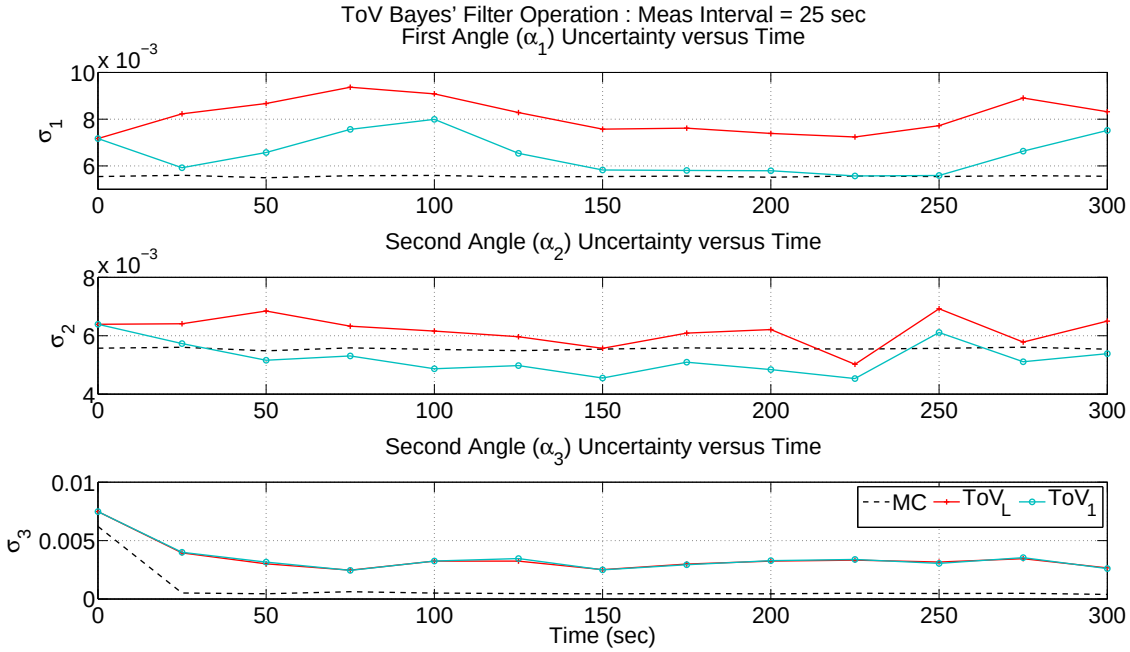

Figure 4.120: TOV Bayes' Filter Standard Deviation Tracking of Monte Carlo Solution with Measurements Every 25 Seconds

5. CONCLUSIONS

5.1 Conclusions

In this work, application of the transformation of variables technique provided valuable assessment of the impact nonlinear transformations have on the uncertainty associated with indirectly observed states, with particular focus to space surveillance and spacecraft attitude estimation applications. The technique exactly mapped analytic forms of probability density functions between spatial and temporal domains instead of proposing higher order corrections to lower order moments or numerically or heuristically approximating the state probability distribution. The nonlinear transformations investigated consisted of spatial domain mappings as well as spatial-temporal mappings used to estimate velocity level states when only position level measurements were available. By effectively utilizing all available information, the transformation of variables technique enabled an analytical approach to hypothesis testing and uncertainty characterization of poorly known system parameters for mathematical model refinement.

Transformation of variables demonstrated that the Gaussian assumption typically used for the likelihood and posterior state distributions may not always be appropriate, due to nonlinearities and non-constant scale factors introduced by nonlinear transformations. The approach was also shown to provide an analytical criterion for the particular conditions under which the similarity transform, commonly applied to map state uncertainties, could be appropriately applied. Application of the technique to commonly encountered nonlinear transformations demonstrated the presence of higher order moments and complicated correlations for certain states. This behavior is in contrast to conventional nonlinear filters which assume statistical behavior only

up through the second moment and that the state distribution exhibits symmetry.

Since the technique allowed for direct utilization of probability density functions, Bayes' Theorem was able to be directly applied to compute the appropriate state posterior probability density function, after calculation of the likelihood and prior probability density functions. The likelihood probability density function, computed from the measurement domain, allowed the filter to capture the actual state distribution dispersion relatively accurately, compared with Monte Carlo analysis of the process. The transformation of variables technique was applied to map the state posterior distribution at a previous time to the present measurement time to serve as prior distribution, which reduced the state error and uncertainty. The approach for construction of the prior via transformation of variables was found to be acceptable because the technique was shown to yield the same solution as Liouville's equation, which describes the evolution of distribution functions for conservative systems.

From the examples shown, the transformation of variables technique allows for appropriate quantification of state uncertainty and correlation due to nonlinear transformations of domain variables. The technique was shown to accurately account for how uncertainty is mapped across domains, which allows for confirmation or refutation of the uncertainty distribution in the desired domain. From the linear minimal smoother, nonlinear over-constrained smoother, and state differential correction examples, transformation of variables provided correct assessment of the state uncertainty and correlation impact. As a byproduct of appropriately accounting for nonlinear transformations, the technique was shown to be a good candidate for automating state and covariance initialization of conventional nonlinear filters, which improved filter operation. Direct computation of the likelihood and prior probability density functions enabled application of Bayes' Theorem in recursive fashion, which produced more accurate state tracking results than the likelihood solution alone.

The constructed Bayes' filter facilitated appropriate combination of sensor measurements, state estimates, and state propagation in different domains while conserving uncertainty across all the utilized domains.

For the linear system examples of the arcing mass and linear oscillator, state estimates of the Bayes' filter using transformation of variables were found to improve as additional data was utilized since the prior distribution was able to better pinpoint areas of maximum likelihood. In cases of position only measurements with the requirement of position and velocity estimation, the Bayes' filter/smoother utilizing transformation of variables was found to produce position error results comparable to the full sensing case with somewhat larger velocity errors. The likelihood solution of the uncertainty and correlation due to the smoothing process was found to mimic the Monte Carlo simulation of the smoothing process. The larger errors in the velocity estimate were to be expected and were attributed to the smoothing algorithm used to estimate velocity states from corrupted position data. The likelihood solution was found to be effective in initializing the state estimate and covariance of the extended Kalman filter, using only the analytic form of the measurement domain probability density function and the measurement data at the initial time. The linear oscillator example demonstrated that the algorithm could be effectively applied to surveillance applications where significant data drop-outs exist between tracks. When damping was treated as an unknown parameter, the presented algorithm was shown to be a viable means to estimate system parameters and their associated uncertainties. Use of the constructed posterior density to hypothesize on the damping coefficient provided a reliable means to generate confidence bounds on the parameter estimate even when significant gaps existed between observations.

In the space surveillance examples, the transformation of variables technique was effectively employed to map the probability density function of the sensor domain to

many different state domains depending on the type of problem considered. In all the space surveillance examples considered, the transformation of variables approach allowed for successful construction of an accurate filter which used a limited amount of data but, was able to appropriately assess the uncertainty and correlation effects of a nonlinear smoother. Analysis of the transformation from spherical measurement frame to the Cartesian frame enabled effective assessment of the uncertainty and correlation associated with the Herrick-Gibbs initial orbit determination routine. By appropriately accounting for the state uncertainty and correlation due to the nonlinear smoother, the technique was shown to be a viable option for automating the initialization of the extended and unscented Kalman filters. Comparison of the transformation of variables likelihood solution to the Monte Carlo solution of nonlinear smoother using nonlinear measurements of state variables showed that one now has an analytic, instead of heuristic, way to estimate state correlation or uncertainty for initializing the covariance of conventional nonlinear filters. The automated initialization improved the convergence of the extended Kalman filter and reduced the error fluctuation of the unscented Kalman filter. Automated initialization of the covariance for the extended and unscented Kalman filters was shown to drastically increase the tracking performance of state uncertainty and correlation.

For the planar Keplerian motion examples, analysis of the transformation to the osculating orbital element frame allowed the use of a single linear equation for state propagation. Additionally, the use of mean anomaly was shown to produce more accurate state estimation results than use of true anomaly across different orbit types. The orbit eccentricity was found to play a vital role in the uncertainty estimation of argument of perigee and mean anomaly. As the considered orbit types became more circular, the eccentricity vector location became less defined, this lead to larger uncertainty into how to appropriately split the argument of latitude. The recom-

mendation of using nonsingular elements was posed for simplicity so that one did not have to switch between domains depending upon orbit type. The transformation of variables approach was able to show when the singular nature of the element set was starting to affect state estimation and a switch to a nonsingular element set was needed, e.g. when state uncertainty was of the same order as the state estimate.

Transformation of variables was further applied to a three-dimensional geopotential perturbed orbit and demonstrated effective combination of different domains for state uncertainty and correlation characterization. The measurements were made in the spherical domain while the Cartesian domain was used for initial orbit determination and the mean element domain was used for uncertainty propagation.

As orbit eccentricity grew closer to zero, the osculating argument of perigee and mean anomaly were affect the most. When mean anomaly was exchanged for argument of latitude, the state uncertainty was well characterized and only the argument of perigee element possessed significant error. However, by exchanging argument of latitude for mean anomaly, one loses the ability to linearly propagate in time which is the lure of the osculating domain. When the osculating domain was mapped into the mean element domain, all orbital elements were affected due to dependence on the osculating eccentricity, whose error was on the order of the true value for both the transformation of variables and Monte Carlo solutions. The accuracy of the similarity transformation for mapping state covariance between domains was also examined and shown to be inappropriate for cases of low eccentricity and only applicable for certain states the mean element domain. For orbit types without the eccentricity singularity affecting state uncertainty, the similarity transformation worked rather well as an approximation. However, the similarity transform solution relied heavily upon the transformation of variables solution of the Herrick-Gibbs initial orbit determination routine which closely agreed with the Monte Carlo solution.

The attitude determination example demonstrated that the transformation of variables technique could be applied with Bayes' Theorem to effectively estimate differential corrections to state variables in lieu of direct state estimation. The computational burden of the transformation of variables Bayes' filter was more than that of the multiplicative extended Kalman filter but, as the measurement sampling rate decreased the transformation of variables filter possessed a more accurate solution. The likelihood solution of the transformation of variables approach possessed lower error than the multiplicative extended Kalman filter until the Kalman filter covariance solution reached steady-state operation.

5.2 Future Work

Coupling the damped linear oscillator, with observation gaps and model uncertainty, results with the space surveillance examples, the transformation of variables Bayes' filter approach appears to be a good candidate for estimating the ballistic coefficient of objects in the low Earth orbit. This would be a good extension to pursue since the two-line element set for the object reports a ballistic coefficient using a cannonball drag model. Since differential correction is often used for computation of the element set, transformation of variables would be able to directly assess the amount of uncertainty associated with the lumped parameter estimation scheme. Continuing along the hypothesis testing line of thought, if an object is observed using only angles and/or angular rates, the associated range and range-rate could be hypothesized using domain constraints from prior work performed in the astrodynamic community for angles-only tracking, e.g. energy and other visibility constraints.

The approach presented could also be used for correlating successive object tracks by propagating the uncertainty, in a canonical space where the momenta are constant, to the next estimated time of object passage and comparing the result with

the measurement likelihood at that time. This could be attractive to the space surveillance community since object states are reported in mean elements where the conjugate momenta are constant, producing a linear time update for the coordinates. With respect to sensor tasking, the technique could be used to determine if additional tracking resources need to be devoted to an object, depending upon the amount of information provided by a given sensor or combination of different sensors or sensor sites.

As alluded to in the attitude determination example, the algorithm in this work did not consider an update to the noise corrupted gyro measurement. Since the effect of process noise was not considered in this research, it should be considered to see if an acceptable approximation to the Fokker-Planck-Kolmogorov equation can be computed for certain applications with nonconservative perturbing forces or processes with a higher degree of uncertainty. The technique could also be employed for rendezvous or proximity operations to more accurately determine when or if the uncertainty volumes of two objects will coincide. This could be done similarly to object correlation with the objects' respective probability density functions propagated to a common epoch and compared. The amount of probability density function overlap could then be used as a metric for determining if vehicles should maneuver or it they should be more closely monitored to prevent unnecessary fuel usage.

REFERENCES

[1] Taylor, B. N. and Kuyatt, C. E., "Guidelines for Evaluating and Expressing the Uncertainty of NIST Measurement Results," Technical Note NIST 1297, United States Department of Commerce Technology Administration: National Institute of Standards and Technology, 1994.

[2] Papoulis, A., *Probability, Random Variables, and Stochastic Processes*, McGraw-Hill, Boston, MA, 3rd ed., 1991, pp. 135-148, 151-154, 164-166, 169-170, 192-195, 297-303, 635-654.

[3] Junkins, J. L., Akella, M. R., and Alfriend, K. T., "Non-Gaussian Error Propagation in Orbital Mechanics," *Journal of Astronautical Sciences*, Vol. 44, No. 4, Oct.-Dec. 1996, pp. 541–563.

[4] Junkins, J. L. and Singla, P., "How Nonlinear Is It? - A Tutorial of Orbit and Attitude Dynamics," *Journal of Astronautical Sciences*, Vol. 52, No. 1-2, 2004, pp. 7–60.

[5] Vallado, D. A., *Fundamentals of Astrodynamics and Applications*, Microcosm, Hawthorne, CA, 3rd ed., 2007, pp. 103-119, 153-167, 708-711, 721-722, 783-792, 806-811, 817-823.

[6] Hill, K., Alfriend, K. T., and Sabol, C., "Covariance-based Uncorrelated Track Association," *AIAA/AAS Astrodynamics Specialist Conference and Exhibit*, Honolulu, HI, Aug. 18-21 2008, AIAA 2008-7211.

[7] Sabol, C., Sukut, T., Hill, K., Alfriend, K. T., adn You Li, B. W., and Schumacher, P., "Linearized Orbit Covariance Generation and Propagation Analysis

via Simple Monte Carlo Simulations," *AAS/AIAA Spaceflight Mechanics Meeting*, San Diego, CA, Feb. 14-17 2010, AAS 10-134.

[8] Scheeres, D. J., Hsiao, F.-Y., Park, R., Villac, B., and Maruskin, J., "Fundamental Limits on Spacecraft Orbit Uncertainty and Distribution Propagation," *Journal of Astronautical Sciences*, Vol. 54, No. 3-4, 2005, pp. 505–523.

[9] Park, R. S. and Scheeres, D. J., "Nonlinear Mapping of Gaussian Statistics: Theory and Applications to Space- craft Trajectory Design," *Journal of Guidance, Control, and Dynamics*, Vol. 29, No. 6, Nov.-Dec. 2006, pp. 1367–1375.

[10] Fujimoto, K., Scheeres, D., and Alfriend, K., "Analytical Nonlinear Propagation of Uncertainty in the Two-Body Problem," *Journal of Guidance, Control, and Dynamics*, Vol. 35, No. 2, Mar.-Apr. 2012, pp. 497–509.

[11] Majji, M., Junkins, J. L., and Turner, J. D., "High Order Keplerian State Transition Tensors," *AAS/AIAA F. Landis Markley Astronautics Symposium*, Cambridge, MD, Jun. 29 - Jul. 2 2008, AAS 08-270.

[12] Turner, J. D., Majji, M., and Junkins, J. L., "High-Order State and Parameter Transition Tensor Calculations," *AIAA/AAS Astrodynamics Specialist Conference*, Honolulu, HI, Aug. 18-21 2009, AIAA-2008-6453.

[13] Manoranjan Majji, John L. Junkins, J. D. T., "A High Order Method for Estimation of Dynamic Systems," *Journal of Astronautical Sciences*, Vol. 56, No. 3, Jul.-Sep. 2008, pp. 401–440.

[14] Manoranjan Majji, John L. Junkins, J. D. T., "A Perturbation Method for Estimation of Dynamic Systems," *Nonlinear Dynamics*, Vol. 60, No. 3, 2010, pp. 303–325.

[15] Ristic, B., Arulampalam, S., and Gordon, N., *Beyond the Kalman Filter: Particle Filters for Tracking Applications*, Artech House, Norwood, MA, 2004, pp. 4-9, 19-32, 35-57.

[16] Crassidis, J. L. and Junkins, J. L., *Optimal Estimation of Dynamic Systems*, CRC Press, Boca Raton, FL, 2004, pp. 24-29, 81-84, 92-95, 123-128, 132-139, 149-154, 285-289, 310-314, 419-430, 450-463, 549, 553-567.

[17] Vallado, D. A. and Seago, J. H., "Covariance Realism," *AAS/AIAA Astrodynamics Specialist Conference*, Pittsburg, PA, Aug. 9-13 2009, AAS 09-304.

[18] Lerro, D. and Bar-Shalom, Y., "Tracking with Debiased Consistent Converted Measurements versus EKF," *IEEE Transactions on Aerospace and Electronic Systems*, Vol. 29, No. 3, Jul. 1993, pp. 1015–1022.

[19] Longbin, M., Xiaoquan, S., Yiyu, Z., Kang, S. Z., and Bar-Shalom, Y., "Unbiased Converted Measurements for Tracking," *IEEE Transactions on Aerospace and Electronic Systems*, Vol. 34, No. 3, Jul. 1998, pp. 1023–1027.

[20] Stone, L. D., Barlow, C. A., and Corwin, T. L., *Bayesian Multiple Target Tracking*, Artech House, Norwood, MA, 1999, pp. 29-34, 55-67, 103-136.

[21] Schneider, M., "Bayesian Linking of Geosynchronous Orbital Debris Tracks as seen by the Large Synoptic Survey Telescope," *Advances in Space Research*, Vol. 49, No. 4, 2011, pp. 655–666.

[22] Muinonen, K. and Bowell, E., "Asteriod Orbit Determination Using Bayesian Probabilities," *Icarus*, Vol. 103, No. 2, 1993, pp. 255–279.

[23] Virtanen, J., Muinonen, K., and Bowell, E., "Statistical Ranging of Asteriods," *Icarus*, Vol. 154, No. 2, 2001, pp. 412–431.

[24] Virtanen, J. and Muinonen, K., "Time Evolution of Orbital Uncertainties for the Impactor Candidate 2004 AS_1," *Icarus*, Vol. 184, No. 2, 2006, pp. 289–301.

[25] Weisman, R. M., Majji, M., and Alfriend, K. T., "Application of the Transformation of Variables Technique for Uncertainty Mapping in Nonlinear Filtering," *AAS/AIAA Astrodynamics Specialist Conference*, Girdwood, AK, Jul. 30 - Aug. 3 2011, AAS 11-604.

[26] Majji, M., Junkins, J. L., and Turner, J. D., "Measurement Model Nonlinearity in Estimation of Dynamical Systems," *The Kyle T. Alfriend Astrodynamics Symposium*, edited by S. L. Coffey, J. L. Junkins, K. K. Luu, I. M. Ross, C. Sabol, and J. Paul W. Schumacher, Monterey, CA, May 18-19 2010, AAS 10-303.

[27] Au, C. and Tam, J., "Transforming Variables Using the Dirac Generalized Function," *The American Statistician*, Vol. 53, No. 3, Aug. 1999, pp. 270–272.

[28] Khuri, A. I., "Applications of Dirac's Delta Function in Statistics," *International Journal of Mathematical Education in Science and Technology*, Vol. 35, No. 2, 2004, pp. 185–195.

[29] Shamilov, A., Yuzer, A. F., Agaoglu, E., and Mert, Y., "A Method of Obtaining Distributions of Transformed Random Variables by using the Heaviside Step Function and Dirac Generalized Functions," *Journal of Statistial Research*, Vol. 40, No. 1, 2006, pp. 23–34.

[30] Hari, B. S. and Venugopalakrishna, Y., "On the Use of Dirac Delta Distribution in Transformation of Random Variables," *14th National Conference on Communications*, IIT Bombay, Mumbai, Feb. 1-3 2008, AIAA 2008-7211.

[31] Izzo, D. and Valente, C., "A Mathematical Model Representing the Statistical Properties of Sets of Orbits," *Acta Astronautica*, Vol. 54, No. 8, 2004, pp. 541–546.

[32] Izzo, D., "Effects of Orbital Parameter Uncertainties," *Journal of Guidance, Control, and Dynamics*, Vol. 28, No. 2, Jan.-Feb. 2005, pp. 212–215.

[33] Izzo, D., "Statistical Distribution of Keplerian Velocities," *Journal of Guidance, Control, and Dynamics*, Vol. 29, No. 1, Mar.-Apr. 2006, pp. 298–305.

[34] Meshcheryakov, S., "Use of Generalized Functions for Definition of Collision Integrals in Orbital Motion," *Proceedings of the Fourth European Conference on Space Debris*, Darmstadt, Germany, Apr. 18-20 2005.

[35] Meshcheryakov, S., "Generalized Functions and Statistical Problems of Orbital Mechanics," *Eighth US/Russian Space Surveillance Workshop : Space Surveillance Detecting and Tracking Innovation*, Maui, HI, Apr. 18-23 2010.

[36] Weisman, R. M., Majji, M., and Alfriend, K. T., "Analytic Assessment of Sensor Uncertainty for Application to Space Object Tracking and Correlation," *62nd International Astronautical Congress : Space Debris Symposium*, Cape Town, South Africa, Oct. 3 - 7 2011, IAC-11-A6.6.7-10729.

[37] Fujimoto, K. and Scheeres, D., "Correlation of Optical Observations of Earth-Orbiting Objects by Means of Probability Distributions," *AIAA/AAS Astrodynamics Specialist Conference*, Toronto, Canada, Aug. 2-5 2010, AIAA-2010-7975.

[38] Fujimoto, K. and Scheeres, D., "Correlation and Initial Orbit Determination for Short-Arc Optical Observation," *Advanced Maui Optical and Space Surveillance Technologies Conference*, Wailea, Maui, HI, Sep. 14-17 2010.

[39] Fujimoto, K. and Scheeres, D., "Correlation of Multiple Singular Observations and Initial State Estimation by Means of Probability Distributions of High Codimension," *American Control Conference*, Toronto, Canada, Jun. 29 - Jul. 1 2011.

[40] Majji, M., Weisman, R. M., and Alfriend, K. T., "Solution of the Liouville Equation for Keplerian Motion: Application to Uncertainty Calculations," *AAS/AIAA Spaceflight Mechanics Conference*, Charleston, SC, Jan. 29 - Feb. 2 2012, AAS 12-262.

[41] Shuster, M. D., "Maximum Likelihood Estimation of Spacecraft Attitude," *Journal of Astronautical Sciences*, Vol. 37, No. 1, Jan.-Mar. 1989, pp. 79–88.

[42] Shuster, M. D., "Effective Direction Measurements for Spacecraft Attitude: III. Defective Directions and Data Fusion," *Journal of Astronautical Sciences*, Vol. 55, No. 4, Oct.-Dec. 2007, pp. 493–510.

[43] Mosegaard, K. and Tarantola, A., *International Handbook of Earthquake and Engineering Seismology: Part A*, Vol. 81A of *International Geophysics Series*, chap. 16 : Probabilistic Approach to Inverse Problems, Academic Press, New York, NY, 2002, pp. 237 - 265 and Appendices A - P.

[44] Kadry, S., "On the Generalization of Probabilistic Transformation Method," *Applied Mathematics and Computation*, Vol. 190, 2007, pp. 1284–1289.

[45] Goldstein, H., Poole, C., and Safko, J., *Classical Mechanics*, Addison Wesley, San Francisco, CA., 3rd ed., 2002, pp. 16-24, 34-36, 45-47, 337-338, 334-338, 341-347, 353-356, 368-375, 377-408, 419-421.

[46] Vinti, J. P., *Orbital and Celestial Mechanics*, Vol. 177 of *Progress in Astronautics and Aeronautics*, AIAA, Reston, VA., 1998, pp. 49-51, 53-58, 71-74, 136-137, 142, 219-251.

[47] Brouwer, D., "Solution of the Problem of Artificial Satellite Theory Without Drag," *Astronomical Journal*, Vol. 64, No. 1274, Nov. 1959, pp. 378–396.

[48] Giacaglia, G. E. O., "Notes of Von Zeipel's Method," Technical Report NASA-TM-X-55058, NASA Goddard Spaceflight Center, 1964.

[49] Vallado, D. A., "Covariance Transformations for Satellite Flight Dynamics Operations," *AAS/AIAA Astrodynamics Specialist Conference*, Big Sky, MT, Aug. 3-7 2003, AAS 03-526.

[50] Kozai, Y., "The Motion of a Close Earth Satellite," *Astronomical Journal*, Vol. 64, No. 1274, Nov. 1959, pp. 367–377.

[51] Hori, G.-I., "Comparison of Two Perturbation Theories Based on Canonical Transformations," *Publications of the Astronomical Society of Japan*, Vol. 22, 1970, pp. 191–198.

[52] Yuasa, M., "The Comparison of Hori's Perturbation Theory and von Zeipel's Theory," *Publications of the Astronomical Society of Japan*, Vol. 23, 1971, pp. 399–403.

[53] Hoots, F. R., Schumacher Jr., P. W., and Glover, R. A., "History of Analytical Orbit Modeling in the U.S. Space Surveillance System," *Journal of Guidance, Control, and Dynamics*, Vol. 27, No. 2, Mar.-Apr. 2004, pp. 174–185.

[54] Temple III, L. P., *Shades of Gray: National Security and the Evolution of Space Reconaissance*, AIAA, Reston, VA, 2005, pp. 97, 110, 152-153, 324.

[55] Lyddane, R., "Small Eccentricities or Inclinations in the Brouwer Theory of the Artificial Satellite," *Astronomical Journal*, Vol. 68, No. 8, Oct. 1963, pp. 555–558.

[56] Kozai, Y., "Second-Order Solution of Artificial Satellite Theory without Air Drag," *Astronomical Journal*, Vol. 67, No. 8, Sep. 1962, pp. 446–461.

[57] Izsak, I. G., "A Note on Perturbation Theory," *Astronomical Journal*, Vol. 68, No. 8, Oct. 1963, pp. 559–561.

[58] Aksnes, K., "On the Use of the Hill Variables in Artificial Satellite Theory: Brouwer's Theory," *Astronomy and Astrophysics*, Vol. 17, 1972, pp. 70–75.

[59] Jazwinski, A. H., *Stochastic Processes and Filtering Theory*, Dover, Mineola, NY, 1998, pp. 34-42, 55-56, 77-81, 85-92, 145-158, 174-175, 189-193.

[60] Davenport, P. B., "A Vector Approach to the Algebra of Rotations with Applications," Technical Report NASA-TN-D-4696, NASA Goddard Spaceflight Center, 1968.

[61] Keat, J., "Analysis of Least-Squares Attitude Determination Routine DOAOP," Technical Report NASA-CR-183450, NASA Goddard Spaceflight Center, 1977.

[62] Black, H., "A Passive System for Determining the Attitude of a Satellite," *AIAA Journal*, Vol. 2, No. 7, Jul. 1964, pp. 1350–1351.

[63] van der Merwe, R., Doucet, A., de Freitas, N., and Wan, E., "The Unscented Particle Filter," Technical Report CUED/F-INFENG/TR 380, Cambridge University Engineering Department, Aug. 2000.

[64] DeRusso, P. M., Roy, R. J., and Close, C. M., *State Variables for Engineers*, John Wiley & Sons, New York, NY, 1965, pp. 249-250, 254-262.

[65] Long, A., Cappellari Jr., J., Velez, C., and Fuchs, A., "Goddard Trajectory Determination System (GTDS) Mathematical Theory (Revision 1)," Technical Report NASA-CR-183462, NASA Goddard Spaceflight Center, Jul. 1989, pp. 5.43-5.63, 8.13-8.16.

[66] Schaub, H. and Junkins, J. L., *Analytical Mechanics of Space Systems*, AIAA, Reston, VA, 1st ed., 2003, pp. 72-82, 87-91, 95-101, 133-135, 404-418, 479-483, 519-525, 693-696.

[67] Stewart, J., *Calculus: Early Transcendentals*, Brooks/Cole, Pacific Grove, CA, 4th ed., 1999, pp. 1020-1022, 1026-1033.

[68] Stark, H. and Woods, J. W., *Probability and Random Processes with Applications to Signal Processing*, Prentice-Hall, Upper Saddle River, NJ, 3rd ed., 2002, pp. 158-159, 174-175.

[69] Tapley, B. D., Schutz, B. E., and Born, G. H., *Statistical Orbit Determination*, Elsevier, Burlington, MA, 2004, pp. 230-233, 244-245, 251-258, 493-497.

[70] Halder, A. and Bhattacharya, R., "Dispersion Analysis in Hypersonic Flight During Planetary Entry Using Stochastic Liouville's Equation," *Journal of Guidance, Control, and Dynamics*, Vol. 34, No. 2, Mar.-Apr. 2011, pp. 459–474.

[71] Escobal, P. R., *Methods of Orbit Determination*, John Wiley & Sons, New York, NY, 1965, pp. 107-121, 228-231, 239, 293, 318.

[72] Battin, R. H., *An Introduction to the Mathematics and Methods of Astrodynamics*, AIAA, Reston, VA., revised ed., 1999, pp. 110-114, 125-130, 135, 109-212, 490-493, 743-744.

[73] Taff, L. G., *Celestial Mechanics: A Computational Guide for the Practitioner*, John Wiley & Sons, New York, NY, 1985, pp. 59-61.

[74] Montenbruck, O. and Gill, E., *Satellite Orbits: Models, Methods, and Applications*, Springer-Verlag, New York, NY, 2000, pp. 24-32, 233-253.

[75] Broucke, R., "On the Matrizant of the Two-Body Problem," *Astronomy and Astrophysics*, Vol. 6, 1970, pp. 173–182.

[76] Chobotov, V., *Orbital Mechanics*, AIAA, Reston, VA, 3rd ed., 2002, pp. 186, 200, 208, 242, 307.

[77] Alfriend, K. T., Vadali, S. R., Gurfil, P., How, J. P., and Breger, L. S., *Spacecraft Formation Flying: Dynamics, Control, and Navigation*, Elsevier, Burlington, MA, 2010, pp. 25, 43-46, 338-351.

[78] Walter, H., "Conversion of Osculating Elements into Mean Elements," *Astronomical Journal*, Vol. 72, No. 8, Oct. 1967, pp. 994–997.

[79] Der, G. J. and Danchick, R., "Conversion of Osculating Orbital Elements to Mean Orbital Elements," Technical Report NASA-CP-3333, NASA Goddard Spaceflight Center, 1999.

[80] Kelso, T., "NORAD Two-Line Element Sets," http://celestrak.com, Aug. 2012, Last Update 27 Jan. 2012.

[81] "General Mission Analysis Tool(GMAT) Mathematical Specifications," Tech. Rep. Draft for Release 2012a Beta, NASA Goddard Spaceflight Center, May 16, 2012 2012, pp. 44-47.

APPENDIX A

TWO-BODY ORBITAL MECHANICS

This appendix serves to introduce the geometry and equations of motion associated with what is known as the "Two-Body Problem", involving only two objects with one object assumed to be much more massive than the other, e.g. the Earth and a closely orbiting spacecraft. First, the inertial and relative coordinate frames are discussed along with time since the Earth cannot be considered fixed over long periods of time. Second, the fundamental Two-Body equations of motion are introduced along with equations accounting for perturbing forces such as drag and the nonspherical shape of the Earth. Finally, state descriptions in domains other than Cartesian and their relative transformations are introduced to allow for more a intuitive study of Two-Body motion since the motion is curvilinear and not rectilinear. This appendix was compiled using the discussions of Vallado [5], Schaub and Junkins [66], Battin [72], and Montenbruck and Gill [74].

A.1 Coordinate Frames of the Two-Body Problem

The state vector solution of the space surveillance problem requires the use of multiple frames of reference with differing coordinate systems. The equations of motion of the space object are with respect to an inertial frame of reference, ECI, while the tracking station(s) make observations in a Earth-Centered Earth-Fixed frame, ECEF. To further complicate matters, tracking station(s) produce observations in coordinate systems that are translated and may be rotated with respect to the ECEF frame. The modeling of tracking stations with respect to the satellite is performed using common modeling assumptions and methods [5].

The ECI reference frame has its origin at the Earth's center and is described by the primary axis pointing toward the Vernal Equinox, tertiary axis points toward the North Pole, and the secondary axis completing the right-handed triad. The primary and secondary axes of the ECI frame lie in the equatorial plane of the Earth. Establishing the position of the Vernal Equinox on the equator on January 1, 2000 as a datum allows for this reference frame to be considered inertial so that Newton's laws are valid. The ECEF reference frame is established with the primary axis pointing from the center of the Earth out along the equatorial plane through the line of Greenwich, England longitude. The tertiary axis of ECEF is aligned with the tertiary axis of the ECI reference frame and the secondary axis of ECEF points due East in the equatorial plane.

The precession of the equatorial plane is neglected in this analysis and only precession of the Vernal Equinox is assumed to differentiate the ECI and ECEF reference frames, see Section A.1.2 for justification of assumption. Transformation of ECI frame coordinates to ECEF coordinates utilizes Greenwich Mean Sidereal Time, θ_{GMST}, which describes the precession of the Vernal Equinox with respect to the longitude of Greenwich, England and assuming a counter-clockwise rotation about the tertiary axis of the ECI frame. The Cartesian position of a satellite calculated from the necessary equations of motion in inertial frame, $\mathbf{r}_{ECI}$, can be expressed in ECEF frame by Equation (A.1).

$$\mathbf{r}_{ECEF} = \mathbf{Rot}\left[3, \theta_{GMST}\right] \mathbf{r}_{ECI} \tag{A.1}$$

The common orthogonal triad rotations are given by Equation (A.2).

$$\begin{aligned}
\mathbf{Rot}\left[1,\phi\right] &= \begin{bmatrix} 1 & 0 & 0 \\ 0 & \cos\phi & \sin\phi \\ 0 & -\sin\phi & \cos\phi \end{bmatrix} \\
\mathbf{Rot}\left[2,\theta\right] &= \begin{bmatrix} \cos\theta & 0 & -\sin\theta \\ 0 & 1 & 0 \\ \sin\theta & 0 & \cos\theta \end{bmatrix} \\
\mathbf{Rot}\left[3,\psi\right] &= \begin{bmatrix} \cos\psi & \sin\psi & 0 \\ -\sin\psi & \cos\psi & 0 \\ 0 & 0 & 1 \end{bmatrix}
\end{aligned} \tag{A.2}$$

The above rotations can be generated using Euler's Theorem of Principal Rotation [66], where any rotation can be described by a single rotation through a principal angle, Φ, about a principal axis, $\hat{\mathbf{e}}$. The above rotations from an inertial frame to body frame can then be generated according to Equation (A.3)

$$\mathbf{Rot}\left[\hat{\mathbf{e}},\mathbf{\Phi}\right] = \cos(\mathbf{\Phi})\mathbf{1}_{3\times 3} + \left(1-\cos(\mathbf{\Phi})\right)\hat{\mathbf{e}}\hat{\mathbf{e}}^{T} - \sin(\mathbf{\Phi})\left[\hat{\mathbf{e}}\times\right] \tag{A.3}$$

To generate a rotation about the primary axis by an angle ϕ, set $\mathbf{\Phi} = \phi$ and $\hat{\mathbf{e}} = [1\ 0\ 0]^{T}$. For compactness in the above equation the identity matrix and the skew-symmetric cross-product matrix are expressed as shown in Equations (A.4)

and (A.5).

$$\underset{n\times n}{\mathbf{I}} = \begin{bmatrix} 1 & 0 & \dots & 0 \\ 0 & 1 & \dots & 0 \\ \vdots & \vdots & \ddots & \vdots \\ 0 & 0 & \dots & 1 \end{bmatrix} \tag{A.4}$$

$$[\boldsymbol{\alpha}\times] = \begin{bmatrix} 0 & -\alpha_3 & \alpha_2 \\ \alpha_3 & 0 & -\alpha_1 \\ -\alpha_2 & \alpha_1 & 0 \end{bmatrix} \tag{A.5}$$

Greenwich Mean Sidereal Time is calculated using the present Julian Date, the number of days elapsed since January 1, 4713 B.C., modified to correct for polar motion so the time is independent of station location. The equation to calculate θ_{GMST} in degrees from arcseconds is given by Equation (A.6).

$$\begin{aligned} \theta^s_{GMST} =& 67310.54841^s + (876600 * 3600^s + 8640184.812866^s)\, T_{UT1} + \\ & 0.093104 T^2_{UT1} - 6.2 \times 10^{-6} T^3_{UT1} \\ \theta^s_{GMST} =& \text{MOD}\,(\theta^s_{GMST}, 86400^s) \\ \theta_{GMST} =& \theta^s_{GMST} \times \frac{1 \text{ degree}}{240 \text{ seconds}} \end{aligned} \tag{A.6}$$

The MOD procedure is the modulus procedure to resolve θ^s_{GMST} inside of 86400 seconds. The universal time correction, T_{UT1}, is calculated from the Julian Date using Equation (A.7) given the observation time formatted in military time, HR:MIN:SEC, with the year given by 4 digits, the FLOOR operation is merely rounding the resul-

tant down.

$$T_{UT1} = \frac{JD - 2451545.0}{36525}$$

$$JD = 367 * \mathrm{YR} - \mathbf{FLOOR}\left\{\frac{7\left(\mathrm{YR} + \mathbf{FLOOR}\left\{\frac{\mathrm{MO}+9}{12}\right\}\right)}{4}\right\} + \mathbf{FLOOR}\left\{\frac{275\mathrm{MO}}{9}\right\} + \mathrm{DAY} + 1721013.5 + \frac{\frac{\mathrm{SEC}}{60} + \mathrm{MIN}}{60} + \mathrm{HR}}{24} \tag{A.7}$$

A.1.1 Conversion of Topocentric Measurements to ECI

The Earth is modeled as a perfect sphere with a radius, $R_{\oplus}$, of 6378 kilometers. The Cartesian position of the tracking station in ECEF frame is by Equation (A.8) in spherical coordinates according to the tracking station's latitude from the equator, ϕ, and longitude from the Prime Meridian, λ.

$$\mathbf{R}_{T.S.-ECEF} = (R_{\oplus} + TS_{alt}) \begin{bmatrix} \cos\lambda\cos\phi \\ \sin\lambda\cos\phi \\ \sin\phi \end{bmatrix} = (R_{\oplus} + TS_{alt})\,\boldsymbol{\psi}\,(\lambda, \phi) \tag{A.8}$$

The tracking station will observe topocentric measurements which must be related to ECEF frame to carry out further analysis. The line-of-sight position vector, ρ_{ECEF} is calculated from Equation (A.9) given the locally observed slant range to satellite, ρ, and topocentric right ascension and declination, α_{TOPO} and δ_{TOPO} respectively. The line-of-sight vector as defined by the differencing of the space object position and tracking station location is expressed in coordinates relative to the ECEF axes. The topocentric right ascension and declination angles are defined relative to the

ECI coordinate frame.

$$\boldsymbol{\rho}_{ECEF} = \mathbf{r}_{ECEF} - \mathbf{R}_{T.S.-ECEF} = \rho \begin{bmatrix} \cos(\alpha_{TOPO})\cos(\delta_{TOPO}) \\ \sin(\alpha_{TOPO})\cos(\delta_{TOPO}) \\ \sin(\delta_{TOPO}) \end{bmatrix} = \rho \boldsymbol{\psi}\left(\alpha_{TOPO}, \delta_{TOPO}\right) \tag{A.9}$$

The line-of-sight vector in ECEF coordinates is not intuitive for an observer at a tracking station which far removed from the equator so the line-of-sight vector is expressed in terms of the "Local Vertical - Local Horizontal" with respect to the tracking station location. This is accomplished through a rotation about the tertiary ECEF axis then a rotation about the resulting secondary axis to yield either the Up-East-North, (UEN), triad or the South-East-Up, (SEZ), triad. This study utilizes the SEZ triad coordinate system with Cartesian position vector given according to Equation (A.10).

$$\boldsymbol{\rho}_{SEZ} = \mathbf{Rot}\left[2, \pi/2 - \phi\right] \mathbf{Rot}\left[3, \lambda\right] \boldsymbol{\rho}_{ECEF} = \rho \begin{bmatrix} -\cos(el)\cos(\beta) \\ \cos(el)\sin(\beta) \\ \sin(el) \end{bmatrix} \tag{A.10}$$

From the above result, the range, azimuth, and elevation of a space object viewed by of an observer at a given tracking station location, with latitude and longitude

(ϕ, λ), are given by Equation (A.11).

$$\begin{aligned}
&\text{Range}: \ \rho_{SEZ} = \|\boldsymbol{\rho}_{SEZ}\| = \left(\rho_S^2 + \rho_E^2 + \rho_Z^2\right)^{1/2} \\
&\text{Elevation}: \ el = \arctan\left\{\frac{\rho_Z}{\left(\rho_S^2 + \rho_E^2\right)^{1/2}}\right\} \\
&\text{If Elevation Angle is Not 90 degrees}: \\
&\qquad \text{Azimuth}: \ \beta = \arctan\left\{\frac{\rho_E}{-\rho_S}\right\} \\
&\text{If Elevation Angle is Not 90 degrees}: \\
&\qquad \text{Azimuth}: \ \beta = \arctan\left\{\frac{\dot{\rho_E}}{-\dot{\rho_S}}\right\}
\end{aligned} \tag{A.11}$$

The velocity of the tracking station location in ECEF is zero because the tracking station remains fixed in ECEF frame. The velocity of the tracking station relative to the ECI frame is not zero due to the rotation of the Earth relative to the Vernal Equinox. The velocity of the tracking station relative to the ECI frame can be found using the transport theorem, Equation (A.12), for simplification the earth is assumed to rotate only about its tertiary axis, $\boldsymbol{\omega}_\oplus = \omega_\oplus \hat{k}$.

$$\begin{aligned}
\dot{\mathbf{R}}_{T.S.-ECEF}\Big|_{Relative\ To\ ECI} &= \boldsymbol{\omega}_\oplus \times \mathbf{R}_{T.S.-ECEF} \\
&= \omega_\oplus R_\oplus \begin{bmatrix} \sin(\lambda)\cos(\phi) \\ \cos(\lambda)\cos(\phi) \\ 0 \end{bmatrix}
\end{aligned} \tag{A.12}$$

The velocity of the ECEF Cartesian coordinates can then be written in terms of the topocentric observations and the rate of change of the tracking station with

respect to the origin, Equations (A.13) and (A.15).

$$\begin{aligned}\mathbf{v}_{ECEF} &= \dot{\boldsymbol{\rho}}_{ECEF} + \cancelto{0}{\dot{\mathbf{R}}_{T.S.-ECEF}} \\ &= \dot{\rho}\boldsymbol{\psi}\left(\alpha_{TOPO}, \delta_{TOPO}\right) + \rho\dot{\boldsymbol{\psi}}\left(\alpha_{TOPO}, \delta_{TOPO}, \dot{\alpha}_{TOPO}, \dot{\delta}_{TOPO}\right)\end{aligned} \tag{A.13}$$

$$\begin{aligned}\boldsymbol{\psi}\left(\theta_1, \theta_2\right) &= \begin{bmatrix} \cos(\theta_1)\cos(\theta_2) \\ \sin(\theta_1)\cos(\theta_2) \\ \sin(\theta_2) \end{bmatrix} \\ \dot{\boldsymbol{\psi}}\left(\theta_1, \theta_2, \dot{\theta}_1, \dot{\theta}_2\right) &= \begin{bmatrix} -\sin(\theta_1)\dot{\theta}_1\cos(\theta_2) - \cos(\theta_1)\sin(\theta_2)\dot{\theta}_2 \\ \cos(\theta_1)\dot{\theta}_1\cos(\theta_2) - \sin(\theta_1)\sin(\theta_2)\dot{\theta}_2 \\ \cos(\theta_2)\dot{\theta}_2 \end{bmatrix}\end{aligned} \tag{A.14}$$

Likewise, Equation (A.13) can be written in terms of the SEZ frame by using the time derivative of Equation (A.10) to compute the local topocentric velocity vector in terms of range, azimuth, and elevation angle as shown by Equations (A.15) and (A.16).

$$\dot{\boldsymbol{\rho}}_{ECEF} = \mathbf{Rot}\left[3, \lambda\right]^T \mathbf{Rot}\left[2, \pi/2 - \phi\right]^T \dot{\boldsymbol{\rho}}_{SEZ} \tag{A.15}$$

$$\dot{\boldsymbol{\rho}}_{SEZ} = \dot{\rho}\begin{bmatrix} -\cos(el)\cos(\beta) \\ \cos(el)\sin(\beta) \\ \sin(el) \end{bmatrix} + \rho\begin{bmatrix} \sin(el)\cos(\beta)\dot{el} + \cos(el)\sin(\beta)\dot{\beta} \\ -\sin(el)\cos(\beta)\dot{el} + \cos(el)\cos(\beta)\dot{\beta} \\ \cos(el)\dot{el} \end{bmatrix} \tag{A.16}$$

A.1.2 Rotation from ECEF to ECI

The conventional transformation used to convert ECEF position and velocity coordinates to ECI goes by "IAU-76/FK5 Classical Transformation" [5]. It is no longer the current theory but is a legacy approach still used by many systems which involves five separate rotation matrices generated by changes in the Earth's pole position, rotation of the Vernal equinox, precession of the Earth, obliquity of the

ecliptic and a frame bias for correction of pole positions. The complete Cartesian position and velocity transformations are given by Equation (A.17).

$$\begin{aligned}\mathbf{r}_{ECI} &= \mathbf{BPNRW}\mathbf{r}_{ECEF} \\ \mathbf{v}_{ECI} &= \mathbf{BPNR}\left[\mathbf{W}\mathbf{v}_{ECEF} + \boldsymbol{\omega}_{\oplus} \times \mathbf{W}\left(\underbrace{\boldsymbol{\rho}_{ECEF} + \mathbf{R}_{T.S.-ECEF}}_{\mathbf{r}_{ECEF}}\right)\right]\end{aligned} \tag{A.17}$$

The $\mathbf{B}$ matrix is a bias correction matrix to allow for use of IAU-2000 pole position calculations and is approximately given by Equation (A.18), see Vallado [5]for exact matrix.

$$\mathbf{B} = \begin{bmatrix} 1 & 7\times10^{-8} & 8\times10^{-8} \\ -7\times10^{-8} & 1 & 3\times10^{-8} \\ 8\times10^{-8} & 3\times10^{-8} & 1 \end{bmatrix} \approx \begin{bmatrix} 1 & 0 & 0 \\ 0 & 1 & 0 \\ 0 & 0 & 1 \end{bmatrix} \tag{A.18}$$

The $\mathbf{P}$ matrix accounts for general precession of the Earth's pole and is a composite of three separate rotations given by Equation (A.19).

$$\mathbf{P} = \mathbf{Rot}\left[3, \zeta\right]\mathbf{Rot}\left[2, -\Theta\right]\mathbf{Rot}\left[3, z\right] \tag{A.19}$$

The general precession angles are computed using Terestial Time [5] which is approximately 32 seconds forward of Atomic time. However, these angles are relatively small , $\mathcal{O}(1\times10^{-2})$degrees, making the general precession rotation matrix approximately Identity. The $\mathbf{N}$ rotation matrix accounts for nutation effects and is a composite rotation considering obliquity of the ecliptic and true obliquity by the difference between the two is extremely small and the correction for the equinox is extremely small allowing for the nutation matrix to be considered Identity, Equa-

tion (A.20).

$$\begin{aligned}\mathbf{N} &= \mathbf{Rot}\left[1,-\bar{\epsilon}\right]\mathbf{Rot}\left[3,\Delta\Psi_{1980}\right]\mathbf{Rot}\left[1,\epsilon\right] \\ &\approx \mathbf{Rot}\left[1,-\bar{\epsilon}\right]\begin{bmatrix}1&0&0\\0&1&0\\0&0&1\end{bmatrix}\mathbf{Rot}\left[1,\epsilon\right] \\ &\approx \begin{bmatrix}1&0&0\\0&1&0\\0&0&1\end{bmatrix}\end{aligned} \tag{A.20}$$

The **R** rotation accounts for complete sidereal time composed of Greenwich Apparent Sidereal Time with the 1982 datum and the equation of the equinoxes to account for Nutation effects. The contribution of nutation is relatively small ($\mathcal{O}(1\times10^{-3})$degrees) so Greenwich Mean Sidereal Time dominates the rotation, Equation (A.21).

$$\mathbf{R} \approx \mathbf{Rot}\left[3,-\theta_{GMST}\right] \tag{A.21}$$

The **W** matrix accounts for motion of the pole and is composite rotation of coordinates given in arcseconds, so the matrix can be considered Identity if error on the order of six meters is considered acceptable, Equation (A.22).

$$\begin{aligned}\mathbf{W} &= \mathbf{Rot}\left[1,y_p\right]\mathbf{Rot}\left[2,x_p\right] \\ &\approx \begin{bmatrix}1&0&-x_p\\0&1&y_p\\x_p&y_p&1\end{bmatrix} \quad ,(x_p,y_p)\ O\left(0.2" = 6\times10^{-5}\,\mathrm{deg}\right)\end{aligned} \tag{A.22}$$

From the above considerations the transformation of ECEF position and velocity

Cartesian vectors reduces to Equation (A.23).

$$\begin{aligned} \mathbf{r}_{ECI} &= \mathbf{R}\left[3, -\theta_{GMST}\right]\mathbf{r}_{ECEF} \\ \mathbf{v}_{ECI} &= \mathbf{R}\left[3, -\theta_{GMST}\right]\left(\mathbf{v}_{ECEF} + \boldsymbol{\omega}_{\oplus} \times \mathbf{r}_{ECEF}\right) \end{aligned} \tag{A.23}$$

The proof of the simplified above equations comes from the fact that the ECEF frame is assumed to be only offset by a rotation about a shared tertiary axis by an angle, θ_{GMST}, measured positively from the primary axis of the ECI frame, hence Equation (A.24).

$$\mathbf{r}_{ECI} = \mathbf{Rot}\left[3, -\theta_{GMST}\right]\mathbf{r}_{ECEF} \tag{A.24}$$

Taking the time derivative of the above equation while noting that one is already in the inertial frame yields Equation (A.25).

$$\mathbf{v}_{ECI} = \frac{d}{dt}\left(\mathbf{Rot}\left[3, -\theta_{GMST}\right]\right)\mathbf{r}_{ECEF} + \mathbf{Rot}\left[3, -\theta_{GMST}\right]\dot{\mathbf{r}}_{ECEF} \tag{A.25}$$

Making use of the time rate change of a direction cosine matrix and noting that the angular velocity of the ECI frame with respect to the ECEF is the negative of the angular of the ECEF frame with respect to the ECI frame yields Equation (A.26).

$$\begin{aligned} \mathbf{v}_{ECI} &= -\left[\boldsymbol{\omega}\times\right]^{ECI/ECEF}\mathbf{Rot}\left[3, -\theta_{GMST}\right]\mathbf{r}_{ECEF} + \mathbf{Rot}\left[3, -\theta_{GMST}\right]\dot{\mathbf{r}}_{ECEF} \\ \left[\boldsymbol{\omega}\times\right]^{ECI/ECEF} &= -\left[\boldsymbol{\omega}\times\right]^{ECEF/ECI} \\ \boldsymbol{\omega}^{ECEF/ECI} &= \omega_{\oplus}\hat{K} \end{aligned} \tag{A.26}$$

A.2 Equations of Motion

The equation governing the unperturbed motion of two bodies separated by a Cartesian position vector, $\mathbf{r}$, is given by Equation (A.27).

$$\ddot{\mathbf{r}} = -\frac{\mu}{||\mathbf{r}||^3}\mathbf{r} = G\mathbf{r} \tag{A.27}$$

Due to the presence of additional conservative and nonconservative forces, the equation of motion for a satellite subject to short-period, long-period, and secular perturbations is given as Equation (A.28).

$$\ddot{\mathbf{r}} = -\frac{\mu}{||\mathbf{r}||^3}\mathbf{r} + \ddot{\mathbf{r}}_{Geopotential} + \ddot{\mathbf{r}}_{Drag} + \ddot{\mathbf{r}}_{n-Body} + \ddot{\mathbf{r}}_{SRP} + \ddot{\mathbf{r}}_{Other} \tag{A.28}$$

The second and third accelerations arise from the shape of the Earth being non-spherical resulting in varying attraction and the presence of air drag. The fourth acceleration term arise from the gravitational attraction of other bodies which are present within the satellite's system. For Earth orbiting satellites, typically only the attraction of the Sun and Moon are accounted for. The fifth term accounts for the acceleration imparted from impacting light photons on the spacecraft. The sixth term accounts for other acceleration sources such as Earth tides (ocean, ground, air), magnetic field effects, and spacecraft commanded motion.

A.2.1 Pertubation due to Geopotential

The acceleration perturbation due to zonal, tesseral, an sectorial harmonics is given by Equation (A.29) [5].

$$\begin{aligned}
\ddot{\mathbf{r}}_{Geopotential} &= \nabla_{\mathbf{r}} \left(U - U_{2-Body} \right) = \nabla_{\mathbf{r}} \left(U - \frac{\mu}{||\mathbf{r}_{Sat}||} \right) \\
U &= \frac{\mu}{r_{Sat}} \Bigg[1 - \sum_{l=2}^{\infty} J_l \left(\frac{R_{\oplus}}{r_{Sat}} \right)^l P_l \left(\sin(\phi_{Sat}) \right) + \sum_{l=2}^{\infty} \sum_{m=0}^{l} \left(\frac{R_{\oplus}}{r_{Sat}} \right)^l P_{l,m} \\
&\qquad \times \left(\sin(\phi_{Sat}) \right) \left\{ C_{l,m} \cos(m\lambda_{Sat}) + S_{l,m} \sin(m\lambda_{Sat}) \right\} \Bigg] \\
U_{2-Body} &= \frac{\mu}{r_{Sat}}
\end{aligned} \tag{A.29}$$

Where r_{Sat} is the geocentric distance the satellite, $(\phi_{Sat}, \lambda_{Sat})$ are the geocentric latitude and longitude respectively, and $P_{l,m}$ is the Legendre polynomial of degree l and order m.

A.2.2 Pertubation due to Drag

The acceleration perturbation due to atmospheric drag is given by Equation (A.30) and is commonly modeled as cannonball drag where the ballistic coefficient of the object, $m/\left(C_D A\right)$, is commonly estimated as a bulk parameter since the coefficient of drag and apparent cross-sectional area can vary largely and mass is not always constant. The atmospheric density is typically modeled using an exponential atmosphere model. Note that the object's velocity relative to the atmosphere is required since the atmosphere of Earth is rotating.

$$\begin{aligned}
\ddot{\mathbf{r}}_{CannonballDrag} &= -\frac{1}{2} \rho_{AtmosDensity} \frac{C_D A}{m} \left(\dot{\mathbf{r}}_{SatRel}^T \dot{\mathbf{r}}_{SatRel} \right) \frac{\dot{\mathbf{r}}_{SatRel}}{||\dot{\mathbf{r}}_{SatRel}||} \\
\dot{\mathbf{r}}_{SatRel} &= \dot{\mathbf{r}}_{Sat} - \boldsymbol{\omega}_{\oplus} \times \mathbf{r}_{Sat}
\end{aligned} \tag{A.30}$$

A.2.3 Pertubation due to Presence of Other Bodies

The acceleration perturbation, Equation (A.31), due to other heavenly bodies, e.g. Sun or Moon, gives rise to "n-Body" dynamics where one can no longer utilize Kepler's first or second laws in order to solve for constants of integration as is done in the Two-Body problem.

$$\ddot{\mathbf{r}}_{ith-Body} = \mu_{ith-Body}\left(\frac{\mathbf{r}_{Sat-ithBody}}{r^3_{Sat-ithBody}} - \frac{\mathbf{r}_{\oplus-ithBody}}{r^3_{\oplus-ithBody}}\right) \tag{A.31}$$

A.2.4 Pertubation due to Solar Radiation Pressure

The acceleration perturbation due to the impact of photons on an object requires consideration when the object is out of typically low Earth orbit range where geopotential and drag perturbations dominate. The commonly used model for this perturbation, Equation (A.32), is analogous to the drag model but with different parameters characterizing how the photons are absorbed or reflected. The incidence angle to the Sun becomes critical in order to determine the cross-sectional area exposed to the Sun.

$$\ddot{\mathbf{r}}_{CannonballSRP} = -\frac{p_{SR}c_R A_{\perp\odot}}{m}\frac{\mathbf{r}_{Sat-\odot}}{||\mathbf{r}_{Sat-\odot}||} \tag{A.32}$$

A.2.5 F and G Solution

In lieu of direct integration of Equation (A.27), there exists an analytical solution to the two body problem based upon constant angular momentum and is known as the F and G solution [66]. The solution is based on the fact that the orbit plane is defined by the initial position and velocity vectors thus any position and velocity vector at a later time can be compute from a linear combination of the

initial condition vectors which lie in the orbital plane.

$$\begin{bmatrix} \mathbf{r}(t) \\ \dot{\mathbf{r}}(t) \end{bmatrix} = \begin{bmatrix} F & G \\ \dot{F} & \dot{G} \end{bmatrix} \begin{bmatrix} \mathbf{r}(t_0) \\ \dot{\mathbf{r}}(t_0) \end{bmatrix} \tag{A.33}$$

With the above relationship substituted into the equations of motion for a two body system, the F and G functions are found to possess the following equations of motion and initial conditions shown in Equation (A.34).

$$\begin{aligned} \ddot{F} &= -\frac{\mu}{r^3}F \quad , \quad F(t_0) = 1 \quad , \quad \dot{F}(t_0) = 0 \\ \ddot{G} &= -\frac{\mu}{r^3}G \quad , \quad G(t_0) = 0 \quad , \quad \dot{G}(t_0) = 1 \end{aligned} \tag{A.34}$$

From the first equation in Equation (A.33) and noting position and velocity vectors are planar, the solution for F and G can be derived as shown in Equation (A.35).

$$\begin{aligned} \begin{pmatrix} F \\ G \end{pmatrix} &= \frac{1}{\sqrt{\mu p}} \begin{bmatrix} x\dot{y}_0 - y\dot{x}_0 \\ yx_0 - xy_0 \end{bmatrix} \\ \mathbf{h} &= \mathbf{r}_0 \times \dot{\mathbf{r}}_0 \\ \sqrt{\mu p} &= h = x_0\dot{y}_0 - y_0\dot{x}_0 \end{aligned} \tag{A.35}$$

In terms of orbital elements the functions governing Equation (A.33) can be shown as Equations (A.36) and (A.37) [5, 66].

$$\begin{aligned} F &= 1 - \frac{a}{r_0}\left(1 - \cos(\hat{E})\right) \\ G &= (t - t_0) + \sqrt{\frac{a^3}{\mu}}\left(\sin(\hat{E}) - \hat{E}\right) \\ \dot{F} &= -\frac{\sqrt{\mu a}}{r r_0}\sin(\hat{E}) \\ \dot{G} &= 1 - \frac{a}{r}\left(1 - \cos(\hat{E})\right) \end{aligned} \tag{A.36}$$

$$
\begin{aligned}
r &= a + (r_0 - a)\cos(\hat{E}) + \sqrt{a}\sigma_0 \sin(\hat{E}) \\
\sigma_0 &= \frac{\mathbf{r}_0^T \dot{\mathbf{r}}_0}{\sqrt{\mu}}
\end{aligned}
\tag{A.37}
$$

The term $\hat{E}$ is the difference in eccentric anomalies, $\hat{E} = E - E_0$ and must be found via iteration on modified Kepler's equation, Equation (A.38), see Appendix A.3.1.3 for solution of Kepler's equation. An alternative solution of the F and G series is presented in Section 4.3.3 utilizing the *fundamental invariants* [72].

$$
\begin{aligned}
Find: &\quad \hat{E} \\
Such\ that: &\quad \hat{M} - f\left(\hat{E}\right) \\
Where: & \\
&\hat{M} = \sqrt{\frac{\mu}{a^3}}\,(t - t_0) \\
&f\left(\hat{E}\right) = \hat{E} - \left(1 - \frac{r_0}{a}\right)\sin(\hat{E}) - \frac{\sigma_0}{\sqrt{a}}\left(\cos(\hat{E}) - 1\right) \\
&\frac{\partial f\left(\hat{E}\right)}{\partial \hat{E}} = \sqrt{\frac{r_0}{a}}
\end{aligned}
\tag{A.38}
$$

A.3 State Space Transformations

The following sections describe the conversion between osculating Orbital Elements and ECI Cartesian states for the Two-Body unperturbed motion, Keplerian Motion, problem. The outlined procedures follow that of Schaub [66] but for orbits that are equatorial and/or circular addition modifications are required to avoid numerical complications [81].

A.3.1 ECI Cartesian to Keplerian Orbital Elements

Given Cartesian position and velocity vectors, $\mathbf{r}_{ECI},\ \mathbf{v}_{ECI}$, the following procedure can be applied to compute the orbital element set, $\{a,\ e,\ i,\ \omega,\ \Omega,\ M\}$.

A.3.1.1 Semi-major Axis, a

The semi-major axis of the conic section describing the orbit of the space object is computed directly from the *vis-viva* equation, Equation (A.39).

$$\begin{aligned} a &= \left(\frac{2}{r} - \frac{v^2}{\mu}\right)^{-1} \\ r &= ||\mathbf{r}_{ECI}|| = \left(r_{ECI}(1)^2 + r_{ECI}(2)^2 + r_{ECI}(3)^2\right)^{1/2} \\ v &= ||\mathbf{v}_{ECI}|| = \left(v_{ECI}(1)^2 + v_{ECI}(2)^2 + v_{ECI}(3)^2\right)^{1/2} \end{aligned} \tag{A.39}$$

A.3.1.2 Eccentricity Vector and Scalar

First, calculate the angular momentum vector, $\mathbf{h}_{ECI}$, given by Equation (A.40). Then Compute Eccentricity Vector and Scalar given by Equation (A.41).

$$\begin{aligned} \mathbf{h}_{ECI} = \mathbf{r}_{ECI} \times \mathbf{v}_{ECI} &= \begin{bmatrix} r_{ECI}(2)v_{ECI}(3) - r_{ECI}(3)v_{ECI}(2) \\ r_{ECI}(3)v_{ECI}(1) - r_{ECI}(1)v_{ECI}(3) \\ r_{ECI}(1)v_{ECI}(2) - r_{ECI}(2)v_{ECI}(1) \end{bmatrix} \\ h &= ||\mathbf{h}_{ECI}|| \end{aligned} \tag{A.40}$$

$$\begin{aligned} \mathbf{e} &= \frac{\mathbf{c}}{\mu} \\ e &= \frac{\left(\mathbf{c}^T\mathbf{c}\right)^{1/2}}{\mu} = \sqrt{1 - \frac{h^2}{\mu a}} \\ \mathbf{c} = \mathbf{v}_{ECI} \times \mathbf{h}_{ECI} - \mu\frac{\mathbf{r}_{ECI}}{r} &= \begin{bmatrix} v_{ECI}(2)h_{ECI}(3) - v_{ECI}(3)h_{ECI}(2) - \mu r_{ECI}(1)/r \\ v_{ECI}(3)h_{ECI}(1) - v_{ECI}(1)h_{ECI}(3) - \mu r_{ECI}(2)/r \\ v_{ECI}(1)h_{ECI}(2) - v_{ECI}(2)h_{ECI}(1) - \mu r_{ECI}(3)/r \end{bmatrix} \end{aligned} \tag{A.41}$$

A.3.1.3 Eccentric Anomaly, True Anomaly, and Mean Anomaly

Compute Eccentric Anomaly, E_0, using Equation (A.42)

$$E_0 = \arctan\left[\frac{\frac{\sigma}{\sqrt{a}}}{1-\frac{r}{a}}\right] = \arctan\left[\frac{\frac{r}{a\sqrt{1-e^2}}\sin(f)}{\frac{r}{a}\cos(f)+e}\right] \tag{A.42}$$

The Eccentric Anomaly makes use of the σ_0 scalar parameter which takes on a zero value when the object is at periapsis or apoapsis for an elliptic orbit or at any point in a circular orbit [66], this useful scalar function is given by Equation (A.43)

$$\begin{aligned}\sigma_0 &= \frac{\mathbf{r}_{ECI}^T\mathbf{v}_{ECI}}{\sqrt{\mu}} = \frac{r_{ECI}(1)v_{ECI}(1)+r_{ECI}(2)v_{ECI}(2)+r_{ECI}(3)v_{ECI}(3)}{\sqrt{\mu}} \\ &= e\sqrt{a}\sin(E_0)\end{aligned} \tag{A.43}$$

Compute Initial True Anomaly, f_0 (Quadrants are not an issue [66]), from Equation (A.44).

$$f_0 = 2\arctan\left[\sqrt{\frac{1+e}{1-e}}\tan\left(\frac{E_0}{2}\right)\right] \tag{A.44}$$

Compute initial Mean Anomaly, M_0, from Equation (A.45).

$$M_0 = E_0 - e\sin(E_0) = E_0 - \frac{\mathbf{r}_{ECI}^T\mathbf{v}_{ECI}}{\sqrt{\mu a}} \tag{A.45}$$

A.3.1.4 Right Ascension of the Ascending Node

The Right Ascension of the Ascending Node, Ω, can be computed from the the angular velocity vector and magnitude using Equation (A.46).

$$\Omega = \arctan\left[-\frac{h_{ECI}(1)}{h_{ECI}(2)}\right] = \arctan\left[\frac{r_{ECI}(3)v_{ECI}(2)-r_{ECI}(2)v_{ECI}(3)}{r_{ECI}(3)v_{ECI}(1)-r_{ECI}(1)v_{ECI}(3)}\right] \tag{A.46}$$

A.3.1.5 Inclination

Inclination can be computed from the angular momentum vector using Equation (A.47).

$$i = \arccos\left[\frac{h_{ECI}(3)}{h}\right] = \arccos\left[\frac{r_{ECI}(1)v_{ECI}(2) - r_{ECI}(2)v_{ECI}(1)}{h}\right] \tag{A.47}$$

A.3.1.6 Argument of Perigee

Argument of Perigee can be computed from the eccentricity vector and the cross-product between the angular momentum vector and the eccentricity vector, Equation (A.48).

$$\begin{aligned}
\omega &= \arctan\left[\frac{\aleph}{\beth}\right] \\
\aleph &= \frac{\mathbf{c}_{ECI}(3)}{\mu e} = \frac{v_{ECI}(1)h_{ECI}(2) - v_{ECI}(2)h_{ECI}(1) - r_{ECI}(3)/r}{\mu e} \\
\beth &= \hat{\mathbf{i}}_p(3) = \frac{h_{ECI}(1)e_{ECI}(2) - h_{ECI}(2)e_{ECI}(1)}{\mu e h_{ECI}} \\
\hat{\mathbf{i}}_p &= \frac{\mathbf{h}_{ECI}}{h_{ECI}} \times \frac{\mathbf{c}_{ECI}}{\mu e} = \frac{1}{\mu e h_{ECI}}\left(\mathbf{h}_{ECI} \times \mathbf{c}_{ECI}\right)
\end{aligned} \tag{A.48}$$

The argument of perigee can be alternatively computed via use of the argument of latitude, u, and true anomaly, f, [74], shown in Equation (A.49).

$$\begin{aligned}
u &= \arctan\left[\frac{r_{ECI}(3)}{r_{ECI}(2)\dfrac{h_{ECI}(1)}{h} - r_{ECI}(1)\dfrac{h_{ECI}(2)}{h}}\right] \\
\sin(u) &= \frac{\mathbf{r}_{Orbit}(3)}{r\sin(i)} \\
\cos(u) &= \frac{\mathbf{r}_{Orbit}(1)}{r}\cos(\Omega) + \frac{\mathbf{r}_{Orbit}(2)}{r}\sin(\Omega) \\
\omega &= u - f
\end{aligned} \tag{A.49}$$

A.3.1.7 Directrix

Using the property of the directrix in the geometry of the conic section, the semi-latus rectum, p, can be related to eccentricity, scalar distance from the primary focus, r, and the projection of the scalar distance from the primary focus along the periapse direction, x_{Orbit}, by Equation (A.50).

$$p = x_{Orbit}e + r \tag{A.50}$$

A.3.2 Keplerian Orbital Elements to ECI Cartesian

To generate the Cartesian position and velocity vectors, $(\mathbf{r}_{ECI}, \mathbf{v}_{ECI})$ associated with the ECI frame from the orbital elements, $a,\ e,\ i,\ \omega,\ \Omega,\ M$ and the time since perigee, $t - t_p$, the following procedure is executed.

A.3.2.1 Mean Angular Motion and Mean Anomaly

The mean motion, n, is computed as Equation (A.51). The mean anomaly of the present position is computed from the Mean Anomaly at Perigee, M_0, and the time since perigree, $t - t_p$, shown by Equation (A.52).

$$n = \sqrt{\frac{\mu}{a^3}} = \frac{2\pi}{\text{Orbit Period}} \tag{A.51}$$

$$M = M_0 + n(t - t_p) \tag{A.52}$$

A.3.2.2 Eccentric Anomaly and True Anomaly

Since Eccentric and Mean anomaly are related by $M = E - e\sin(E)$, Kepler's equation must be solved from a root finding algorithm which Newton's method works extremely well for. The initial guess for eccentric anomaly is computed from mean

anomaly and eccentricity and shown by Equation (A.53).

$$E_0 = \begin{cases} M + e/2 & M \leq \pi \\ M - e/2 & M > \pi \end{cases} \tag{A.53}$$

Newton's method is then used to iterate on Eccentric using the Eccentric anomaly equation and its derivative to compute the update ratio, Equation (A.54). For true anomaly apply Equation (A.44).

$$\begin{aligned} &WHILE && CONVERGE = FALSE \\ &&& ratio = \frac{E - e\sin(E)}{1 - e\cos(E)} \\ &&& IF \qquad\qquad ratio < tol \\ &&&\qquad\qquad CONVERGE = TRUE \\ &&& ELSE \\ &&&\qquad\qquad E = E - ratio \\ &&&\qquad\qquad i = i + 1 \\ &&& END\ IF \\ &END\ WHILE \end{aligned} \tag{A.54}$$

A.3.2.3 Orbit Position Vectors

With eccentric anomaly, Cartesian vector in the orbit frame can be computed for position and velocity, Equation (A.55). With true anomaly, Cartesian vector in the

orbit frame can be computed for position and velocity, Equation (A.56).

$$\begin{aligned}
\mathbf{r}_{Orbit} &= \begin{bmatrix} x \\ y \\ 0 \end{bmatrix}_{Orbit} = \begin{bmatrix} a\left(\cos(E) - e\right) \\ a\sqrt{1-e^2}\sin(E) \\ 0 \end{bmatrix} \\
\mathbf{v}_{Orbit} &= \begin{bmatrix} \dot{x} \\ \dot{y} \\ 0 \end{bmatrix}_{Orbit} = \begin{bmatrix} \dfrac{-\sqrt{\mu a}\sin(E)}{r} \\ \dfrac{\sqrt{\mu a(1-e^2)}\cos(E)}{r} \\ 0 \end{bmatrix} \\
& r = a\left(1 - e\cos(E)\right)
\end{aligned} \tag{A.55}$$

$$\begin{aligned}
\mathbf{r}_{Orbit} &= \begin{bmatrix} x \\ y \\ 0 \end{bmatrix}_{Orbit} = \begin{bmatrix} r\cos(f) \\ r\sin(f) \\ 0 \end{bmatrix} \\
\mathbf{v}_{Orbit} &= \begin{bmatrix} \dot{x} \\ \dot{y} \\ 0 \end{bmatrix}_{Orbit} = \begin{bmatrix} \dot{r}\cos(f) - r\dot{f}\sin(f) \\ \dot{r}\sin(f) + r\dot{f}\cos(f) \\ 0 \end{bmatrix} \\
& r = \frac{p}{1 + e\cos(f)} \quad , \quad p = a\left(1 - e^2\right) \\
& \dot{f} = \frac{h}{r^2} = \frac{\sqrt{\mu p}}{r^2} \quad , \quad \dot{r} = \sqrt{\frac{\mu}{p}}e\sin(f)
\end{aligned} \tag{A.56}$$

A.3.2.4 Rotation Matrix from Orbit Frame to ECI Frame

Equation (A.57) is the 3-1-3 Direction Cosine Matrix from Cartesian ECI to Orbital Elements. The Direction Cosine Matrix can also be represented in terms of the unit vectors chosen to define the principal axes of the local orbit frame shown by

Equation (A.58).

$$\begin{aligned} C_{ECI2Orbit} &= C_\omega C_i C_\Omega \\ C_\omega &= \mathbf{Rot}\left[3, \omega\right] \\ C_i &= \mathbf{Rot}\left[1, i\right] \\ C_\Omega &= \mathbf{Rot}\left[3, \Omega\right] \end{aligned} \tag{A.57}$$

$$C_{ECI2Orbit} = \begin{bmatrix} \hat{\mathbf{i}}_e^T \\ \hat{\mathbf{i}}_p^T \\ \hat{\mathbf{i}}_h^T \end{bmatrix} = \begin{bmatrix} \left[\dfrac{\mathbf{c}}{\mu e}\right]^T \\ \left[\dfrac{\mathbf{h}}{|\mathbf{h}|} \times \dfrac{\mathbf{c}}{\mu e}\right]^T \\ \left[\dfrac{\mathbf{h}}{|\mathbf{h}|}\right]^T \end{bmatrix} \tag{A.58}$$

With the direction cosine matrix, the orbital frame Cartesian vectors can be rotated into ECI frame according to Equation (A.59).

$$\begin{aligned} \mathbf{r}_{ECI} &= C_{ECI2Orbit}^T \mathbf{r}_{Orbit} \\ \mathbf{v}_{ECI} &= C_{ECI2Orbit}^T \mathbf{v}_{Orbit} \end{aligned} \tag{A.59}$$

The transposed direction cosine matrix can be decomposed into columns which correspond to the unit vector triad describing the orbital plane, $\left\{\hat{\mathbf{P}}, \hat{\mathbf{Q}}, \hat{\mathbf{W}}\right\}$, which

are given by Equation (A.60).

$$
\begin{aligned}
C^{T}_{ECI2Orbit} &= \left[\begin{array}{c:c:c} \hat{\mathbf{P}} & \hat{\mathbf{Q}} & \hat{\mathbf{W}} \end{array} \right] \\
\hat{\mathbf{P}} &= \begin{bmatrix} \cos(\omega)\cos(\Omega) - \sin(\omega)\cos(i)\sin(\Omega) \\ \cos(\omega)\sin(\Omega) + \sin(\omega)\cos(i)\cos(\Omega) \\ \sin(\omega)\sin(i) \end{bmatrix} \\
\hat{\mathbf{Q}} &= \begin{bmatrix} -\sin(\omega)\cos(\Omega) - \cos(\omega)\cos(i)\sin(\Omega) \\ -\sin(\omega)\sin(\Omega) + \cos(\omega)\cos(i)\cos(\Omega) \\ \cos(\omega)\sin(i) \end{bmatrix} \\
\hat{\mathbf{W}} &= \begin{bmatrix} \sin(i)\sin(\Omega) \\ -\sin(i)\cos(\Omega) \\ \cos(i) \end{bmatrix}
\end{aligned}
\tag{A.60}
$$

Using the argument of latitude, $u = \omega + f$, in association with the orbital plane vector in terms of true anomaly allows for the inertial position and velocity vectors which are given by Equation (A.61).

$$
\begin{aligned}
\mathbf{r}_{ECI} &= r \begin{bmatrix} \cos(u)\cos(\Omega) - \sin(u)\cos(i)\sin(\Omega) \\ \cos(u)\sin(\Omega) + \sin(u)\cos(i)\cos(\Omega) \\ \sin(u)\sin(i) \end{bmatrix} \\
\mathbf{v}_{ECI} &= -\frac{\mu}{h} \begin{bmatrix} \cos(\Omega)\left(\sin(u) + e\sin(\omega)\right) + \sin(\Omega)\left(\cos(u) + e\cos(\omega)\right)\cos(i) \\ \sin(\Omega)\left(\sin(u) + e\sin(\omega)\right) - \cos(\Omega)\left(\cos(u) + e\cos(\omega)\right)\cos(i) \\ -\left(\cos(u) + e\cos(\omega)\right)\sin(i) \end{bmatrix}
\end{aligned}
\tag{A.61}
$$

APPENDIX B

FIRST-ORDER TRANSFORMATION BETWEEN OSCULATING KEPLERIAN ORBITAL ELEMENTS AND MEAN KEPLERIAN ORBITAL ELEMENTS

This appendix presents Lyddane's modification to Brouwer's theory [55] up to the first-order of the J_2 zonal perturbation Hamiltonian. For explicit equations of Lyddane's modification up through second-order see Long et al. [65]. The first-order solution is utilized so that no iterations are needed to convert from osculating orbital elements to mean orbital element as would be required by including higher-order effects [78, 79]. The format of the algorithm follows that given by Schaub and Junkins [66] to reduce clutter, where the transformed-to element space is denoted with a single prime and the initial space elements possess no superscript. For small eccentricity one could also use the approach of Born et al. [69], where eccentricity, argument of perigee, and mean anomaly are replaced with $e\sin(\omega)$, $e\cos(\omega)$, and $\omega + M$, but the long-period terms are neglected.

When transforming between osculating and mean element spaces the modification made to Brouwer's γ_2 variable is given by Equation (B.1). Other simplifying variables are given by Equation (B.2). The true anomaly variable for the initial domain is computed from the eccentric anomaly solution to Kepler's equation if it is not already known.

$$\gamma_2 = \natural \frac{J_2}{2}\left(\frac{R_\oplus}{a}\right)^2$$
$$\natural = \begin{cases} -1 & \text{Osculating to Mean} \\ +1 & \text{Mean to Osculating} \end{cases} \tag{B.1}$$

$$\begin{aligned}
\gamma_2' &= \frac{\gamma_2}{\eta^4} \\
\frac{a}{r} &= \frac{1 + e\cos(f)}{\eta^2} \\
\eta &= \sqrt{1 - e^2}
\end{aligned} \tag{B.2}$$

The new domain's semi-major axis is then computed from the first-order J_2 mapping given by Brouwer with the modified γ_2 variable as shown by Equation (B.3). Note that the semi-major axis only contains secular and short-period results.

$$\begin{aligned}
\Rightarrow a' = a \Bigg\{ 1 + \gamma_2 \Bigg[\left(3\cos^2(i) - 1\right) \left(\left(\frac{a}{r}\right)^3 - \eta^{-3} \right) \\
+3\left(1 - \cos^2(i)\right) \left(\frac{a}{r}\right)^3 \cos(2\omega + 2f) \Bigg] \Bigg\}
\end{aligned} \tag{B.3}$$

The long-period and short-period corrections for eccentricity are modified using Lyddane's expressions in order to avoid errors when the eccentricity is small. The modifications are given by Equation (B.4). The short-period results for eccentricity are given by Equation (B.5) and since the long-period eccentricity and inclination are related by a scale factor both are given in Equation (B.6). The short-period results for inclination are given in Equation (B.7). If in the present domain, true anomaly is not available it must be computed from mean anomaly and eccentricity either by Newton's method for Kepler's equation, Appendix A.3.1.3, or the series or Bessel function expansions given in Section 4.3.4.

$$\begin{aligned}
\frac{1}{e}\left[\left(\frac{a}{r}\right)^3 - \eta^{-3}\right] &= \eta^{-6}\left[e\eta + e\left(1+\eta\right)^{-1} + 3\cos(f) + 3e\cos^2(f) + e^2\cos^3(f)\right] \\
\frac{1}{e}\left[\left(\frac{a}{r}\right)^3 - \eta^{-4}\right] &= \eta^{-6}\left[e + 3\cos(f) + 3e\cos^2(f) + e^2\cos^3(f)\right]
\end{aligned} \tag{B.4}$$

$$
\begin{aligned}
e_{SP} &= \frac{\eta^2}{2}\left(\gamma_2 e_{SP1} + \gamma_2 e_{SP2} - \gamma_2' e_{SP3}\right) \\
e_{SP1} &= \frac{3\cos^2(i)-1}{\eta^6}\left(e\eta + \frac{e}{1+\eta} + 3\cos(f) + 3e\cos^2(f) + e^2\cos^3(f)\right) \\
e_{SP2} &= 3\frac{1-\cos^2(i)}{\eta^6}\left(e + 3\cos(f) + 3e\cos^2(f) + e^2\cos^3(f)\right)\cos(2\omega + 2f) \\
e_{SP3} &= \left(1-\cos^2(i)\right)\left(3\cos(2\omega+f) + \cos(2\omega+3f)\right)
\end{aligned}
\tag{B.5}
$$

$$
\begin{aligned}
e_{LP} &= \frac{\gamma_2' e\eta^2\cos(2\omega)}{8}\left(1 - 11\cos^2(i) - 40\frac{\cos^4(i)}{1-5\cos^2(i)}\right) \\
i_{LP} &= -\frac{e}{\eta^2\tan(i)}e_{LP}
\end{aligned}
\tag{B.6}
$$

$$
i_{SP} = \frac{1}{2}\gamma_2'\cos(i)\left[3\cos(2\omega+2f) + 3e\cos(2\omega+f) + e\cos(2\omega+3f)\right] \tag{B.7}
$$

The long and short-period terms of mean anomaly are given by Equations (B.8) and (B.9).

$$
M_{LP} = \frac{\gamma_2'\eta^3}{8}\left(1 - 11\cos^2(i) - 40\cos^4(i)\left(1-5\cos^2(i)\right)^{-1}\right)\sin(2\omega) \tag{B.8}
$$

$$
\begin{aligned}
M_{SP} = -\frac{\gamma_2'\eta^3}{4e}\Bigg\{ & 2\left(3\cos^2(i)-1\right)\left(\left(\frac{a\eta}{r}\right)^2 + \frac{a}{r} + 1\right)\sin(f) \\
& + 3\left(1-\cos^2(i)\right)\Bigg[\left(-\left(\frac{a\eta}{r}\right)^2 - \frac{a}{r} + 1\right)\sin(2\omega+f) \\
& + \left(\left(\frac{a\eta}{r}\right)^2 + \frac{a}{r} + \frac{1}{3}\right)\sin(2\omega+3f)\Bigg]\Bigg\}
\end{aligned}
\tag{B.9}
$$

The new domain eccentricity and mean anomaly can be computed using from

Equation (B.10).

$$\begin{aligned} e'\cos(M') &= (e + e_{LP} + e_{SP})\cos(M) - e\,(M_{LP} + M_{SP})\sin(M) \\ e'\sin(M') &= (e + e_{LP} + e_{SP})\sin(M) + e\,(M_{LP} + M_{SP})\cos(M) \\ \Rightarrow e' &= \sqrt{(e'\cos(M'))^2 + (e'\sin(M'))^2} \\ \Rightarrow M' &= \arctan\left\{\frac{e'\sin(M')}{e'\cos(M')}\right\} \end{aligned} \tag{B.10}$$

The long and short-period terms of right ascension of ascending node are given by Equations (B.11) and (B.12).

$$\Omega_{LP} = -\frac{\gamma_2' e^2\cos(i)}{8}\left(11 + \frac{80\cos^2(i)}{1-5\cos^2(i)} + \frac{200\cos^4(i)}{(1-5\cos^2(i))^2}\right)\sin(2\omega) \tag{B.11}$$

$$\begin{aligned} \Omega_{SP} = -\frac{\gamma_2'\cos(i)}{2}\big[&6\,(f - M + e\sin(f)) - 3\sin(2\omega + 2f) - 3e\sin(2\omega + f) \\ &-e\sin(2\omega + 3f)\big] \end{aligned} \tag{B.12}$$

The long and short-period terms of argument of perigee are given by Equations (B.13) through (B.16). Note that the first part of short-period term of argument of perigee and the short-period terms of mean anomaly do differ by a factor of η.

$$\begin{aligned} \omega_{LP} = -\frac{\gamma_2'}{16}\Bigg[&2 + e^2 - 11\left(2 + 3e^2\right)\cos^2(i) \\ &- \frac{40\,(2 + 5e^2)\cos^4(i)}{1 - 5\cos^2(i)} - \frac{400e^2\cos^6(i)}{(1-5\cos^2(i))^2}\Bigg]\sin(2\omega) \end{aligned} \tag{B.13}$$

$$\omega_{SP} = \omega_{SP1} + \omega_{SP2} \tag{B.14}$$

$$\omega_{SP1} = \frac{\gamma_2' \eta^2}{4e} \left\{ 2\left(3\cos^2(i) - 1\right) \left(\left(\frac{a\eta}{r}\right)^2 + \frac{a}{r} + 1 \right) \sin(f) \right.$$
$$+ 3\left(1 - \cos^2(i)\right) \left[\left(- \left(\frac{a\eta}{r}\right)^2 - \frac{a}{r} + 1 \right) \sin(2\omega + f) \right. \tag{B.15}$$
$$\left. \left. + \left(\left(\frac{a\eta}{r}\right)^2 + \frac{a}{r} + \frac{1}{3} \right) \sin(2\omega + 3f) \right] \right\}$$

$$\omega_{SP2} = \frac{\gamma_2'}{4} \left\{ 6\left(5\cos^2(i) - 1\right) (f - M + e\sin(f)) \right.$$
$$\left. + \left(3 - 5\cos^2(i)\right) \left[3\sin(2\omega + 2f) + 3e\sin(2\omega + f) + e\sin(2\omega + 3f) \right] \right\} \tag{B.16}$$

The composite longitude is then computed by Equation (B.17). Note that when the short-period terms of mean anomaly and the first short-period term of argument of perigee are added together the result of $\left(\eta^{-2} - \eta^{-1}\right)/e$ has eccentricity as a factor not divisor when simplified so the expression goes to 0/1 since $(1 - e^2) \to 1$ faster than $e \to 0$ as $e \to 0$, see Brouwer's remark after his Equation (23) [47], Equation (B.18) shows the rearrangement effect.

$$(M' + \omega' + \Omega') = M + M_{LP} + M_{SP} + \omega + \omega_{LP} + \omega_{SP} + \Omega + \Omega_{LP} + \Omega_{SP} \tag{B.17}$$

$$\begin{aligned} \frac{\gamma_2'}{4e}\left(\eta^2 - \eta^3\right) &= \frac{\gamma_2}{4e}\left(\eta^{-2} - \eta^{-1}\right) \\ &= \frac{\gamma_2}{4}\left(\frac{(\eta - 1)\dfrac{1}{e} + e}{\eta^3}\right) \end{aligned} \tag{B.18}$$

The new domain inclination, right ascension of ascending node, and argument of perigee can be computed using from Equations (B.19) and (B.20). When computing the transformed argument of perigee, Equations (B.17) and (B.18) are applied to compute the parenthetical term then the transformed Mean Anomaly solution from Equation (B.10) and transformed Right Ascension of Ascending Node solution from

Equation (B.20) are subtracted out.

$$\begin{aligned}
\sin\left(\frac{i'}{2}\right)\sin(\Omega') &= \left(\sin\left(\frac{i}{2}\right)+\frac{1}{2}\cos\left(\frac{i}{2}\right)(i_{SP}+i_{LP})\right)\sin(\Omega) \\
&\quad +\sin\left(\frac{i}{2}\right)(\Omega_{SP}+\Omega_{LP})\cos(\Omega) \\
\sin\left(\frac{i'}{2}\right)\cos(\Omega') &= \left(\sin\left(\frac{i}{2}\right)+\frac{1}{2}\cos\left(\frac{i}{2}\right)(i_{SP}+i_{LP})\right)\cos(\Omega) \\
&\quad -\sin\left(\frac{i}{2}\right)(\Omega_{SP}+\Omega_{LP})\sin(\Omega)
\end{aligned} \tag{B.19}$$

$$\begin{aligned}
\Rightarrow i' &= 2\arcsin\left\{\sqrt{\left(\sin\left(\frac{i'}{2}\right)\sin(\Omega')\right)^2+\left(\sin\left(\frac{i'}{2}\right)\cos(\Omega')\right)^2}\right\} \\
\Rightarrow \Omega' &= \arctan\left\{\frac{\sin\left(\frac{i'}{2}\right)\sin(\Omega')}{\sin\left(\frac{i'}{2}\right)\cos(\Omega')}\right\} \\
\Rightarrow \omega' &= (M'+\omega'+\Omega')-M'-\Omega'
\end{aligned} \tag{B.20}$$

An alternative but similar implementation of Lyddane's modification to Brouwer's theory is given by Long et al. [65]. Both versions were implemented and tested with differences found to be on the order of 1×10^{-9} for each element's respective units. The results of the Lyddane conversion between first order elements was also compared to those of Aksnes [58] who presented numerical results as well as explicit expressions of Izsak's approach which utilized Hill variables [57] in order to reduce the complexity of the Brouwer and Lyddane solutions.

For an example of conversion between orbital element space, the Two-Line element(TLE) of Hubble Space telescope(HST) was converted from mean to osculating then back to mean space with the results shown in Table B.1. The element conversion errors of mean to osculating back to mean (M→O→M) and osculating to mean back to osculating (O→M→O) are shown in Table B.2. The value of J_2 is approximately

0.00108, when converted to degrees from radians the value is approximately 0.0620. The tables show that the errors of semi-major axis, eccentricity, right ascension of ascending node, and inclination angle are below the order of J_2. The errors of the anomalies and argument of perigee are on the order of J_2, approximately 0.09 to 0.12 degrees which is 1.5 to 2 times J_2.

Table B.1: Keplerian Elements for HST TLE for Day 23 of Year 2011

Parameter	Original Mean	Converted Osculating	Converted Mean
Semi-Major Axis (km)	6941.499	6943.690	6941.498
Eccentricity	3.35×10^{-4}	1.45×10^{-3}	3.27×10^{-4}
RAAN (Deg)	238.23	237.79	238.23
Inclination (Deg)	28.47	28.48	28.47
Argument of Perigee (Deg)	30.04	6.530	30.14
True Anomaly (Deg)	330.02	354.46	329.92
Mean Anomaly (Deg)	330.04	354.47	329.94

Table B.2: Conversion Errors of HST TLE for Day 23 of Year 2011

Parameter	M→O→M Error	O→M→O
Semi-Major Axis (km)	0.0034	0.0035
Eccentricity	7.820×10^{-6}	7.983×10^{-6}
RAAN (Deg)	2.639×10^{-7}	1.305×10^{-6}
Inclination (Deg)	2.069×10^{-5}	2.083×10^{-5}
Argument of Perigee (Deg)	0.0993	0.1241
True Anomaly (Deg)	0.0988	0.1167
Mean Anomaly (Deg)	0.0993	0.1167

APPENDIX C

PARTIAL DERIVATIVES OF FIRST-ORDER MAPPING BETWEEN OSCULATING AND MEAN KEPLERIAN ELEMENTS

This appendix computes the partial derivatives for the planar orbit considered in Section 4.3.5. The short-hand variables such as γ_2, γ_2', η, $\frac{a}{r}$ and variables with subscripts SP or LP are taken from Appendix B. The traditional nomenclature of double primes representing mean elements and unprimed variables representing osculating elements is now implemented.

For the planar example, the partial derivatives of the mapping from mean elements to osculating semi-major axis are given by Equation (C.1) through (C.3).

$$\frac{\partial a}{\partial a''} = 1 + \left(\gamma_2 + a''\frac{\partial \gamma_2}{\partial a''}\right)\left[\left(3\cos^2(i'') - 1\right)\left(\left(\frac{a''}{r''}\right)^3 - \eta^{-3}\right) + 3\left(1 - \cos^2(i'')\right)\left(\frac{a''}{r''}\right)^3 \cos(2\omega'' + 2f'')\right] \tag{C.1}$$

$$\frac{\partial a}{\partial e''} = a''\gamma_2\left[\left(3\cos^2(i'') - 1\right)\left(3\left(\frac{a''}{r''}\right)^2 \frac{\partial \frac{a''}{r''}}{\partial e''} + \frac{3}{\eta^4}\frac{\partial \eta}{\partial e''}\right) + 9\left(1 - \cos^2(i'')\right)\left(\frac{a''}{r''}\right)^2 \frac{\partial \frac{a''}{r''}}{e''}\cos(2\omega'' + f'')\right] \tag{C.2}$$

$$\frac{\partial a}{\partial M''} = 0 \tag{C.3}$$

The partial derivatives of the osculating eccentricity with respect to the mean variables are given in general form by Equation (C.4). The partial derivatives of the

osculating mean anomaly are given in general form by Equation (C.5). For brevity, only the general forms of the remaining derivatives are provided in lieu of the explicit forms as shown for the partial derivatives with respect to mean semi-major axis.

$$\begin{aligned}
\frac{\partial e}{\partial \aleph} &= \left(d_1^2 + d_2^2\right)^{-1/2} \left(d_1 \frac{\partial d_1}{\partial \aleph} + d_2 \frac{\partial d_2}{\partial \aleph}\right) \\
d_1 &= e\sin(M) = (e'' + e_{LP} + e_{SP})\sin(M'') + e''\left(M_{LP} + M_{SP}\right)\cos(M'') \\
d_2 &= e\cos(M) = (e'' + e_{LP} + e_{SP})\cos(M'') - e''\left(M_{LP} + M_{SP}\right)\sin(M'') \\
\aleph &= a'',\ e'',\ \text{or}\ M''
\end{aligned} \tag{C.4}$$

$$\frac{\partial M}{\partial \aleph} = \left(1 + \left(\frac{d_1}{d_2}\right)^2\right)^{-1} \left(\frac{1}{d_2}\frac{\partial d_1}{\partial \aleph} - \frac{d_1}{d_2^2}\frac{\partial d_2}{\partial \aleph}\right) \tag{C.5}$$

The nonzero intermediate partial derivatives of γ_2, γ_2', η, and $\dfrac{a''}{r''}$ with respect to the mean variables are given by Equation (C.6).

$$\begin{aligned}
\frac{\partial \gamma_2}{\partial a''} &= -J_2 R_\oplus^2 a''^{-3} \\
\frac{\partial \gamma_2'}{\partial a''} &= -J_2 R_\oplus^2 a''^{-3}\eta^{-4}
\end{aligned}
\quad\Bigg|\quad
\begin{aligned}
\frac{\partial \eta}{\partial e''} &= -e''\left(1 - e''^2\right)^{-1/2} \\
\frac{\partial \gamma_2'}{\partial e''} &= -2\natural J_2 R_\oplus^2 a''^{-2}\eta^{-5}\frac{\partial \eta}{\partial e''} \\
\frac{\partial \dfrac{a''}{r''}}{\partial e''} &= \frac{\cos(f'')}{\eta^2} + \frac{2e''\left(1 + e''\cos(f'')\right)}{\eta^4}
\end{aligned} \tag{C.6}$$

For the three-dimensional case partial derivatives, the process is carried out in exactly the same way. When taking partial derivatives of the argument of perigee equation, Equation (B.20), one should again note that the addition of the short-period of mean anomaly and the first short-period of argument of perigee will remove the eccentricity divisor and it is this result that the partial derivative with respect to eccentricity should be taken.

APPENDIX D

ADDITIONAL FIGURES

D.1 From Section 4.3.7.2, Geopotential Perturbed Motion: Osculating Orbital Element Results

This section presents the osculating orbital element contour and scatter plots for the HEO RSO subjected to planar geopotential perturbed motion examined in Section 4.3.7.2. Figure D.1 presents the contour plots of the marginal PDFs computed from the Monte Carlo analysis while Figure D.2 presents the contour plots of the marginal PDFs computed from the TOV likelihood PDF. Figure 4.57 plots the scatter plot of the marginal PDFs from the TOV likelihood PDF which were used to generate the contour figure.

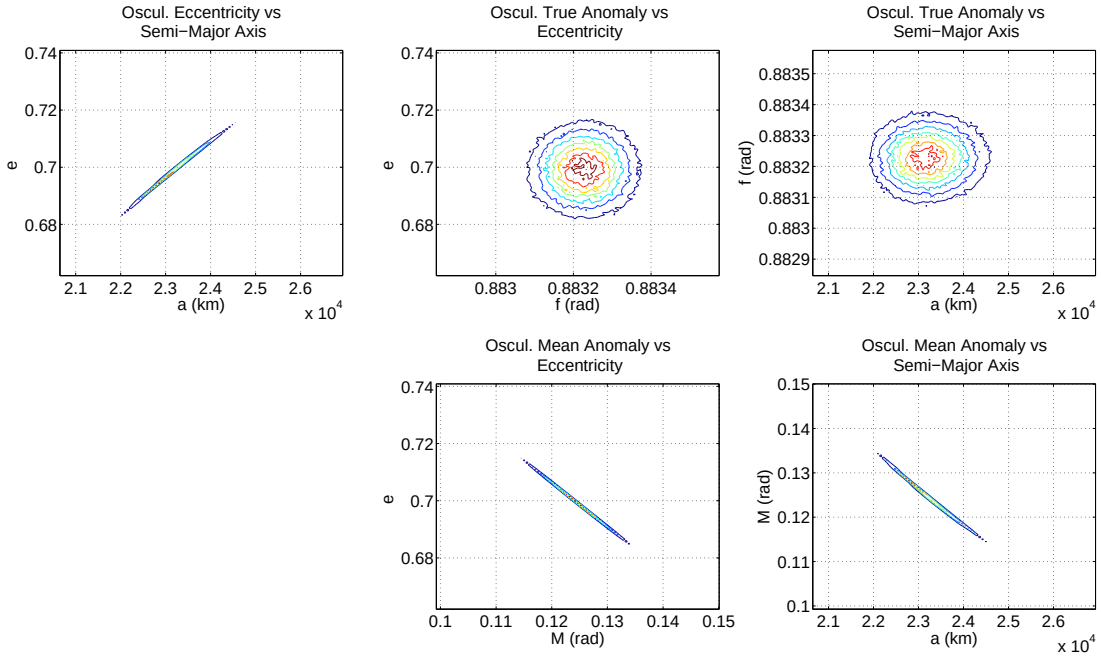

Figure D.1: HEO RSO Monte Carlo Osculating Orbital Element Marginal PDF Contour Results

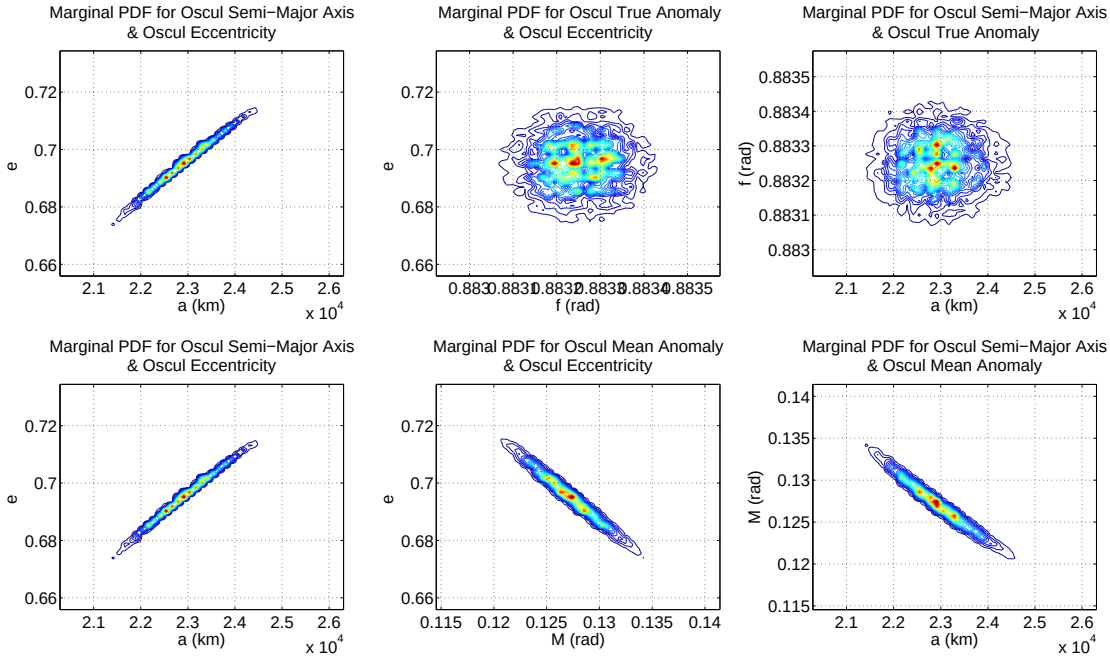

Figure D.2: HEO RSO TOVLikelihood Osculating Orbital Element Marginal PDF Contour Results

D.2 From Section 4.3.7.3, Geopotential Perturbed Motion: Mean Orbital Element Results

This section presents the mean orbital element contour and scatter plots for the HEO RSO subjected to planar geopotential perturbed motion examined in Section 4.3.7.3. Figure D.3 presents the contour plots of the marginal PDFs computed from the Monte Carlo analysis while Figure D.4 presents the contour plots of the marginal PDFs computed from the TOV likelihood PDF. Figure D.5 plots the scatter plot of the marginal PDFs from the TOV likelihood PDF which were used to generate the contour figure.

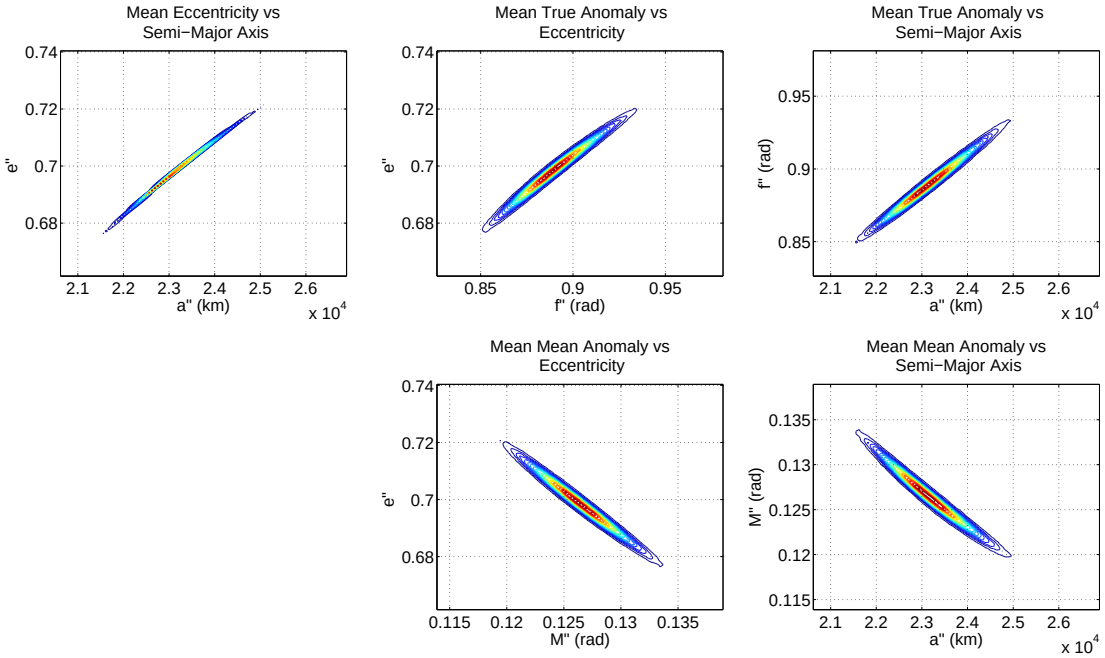

Figure D.3: HEO RSO Monte Carlo Mean Orbital Element Marginal PDF Contour Results

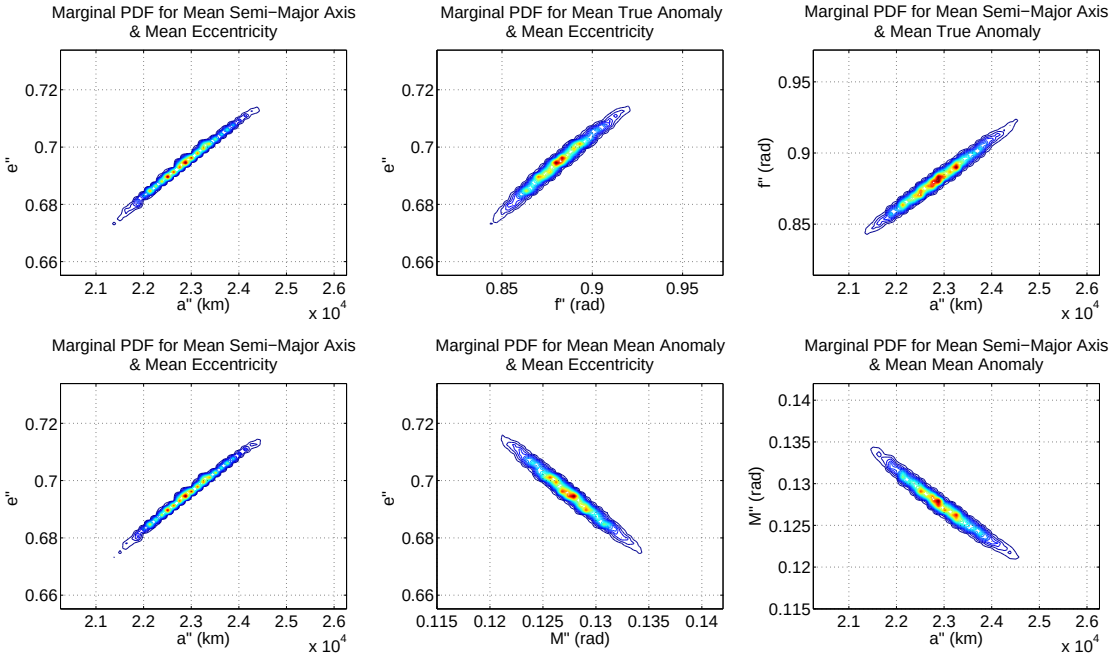

Figure D.4: HEO RSO TOVLikelihood Mean Orbital Element Marginal PDF Contour Results

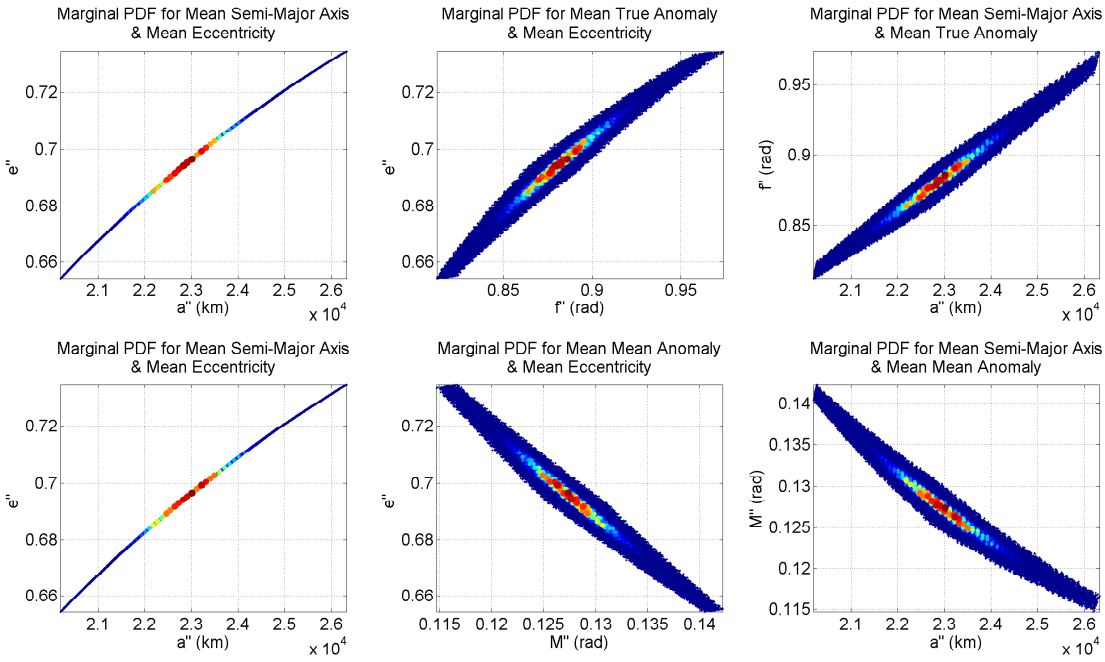

Figure D.5: HEO RSO TOVLikelihood Mean Orbital Element Marginal PDF Color-Coded Scatter Results

D.3 From Section 4.3.8.2, Three-Dimensional Geopoential Perturbed Motion: Osculating Keplerian Domain Results

This section presents the remaining osculating marginal PDF contour results for the three-dimensional simulation of an HST two-line element set as discussed in Section 4.3.8.2. Figure D.6 plots the TOV likelihood marginal PDF solutions with respect to orientation angles and Figure D.7 does the same for the Monte Carlo solution. Comparison of the two figures show the shortened flow in the mean anomaly and argument of perigee domains as was discussed in the main matter section, however the shape of the TOV likelihood solution approximates most of the Monte Carlo solution.

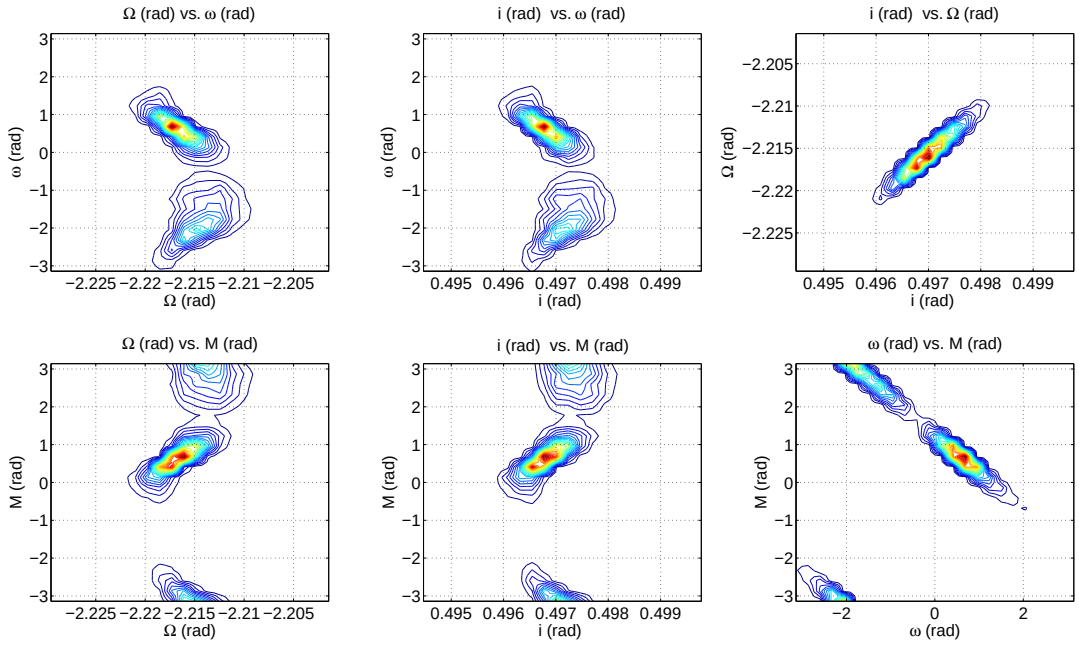

Figure D.6: Track 1 Osculating Orbital Element Marginal PDFs with respect to Orientation Angle from TOV Likelihood Solution

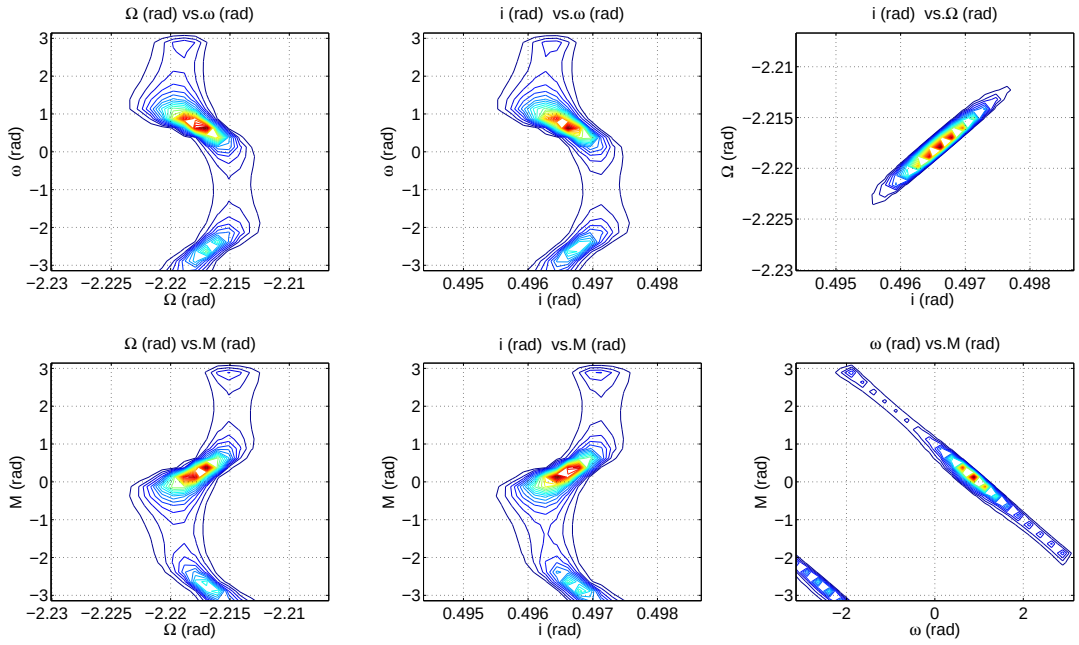

Figure D.7: Track 1 Osculating Orbital Element Marginal PDFs with respect to Orientation Angle from Monte Carlo Solution

D.4 From Section 4.3.8.3, Three-Dimensional Geopotential Perturbed Motion: Mean Keplerian Domain Results

This section presents the mean marginal PDF contour results for the three-dimensional simulation of an HST two-line element set as discussed in Section 4.3.8.3. Figures D.8 through D.13 present the marginal PDF results for the TOV likelihood and Monte Carlo solutions for with respect to semi-major axis, eccentricity, and orientation angles.

Figures D.8 and D.9 compare the TOV likelihood and Monte Carlo solution contours for the marginal PDFs with respect to the semi-major axis while Figures D.10 and D.11 compare the solution contours for the marginal PDFs with respect to eccentricity, except for the (a, e) PDF already reported. Finally, Figures D.12 and D.13 compare the solution contours for the marginal PDFs remaining after the semi-major axis and eccentricity combinations. The figures show that the TOV likelihood solutions for mean mean anomaly and argument of perigee possess a shorter flow of regions of high likelihood, however the regions of high likelihood for the TOV solution encompass the true mean solution while the Monte Carlo solution possesses a bifurcated solution for the coordinate variables of right ascension of ascending node, argument of perigee, and mean anomaly. The bifurcated solution clearly indicated by the mean anomaly and argument of perigee plots indicates that the apoapsis cannot be distinguished from the periapsis for the eccentricity value considered.

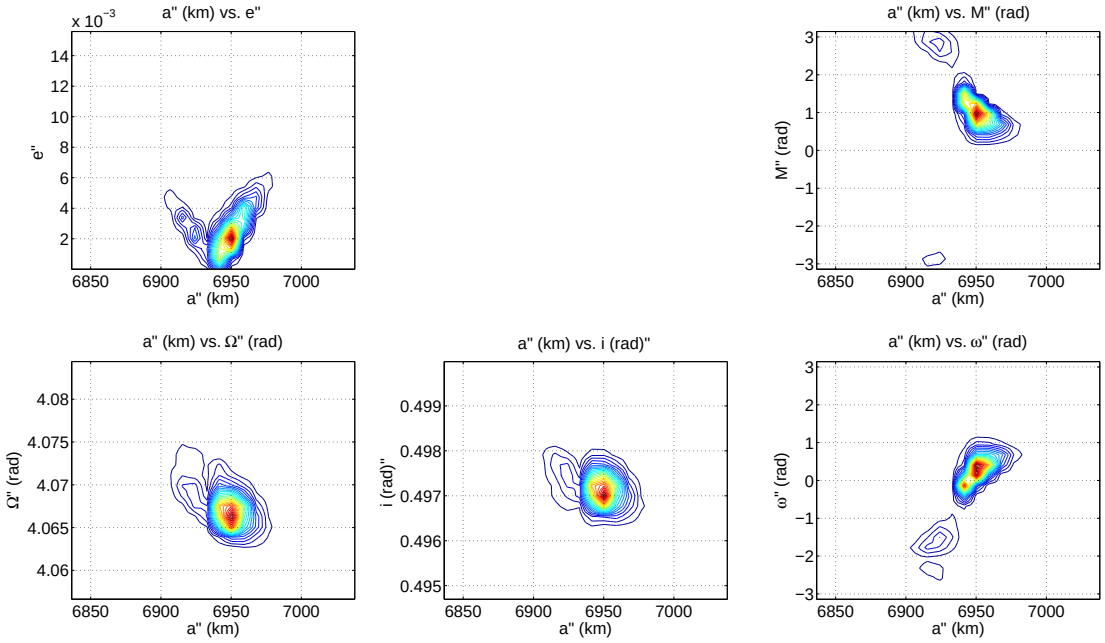

Figure D.8: Track 1 Mean Orbital Element Marginal PDFs with respect to Semi-Major Axis from TOV Likelihood Solution

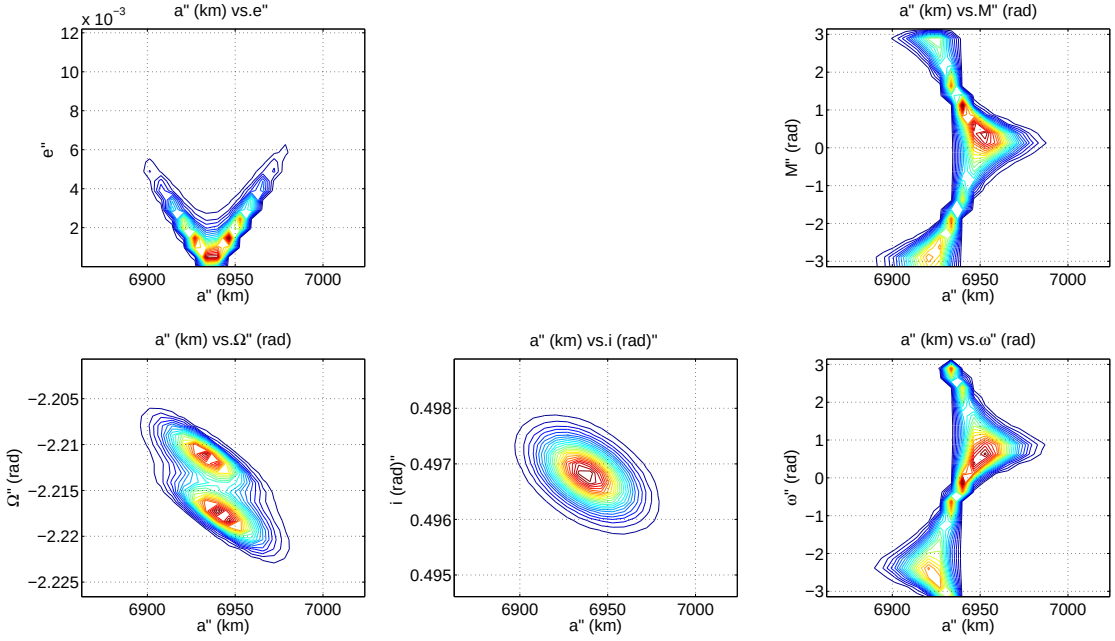

Figure D.9: Track 1 Mean Orbital Element Marginal PDFs with respect to Semi-Major Axis from Monte Carlo Solution

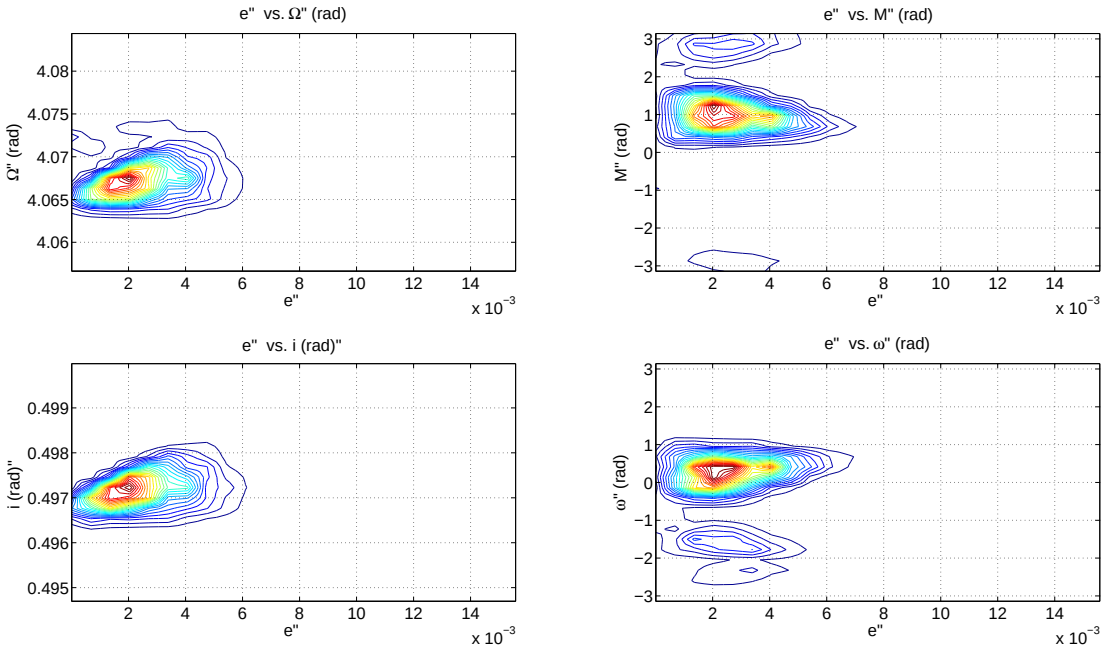

Figure D.10: Track 1 Mean Orbital Element Marginal PDFs with respect to Eccentricity from TOV Likelihood Solution

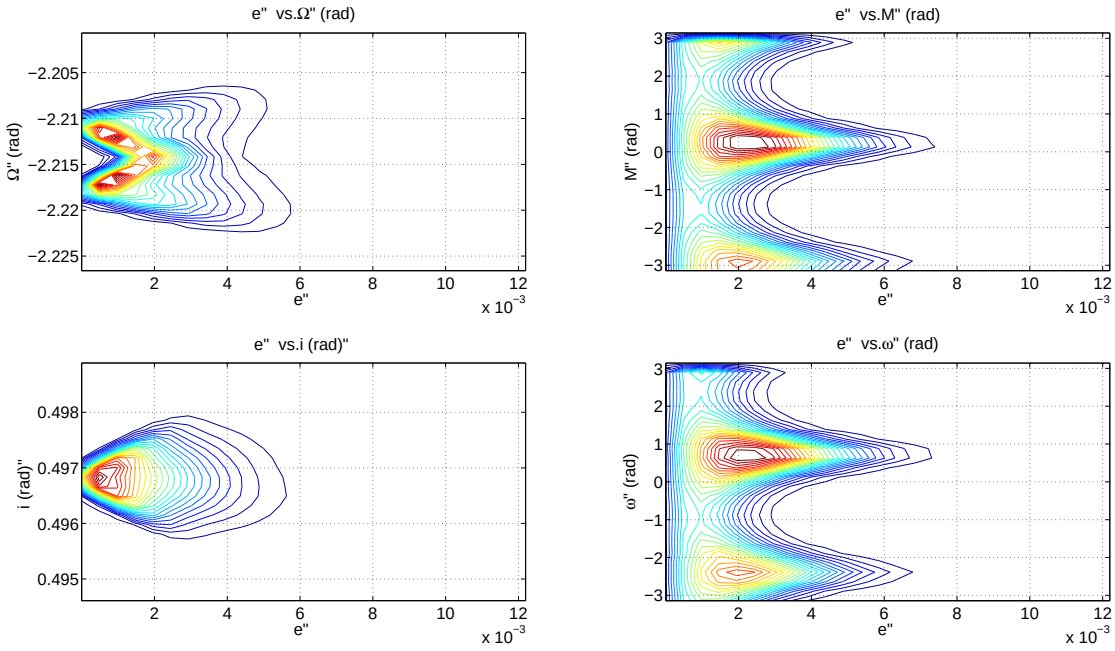

Figure D.11: Track 1 Mean Orbital Element Marginal PDFs with respect to Eccentricity from Monte Carlo Solution

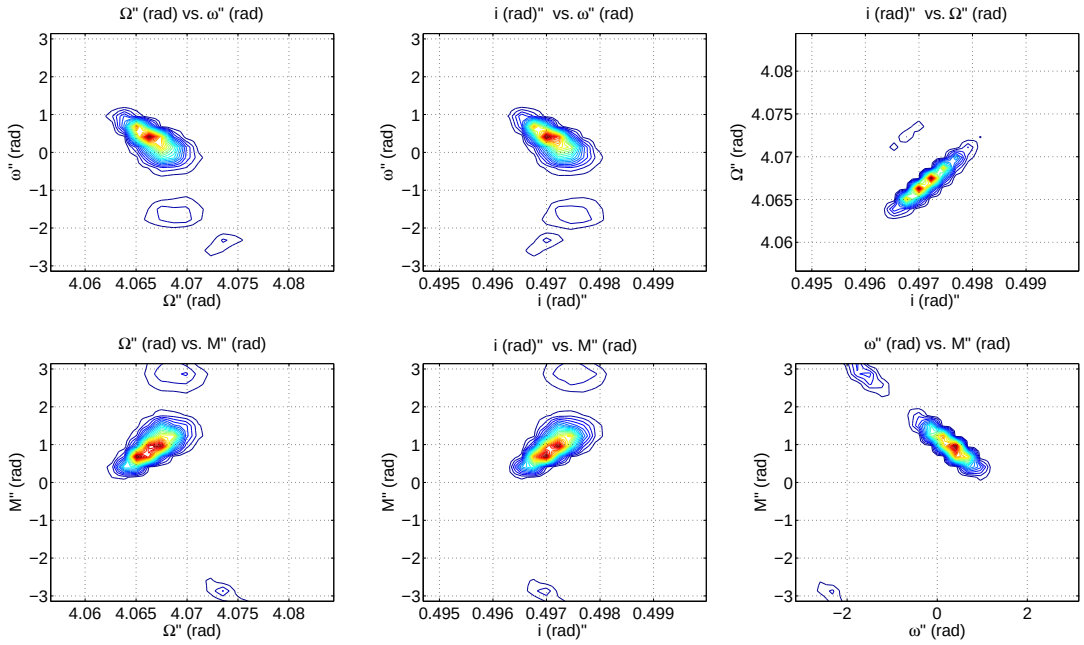

Figure D.12: Track 1 Mean Orbital Element Marginal PDFs with respect to Orientation Angle from TOV Likelihood Solution

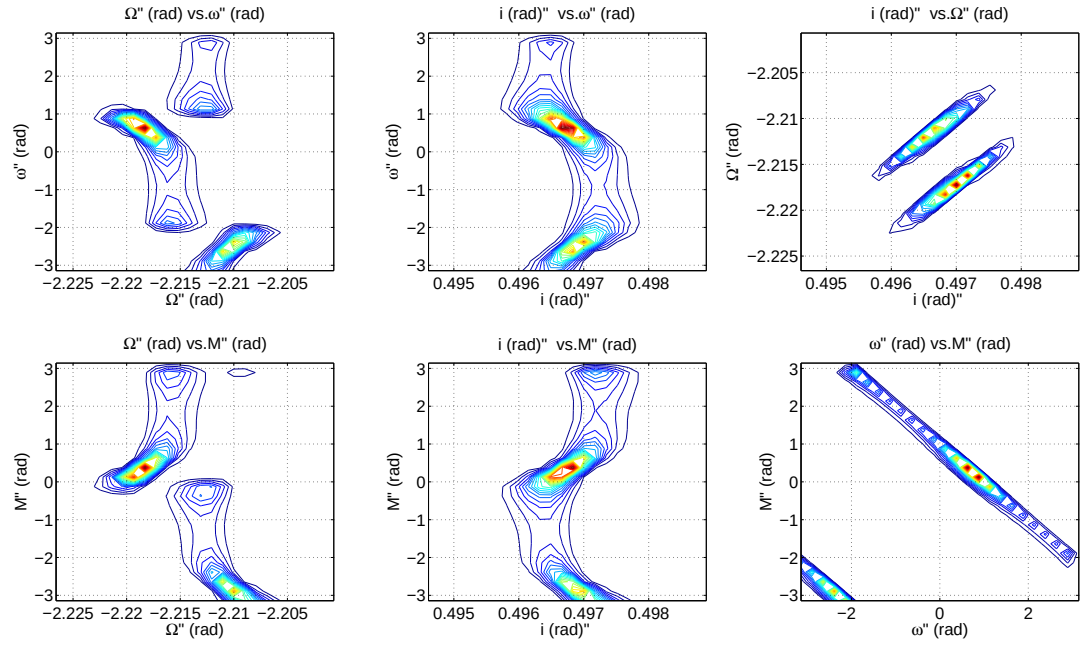

Figure D.13: Track 1 Mean Orbital Element Marginal PDFs with respect to Orientation Angle from Monte Carlo Solution

D.5 From Section 4.3.8.4, Three-Dimensional Geopotential Perturbed Motion: Increased Initial Osculating Eccentricity Results

This section presents the additional contour PDF results for the three-dimensional simulation of HST with an initial osculating eccentricity increased by an order of magnitude with the other orbital parameters kept the same as those from the TLE from Section 4.3.8.4. For comparison purposes, first the TOV solution results for the particular PDF are shown then the Monte Carlo results for the particular marginal PDF are shown.

Figures D.14 and D.15 plot the marginal PDF solutions with respect to eccentricity for the TOV likelihood solution and Monte Carlo solution respectively while Figures D.16 and D.17 repeat the analysis for the orientation angle marginal PDFs not given with respect to semi-major axis and eccentricity. Figures D.18 through D.23 repeat the results of the osculating analysis for the mean orbital element marginal PDF solutions of the TOV likelihood and Monte Carlo approaches. When comparing Figures D.14 through D.23 to their counterparts in the previous section, it is clear that uncertainty in the direction and magnitude of the eccentricity vector plays a significant role in being able to estimate the coordinate variables of right ascension of ascending node, argument of perigee, and mean anomaly.

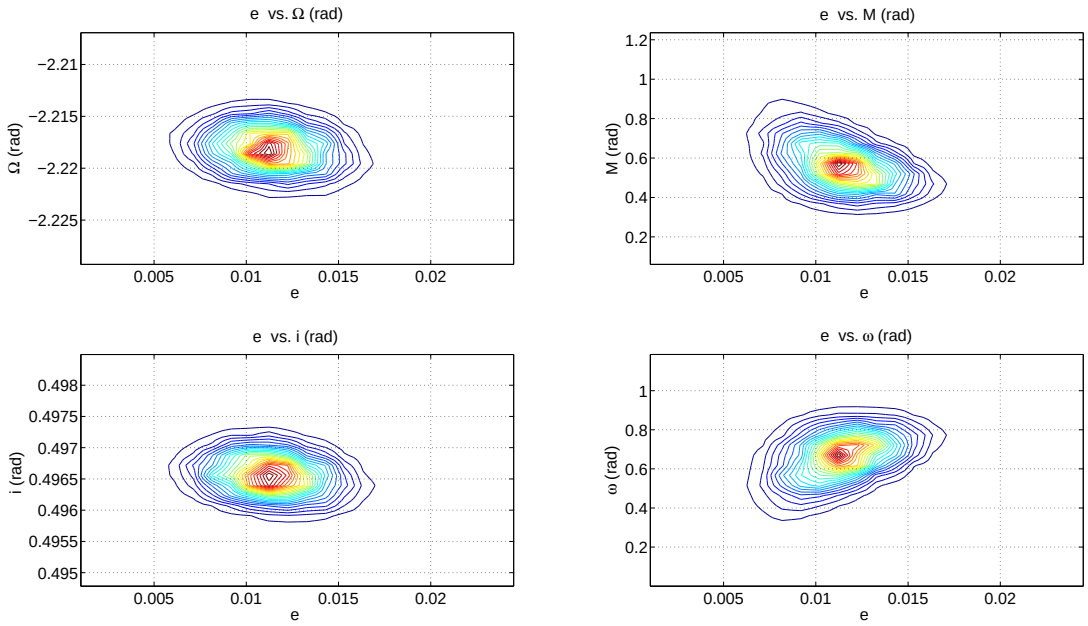

Figure D.14: Increased Eccentricity Track 1 Osculating Orbital Element Marginal PDFs with respect to Eccentricity from TOV Likelihood Solution

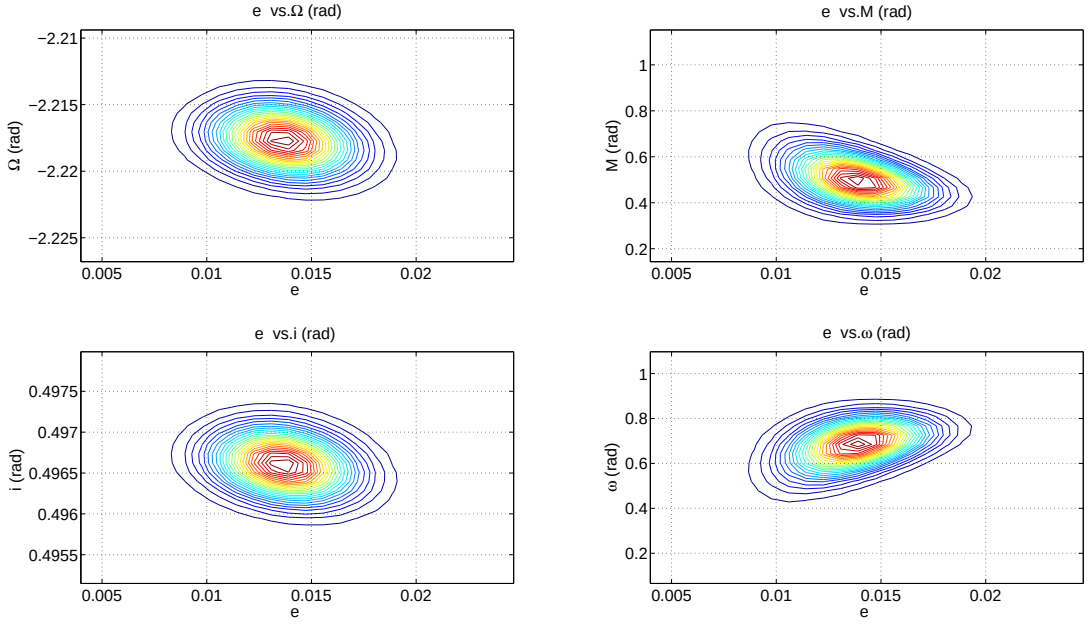

Figure D.15: Increased Eccentricity Track 1 Osculating Orbital Element Marginal PDFs with respect to Eccentricity from Monte Carlo Solution

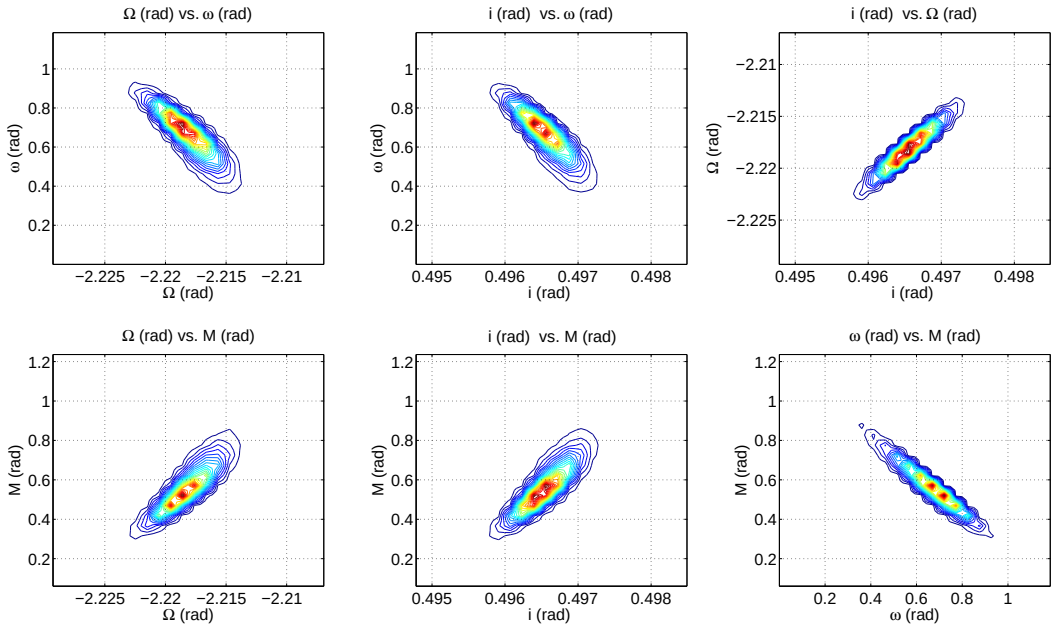

Figure D.16: Increased Eccentricity Track 1 Osculating Orbital Element Marginal PDFs with respect to Orientation Angle from TOV Likelihood Solution

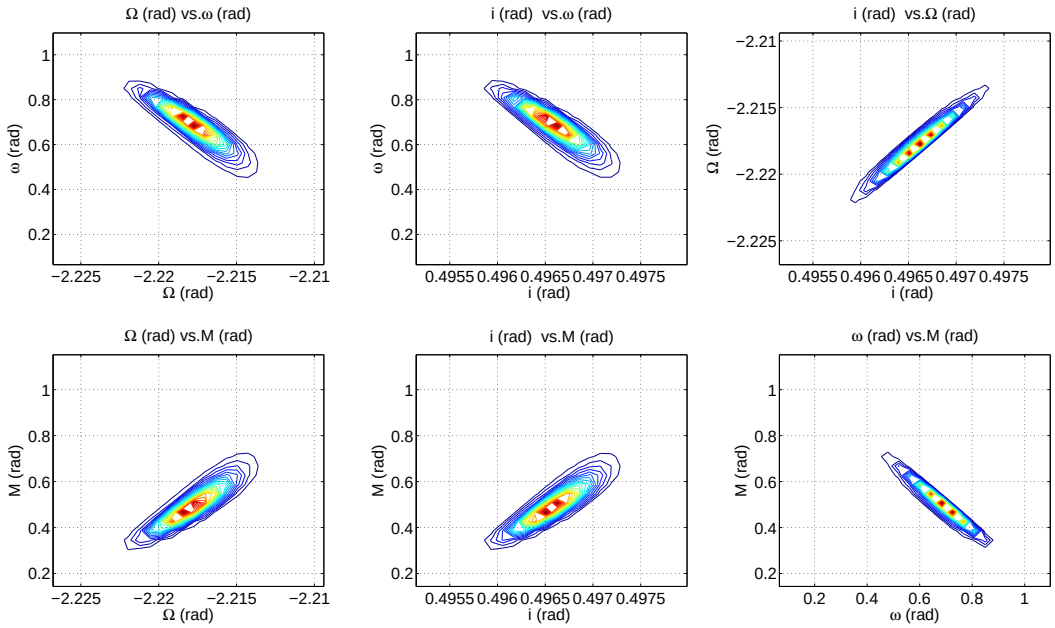

Figure D.17: Increased Eccentricity Track 1 Osculating Orbital Element Marginal PDFs with respect to Orientation Angle from Monte Carlo Solution

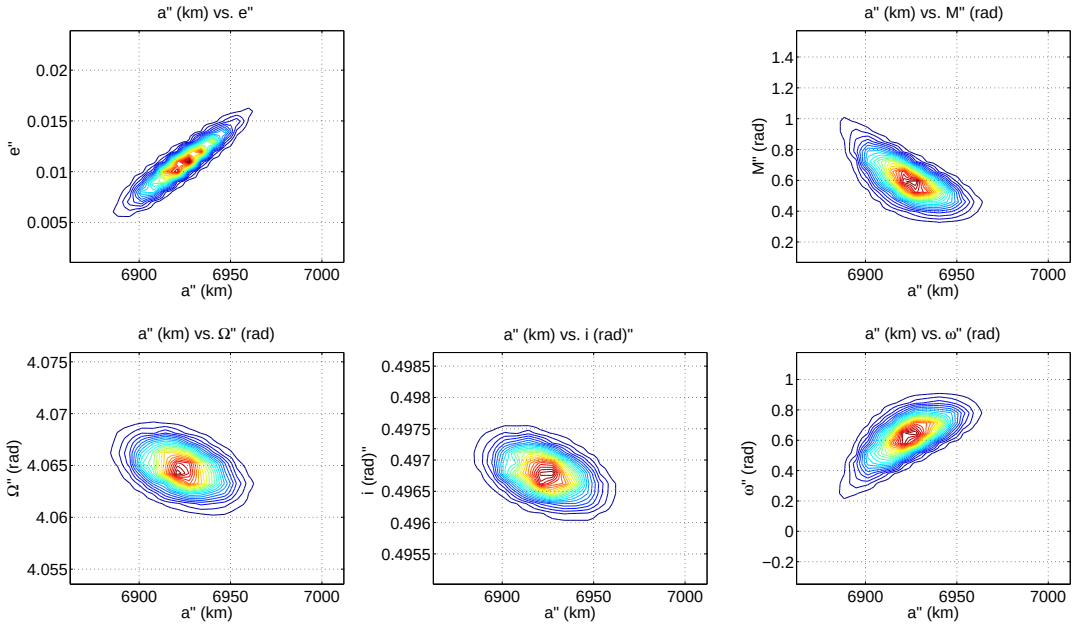

Figure D.18: Increased Eccentricity Track 1 Mean Orbital Element Marginal PDFs with respect to Semi-Major Axis from TOV Likelihood Solution

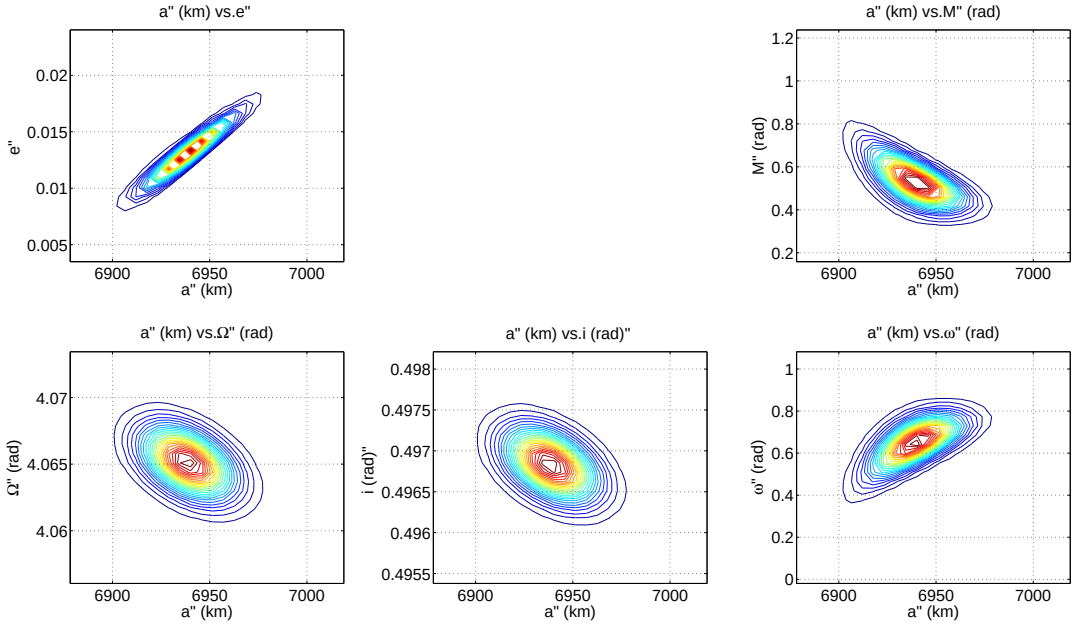

Figure D.19: Increased Eccentricity Track 1 Mean Orbital Element Marginal PDFs with respect to Semi-Major Axis from Monte Carlo Solution

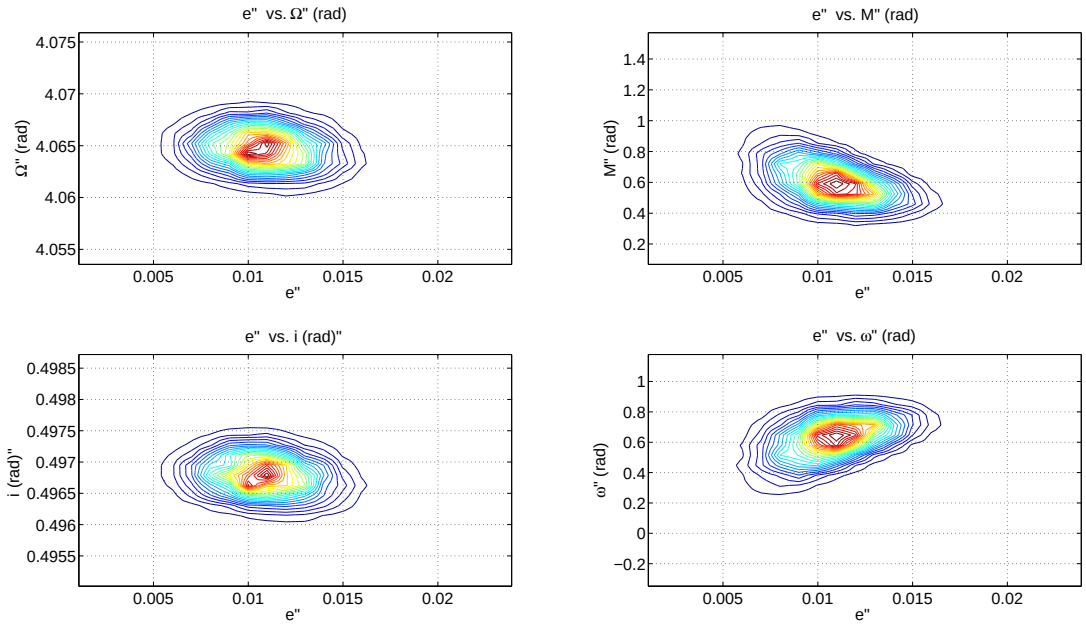

Figure D.20: Increased Eccentricity Track 1 Mean Orbital Element Marginal PDFs with respect to Eccentricity from TOV Likelihood Solution

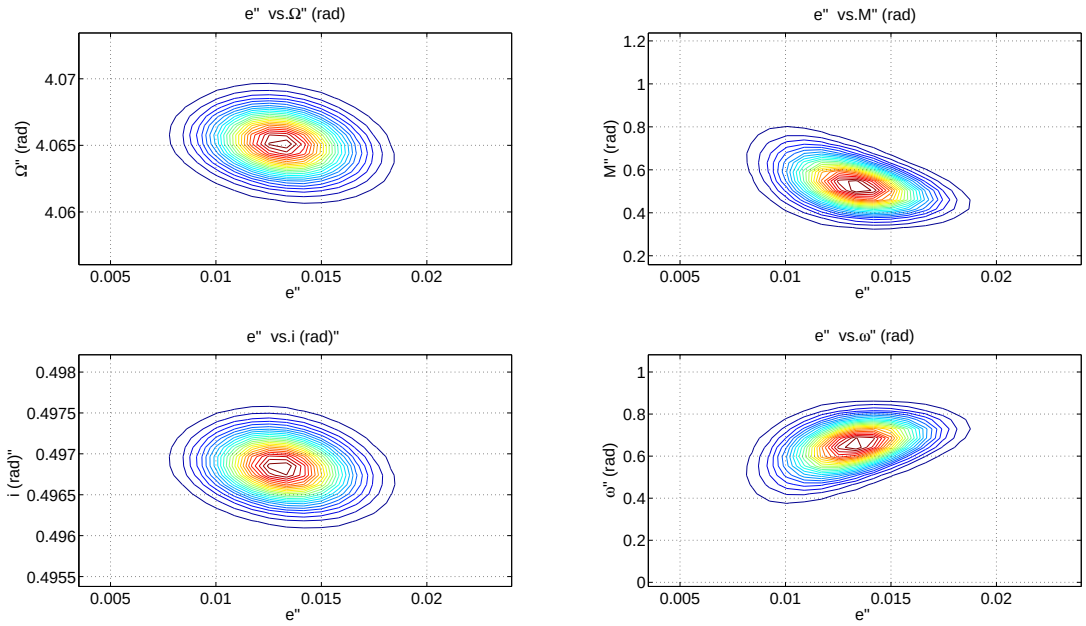

Figure D.21: Increased Eccentricity Track 1 Mean Orbital Element Marginal PDFs with respect to Eccentricity from Monte Carlo Solution

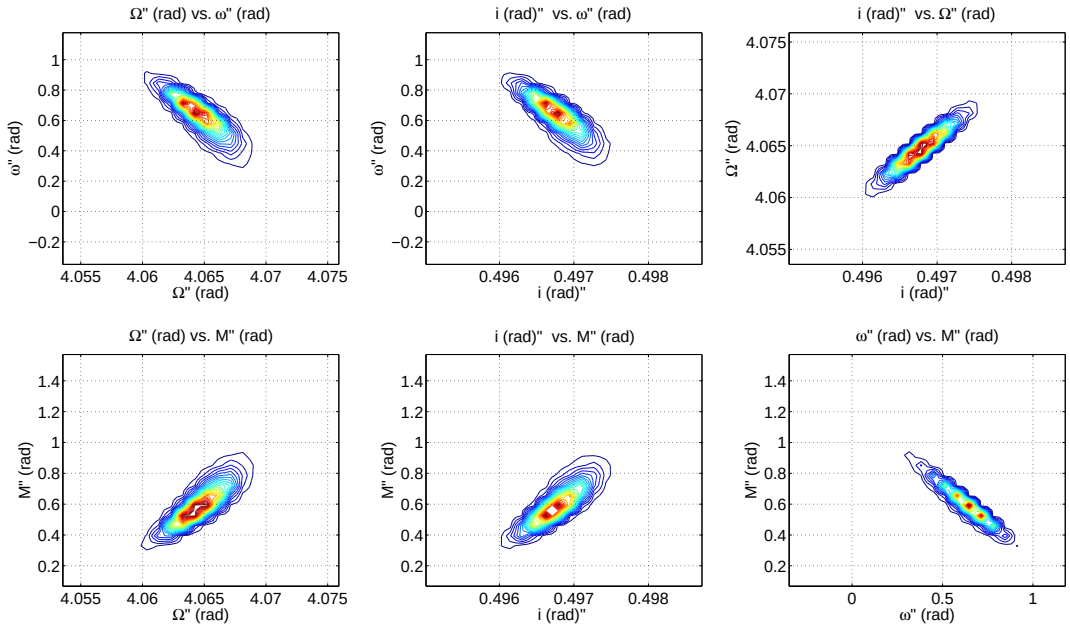

Figure D.22: Increased Eccentricity Track 1 Mean Orbital Element Marginal PDFs with respect to Orientation Angle from TOV Likelihood Solution

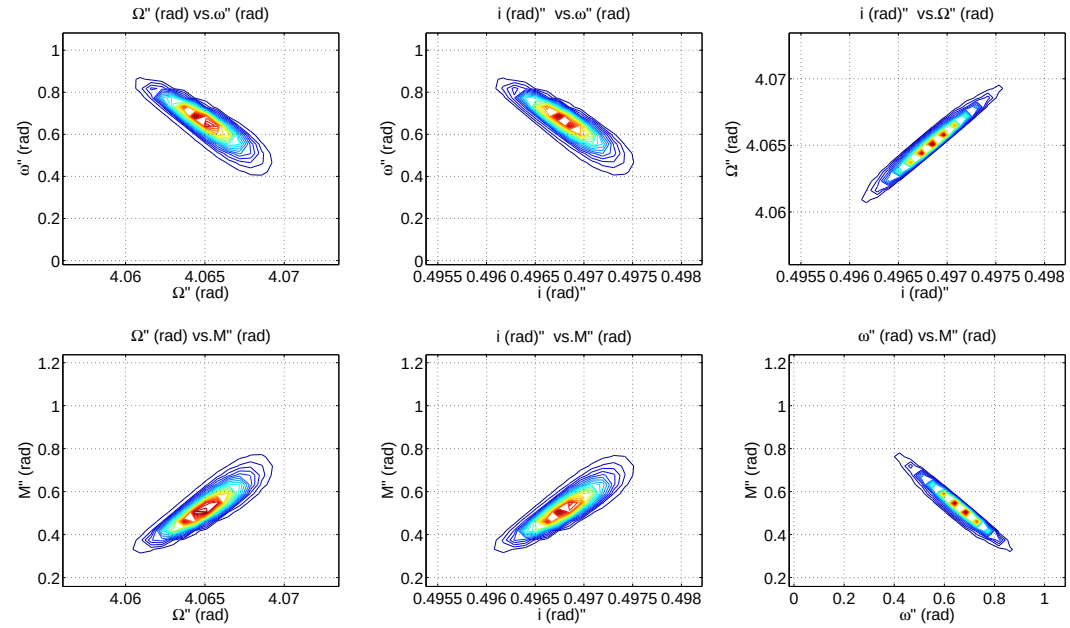

Figure D.23: Increased Eccentricity Track 1 Mean Orbital Element Marginal PDFs with respect to Orientation Angle from Monte Carlo Solution

APPENDIX E

ATTITUDE DETERMINATION FROM Q-METHOD

This appendix presents the q-Method [60,61] of initial attitude determination via finding the optimal quaternion, $\mathbf{q}_{Opt}$, which maximizes the trace of the direction cosine matrix, C, and transpose of the attitude profile matrix, B. The direction cosine matrix relating the body frame of the spacecraft to the inertial frame is unknown but the attitude profile matrix can be computed using the body frame vector measurements, $\tilde{\mathbf{b}}_i$ of observed reference stars and the assumed inertial position vector of the reference stars, $\hat{\mathbf{r}}_i$, which is stored in an onboard catalog. The attitude profile matrix is shown in Equation (E.1) for 1 to n instantaneously available measurements.

$$B = \sum_{i=1}^{n} \tilde{\mathbf{b}}_i \hat{\mathbf{r}}_i^T \tag{E.1}$$

The q-Method then seeks to maximize the produce of $\mathbf{q}^T K \mathbf{q}$ with respect to $\mathbf{q}$ which is done by spectrally decomposing the matrix K and then $\mathbf{q}_{Opt}$ corresponds to the maximum eigenvalue of K. The K matrix is given by Equation (E.2).

$$K = \left[\begin{array}{c:c} B + B^T - \mathbf{tr}\left[B\right]\mathbf{1}_{3\times 3} & \sum_{i=1}^{n}\left[\tilde{\mathbf{b}}_i\times\right]\hat{\mathbf{r}}_i \\ \hdashline \left[\sum_{i=1}^{n}\left[\tilde{\mathbf{b}}_i\times\right]\hat{\mathbf{r}}_i\right]^T & \mathbf{tr}\left[B\right] \end{array}\right] \tag{E.2}$$

The direction cosine matrix, C, can then be estimated from the optimal quaternion estimate, $\mathbf{q}_{Opt}$, shown in Equation (E.3).

$$C_{Est} = \mathbf{1}_{3\times 3} - 2q_{Scalar}\left[2q_{Vector}\times\right] + 2\left[q_{Vector}\times\right]\left[q_{Vector}\times\right] \tag{E.3}$$